Observatório Nacional

TESE DE DOUTORADO

# ANÁLISES ESPECTROSCÓPICAS DE ESTRELAS HOSPEDEIRAS DE PLANETAS KEPLER 2 E DE ESTRELAS DO AGLOMERADO ABERTO NGC 6705: CARACTERIZAÇÃO E ATIVIDADE ESTELAR, RAIOS PLANETÁRIOS E ABUNDÂNCIAS QUÍMICAS

VERÓNICA LOAIZA TACURI

RIO DE JANEIRO
2024

Ministério da Ciência, Tecnologia, Inovações e Comunicações
Observatório Nacional
Programa de Pós-Graduação

Tese de Doutorado

# ANÁLISES ESPECTROSCÓPICAS DE ESTRELAS HOSPEDEIRAS DE PLANETAS KEPLER 2 E DE ESTRELAS DO AGLOMERADO ABERTO NGC 6705: CARACTERIZAÇÃO E ATIVIDADE ESTELAR, RAIOS PLANETÁRIOS E ABUNDÂNCIAS QUÍMICAS

por

Verónica Loaiza Tacuri

Tese submetida ao Corpo Docente do Programa de Pós-graduação em Astronomia do Observatório Nacional, como parte dos requisitos necessários para a obtenção do Grau de Doutor em Astronomia.

Orientadora: Dra. Katia Cunha

Rio de Janeiro, RJ – Brasil
Fevereiro de 2024

L837 Loaiza Tacuri, Verónica
Análises Espectroscópicas de Estrelas Hospedeiras de Planetas Kepler 2 e de Estrelas do Aglomerado Aberto NGC 6705: Caracterização e Atividade Estelar, Raios planetários e Abundâncias químicas [Rio de Janeiro] 2024.
xxii, 158 p. 29,7 cm: graf. il. tab.

Tese (doutorado) - Observatório Nacional - Rio de Janeiro, 2024.

1. palavra chave 1. 2. palavra chave 2. 3. palavra chave 3. 4. palavra chave 4. I. Observatório Nacional. II. Título.

CDU 000.000.000

"ANÁLISES ESPECTROSCÓPICAS DE ESTRELAS HOSPEDEIRAS DE PLANETAS KEPLER 2 E DE ESTRELAS DO AGLOMERADO ABERTO NGC 6705: CARACTERIZAÇÃO E ATIVIDADE ESTELAR, RAIOS PLANETÁRIOS E ABUNDÂNCIAS QUÍMICAS"

VERÓNICA LOAIZA TACURI

TESE SUBMETIDA AO CORPO DOCENTE DO PROGRAMA DE PÓS-GRADUAÇÃO EM ASTRONOMIA DO OBSERVATÓRIO NACIONAL COMO PARTE DOS REQUISITOS NECESSÁRIOS PARA A OBTENÇÃO DO GRAU DE DOUTOR EM ASTRONOMIA.

Aprovada por:

---

Dra. Katia Cunha – Observatório Nacional (Orientadora)

---

Dr. Claudio Bastos Pereira – Observatório Nacional

---

Dra. Adriana Valio – Universidade Presbiteriana Mackenzie

---

Dr. Ivan Ramirez Carrascal – Tacoma Community College

---

Dra. Beatriz Barbuy – Universidade de São Paulo

RIO DE JANEIRO, RJ – BRASIL
2 DE FEVEREIRO DE 2024

*Dedico esta tese à memória da*
*minha querida irmã Frishiam*
*Loaiza Tacuri.*

# Agradecimentos

Quero expressar meu sincero agradecimento, em primeiro lugar, à minha família. Aos meus pais, Basilia Magdalena e Wilber, cujo desejo de construir uma carreira profissional, mesmo sacrificando muito, foi um exemplo que me motivou a prosseguir com meus estudos. Agradeço também aos meus irmãos, Frank, Wilber e Lenin, por me apoiarem à distância e pela confiança depositada em mim para continuar minha trajetória acadêmica.

Ao Fredi, meu parceiro, a quem admiro muito. Agradeço por estar ao meu lado durante mais esta etapa da minha vida e por prestar ajuda incondicional durante a última parte do meu doutorado.

À Dra. Katia Cunha, minha orientadora, expresso minha profunda gratidão pela orientação, paciência e dedicação ao desenvolvimento deste trabalho e ao meu crescimento acadêmico. Encontrar palavras que expressem completamente minha gratidão pela sua contribuição significativa ao longo do mestrado e doutorado é desafiador, mas sua dedicação fez uma diferença notável em minha jornada.

Ao Dr. Verne Smith por me ajudar no meu crescimento acadêmico sendo um colaborador ativo em todos os trabalhos que desenvolvi durante o período do doutorado.

Ao Dr. Iván Ramírez por ter me dado a oportunidade de explorar a espectroscopia estelar durante minha estadia na direção de astrofísica da CONIDA em Perú antes de começar o pósgrado em Astronomia.

Aos professores da pós-graduação do Observatório Nacional que participaram diretamente da minha formação acadêmica na Astronomia.

A todos meus colaboradores, em especial aos doutores Diogo Souto, Cintia Martinez, Rafael Guerço, Fredi Quispe, Luan Ghezzi, João Victor Sales e Jorge Melendez, que me ajudaram com as dúvidas durante o desenvolvimento dos trabalhos dos quais fizeram parte.

Aos meus colegas Nacizo, Fredi e Marçãl pela revisão da gramática, ortografia e semântica dessa tese e pelas sugestões feitas.

A todas as novas amizades que surgiram durante este período, tanto dentro quanto fora do âmbito acadêmico. Em especial, ao meu amigo Marçãl pela amizade desinteressada.

Aos colegas Nacizo, Weslley, Jonthan e Romualdo pelo tempo compartilhado, tanto dentro quanto fora do meio acadêmico, e pelas conversas realizadas junto com Marçal e Fredi durante a hora do café no grupo “Cometa Café”.

À CAPES pela concessão da bolsa de doutorado e ao Observatório Nacional pela oportunidade de ser parte da instituição.

Finalmente, aos meus “gatijos” Curiosty e Perseverance por me dar momentos alegres e divertidos com suas travessuras.

Verónica Loaiza Tacuri

ANÁLISES ESPECTROSCÓPICAS DE ESTRELAS HOSPEDEIRAS DE PLANETAS KEPLER 2 E DE ESTRELAS DO AGLOMERADO ABERTO NGC 6705: CARACTERIZAÇÃO E ATIVIDADE ESTELAR, RAIOS PLANETÁRIOS E ABUNDÂNCIAS QUÍMICAS

# RESUMO

Nesta tese apresentamos um estudo espectroscópico de 201 estrelas de tipos F, G e K que hospedam exoplanetas descobertos pela missão Kepler e Kepler 2 (K2). Analisamos duas amostras, uma contendo 81 estrelas de K2 e 33 da Kepler, cujos espectros foram obtidos com o espectrógrafo Hydra (R$\sim$ 18.500) montado no telescópio WIYN de 3,5 m e cobrindo uma faixa espectral de 6050 a 6350 Å, e outra, contendo 86 estrelas K2, cujos espectros Echelle foram obtidos pelo programa *California Planet Search* (CPS) observados com o espectrógrafo HIRES (R $\sim$ 60.000) no telescópio Keck I de 10 m, abrangendo uma faixa espectral de aproximadamente 3600 a 8000 Å. Determinamos as temperaturas efetivas ($T_{ef}$), gravidades superficiais (log $g$) e metalicidades ([Fe/H]) para todas as estrelas adotando a metodologia espectroscópica que se baseia em medidas de larguras equivalentes e nos equilíbrios de excitação e ionização das linhas de Fe I e Fe II. Os cálculos foram realizados em ETL, usando os modelos de atmosferas de Kurucz e o pacote `qoyllur-quipu` ($q^2$) que utiliza o código de transferência radiativa MOOG. Construímos uma lista de linhas de Fe I e II adequada para a análise dos espectros Hydra, composta por 25 linhas de Fe I e 5 linhas de Fe II. A lista de linhas utilizada para a análise dos espectros do HIRES contém 61 linhas de Fe I e 13 linhas de Fe II, notando que esta lista não inclui linhas consideradas na literatura como sendo sensíveis a campos magnéticos. As massas e raios estelares para as estrelas da amostra foram determinados combinando os parâmetros estelares ($T_{ef}$ e [Fe/H]), a magnitude V e as paralaxes do Gaia DR3 através do método das isócronas. Os raios estelares medidos apresentam uma precisão interna mediana de 4,2% para a amostra Hydra e 4,6% para a amostra HIRES, resultando em uma incerteza interna mediana de 4,4% e 2,6% nos raios planetários derivados, respectivamente. A distribuição dos raios planetários das amostras Hydra e HIRES para planetas confirmados pequenos revelou o bem conhecido "vale do raio", havendo uma ausência de planetas com raios em torno de $R_{planet} \sim 1,9\ R_{\oplus}$, o que não seria observado se nossos resultados apresentassem baixa precisão interna. Para a amostra do Hydra, foram exploradas relações entre o raio planetário, o período orbital e a metalicidade. Encontramos que a metalicidade das estrelas K2 aumenta com o raio planetário, tornando-se mais evidente na transição de planetas menores ($< 4,4\ R_{\oplus}$) para planetas maiores ($> 4,4\ R_{\oplus}$). Além disso, observou-se que a mediana da metalicidade das estrelas K2 que possuem planetas com P $<$ 10 dias é

levemente mais rica em metais, enquanto que para planetas com P $\geqslant$ 10 dias é levemente mais pobre em metais. Para a amostra do HIRES, a atividade cromosférica foi medida em 725 espectros correspondentes a 144 estrelas a partir das linhas de Ca II H ($\lambda$ 3968,47 Å) e K ($\lambda$ 3933,66 Å), utilizando o índice $S_{HK}$ do Monte Wilson; os valores de $S_{HK}$ também foram convertidos para o indicador de atividade cromosférica log $R'_{HK}$. Os valores de log $R'_{HK}$ foram investigados em função do período de rotação estelar (P$rot$), e observamos que a atividade cromosférica diminui com o aumento de P$rot$, embora haja uma grande dispersão em log $R'_{HK}$ (aproximadamente 0,5 dex) para um dado P$rot$. A distribuição dos índices $R'_{HK}$ em nossa amostra de estrelas anãs evidenciou uma escassez de estrelas F e G com níveis intermediários de atividade, conforme encontrado por estudos anteriores: a "lacuna Vaughan-Preston". Por fim, para as amostras Hydra e HIRES, investigou-se o efeito que a atividade estelar pode ter na obtenção dos parâmetros estelares, incluindo na análise linhas de Fe I que são dadas como sendo sensíveis ao campo magnético. Nossos resultados não indicam que haja diferenças significativas entre os resultados das análises sem incluir ou incluindo linhas sensíveis ao campo magnético. No entanto, notamos que as estrelas mais ativas (log $R'_{HK} > -5,0$) apresentam uma dispersão maior nas diferenças em $T_{ef}$ e [Fe/H] entre as duas análises. A segunda parte desta Tese consistiu em determinar as abundâncias químicas de 16 elementos (C, N, O, Na, Mg, Al, Si, K, Ca, Ti, V, Cr, Mn, Fe, Co e Ni) em uma amostra de 11 estrelas gigantes vermelhas do aglomerado do disco galáctico NGC 6705. A análise é baseada em espectros do infravermelho próximo (1,51 - 1,70 $\mu$m) do levantamento APOGEE utilizando a técnica de síntese espectral. Os espectros sínteticos foram calculados em ETL utilizando modelos MARCS com geometria esférica com o código de transferência radiativa Turbospectrum. As temperaturas efetivas das estrelas da amostra foram determinadas por meio de calibrações fotométricas, e as gravidades superficiais foram obtidas a partir de equações fundamentais. Nossos resultados indicam que possivelmente sete estrelas da amostra pertencem ao ramo das gigantes vermelhas e quatro ao agrupamento vermelho. Encontramos uma metalicidade média para o aglomerado de $\langle$[Fe/H]$\rangle = +0,13 \pm 0,04$, indicando que o NGC 6705 é rico em metais, como esperado para um aglomerado jovem no disco interno da Galáxia. As gigantes vermelhas do NGC 6705 exibem baixas abundâncias de $^{12}$C ($\langle[^{12}\mathrm{C/Fe}]\rangle = -0,16$) e um enriquecimento de $^{14}$N ($\langle[^{14}\mathrm{N/Fe}]\rangle = +0,51$), que são assinaturas importantes da primeira dragagem do ramo das gigantes vermelhas. O NGC 6705 também fornece informações valiosas para o estudo da mistura estelar, dada sua massa '*turn-off*' que é de aproximadamente M$\sim$3,3 $M_\odot$. Um resultado interessante dessa Tesa é a identificação de uma assinatura adicional de dragagem nas abundâncias de Na, que são enriquecidas de $\langle$[Na/Fe]$\rangle = +0,29$, tendo uma correção não-LTE muito pequena. As abundâncias de $^{16}$O e Al foram encontradas próximas ao valor solar. Todas as abundâncias derivadas sensíveis à mistura são consistentes com modelos estelares de aproximadamente 3,3 $M_\odot$ evoluindo ao longo do ramo das gigantes vermelhas e para o agrupamento vermelho.

Resultados anteriores na literatura sugeriram que o jovem aglomerado aberto de disco interno NGC 6705 é enriquecido em elementos-$\alpha$. Investigamos essa possibilidade por meio de uma análise independente da abundância química de cinco elementos-$\alpha$ (O, Mg, Si, Ca e Ti) e encontramos que abundância média dos elementos-$\alpha$ em relação ao ferro é $\langle[\alpha/\mathrm{Fe}]\rangle = -0,03 \pm 0,05$, o que não está em desacordo com as expectativas das tendências gerais de abundância do disco Galáctico.

Verónica Loaiza Tacuri

SPECTROSCOPIC ANALYSES OF PLANET HOSTING STARS FROM KEPLER 2 AND FROM THE OPEN CLUSTER NGC 6705: STELLAR CHARACTERIZATION AND ACTIVITY, PLANETARY RADII AND CHEMICAL ABUNDANCES

# ABSTRACT

In this thesis we present a spectroscopic study of 201 stars of F-, G-, and K-type stars that host exoplanets discovered by the Kepler and Kepler 2 (K2) mission. We analyzed two samples, one containing 81 stars from K2 and 22 from Kepler, whose spectra were obtained with the Hydra spectrograph (R$\sim 18,500$) mounted on the WIYN 3.5 m telescope, covering the spectral range between 6050 to 6350 Å, and another, containing 86 K2 stars, whose Echelle spectra were obtained by the California Planet Search (CPS) program, observed with the HIRES spectrograph (R $\sim$ 60,000) at the Keck I 10 m telescope and spanning the spectral range between approximately 3600 to 8000 Å. We determined the effective temperatures ($T_{\rm eff}$), surface gravities (log $g$), and metallicities ([Fe/H]) by adopting the spectroscopic methodology based on measurements of equivalent widths and the excitation and ionization equilibria of the Fe I and Fe II lines. The calculations were carried out in ETL, using the Kurucz atmospheric models and the `qoyllur-quipu` ($q^2$) package which uses the MOOG radiative transfer code. We constructed a Fe I and II line list adequate for the analysis of Hydra spectra, consisting of 25 lines of Fe I and 5 lines of Fe II. The line list used to analyze HIRES spectra contains 61 lines of Fe I and 13 lines of Fe II, noting that this list does not include lines which are deemed as being sensitive to magnetic fields. Stellar masses and radii were derived by combining the stellar parameters ($T_{\rm eff}$ and [Fe/H]) with Gaia DR3 parallaxes and V magnitudes using isochrones methods and $q^2$ code. The measured stellar radii have a median internal precision of 4.2% for the Hydra sample and 4.6% for the HIRES sample, leading to a median internal uncertainty of 4.4% and 2.6% in the derived planetary radii, respectively. The distribution of planetary radii of the Hydra and HIRES samples for confirmed small planets revealed the well-known radius gap, with a dearth os planets with radii around $R_{\rm planet} \sim 1.9\ R_\oplus$, what would not be observed if our results had lower internal precision. For the Hydra sample, relationships between planetary radius, orbital period, and metallicity were explored. We found that the metallicity of K2 stars increases with planetary radius, becoming more pronounced in the transition from smaller planets ($< 4.4\ R_\oplus$) to larger planets ($> 4.4\ R_\oplus$). Furthermore, it was observed that the median metallicity of K2 stars hosting planets with P $<$ 10 days is slightly metal-rich, while for planets with P $\geqslant$ 10 days it is slightly metal-poor. For the HIRES sample, chromospheric activity was measured in 725 spectra corresponding to 144 stars from the Ca II H ($\lambda$ 3968.47 Å) and K

($\lambda$ 3933.66 Å) lines using the Mt. Wilson $S_{HK}$ index; the $S_{HK}$ values were also converted to the chromospheric activity indicator log $R'_{HK}$. Values of log $R'_{HK}$ were investigated as a function of stellar rotational period (P*rot*), and we found that chromospheric activity decreases with increasing P*rot*, although there is a large scatter in log $R'_{HK}$ ($\sim$0.5 dex) for a given P*rot*. The distribution of the R' HK indices in our sample of dwarf stars showed a lack of F and G stars with intermediate activity levels, as found by previous studies: the "Vaughan-Preston gap". Finally, for the Hydra and HIRES samples, we investigated the effect of stellar activity on the determination of stellar parameters, including magnetic field sensitive Fe I lines in the spectroscopic analysis. No significant differences were found between the analyses with and without magnetic field sensitive lines. However, it is noted that the most active stars (log $R'_{HK} > -5.0$) show a larger scatter in the differences in $T_{eff}$ and [Fe/H] between the two analyses. In the second part of this thesis we determined the chemical abundances of 16 elements (C, N, O, Na, Mg, Al, Si, K, Ca, Ti, V, Cr, Mn, Fe, Co, and Ni) in a sample of 11 red giant stars from the Galactic disk cluster NGC 6705. The analysis was based on near-infrared spectra (1.51 - 1.70 $\mu$m) from the APOGEE survey using the spectral synthesis technique. The synthetic spectra were calculated in LTE using MARCS models with spherical geometry with the Turbospectrum radiative transfer code. The effective temperatures of the sample stars were determined using photometric calibrations, and the surface gravities were obtained from fundamental equations. Our results suggest that seven stars in the sample may belong to the red giant branch, while four may belong to the red clump. We find a mean cluster metallicity of $\langle$[Fe/H]$\rangle = +0.13 \pm 0.04$, indicating that NGC 6705 is metal-rich, as expected for a young cluster in the inner disk of the Galaxy. The red giants of NGC 6705 exhibit low $^{12}$C abundances ($\langle[^{12}C/Fe]\rangle = -0.16$) and enhanced $^{14}$N abundances ($\langle[^{14}N/Fe]\rangle = +0.51$), which are key signatures of the first dredge-up on the red giant branch. NGC 6705 also provides valuable insights for studying stellar mixing, given its turn-off mass of M$\sim$3.3 $M_\odot$. An interesting result from this detailed study of chemical abundances is the identification of an additional signature of dredge-up in the Na abundances, which are enriched with $\langle$[Na/Fe]$\rangle = +0.29$, along with a very small non-LTE correction. The $^{16}$O and Al abundances are found to be near-solar. All derived mixing-sensitive abundances are consistent with stellar models of approximately 3.3 $M_\odot$ evolving along the red giant branch and onto the red clump. Previous results in the literature have suggested that the young inner-disk open cluster NGC 6705 is $\alpha$-enhanced. We have investigated this possibility via an independent chemical abundance analysis and found that the mean $\alpha$-element abundance relative to iron is $\langle[\alpha/Fe]\rangle = -0.03 \pm 0.05$, which is not at odds with expectations from general Galactic disc abundance trends.

# Lista de Figuras


1.1 Representação esquemática de um trânsito planetário . . . . . 5
1.2 Regiões do céu observadas pela missão Kepler 2 . . . . . 6
1.3 Relação entre a taxa de ocorrência de planetas gigantes e a metalicidade das estrelas . . . . . 8
1.4 Raio planetário como função do período orbital . . . . . 11
1.5 Índice do fluxo (S) como função do índice de cor instrumental ($C_{RV}$) . . . 14
1.6 Representação esquemática da distribuição da razão O/Fe vs. metalicidade 16

3.1 Comparação das temperaturas efetivas . . . . . 78
3.2 Comparação das temperaturas efetivas incluindo linhas sensíveis a campo magnético . . . . . 79
3.3 Comparações das gravidades superficiais . . . . . 81
3.4 Comparações das gravidades superficiais incluindo linhas sensíveis a campos magnéticos . . . . . 82
3.5 Comparação das gravidades superficiais espectroscópicas e asterosismologicas 83
3.6 Comparação das metalicidades . . . . . 84
3.7 Comparação das metalicidades incluindo linhas sensíveis a campo magnético 85

A.1 Camadas que compõem a atmosfera estelar. . . . . 128
A.2 Largura equivalente ($W_\lambda$) do perfil de uma linha isolada . . . . . 136
A.3 Curva de crescimento . . . . . 137
A.4 Comparação entre o espectro observado e o espectro sintético . . . . . 138

# Lista de Tabelas

B.1 Main sample data (Table 1 of Paper I) . . . . . 141
B.2 Stellar Parameters, Radii and Masse (Table 3 of Paper I) . . . . . 143
B.3 Planetary Radii (Table 6 of Paper I) . . . . . 145
B.4 Sample K2 Stars (Table 1 of Paper II) . . . . . 149
B.5 Iron Line List (Table 2 of Paper II) . . . . . 152
B.6 Stellar Parameters (Table 3 of Paper II) . . . . . 154
B.7 Planetary Radii (Table 4 of Paper II) . . . . . 156

# Sumário

**Lista de Figuras** **xvii**

**Lista de Tabelas** **xix**

**1 Introdução** **1**
1.1 Estrelas e Exoplanetas da Missão Kepler e K2 . . . . . 4
1.1.1 A Conexão Estrela - Planeta . . . . . 7
1.1.2 Atividade Cromosférica Estelar . . . . . 11
1.2 O Aglomerado Aberto Jovem NGC 6705 . . . . . 14
1.3 Este Trabalho de Tese . . . . . 18

**2 Análise Espectroscópica de Estrelas K2 Hospedeiras de Planetas** **21**

**3 Caracterização Estelar e Atividade Cromosférica de Estrelas K2** **47**
3.1 Comparações com Resultados Prévios da Literatura . . . . . 77
3.1.1 Temperaturas Efetivas e Gravidades Superficiais . . . . . 77
3.1.1.1 Gravidades Superficiais Espectroscópicas versus Asterosísmicas . . . . . 80
3.1.2 Metalicidades . . . . . 80

**4 Análise Espectroscópica de Gigantes Vermelhas do NGC 6705** **87**

**5 Conclusões** **105**
5.1 Estrelas K2 . . . . . 105
5.2 NGC 6705 . . . . . 108
5.3 Perspectivas Futuras . . . . . 110

**Referências Bibliográficas** **111**

**A A Formação de Linhas Espectrais** **127**
A.1 Interação entre radiação e matéria . . . . . 127
A.2 Equilíbrio Termodinâmico Local . . . . . 129
A.3 Modelos de Atmosfera . . . . . 129

A.4 Formação de linhas espectrais . . . . . 131
A.4.1 Perfil de linhas espectrais . . . . . 131
A.4.1.1 Alargamentos das linhas Espectrais . . . . . 132
A.5 Métodos para Determinar a Composição Química Estelar . . . . . 134
A.5.1 Medidas de Larguras Equivalentes . . . . . 135
A.5.1.1 Curva de Crescimento . . . . . 135
A.5.2 Síntese Espectral . . . . . 137

**B Tabelas Eletrônicas** **141**

# Capítulo 1

# Introdução

As estrelas, embora pareçam apenas pequenos pontos de luz no céu, revelam uma história rica por meio da luz que emitem. Utilizando a espectroscopia astrônomos podem decifrar a composição química, temperatura e movimento das estrelas, identificando adicionalmente, sistemas estelares múltiplos, como sistemas binários, associações estelares e aglomerados estelares.

Os primórdios da espectroscopia remontam aos experimentos de Isaac Newton em 1666, quando ele dispersou a luz branca utilizando um prisma. Embora Newton não compreendesse totalmente o fenômeno na época, ele demonstrou que o prisma não cria cores, mas revela que aquelas estão presentes na luz branca. Mais tarde, em 1817, Joseph Fraunhofer determinou que estrelas diferentes têm espectros distintos. Os espectros estelares foram inicialmente classificados em esquemas simples, reconhecendo apenas três tipos de espectros. Por outro lado, uma descoberta de grande importância foi realizada por Fraunhofer ao observar pela primeira vez padrões de linha de absorção no espectro solar.

À medida que os instrumentos melhoraram, tornou-se possível fazer distinções cada vez mais sutis através dos espectros de diferentes estrelas. Os astrônomos Angelo Secchi e Edward Charles Pickering foram os primeiros a notar que os espectros estelares podiam ser divididos em grupos pela aparência geral dos seus espectros. Nos vários esquemas de classificação que propuseram, as estrelas foram agrupadas pela proeminência de linhas espectrais específicas. No esquema de Secchi, por exemplo, estrelas com linhas de hidrogênio muito fortes eram chamadas de tipo I, estrelas com linhas fortes de íons metálicos como ferro e cálcio eram chamadas de tipo II, estrelas com faixas largas de absorção que ficavam mais escuras em direção ao azul eram chamadas de tipo III, entre outras categorias. Com base neste trabalho inicial, os astrônomos do Observatório de Harvard refinaram os tipos espectrais e os renomearam com letras, A, B, C, etc. Eles também embarcaram em um grande projeto conduzido por um grupo de astrônomas, Williamina Fleming, Annie Jump

Cannon e Antonia Maury. Os resultados desse trabalho, o Catálogo Henry Draper[1], foram publicados entre 1918 e 1924 e forneceram classificações de 225.300 estrelas.

Em 1901, Annie Jump Cannon, também do grupo de Pickering, deu contribuição fundamental ao refinar significativamente o sistema de classificação espectral. Indo além do estabelecido pelo esquema de Pickering e Fleming, Cannon reestruturou a sequência de espectros, colocando as classes O e B antes da A. Além disso, ela introduziu subdivisões decimais (por exemplo, A0–A9) e consolidou diversas categorias espectrais a partir da análise dos espectros. Essas alterações resultaram na transformação do esquema de classificação de Harvard, originalmente "O B A F G K M", em uma sequência que reflete as temperaturas estelares. Presentemente, a sequência vai desde as estrelas O, azuis mais quentes, até as estrelas M, vermelhas mais frias. Cannon contribuiu fortemente para a compreensão mais refinada da diversidade estelar, proporcionando uma organização mais precisa e abrangente das classes espectrais. Estrelas mais próximas do início desta sequência são chamadas de estrelas do tipo 'inicial' (do inglês *early-type stars*), e aquelas mais próximas do final são chamadas de estrelas do tipo tardio (do inglês *late-type stars*). Essas denominações também distinguem as estrelas dentro das subdivisões espectrais, permitindo que os astrônomos se refiram a uma estrela K0 como uma "estrela K inicial" ou mencionem uma estrela B9 como uma "estrela B tardia". Entre 1911 e 1914 Cannon classificou cerca de 200,000 espectros, os quais também foram incluídos no catálogo de Henry Draper. Finalmente, vale notar que essa classificação espectral continua a ser utilizada até o presente.

Nas últimas décadas, por um lado dados os avanços instrumentais que culminaram em espectrógrafos e telescópios cada vez mais otimizados, aliados a avanços computacionais, um grande número de estudos espectroscópicos detalhados baseados em espectros estelares de alta e média resolução espectral determinaram parâmetros estelares tais como a temperatura efetiva, gravidade superficial, metalicidade global, assim como abundâncias detalhadas de um grande número de elementos químicos em estrelas da Via Lactea – algumas referências relevantes podem ser encontradas na compilação PASTEL (SOUBIRAN *et al.*, 2016) ou de Hypatia (HINKEL *et al.*, 2014), por exemplo.

Há aproximadamente quinze anos, entretanto, entramos na era dos grandes levantamentos estelares da Galáxia, o que levou a área de espectroscopia estelar a um patamar ainda avançado, com a produção de uma enorme quantidade de resultados de parâmetros estelares e abundâncias de elementos químicos formados em diferentes sítios nucleosintéticos para pelo menos um milhão de estrelas de diferentes populacões estelares da Galáxia. Entre os principais grandes levantamentos espectroscópicos de alta resolução temos o SDSS *Apache Point Observatory Galactic Evolution Experiment* (MAJEWSKI *et al.*, 2017, APOGEE), cujo principal objetivo foi mapear a Via Láctea através do estudo químico e dinâmico detalhado de estrelas anãs e gigantes vermelhas distribuídas

[1] Em homenagem ao benfeitor que financiou o estudo

por toda a Galáxia, a partir de espectros estelares obtidos com dois espectrógrafos multifibras de alta resolução (300 fibras, R $\sim$ 22.500) no infravermelho próximo (1,51 - 1,7 $\mu$m). (Espectros APOGEE serão analizados nesta tese, ver Capitulo 4). O levantamento GAIA-ESO (RANDICH *et al.*, 2022) que usou o instrumento FLAMES no ESO VLT (espectrógrafos no óptico GIRAFFE (R$\sim$ 5.000 até $\sim$ 30.000) e UVES (R$\sim$ 47.000)), para observar estrelas abrangendo todas as populações da Via Láctea, com foco especial em aglomerados estelares abertos. Temos também o levantamento GALactic Archeology with Hermes (BUDER *et al.*, 2021, GALAH) que utiliza o espectrógrafo óptico HERMES (R$\sim$ 28.000) no Telescópio Anglo-Australiano, que possibilita a obtenção simultânea de espectros ópticos de 400 estrelas e tem observado estrelas de todas as populações estelares.

Entretanto, apesar de todo este avanço, estudos espectroscópicos detalhados e de precisão de estrelas que têm planetas conhecidos ainda são relativamente raros. O conhecimento das caracteristicas físicas de uma estrela hospedeira, tal como raio, massa, temperatura efetiva, metalicidade, campo magnético, atividade estelar, etc, é fundamental também para a área de exoplanetas e para se compreender mais profundamente conexões entre estrela e exoplanetas, assim como os processos de formação planetária. Por exemplo, foi a partir de estudos espectroscópicos de alta-resolução que parâmetros estelares e raios precisos puderam ser obtidos para estrelas hospedeiras de planetas observadas pela missão Kepler (BORUCKI *et al.*, 2010; KOCH *et al.*, 2010), que aliados a distâncias estelares precisas obtidas pela missão GAIA (GAIA COLLABORATION *et al.*, 2023) propiciaram a descoberta de características importantes sobre a formação de planetas de tamanho terrestre, como a existência de uma lacuna na distribuição de raios de pequenos planetas chamada de "vale do raio" (do inglês "*radius gap*") ou vale de evaporação, onde observa-se uma ausência de planetas com raios aproximadamente entre 1,5 e 2 vezes o raio da Terra, possivelmente devido à perda de massa causada pelo processo de fotoevaporação (OWEN e WU, 2013). Em particular com raios estelares precisos, foi possível também observar que a relação entre o raio planetário versus período orbital no vale de evaporação possui uma inclinação, diminuindo conforme aumenta o período orbital (MARTINEZ *et al.*, 2019), conforme discutiremos em mais detalhes na próxima seção. Uma primeira parte deste trabalho de tese analisa estrelas hospedeiras de planetas da missão K2 (HOWELL *et al.*, 2014), e também desenvolve metodologia que consegue analisar espectros com cobertura espectral bastante reduzida e de mais baixa resolução, produzindo ainda assim resultados de mesma precisão alcançada, por exemplo, pelo trabalho de alta-resolução de MARTINEZ *et al.* (2019), além de investigar atividade estrelar em estrelas K2. A seguir, faremos uma breve introdução aos principais tópicos que serão abordadas nesta tese.

## 1.1 Estrelas e Exoplanetas da Missão Kepler e K2

Desde a descoberta do primeiro planeta orbitando uma estrela de tipo solar (MAYOR e QUELOZ, 1995), já se passaram mais de duas décadas, e atualmente, foram confirmados mais de 5500 exoplanetas[2] orbitando mais de 4250 estrelas[3]. As técnicas que proporcionaram o maior número de descobertas de exoplanetas são a de velocidade radial e o trânsito planetário.

O método de velocidade radial é uma técnica que detecta exoplanetas monitorando as variações na velocidade radial de uma estrela hospedeira. Quando um planeta orbita uma estrela, a estrela também se move devido à gravidade do planeta. Esse movimento é detectado pelo deslocamento Doppler nas linhas espectrais da estrela. Ao analisar mudanças na velocidade radial ao longo do tempo, podem-se inferir a presença, massa mínima e elementos orbitais de exoplanetas. Este método tem sido crucial na descoberta de muitos exoplanetas, especialmente os massivos e próximos às suas estrelas. Foi usando este método que MAYOR e QUELOZ (1995) detectaram o exoplaneta 51 Pegasi b e que MARCY *et al.* (1997) demonstraram que o 51 Pegasi b apresentava um raio orbital de 0,05 UA, um período orbital de 4,2 dias e uma massa mínima de 0,46 vezes a massa de Júpiter. Atualmente, segundo a NASA Exoplanet Archive o número de exoplanetas detectados a partir de medidas de velocidade radial é de $\sim$ 19% do número total de planetas descobertos, ou seja, 1075 planetas.

A técnica do trânsito planetário é um método de detecção de exoplanetas, pelo qual um planeta passa entre sua estrela hospedeira e a Terra, causando uma diminuição temporária no brilho estelar. Telescópios espaciais, como Kepler (BORUCKI *et al.*, 2010; KOCH *et al.*, 2010), TESS (*Transiting Exoplanet Survey Satellite*; RICKER *et al.*, 2015, e a missão CoRot (DELEUIL *et al.*, 2000, 2018), monitoram essas variações de luz ao longo do tempo para identificar planetas orbitando a estrela. A análise dos trânsitos fornece informações sobre o tamanho do planeta, sua órbita e até mesmo sua atmosfera. Um dos parâmetros obtidos durante um trânsito planetário é a profundidade de trânsito, que refere-se à redução temporária no brilho de uma estrela quando um planeta passa à sua frente. Essa medida é expressa como a fração do fluxo estelar bloqueado pelo planeta durante o evento. Uma representação esquemática do transito planetário é mostrada na Figura 1.1. A duração do trânsito é medida desde o momento que o planeta começa a passar na frente da estrela (t1) até o momento em que o planeta termina de passar na frente da estrela (t4). Nos pontos t2 até t3 é quando o planeta diminui o brilho da estrela (profundidade de trânsito, $\Delta F$), sendo que a profundidade de trânsito é definida como $\Delta F = \left(\frac{R_{pl}}{R_\star}\right)^2$. Existem muitos estudos na literatura que fornecem as profundidades de trânsito de planetas detectados, em particular pela missão Kepler (ver por exemplo,

[2] https://exoplanetarchive.ipac.caltech.edu/
[3] https://exoplanets.nasa.gov/discovery/exoplanet-catalog/

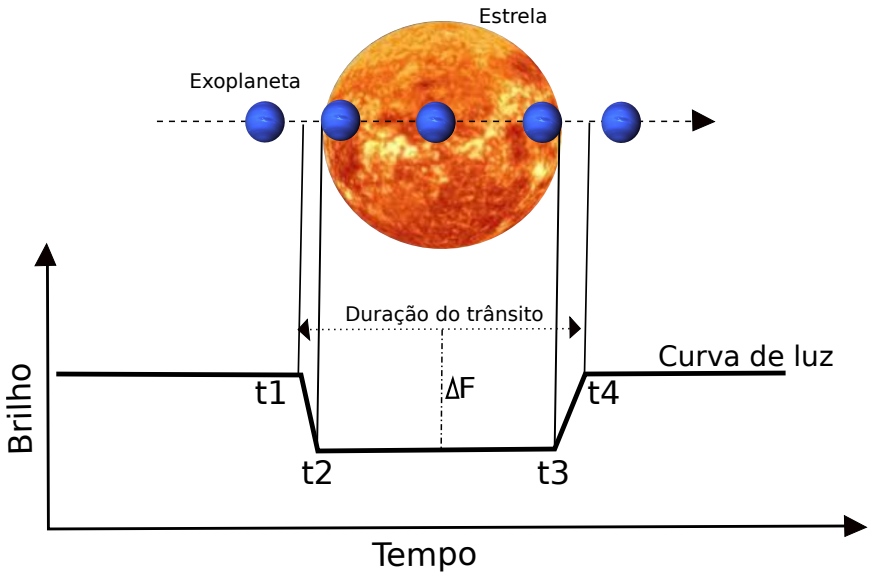


**Figura 1.1** – Representação esquemática de um trânsito planetário. O brilho da estrela começa a diminuir quando o planeta passa na frente da estrela, isso é observado nos pontos t1 até t4 da curva de luz.

CHRISTIANSEN *et al.*, 2017; KRUSE *et al.*, 2019; LIVINGSTON *et al.*, 2018; VANDERBURG *et al.*, 2016). Utilizando esta técnica já foram confirmados até o presente 4150 exoplanetas ($\sim$ 74% do número total).

A detecção de exoplanetas orbitando diferentes tipos de estrelas oferece perspectivas sobre os diversos cenários nos quais esses planetas se originam. A missão Kepler (BORUCKI, 2016; BORUCKI *et al.*, 2010; KOCH *et al.*, 2010), lançada em 2009, foi a primeira missão da NASA que tinha como objetivo detectar exoplanetas, especialmente aqueles do tamanho da Terra, na região habitável de suas estrelas. Utilizando o método de trânsito planetário, o telescópio espacial Kepler monitorou continuamente durante cerca de quatro anos o brilho de 156,000 estrelas, identificando diminuições regulares que indicavam a presença de exoplanetas. A missão Kepler superou a expectativa inicial que era de 3,5 anos e descobriu milhares de candidatos a exoplanetas.

A missão estendida da Kepler, chamada K2 (HOWELL *et al.*, 2014), ocorreu após a fase principal da missão e começou em 2014. Diante de problemas com os giroscópios do telescópio, a missão K2 reposicionou o Kepler para observar diferentes partes do céu limitadas a campos próximos ao plano da eclíptica em 20 campanhas de aproximadamente 80 dias cada (ver Figura 1.2). Em particular, ao continuar a busca de estrelas com potenciais planetas, a K2 expandiu suas observações para estrelas de pre-sequência principal, anãs-M, estrelas membros de aglomerados abertos próximos, dentre outros. A missão K2 contribuiu significativamente para a astronomia até seu término em 30 de outubro de 2018, consolidando o impacto duradouro da missão Kepler como um todo, elevando o número de estrelas monitoradas para 500.000.

Compreender a relação entre as propriedades dos exoplanetas e as características das

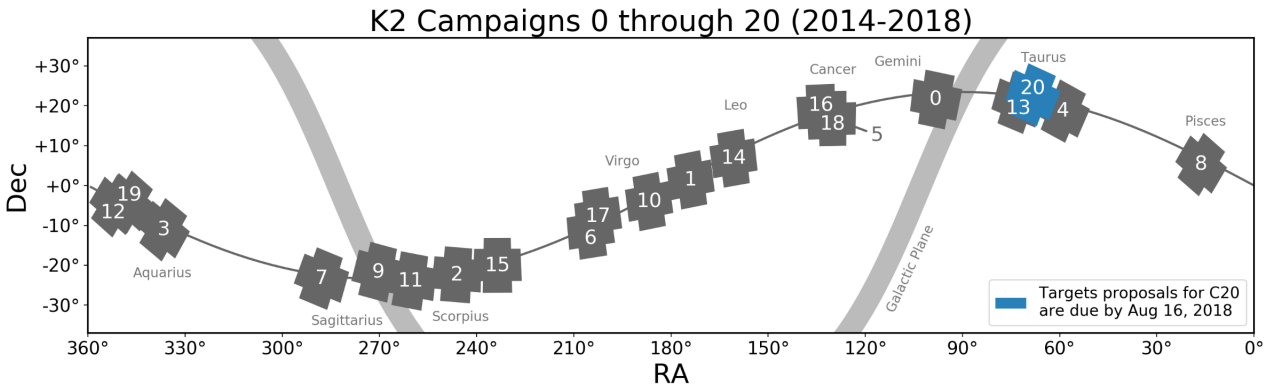


**Figura 1.2** – Regiões do céu observadas pela missão K2. Imagem produzida pela NASA e STScI.

estrelas hospedeiras desempenha um papel crucial na modelagem das condições dos discos protoplanetários e, por conseguinte, do processo de formação planetária (LISSAUER e STEWART, 1993). Em particular, a caracterização adequada das estrelas é um elemento chave para detectar os planetas e compreender suas propriedades. O raio planetário é determinado por meio de observações de trânsito, e a massa planetária por meio de medições de velocidade radial. A obtenção desses parâmetros depende das propriedades das estrelas hospedeiras, portanto, é limitada pela precisão com que essas são medidas (ADIBEKYAN *et al.*, 2021). Ao se determinar com precisão o raio e a massa de uma estrela, obtêm-se também raios e massas planetários precisos. Em última análise, a combinação desses parâmetros fornece informações sobre a composição química dos planetas.

Com o objetivo de conhecer as propriedades físicas das estrelas hospedeiras de exoplanetas descobertos em particular pela missão Kepler (daqui para frente, referidas como Estrelas Kepler), diferentes estudos na literatura têm focado na caracterização estelar, determinando a temperatura efetiva ($T_{eff}$), a gravidade superficial (log $g$) e a metalicidade ([Fe/H]) das estrelas, bem como a massa e o raio estelares, com bastante precisão interna (valores típicos de $\delta T_{eff}$ ∼40–60 K, $\delta$ log $g$ ∼0,05 dex, $\delta$[Fe/H] ∼0,02 dex, $\delta M_\star$ ∼4% e $\delta R_\star$ ∼3%). Conforme discutido anteriormente, esses parâmetros estelares são obtidos prevalentemente via análises espectroscópicas, usando método de síntese espectral (como por exemplo, BREWER e FISCHER, 2018; BUCHHAVE *et al.*, 2012; EVERETT *et al.*, 2013; PETIGURA *et al.*, 2017, dentre outros) ou, usando a técnica clássica da espectroscopia estelar com medidas das larguras equivalentes (EW) das linhas de Fe I e Fe II, baseada no equilíbrio de excitação e ionização dessas linhas de ferro (GHEZZI *et al.*, 2010, 2018, 2021; MARTINEZ *et al.*, 2019). Parâmetros estelares das estrelas Kepler também foram determinados utilizando apenas fotometria (BERGER *et al.*, 2020b), e de modo mais preciso a partir de asterosismologia foram determinadas as gravidades superficiais das estrelas Kepler (como por exemplo, HUBER *et al.*, 2016; PINSONNEAULT *et al.*, 2018; SILVA AGUIRRE *et al.*, 2018, dentre outros), e foram determinados os raios e massas das estrelas Kepler (ver por exemplo, BERGER *et al.*, 2020a; FULTON e PETIGURA, 2018;

JOHNSON *et al.*, 2017; MARTINEZ *et al.*, 2019; VAN EYLEN *et al.*, 2018). Diferentemente das estrelas Kepler, para as estrelas da missão K2 (daqui para frente, estrelas K2), não existem na literatura muitos estudos espectroscópicos que determinam parâmetros estelares incluindo raios e massas estelares. De fato, a maioria das compilações de resultados para estrelas K2 baseou-se em análises fotométricas ou em métodos trigonométricos (por exemplo, BERGER *et al.*, 2020b; BOYAJIAN *et al.*, 2013; VANDERBURG *et al.*, 2016).

### 1.1.1 A Conexão Estrela - Planeta

O estudo da composição química, em particular da metalicidade, de estrelas hospedeiras de exoplanetas tem revelado uma possível conexão com a frequência, arquitetura e composição química dos planetas descobertos que decorreriam do fato que a formação planetária seria o resultado natural do processo de formação das estrelas (ver por exemplo, BUCHHAVE *et al.*, 2014; GHEZZI *et al.*, 2010; MALDONADO *et al.*, 2018; SANTOS *et al.*, 2004).

A hipótese de uma possível correlação entre a frequência de planetas gigantes e a metalicidade estelar foi inicialmente proposta por GONZALEZ (1997). No entanto, essa hipótese baseou-se inicialmente em uma amostra de 4 planetas gigantes orbitando 4 estrelas ricas em metais. Posteriormente, com uma amostra maior, outros estudos encontraram que estrelas F, G e K de sequência principal, e estrelas subgigantes hospedeiras de planetas gigantes ($M_p \sin i \gtrsim 1$ M$_J$), apresentam, em média, metalicidades mais altas (aproximadamente 0,2 dex) em comparação com suas contrapartes estelares de campo, que pertencem aos tipos espectrais F, G e K (ver por exemplo; FISCHER e VALENTI, 2005; GHEZZI *et al.*, 2010, 2018; MORTIER *et al.*, 2013; SANTOS *et al.*, 2001, 2004; SOUSA *et al.*, 2011; ZHU, 2019). Para explicar tal enriquecimento metálico, foram propostas duas hipóteses: o mecanismo de poluição e a origem primordial. A hipótese da poluição sugere que a metalicidade de uma estrela pode ser modificada pela presença de planetas ao seu redor. À medida que esses objetos migram, material sólido do disco protoplanetário, incluindo planetesimais e planetas, pode ser incorporado à zona convectiva da estrela. Já a hipótese primordial sugere que a probabilidade de formação de um planeta gigante está fortemente relacionada à metalicidade da nuvem de gás e poeira que deu origem ao sistema. Portanto, a abundância de metais nas estrelas hospedeiras de planetas gigantes é atribuída à alta metalicidade da nuvem primordial, indicando que os planetas gigantes têm sua origem em ambientes de alta metalicidade.

Os dois principais modelos que explicam a formação planetária são a acreção do núcleo (POLLACK *et al.*, 1996) e a instabilidade gravitacional (BOSS, 1997). No primeiro modelo, um núcleo sólido se formaria inicialmente pela aglomeração resultante de colisões sucessivas dos pequenos grãos que compõem o disco protoplanetário. Conforme a massa

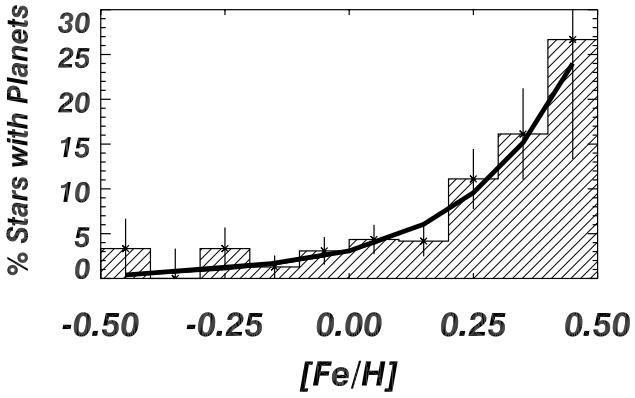


**Figura 1.3** – Relação entre a taxa de ocorrência de planetas gigantes e a metalicidade em estrelas do tipo solar. A linha sólida preta ilustra o ajuste quadrático da expressão $P(planeta) = 0,03 \times 10^{2,0[Fe/H]}$. Figura adaptada de FISCHER e VALENTI (2005).

desse núcleo aumentasse, sua capacidade de retenção de materiais gasosos se aprimoraria de maneira mais eficaz. Ao atingir uma massa crítica específica de 5 a 10 massas terrestres (MORDASINI *et al.*, 2014), ocorre a rápida acreção de gás, dando origem aos planetas. No segundo modelo, em contraste, as instabilidades gravitacionais seriam responsáveis pelo surgimento de regiões mais densas no disco protoplanetário. Os planetas se formariam como resultado do colapso gravitacional dessas regiões.

Voltando à correlação "planeta-metalicidade", que revelou que a formação de planetas gigantes é favorecida em torno de estrelas com maior teor metálico, encontra-se que essa correlação está alinhada com as previsões do modelo de acreção do núcleo (IDA e LIN, 2004). A incidência de planetas gigantes está fortemente associada à metalicidade, aumentando proporcionalmente ao quadrado do número de átomos de ferro. FISCHER e VALENTI (2005) quantificaram essa relação a partir de um estudo de 1040 estrelas do tipo solar, observadas em um levantamento de velocidade radial e para as quais foram determinados parâmetros estelares e metalicidades. Nesse estudo calcularam a incidência relativa de exoplanetas em cada intervalo de metalicidade usando as estrelas de seus respectivos grupos de controle e derivaram a expressão para planetas gigantes detectados pelo método de velocidade radial, $\mathrm{P(planeta)} = 0,03 \times 10^{2,0[\mathrm{Fe/H}]}$, que é valida no intervalo $-0,5 \gtrsim [\mathrm{Fe/H}] \gtrsim +0,5$, e para planetas com períodos orbitais menores que 4 anos e com semiamplitudes de velocidade radial $K > 30$ m/s. A Figura 1.3 adaptada de FISCHER e VALENTI (2005) ilustra esse aumento proporcional.

Indo para o regime de planetas do tamanho de Netuno ou menores ainda não se tem evidências claras se há ou não uma correlação com a metalicidade da estrela hospedeira, dado que tais planetas são encontrados orbitando estrelas com uma ampla gama de metalicidades (ADIBEKYAN, 2019; BUCHHAVE e LATHAM, 2015; BUCHHAVE *et al.*, 2012, 2014; MAYOR *et al.*, 2011; NARANG *et al.*, 2018; PETIGURA *et al.*, 2018a; SOUSA *et al.*, 2008, 2011; ZHU *et al.*, 2016). O grande número de exoplanetas menores do que Netuno, obtidos pelas descobertas da missão Kepler, possibilitou aprimorar a análise da

relação entre a composição estelar e a ocorrência de planetas do tamanho da Terra. No entanto, para confirmar ou refutar se a formação de planetas rochosos é mais prevalente ao redor de estrelas com menor metalicidade, é necessário estudar a dependência da taxa de ocorrência desses planetas em relação à metalicidade. PETIGURA *et al.* (2018b) mostraram que a taxa de ocorrência de super-Terras quentes (P = 10 − 100 dias e $R_{pl} = 1,0-1,7$ $R_\oplus$) é praticamente independente da metalicidade, apresentando apenas uma leve diminuição com a metalicidade. A maioria dos estudos na literatura (p.e, SOUSA *et al.*, 2011; BUCHHAVE e LATHAM, 2015; NARANG *et al.*, 2018), utiliza o número médio de planetas por estrela ao investigar a dependência da ocorrência de planetas em relação à metalicidade, e não a dependência da ocorrência de mais de um planeta por estrela (sistema planetário). Conforme observado por ZHU (2019), essas duas estimativas das taxas de ocorrência são diferentes e apresentam dependências distintas da metalicidade estelar. Os autores demonstraram que, ao utilizar a taxa de ocorrência de um sistema planetário, mesmo incluindo os planetas menores, a tendência de aumento da metalicidade com o tamanho do planeta persiste. No entanto, ao considerar a taxa de ocorrência como o número médio de planetas, essa tendência não é observada.

Contrariamente aos resultados mencionados anteriormente, WANG e FISCHER (2015), baseados em uma amostra de 406 "Objetos De Interesse" da missão Kepler (do inglês "Kepler objects of interest, KOI"), sugeriram que existe uma correlação universal entre planetas e metalicidade para planetas de todos os tamanhos, indicando que não apenas planetas gigantes gasosos, mas também planetas anões gasosos e planetas terrestres ocorrem com mais frequência em estrelas ricas em metais, encontrando também que a dependência da taxa de ocorrência do planeta com a metalicidade diminui com a diminuição do tamanho do planeta. ZHU *et al.* (2016) sugeriram que a alta taxa de ocorrência e a baixa eficiência de detecção de planetas de baixa massa podem explicar os resultados discrepantes em relação às correlações entre planetas de pequeno porte e metalicidade obtidas por diferentes autores. Em resumo, ainda não se sabe ao certo como a correlação entre o tamanho do planeta e a metalicidade da estrela mãe se estende para o regime dos exoplanetas pequenos. Embora a frequência de planetas versus metalicidade seja crucial para restringir as teorias de formação, é difícil, do ponto de vista da observação, criar uma amostra de comparação, especialmente nos levantamentos de trânsito.

Em relação à metalicidade versus período orbital do planeta, diferentes estudos teóricos e observacionais ilustraram as ligações entre a metalicidade e as distribuições orbitais (ver, por exemplo; ADIBEKYAN *et al.*, 2013; BEAUGÉ e NESVORNÝ, 2013; MULDERS *et al.*, 2016; WILSON *et al.*, 2018). Planetas pequenos ($R_p < 4$ $R_\oplus$) orbitando estrelas pobres em metais apresentam períodos mais longos ($P > 5$ dias) que planetas pequenos que orbitam estrelas ricas em metais (ex.; ADIBEKYAN *et al.*, 2013; BEAUGÉ e NESVORNÝ, 2013; GHEZZI *et al.*, 2021). Analisando uma amostra de 221 estrelas Kepler com espectros observados pelo APOGEE, WILSON *et al.* (2018) identificaram um

período crítico, $P_{crit} = 8,3$ dias. Eles observaram que, para planetas com P$\leqslant 8,3$ dias, há uma tendência de orbitarem estrelas mais ricas em metal ([Fe/H] = 0,11 $\pm$ 0,17 dex) em comparação com planetas cujos períodos são maiores que 8,3 dias.

Outra correlação que tem sido investigada é a influência da metalicidade estelar na arquitetura do sistema planetário (GHEZZI *et al.*, 2021; WEISS *et al.*, 2018). GHEZZI *et al.* (2021) realizaram uma análise abrangente de centenas de estrelas da missão Kepler, explorando a relação entre a metalicidade dessas estrelas e as características dos exoplanetas formados ao seu redor. Este estudo analisou a metalicidade das estrelas hospedeiras e classificou os 961 exoplanetas de sua amostra com base no tamanho, período orbital e se fazem parte de um sistema, identificaram padrões interessantes. Descobriram que a formação de planetas com raios semelhantes aos da Terra não é fortemente influenciada pela metalicidade da estrela hospedeira. No entanto, sistemas com várias Super Terras e períodos orbitais mais longos são mais comuns em estrelas com metalicidade baixa. Além disso, notaram que a formação de planetas quentes com órbitas curtas (menos de 10 dias) e planetas gigantes, como Sub-Saturnos e Júpiteres, tende a ser mais frequente em torno de estrelas com metalicidade mais elevada. Esses resultados proporcionam uma compreensão mais aprofundada da relação entre estrelas e seus sistemas planetários.

Conforme mencionado anteriormente, a determinação precisa de parâmetros estelares, tais como a temperatura efetiva, leva à determinação precisa dos raios estelares e, consequentemente, à determinação precisa dos raios planetários, já que o que se mede via trânsito, é a razão Raio da estrela, $R_\star$ / Raio do planeta, $R_{pl}$. Os estudos de PETIGURA *et al.* (2017) e MARTINEZ *et al.* (2019) determinaram parâmetros estelares das estrelas Kepler com boa precisão. Um resultado muito interessante que surgiu da caracterização de estrelas Kepler usando espectros de alta resolução, obtidos pelo *California-Kepler Survey* (CKS, JOHNSON *et al.*, 2017; PETIGURA *et al.*, 2017), foi a bimodalidade na distribuição dos raios planetários no regime dos planetas menores ($R_{pl} < 4\ R_\oplus$). Este resultado foi obtido no estudo de FULTON *et al.* (2017) e posteriormente confirmado em outros estudos, como VAN EYLEN *et al.* (2018), cujos resultados foram obtidos a partir de asterosismologia, e por MARTINEZ *et al.* (2019). O vale da distribuição bimodal nos raios planetários no regime dos planetas menores, é conhecida como "lacuna do raio" ou "vale do raio". Este vale representa a ausência de planetas entre as super-Terras e os sub-Netunos, já que está localizado entre 1,7 e 2,0 raios terrestres, segundo os estudos mencionados anteriormente.

De acordo com os dois modelos teóricos de formação planetária que preveem a lacuna de raio, a perda de massa impulsionada pelo núcleo (do inglês, "*core-powered mass loss*") e a perda de massa por foto-evaporação, em ambos os casos há uma variação com a massa estelar (FULTON e PETIGURA, 2018). Modelos de foto-evaporação preveem que a perda das camadas externas de planetas gasosos está associada à radiação (raios X e UV extremos, EUV) de suas estrelas hospedeiras (LOPEZ e FORTNEY, 2013; OWEN e

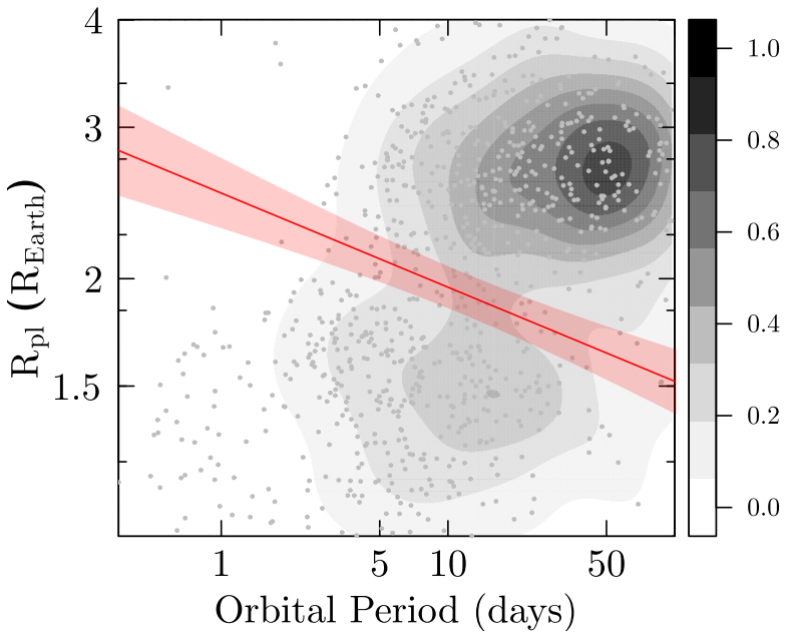


**Figura 1.4** – Raio planetário como função do período orbital mostrando a inclinação onde aparece o vale do raio. Figura retirada de MARTINEZ *et al.* (2019).

WU, 2013), enquanto modelos de perda de massa impulsionada pelo núcleo indicam que a perda da massa atmosférica do planeta é causada pela energia dos núcleos planetários jovens e quentes (GINZBURG *et al.*, 2016, 2018; GUPTA e SCHLICHTING, 2019).

A alta precisão interna alcançada nos raios planetários determinados no estudo de MARTINEZ *et al.* (2019) revela claramente a presença de uma inclinação no vale de foto-evaporação para a amostra CKS, indicando que a posição do vale dos raios diminui com o período orbital. O ajuste dessa diminuição segue uma lei de potência na forma $R_{pl} \propto P^{-0,11}$, que é consistente com os modelos de foto-evaporação e composição do núcleo semelhante ao da Terra na formação de planetas. Na Figura 1.4 podemos observar essa inclinação (região vermelhas com o valor $-0,11$ representado pela linha sólida vermelha) no vale de raio, no regime dos planetas menores.

Dada a grande amostra de estrelas Kepler que hospedam planetas em comparação com a amostra de estrelas K2 que hospedam planetas, fica claro porque há uma quantidade significativamente menor de estudos espectroscópicos detalhados sobre estrelas observadas durante a missão estendida K2. Dentre esses estudos estão, por exemplo, MAYO *et al.* 2018 e PETIGURA *et al.* 2018a, utilizando espectros TRES e Keck HIRES, respectivamente.

### 1.1.2 Atividade Cromosférica Estelar

Com o crescente número de exoplanetas descobertos e confirmados, um aspecto crucial a ser considerado é a atividade estelar, pois esta pode afetar a detecção dos planetas (DU-

MUSQUE *et al.*, 2011; QUELOZ *et al.*, 2001), a caracterização das estrelas que os hospedam (YANA GALARZA *et al.*, 2019), e a evolução dos próprios planetas (HAYWOOD *et al.*, 2014).

A intensidade da atividade magnética pode ser rastreada por vários indicadores, incluindo manchas, explosões, emissões cromosféricas e emissões de raios X e rádio (HAN *et al.*, 2023). Dentre os indicadores de atividade cromosférica amplamente utilizados na literatura estão as linhas de emissão de Ca II H e K ($\lambda$ 3933,66 Å; 3968,47 Å), Mg II ($\lambda$ 2796,35 Å; 2803,53 Å), $H_\alpha$ ($\lambda$ 6562,85 Å), o tripleto infra-vermelho do Ca II ($\lambda$ 8498, 8542, 8662 Å), etc. Em seu artigo de revisão, LINSKY (2017) menciona que todas as estrelas de tipos espectrais F-médio a M-tardio da sequência principal, que sejam observadas com resolução espectral e sinal-ruído adequados, exibem características de emissão cromosférica nos centros das linhas Ca II H e K e Mg II h e k, além de terem forte absorção ou emissão na linha $H_\alpha$.

As linhas mais utilizadas como indicadores de atividade cromosférica são as linhas de Ca II H e K, que têm origem na fotosfera estelar. Dado que os centros dessas linhas são extremamente sensíveis a campos magnéticos (LEIGHTON, 1959), elas apresentam reversões em seus centros quando a estrela é ativa, tornando-as excelentes diagnósticos de atividade cromosférica. A pesquisa do comportamento a longo prazo da atividade cromosférica estelar foi inicialmente e principalmente realizada a partir do Projeto "HK" no Observatório Mount Wilson (MWO), que operou durante quase 40 anos, desde 1966 a 2003. Vale notar que as observações iniciais publicadas em WILSON (1963); WILSON e SKUMANICH (1964) já indicavam que a atividade cromosférica em estrelas da sequência principal decrescia com a idade (LINSKY, 2017). Posteriormente, tal comportamento foi mais detalhadamente estudado por SKUMANICH (1972), que demonstrou que a emissão do Ca II decresce conforme a raiz quadrada inversa da idade.

Os estudos de WILSON (1978), DUNCAN *et al.* (1991) e BALIUNAS *et al.* (1995) resumem as observações do Projeto HK. Por exemplo, no trabalho de WILSON (1978), foram analisadas as variações cromosféricas de estrelas de sequência principal de tipos espectrais F5 − M2. Nesse estudo, concluiu-se que todas as cromosferas estelares eram variáveis em algum grau, que as variações cíclicas muito provavelmente existiam e que deveriam ser consideradas como geradas e dissipadas por processos e estruturas análogas às observadas no Sol. DUNCAN *et al.* (1991) obtiveram as medidas das intensidades das linhas de Ca II H e K para $\sim$ 1300 estrelas observadas durante 1966 e 1983. BALIUNAS *et al.* (1995) mostraram evidências de periodicidades múltiplas em doze das estrelas que analisaram.

Para melhor quantificar as atividades cromosféricas de Ca II H e K, VAUGHAN *et al.* (1978) introduziram o amplamente utilizado índice S (ver equação 2 do Capítulo 3) que é comumente conhecido como índice de Mount Wilson. Esse índice S é adimensional e inclui um termo de cor e da contribuição fotosférica. Isso levou vários autores a explorarem a

conversão de S em unidades físicas. MIDDELKOOP (1982) desenvolveu um método para remover o termo de cor de S, enquanto NOYES *et al.* (1984) ampliaram esse trabalho, criando o índice sem dimensão $R'_{HK}$ (ver equação 3 do Capítulo 3). Essencialmente, o $R'_{HK}$ fornece a fração da luminosidade bolométrica de uma estrela irradiada como emissão cromosférica de H e K.

VAUGHAN e PRESTON (1980) utilizaram a distribuição geral dos fluxos cromosféricos HK em uma amostra de 486 estrelas do MWO e encontraram uma interessante bifurcação nos níveis de atividade das estrelas da amostra, usualmente conhecida como a "Lacuna Vaughan–Preston" (do inglês "*Vaughan–Preston gap*"). Em resumo, este estudo reporta uma ausência relativa de estrelas F-G com níveis de atividade cromosférica intermediária, ou seja, entre as estrelas muito ativas e as menos ativas da amostra. A Figura 1.5, retirada de VAUGHAN e PRESTON (1980), apresenta o diagrama do índice do fluxo S como função do índice de cor instrumental interno $C_{RV}$[4]. A região da "Lacuna Vaughan–Preston" encontra-se delineada em azul na figura indicando a ausência de estrelas F-G com níveis de atividade intermediárias. VAUGHAN e PRESTON (1980) especularam duas possíveis explicações para esta lacuna. A primeira, seria devido a atividade cromosférica diminuir abruptamente em uma idade de $\sim 10^9$ anos, e a segunda seria que a lacuna é uma característica acidental da amostra.

Posteriormente, a presença de uma distribuição bimodal na atividade estelar, foi corroborada por HENRY *et al.* (1996) a partir de um estudo de uma amostra de estrelas semelhantes ao Sol. Adicionalmente, neste estudo as estrelas da amostra foram classificadas de acordo com seus níveis de atividade em quatro classes de atividade: estrelas muito ativas ($\log R'_{HK} > -4,20$) correspondendo a 2,6% da amostra, estrelas ativas ($-4,75 < \log R'_{HK} < -4,2$) correspondendo a 27% da amostra, estrelas inativas ($-5,10 < \log R'_{HK} < -4,75$) correspondendo a 62% da amostra e estrelas muito inativas ($\log R'_{HK} < -5,10$) correspondendo a 8% da amostra. A lacuna Vaughan–Preston também foi observada em levantamentos posteriores que utilizaram tanto $R'$ quanto fluxo absoluto (GRAY *et al.*, 2006; HALL *et al.*, 2007). A consistência de todos estes resultados parece indicar que a lacuna Vaughan–Preston é um aspecto real da atividade cromosférica em estrelas semelhantes ao Sol e não um artefato estatístico como foi especulado anteriormente por VAUGHAN e PRESTON (1980).

O primeiro estudo a não encontrar fortes evidências da presença da lacuna Vaughan-Preston foi o estudo não homogêneo de BORO SAIKIA *et al.* (2018), que analisa uma grande amostra contendo mais de 4000 estrelas, cujos índices S foram majoritariamente coletados de diferentes estudos e levantamentos da literatura. Os resultados não parecem indicar a presença de uma bimodalidade clara, o que leva os autores a concluírem que a lacuna Vaughan-Preston pode não ser tão significativa. Por outro lado, mais recentemente

[4] VAUGHAN *et al.* (1978) definem o índice de cor instrumental como $C_{RV} \equiv 2,5 \log_{10}(N_R/N_V)$, onde $N_V$ e $N_R$ são as contagens das bandas de referencia nos lados V e R das regiões H e K.

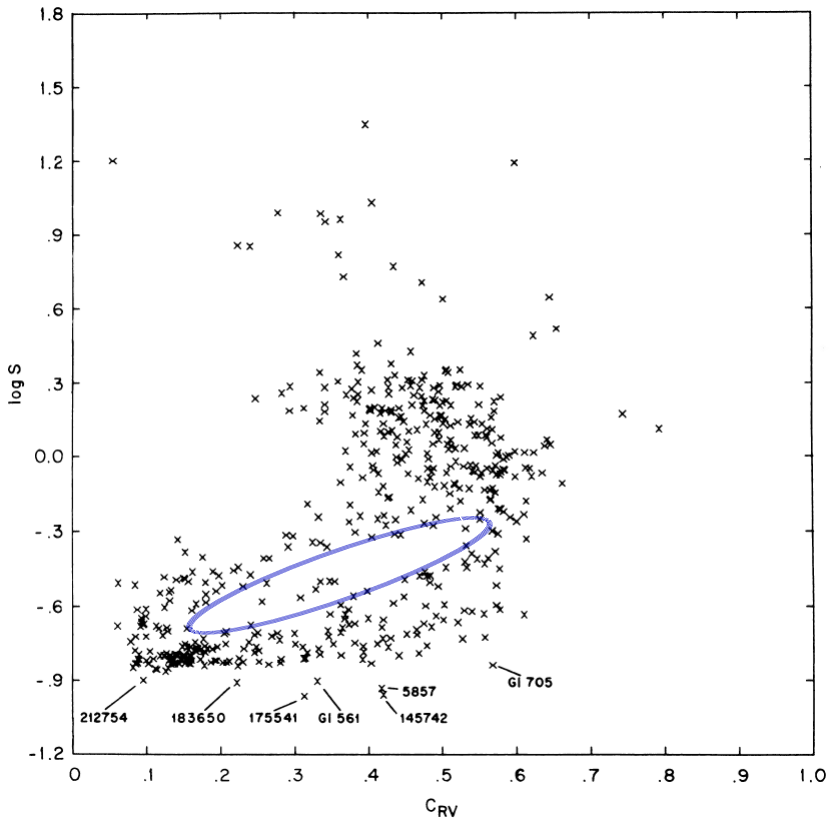


**Figura 1.5** – Índice do fluxo (S) como função do índice de cor instrumental interno ($C_{RV}$). A região delineada pela cor azul mostra a ausência de estrelas F e G com níveis intermediários de atividade chamada de "lacuna Vaughan-Preston". Figura obtida e adaptada de VAUGHAN e PRESTON (1980).

GOMES DA SILVA *et al.* (2021), usando espectros HARPS (MAYOR *et al.*, 2003) de alta resolução (R $=\lambda/\Delta\lambda \sim$ 115.000) de uma amostra de ∼1500 estrelas F, G e K, tanto de sequência principal quanto evoluídas, também encontrou evidências contundentes da presença da lacuna Vaughan-Preston.

No capítulo 3 analisaremos qual o comportamento da atividade em nossa amostra de estrelas K2 e se nesta amostra estudada também observamos uma lacuna de estrelas com atividade intermediaria. Na próxima seção mudaremos de tema para dar uma introdução a parte do trabalho de tese apresentada no Capítulo 4 que trata dos padrões de abundancia química do aglomerado aberto NGC 6705.

## 1.2 O Aglomerado Aberto Jovem NGC 6705

O estudo da evolução química da Galáxia é um campo de grande interesse na Astrofísica, cujos dados observacionais são adquiridos por meio da análise detalhada das abundâncias químicas de estrelas do campo que pertencem às distintas populações estelares do disco, bojo e halo, assim estrelas pertencentes a associações e aglomerados estelares. Os aglomerados abertos, em particular, desempenham um papel fundamental na compreensão da

dinâmica e cinemática das diferentes componentes do disco galáctico, contribuindo significativamente para a compreensão da evolução química da Via Láctea. Uma das vantagens dos aglomerados abertos é a uniformidade de idade de suas estrelas, pois em princípio nascem simultaneamente. Em contraste, a idade desses aglomerados varia desde alguns milhões até vários bilhões de anos. Características importantes, como idade, distância e composição química das estrelas em aglomerados abertos, fornecem valiosas informações sobre o histórico da formação estelar e detalhes dos processos físicos que moldaram nossa Galáxia. Neste trabalho de tese analisamos uma amostra de estrelas pertencentes ao aglomerado de estrelas NGC 6705.

NGC 6705 (Messier 11, M11), é um aglomerado aberto jovem com uma idade bem definida de $316 \pm 50$ milhões de anos, determinada por meio do ajuste de isócronas (CANTAT-GAUDIN *et al.*, 2014; DIAS *et al.*, 2021). Além de ser relativamente rico em estrelas, NGC 6705 é compacto e está localizado no disco interno, a uma distância Galactocêntrica de 6,5 kpc (CANTAT-GAUDIN *et al.*, 2020). Devido à sua juventude, é provável que NGC 6705 não tenha migrado significativamente de seu local de nascimento, possuindo um raio de nascimento estimado entre $6,8 - 7,5$ kpc (CASAMIQUELA *et al.*, 2018).

Um aspecto notável desse aglomerado aberto é que estudos espectroscópicos da literatura como, por exemplo, MAGRINI *et al.* (2014), TAUTVAIŠIENĖ *et al.* (2015) e CASAMIQUELA *et al.* (2018) encontraram que as estrelas de NGC 6705 são enriquecidas em elementos-$\alpha$ em relação ao ferro ([$\alpha$/Fe] mesmo tendo uma idade estimada de apenas algumas centenas de milhões de anos. Tais resultados são inesperados conforme discutiremos a seguir.

Acredita-se que as primeiras estrelas a se formarem no universo foram estrelas muito massivas (BROMM *et al.*, 1999; SUSA *et al.*, 2014) e compostas principalmente de H e He. Por serem massivas o tempo de vida dessas estrelas é muito curto ($\sim$ milhões de anos) quando comparado com o tempo de vida de estrelas de tipo solar (da ordem de bilhões de anos).

As estrelas massivas, aquelas com massas maiores que 8 $M_{\odot}$, encerram seu ciclo de vida em explosões de supernovas do tipo II (SN II). SN II são consideradas um dos eventos astrofísicos mais extremos na Galáxia. Estas enriquecem o meio interestelar com uma variedade de elementos, em particular o oxigênio, além de produzirem os elementos conhecidos como elementos-$\alpha$, tais como, Ne, Mg, Si e S. A formação desses elementos ocorre por meio da captura de partículas $\alpha$ (núcleos de hélio-4). As SN Ia acontecem em escalas de tempo muito mais longas que as SN II. SN Ia resultam da explosão de estrelas anãs brancas que consomem o material de uma binária companheira. Ao atingir o limite de Chandrasekhar (1,4 $M_{\odot}$), a estrela explode, lançando a maior parte de seu material no meio interestelar. As SN Ia dão origem a elementos mais pesados principalmente aqueles do pico do ferro. As SN Ia contribuíram com aproximadamente o 70% do ferro que observamos hoje na Galáxia (CHIAPPINI, 2001), mas estas também produzem S, Si

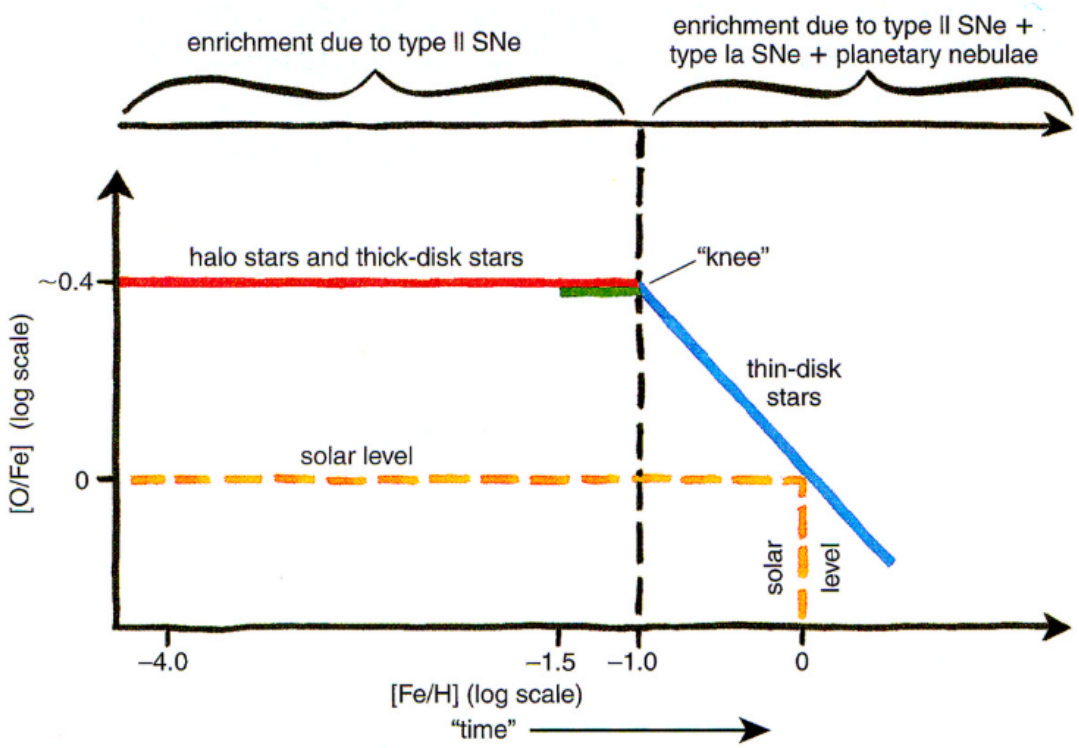


**Figura 1.6** – Representação esquemática da distribuição da razão [O/Fe] como função da metalicidade na Galáxia. Figura obtida de CHIAPPINI (2001).

e Ca, embora em menor quantidade que as SN II (TRURAN e HEGER, 2003).

Devido às diferentes escalas de tempo entre as SN II e as SN Ia na Galáxia, a distribuição da razão do oxigênio (elemento-$\alpha$) e do ferro, [O/Fe], como função da metalicidade, [Fe/H], é um bom indicador da taxa de enriquecimento em metais do meio interestelar. A expectativa é que a história inicial da Galáxia exiba uma relação quase plana entre oxigênio e ferro, formando um platô com valor de [O/Fe] alto, conforme ilustrado esquematicamente na Figura 1.6, uma vez que esses elementos são, inicialmente, criados na mesma taxa dentro de SN II. No entanto, à medida que as SN Ia começam a contribuir com Fe, a razão [O/Fe] diminui, resultando na diminuição da inclinação da linha. Na representação esquemática da Figura 1.6, o platô é ocupado por estrelas do Halo e estrelas do disco espesso, que tem razão [O/Fe] alta, enquanto que a diminuição da inclinação é observada para estrelas do disco fino. O ponto em que a inclinação começa a diminuir, conhecido como o "joelho" (do inglês, *knee*), é um indicador crucial de quando a maioria das SN Ia começou a enriquecer o meio interestelar com ferro. Como esse processo leva cerca de um bilhão de anos para ocorrer, temos a compreensão de que o halo galáctico deve ter se formado nos primeiros bilhões de anos da vida da Galáxia, enquanto o disco fino nas proximidades do Sistema Solar teve uma formação mais gradual (CHIAPPINI, 2001).

Baseado no discutido acima, a medida das abundâncias dos elementos-$\alpha$ em relação ao ferro ([$\alpha$/Fe]) possibilita uma estimativa indireta das idades das estrelas, dado que o

enriquecimento na razão [$\alpha$/Fe] indica que a estrela se formou a partir de gás enriquecido pelo colapso do núcleo de uma ou mais supernovas antes da contribuição efetiva das SN Ia. No contexto específico do aglomerado NGC 6705, a juventude do NGC 6705 (idade ~300,000 anos) sugeriria que suas estrelas não sejam enriquecidas na razão [$\alpha$/Fe]. Finalmente, no Capitulo 4, também será discutida a possibilidade que estrelas enriquecidas em elementos-$\alpha$, que aparentam ser jovens, na verdade, podem ser produtos de interações/fusões binárias (por exemplo, HEKKER e JOHNSON, 2019; IZZARD *et al.*, 2018; JOFRÉ *et al.*, 2023; SILVA AGUIRRE *et al.*, 2018). Neste trabalho de Tese determinaremos as abundancias dos elementos-$\alpha$ assim como a metalicidades de estrelas pertencentes a NGC 6705.

Outro tema que pode ser explorado com o estudo de estrelas evoluídas pertencentes a aglomerados abertos é o estudo de assinaturas químicas de mistura estelar. Devido à sua relativa juventude e riqueza estelar em comparação com outros aglomerados abertos, NGC 6705 contém uma amostra populosa de gigantes vermelhas, que nos permite em principio investigar a mistura estelar em detalhe. Em particular, NGC 6705 possui gigantes vermelhas de massa intermediária, com massas entre M $\sim$ 3,0 – 3,5 $M_{\odot}$, que podem exibir mudanças mensuráveis nas abundâncias químicas, incluindo possíveis alterações nas abundâncias de $^{16}$O, ou Na, além das variações usuais em $^{12}$C, $^{13}$C e $^{14}$N observadas em gigantes vermelhas de menor massa. Nesse contexto, SMILJANIC *et al.* (2016) investigaram as abundâncias de Na e Al em gigantes de aglomerados de baixa e média massa, incluindo NGC 6705, no âmbito do levantamento Gaia-ESO. Eles encontraram tanto Na quanto Al enriquecidos em NGC 6705. Embora os resultados de Na para este aglomerado estivessem de acordo com as previsões dos modelos de evolução estelar, as abundâncias de Al estavam acima das previsões dos modelos, uma vez que se espera que o alumínio não seja afetado pela mistura na faixa de massa das gigantes de NGC 6705 (LAGARDE *et al.*, 2012). Eles interpretaram o resultado de alto Al como possivelmente relacionado ao ambiente onde o aglomerado foi formado que seria mais rico em Al.

As estrelas que são predominantes em nossa Galáxia são as estrelas de baixa e média massa. Para essas estrelas, a nucleossíntese mais importante ocorre quando elas atingem o ramo das gigantes. Durante a ascensão ao ramo das gigantes vermelhas (*Red Giant Branch*: RGB) ocorre a primeira dragagem (1DUP do inglês *First Dredge Up*, IBEN, 1967). Nessa fase, a envoltória convectiva dilui as camadas estelares convectivas externas com material processado pelo hidrogênio em seu interior durante a sequência principal, resultando em uma alteração nas abundâncias superficiais. Como consequência, as abundâncias superficiais de $^{7}$Li, $^{9}$Be, $^{12}$C e $^{18}$O diminuem, enquanto as de $^{3}$He, $^{4}$He, $^{13}$C, $^{14}$N, $^{17}$O e $^{23}$Na aumentam. Consequentemente, as razões isotópicas $^{12}$C/$^{13}$C, $^{12}$C/$^{14}$N, $^{16}$O/$^{17}$O e $^{18}$O/$^{16}$O diminuem na superfície (KARAKAS e LATTANZIO, 2014; LAGARDE *et al.*, 2012).

Após a conclusão do 1DUP, tanto os modelos padrão quanto os modelos recentes que

consideram rotação (CHANAMÉ *et al.*, 2005; PALACIOS *et al.*, 2006) preveem nenhuma variação adicional nos padrões de abundância superficial até que as estrelas comecem a ascender ao ramo assintótico das gigantes (do inglês *Asymptotic Giant Branch*: AGB). Outro mecanismo além do 1DUP que governa a composição fotosférica de estrelas gigantes brilhantes de baixa massa é a mistura termohalina (CHARBONNEL e ZAHN, 2007). A mistura termohalina é uma instabilidade hidrodinâmica que ocorre quando um gradiente na temperatura passa a ser responsável por estabilizar um gradiente na composição química (CANTIELLO e LANGER, 2010). A instabilidade termohalina é esperada ocorrer após o 1DUP, onde o impacto da mistura termohalina nas propriedades químicas estelares parece depender da massa inicial da estrela e da metalicidade, conforme sugerido pelas observações da razão isotópica de carbono (que é a assinatura mais confiável desse mecanismo) em estrelas gigantes abrangendo amplas faixas de massa e metalicidade (CHARBONNEL e LAGARDE, 2010). Neste trabalho de tese analisaremos estrelas gigantes vermelhas pertencentes ao aglomerado aberto NGC 6705 a partir dos espectros do levantamento APOGEE e analisaremos as abundâncias de vários elementos, incluindo aqueles que são traçadores do 1DUP.

## 1.3 Este Trabalho de Tese

Esta tese apresenta um estudo espectrocópico de estrelas de tipo FGK de sequência principal e de estrelas gigantes vermelhas de tipo espectral K. A caracterização das estrelas de três diferentes amostras é realizada através da análise de espectros de alta e média resolução espectral, diferentes coberturas espectrais e obtidos tanto no óptico quanto no infra-vermelho próximo (entre 1,5 e 1,7 $\mu$m). A primeira amostra analisada é composta de estrelas hospedeiras de planetas e consiste em 81 estrelas K2 e 34 estrelas Kepler, cujos espectros foram observados com o espectrógrafo Hydra no telescópio WYIN. A segunda amostra consiste em 144 estrelas K2 hospedeiras de planetas, cujos espectros foram obtidos com o espectrógrafo HIRES no telescópio Keck. Finalmente, nossa última amostra analisada é composta por 11 estrelas pertencentes ao aglomerado NGC 6705, cujos espectros no infravermelho próximo são provenientes dos dados do levantamento APOGEE.

Esta tese será apresentada na forma de uma compilação de três artigos, cada um deles exposto em um capítulo e precedido por uma breve introdução. Vale notar que a organização não segue a ordem cronológica de publicação dos artigos. No Capítulo A descrevemos a formação de linhas espectrais. No Capítulo 2 apresentamos o artigo (publicado na revista *Astrophysical Journal*) que discute a caracterização de uma amostra de estrelas hospedeiras de planetas, bem como a determinação do raio planetário para planetas confirmados e orbitando estrelas observadas majoritariamente pela missão K2. Em seguida, o Capítulo 3 aborda o artigo (submetido à revista *AAS Journals*) que discute tanto a caracterização estelar quanto a análise da atividade cromosférica de uma amostra

de estrelas estrelas K2. No Capítulo 4, é apresentado o artigo (publicado na revista *Monthly Notices of the Royal Astronomical Society*) que aborda a caracterização estelar e as abundâncias químicas de gigantes vermelhas pertencentes ao aglomerado aberto NGC 6705. Finalmente, o Capítulo 5 apresenta as conclusões gerais obtidas nesta tese.

# Capítulo 2

# Análise Espectroscópica de uma Amostra de Estrelas K2 Hospedeiras de Planetas.

Neste capítulo, apresentamos o artigo publicado na revista *Astrophysical Journal*: "A Spectroscopic Analysis of a Sample of K2 Planet-host Stars: Stellar Parameters, Metallicities and Planetary Radii" [1], que aborda a análise espectroscópica homogênea de uma amostra de estrelas dos tipos espectrais F, G e K. Os espectros analisados foram obtidos em diversas missões observacionais, incluindo 81 estrelas do *Ecliptic Plane Input Catalog* (EPIC) para a missão K2 e, com prioridade mais baixa, 34 *Kepler Objects of Interest* (KOI) da missão Kepler. A maioria das estrelas observadas pertence à missão K2 dado que estas foram ainda pouco estudadas na literatura. As observações ocorreram entre 2015 e 2019 e utilizaram o espectrógrafo Hydra instalado no telescópio WIYN de 3,5 m no Observatório Kitt Peak. Os espectros analisados têm uma resolução R $\sim 18,500$ e abrangem um pequeno intervalo espectral entre $\lambda$ 6050 e 6350 Å. A redução dos espectros Hydra foi feita usando as rotinas do IRAF e seguindo os passos e procedimentos usuais apresentados em JACOBSON *et al.* (2011) para espectros Hydra.

Os parâmetros estelares e metalicidades foram obtidos a partir de medições das larguras equivalentes das linhas de Fe I e Fe II, exigindo equilíbrio de excitação e ionização, além de garantir a independência das abundâncias das linhas de ferro em relação às larguras equivalentes. Para isso foi crucial construímos uma lista de linhas cuidadosamente selecionada de linhas de Fe I e II para a análise de espectros baseados na resolução e o intervalo espectral dos espectros analisados. Todos os cálculos foram realizados em equilíbrio termodinâmico local (LTE) utilizando modelos de atmosferas de Kurucz. Nossa metodologia e lista de linhas foram validadas analisando os espectros de dois proxies solares, os asteroides Astraea e Parthenope, e uma estrela gêmea solar (HIP 81512). Além

[1] https://iopscience.iop.org/article/10.3847/1538-4357/acb137

disso, estimamos os efeitos da inclusão de linhas de Fe I sensíveis ao efeito Zeeman nos parâmetros estelares derivados de estrelas jovens e possivelmente ativas em nossa amostra.

Uma vez determinados os parâmetros estelares, usamos a temperatura efetiva, a metalicidade e combinamos com as magnitudes V e a paralaxe para determinar os raios e massas das estrelas de nossa amostra usando o método das isócronas. Finalmente, calculamos os raios planetários para os sistemas com planetas confirmados a partir dos raios estelares e as profundidades de trânsito da literatura.

Os raios planetários obtidos revelaram resultados interessantes em nossa pequena amostra de planetas K2, especialmente no que diz respeito ao "vale do raio", onde o mínimo da distribuição bimodal encontra-se localizado em $\sim 1,9$ $R_\oplus$, para planetas menores ($R_{pl} < 4$ $R_\oplus$). Este resultado confirma a boa precisão alcançada para os raios estelares e planetários.

Por fim, investigamos a conexão estrela-planeta apenas para a amostra de K2, considerando a metalicidade da estrela hospedeira e parâmetros planetários como o raio planetário e o período orbital. Observamos que a metalicidade aumenta com o raio planetário e fica mais evidente na transição de Sub-Netunos para Sub-Saturnos.

The Astrophysical Journal, 946:61 (24pp), 2023 April 1 https://doi.org/10.3847/1538-4357/acb137


# A Spectroscopic Analysis of a Sample of K2 Planet-host Stars: Stellar Parameters, Metallicities and Planetary Radii

V. Loaiza-Tacuri[1], Katia Cunha[1,2,3], Verne V. Smith[3,4], Cintia F. Martinez[5], Luan Ghezzi[6], Simon C. Schuler[7], Johanna Teske[8], and Steve B. Howell[9]
[1] Observatório Nacional, Rua General José Cristino, 77, 20921-400 São Cristóvão, Rio de Janeiro, RJ, Brazil; vtacuri@on.br
[2] Steward Observatory, University of Arizona, 933 North Cherry Avenue, Tucson, AZ, 85721, USA
[3] Institut d'Astrophysique de Paris, UMR 7095 CNRS, Sorbonne Université, 98bis Bd. Arago, 75014 Paris, France
[4] NSF's NOIRLab, 950 North Cherry Avenue, Tucson, AZ, 85719, USA
[5] Instituto de Astronomía y Física del Espacio, Universidad de Buenos Aires, Ciudad Universitaria S/N, Buenos Aires, Argentina
[6] Universidade Federal do Rio de Janeiro, Observatório do Valongo, Ladeira do Pedro Antônio, 43, Rio de Janeiro, RJ 20080-090, Brazil
[7] University of Tampa, 401 W Kennedy Boulevard, Tampa, FL, 33606, USA
[8] Carnegie Earth & Planets Lab, 5241 Broad Branch Road, NW, Washington, DC, 20015, USA
[9] NASA Ames Research Center, Moffett Field, CA, 94035, USA
*Received 2022 September 22; revised 2023 January 6; accepted 2023 January 6; published 2023 March 30*

## Abstract

The physical properties of transiting exoplanets are connected with the physical properties of their host stars. We present a homogeneous spectroscopic analysis based on the spectra of FGK-type stars observed with the Hydra spectrograph on the WIYN telescope. We derived the effective temperatures, surface gravities, and metallicities, for 81 stars observed by K2 and 33 by Kepler 1. We constructed an Fe I and II line list that is adequate for the analysis of $R \sim 18{,}000$ spectra covering 6050–6350 Å and adopted the spectroscopic technique based on equivalent-width measurements. The calculations were done in LTE using Kurucz model atmospheres and the `qoyllur-quipu` ($q^2$) package. We validated our methodology via an analysis of a benchmark solar twin and solar proxies, which are used as a solar reference. We estimated the effects that including Zeeman-sensitive Fe I lines have on the derived stellar parameters for young and possibly active stars in our sample and found them not to be significant. Stellar masses and radii were derived by combining the stellar parameters with Gaia EDR3 and $V$ magnitudes and isochrones. The measured stellar radii have a 4.2% median internal precision, leading to a median internal uncertainty of 4.4% in the derived planetary radii. With our sample of 83 confirmed planets orbiting K2 host stars, the radius gap near $R_{\rm planet} \sim 1.9\,R_{\oplus}$ is detected, in agreement with previous findings. Relations between the planetary radius, orbital period, and metallicity are explored and these also confirm previous findings for Kepler 1 systems.

*Unified Astronomy Thesaurus concepts:* Fundamental parameters of stars (555); Spectroscopy (1558); Exoplanet systems (484); F stars (519); G stars (558); K stars (878)

*Supporting material:* machine-readable tables

## 1. Introduction

To date, according to the NASA Exoplanet Archive[10] and Exoplanet Catalog,[11] there are more than ∼5000 detected exoplanets orbiting ∼3800 parent stars, with most of these planets (∼3900) discovered via the transit method. This impressive number of planets detected via transits so far, is thanks to the Corot mission (37 planets; Deleuil et al. 2000, 2018), the more recent TESS mission (249 planets; Ricker et al. 2015), and mostly thanks to the Kepler Mission (2708 planets; Borucki et al. 2010; Koch et al. 2010; Borucki 2016), along with the extended K2 mission (537 planets; Howell et al. 2014). The original Kepler mission (Kepler 1; operating between 2009 and 2013) pointed at a single field of view in the constellations of Cygnus and Lyra. For the K2 mission (operating between 2014 and 2018), the Kepler telescope was reoriented to point at different fields along the ecliptic plane for about 80 days each, with a latency period between them as the spacecraft orbited the Sun. One advantage of the change in targeting strategy during the Kepler mission, due to the loss of two of the guidance gyros in the Kepler telescope, is that K2 observed Galactic targets in regions of the disk that Kepler 1 had not reached. It is also relevant to note that K2 targeted a larger and more diverse sample compared to Kepler 1.

Determining stellar atmospheric parameters (effective temperatures, metallicities, and surface gravities) of exoplanet host stars is crucial to exoplanet studies because host-star parameters must be known with precision in order to derive precise fundamental planetary properties. One key stellar parameter that needs to be determined as precisely as possible is the stellar radius, as planetary transits essentially measure the ratio of the planet radius to stellar radius. Using a quantitative high-resolution stellar spectroscopic analysis to derive more precise stellar radii, the California Kepler Survey (CKS; Petigura et al. 2017) made the important discovery of a bimodal distribution in the radii of small planets, where the separation between the peaks falls at $R_{\rm pl} \sim 1.8\,R_{\oplus}$ (see Figure 7 of Fulton et al. 2017). The gap in planet radius (now known as the Fulton gap, or also referred to as the radius valley) represents the

[10] https://exoplanetarchive.ipac.caltech.edu/
[11] https://exoplanets.nasa.gov/discovery/exoplanet-catalog/

transition from super-Earths to mini-Neptunes and had been predicted by models (Lopez & Fortney 2013; Owen & Wu 2013; Ginzburg et al. 2018; Gupta & Schlichting 2019). This bimodal distribution has been confirmed independently by other studies that reached high-enough precision in their derived radii to uncover and confirm the radius gap (Berger et al. 2018; Fulton & Petigura 2018; Van Eylen et al. 2018; Martinez et al. 2019). Van Eylen et al. (2018) used asteroseismology for a small sample of host stars (75 host stars and 117 planets) and derived a negative slope for the value of the radius gap versus orbital period, while Martinez et al. (2019), using a precise classical high-resolution spectroscopic analysis, measured a similar slope for the radius gap using the larger CKS sample (1232 host stars and 1633 planets).

According to the two theoretical models that predict the radius gap, core-powered mass loss and mass loss by photoevaporation, there is a variation with stellar mass (Fulton & Petigura 2018). Photoevaporation models predict that the loss of the outer layers of gaseous planets is associated with the radiation (X-rays and EUV) from their host stars (Lopez & Fortney 2013; Owen & Wu 2013), while core-powered mass-loss models predict that the loss of the atmospheric mass of the planet is caused by the energy of the young and hot planetary cores (Ginzburg et al. 2016, 2018; Gupta & Schlichting 2019). In that sense, several studies have shown that there is a dependence of the radius gap on stellar mass (i.e., Fulton & Petigura 2018; Berger et al. 2020a; Cloutier & Menou 2020; Van Eylen et al. 2021). Importantly, Cloutier & Menou (2020) showed that the radius gap persists in low-mass stars ($M_{\rm star} = 0.08$–$0.93\ M_{\odot}$). However, Petigura et al. (2022) investigated the radius gap and found no evidence that it is a function of the stellar mass of host stars (for $M_{\rm star} = 0.5$–$1.4\ M_{\odot}$).

Besides stellar radii, the stellar metallicity of host stars is another parameter that is important in studying possible star–planet connections. Several studies have investigated and found the well-known correlation between the occurrence of giant planets and host-star metallicity; the formation of giant planets is favored around stars with larger metal content (e.g., Gonzalez 1997; Santos et al. 2004; Fischer & Valenti 2005; Ghezzi et al. 2010; Sousa et al. 2011; Ghezzi et al. 2018; Adibekyan 2019). This correlation has played an important role in the exoplanet field, especially in planet formation theory (e.g., Ida & Lin 2004a, 2004b, 2005; Nayakshin 2010; Mordasini et al. 2012, 2015; Owen & Murray-Clay 2018; Venturini et al. 2020).

Unlike the well-established planet–metallicity correlation for giant planets, it is still unclear whether smaller planets (planet radius $R_{\rm pl} < 4\ R_{\oplus}$, or planet mass $M_{\rm pl} < M_{\rm Neptune}$), especially terrestrial planets ($R_{\rm pl} < 1.7 R_{\oplus}$; Buchhave et al. 2014), also follow a planet–metallicity correlation. Early studies showed that planets with a radius $R_{\rm pl} < 4\ R_{\oplus}$ display a wide range of metallicities indistinguishable from the distribution of stars without planets (e.g., Buchhave et al. 2012; Everett et al. 2013). Several additional studies have analyzed the small planet–metallicity correlation based on a large sample of transiting exoplanets from the Kepler catalog. These studies used spectroscopic stellar metallicities and concluded that small-rocky planets ($R_{\rm pl} < 1.7\ R_{\oplus}$) do not show a preference for metal-rich stars (e.g., Sousa et al. 2008; Batalha et al. 2013; Buchhave et al. 2014; Buchhave & Latham 2015; Schuler et al. 2015; Mulders et al. 2016; Petigura et al. 2018a; Narang et al. 2018; Adibekyan 2019), while the occurrence rate of larger transiting planets ($R_{\rm pl} \sim 1.7$–$3.9\ R_{\oplus}$) show a correlation with metallicity (Buchhave & Latham 2015; Mulders et al. 2016; Narang et al. 2018). But Wang & Fischer (2015) suggested a universality around the planet–metallicity correlation, indicating that not only giant planets ($R_{\rm pl} > 4\ R_{\oplus}$), but also gas dwarf planets ($R_{\rm pl} \sim 1.7$–$3.9\ R_{\oplus}$) and terrestrial planets ($<1.7\ R_{\oplus}$) occur most often in metal-rich stars. Zhu et al. (2016) tried to explain this discrepancy, i.e., if the planet–metallicity correlation is universal or not, by suggesting that it is due to a high rate of planet occurrence and low detection efficiency. Aside from the rate of occurrence, various studies analyzed the relationship between orbital period and metallicity, concluding that small and hot planets (orbital periods of $P \lesssim 10$ days) appear preferentially around metal-rich stars (e.g., Adibekyan et al. 2013; Beauge & Nesvorny 2013; Adibekyan et al. 2015; Dawson et al. 2015; Mulders et al. 2016; Petigura et al. 2018a; Dong et al. 2018; Owen & Murray-Clay 2018; Wilson et al. 2018). Another correlation that has been investigated is the influence of the stellar metallicity on the planetary system architecture (Weiss et al. 2018; Ghezzi et al. 2021).

The studies highlighted above demonstrate that it is important to characterize well exoplanet stellar hosts in terms of their stellar parameters and metallicities. For example, via community effort (ExoPAG; Gaudi 2013),[12] significant progress has been made toward this goal in recent years. We point out, however, that there have been far fewer detailed spectroscopic studies of stars observed in the extended K2 mission when compared to the Kepler 1 mission, with most of the K2 star compilations of results so far being based on photometric and asteroseismic analyses, or trigonometric methods (e.g., Boyajian et al. 2013; Vanderburg et al. 2016; Huber et al. 2017; Berger et al. 2020b). Together with precise EDR3 Gaia (Gaia Collaboration et al. 2021) parallaxes, deriving precise stellar parameters for K2 stars via high-resolution spectra can be considered a necessity for the community. This study focuses on the homogeneous spectroscopic analysis of a sample of K2 stars using optical spectra obtained with the Hydra Spectrograph on the WIYN 3.5 m telescope and measurements of selected Fe I and Fe II lines to derive fundamental stellar properties, such as $T_{\rm eff}$, log $g$, [Fe/H], mass, and radius. Most of the target K2 stars in this study have confirmed planets and their stellar radii are used to compute precise radii for K2 planets.

This paper is organized as follows. In Section 2, we describe the observations and data reduction. In Section 3, we discuss the methodology employed in the derivation of the stellar parameters, effective temperatures, surface gravities, metallicities, stellar masses, and radii, along with planetary radii. In Section 4, our results are presented. Finally, discussions and conclusions are presented in Sections 5 and 6, respectively.

## 2. Observations

The spectra analyzed in this study were obtained in several observing runs targeting stars from the Ecliptic Plane Input Catalog (EPIC) for the K2 mission and, as a lower priority, Kepler objects of interest (KOI) from the Kepler 1 mission. The observing runs took place between 2015 and 2019 using the Hydra multifiber spectrograph ($R \sim 18{,}500$) mounted on the WIYN 3.5 m telescope at Kitt Peak.[13] Most of the observed stars are from the K2 mission.

[12] https://exoplanets.nasa.gov/exep/exopag/overview/

[13] The WIYN Observatory is a joint facility of the University of Wisconsin–Madison, Indiana University, NSF's NOIRLab, the Pennsylvania State University, Purdue University, University of California, Irvine, and the University of Missouri.

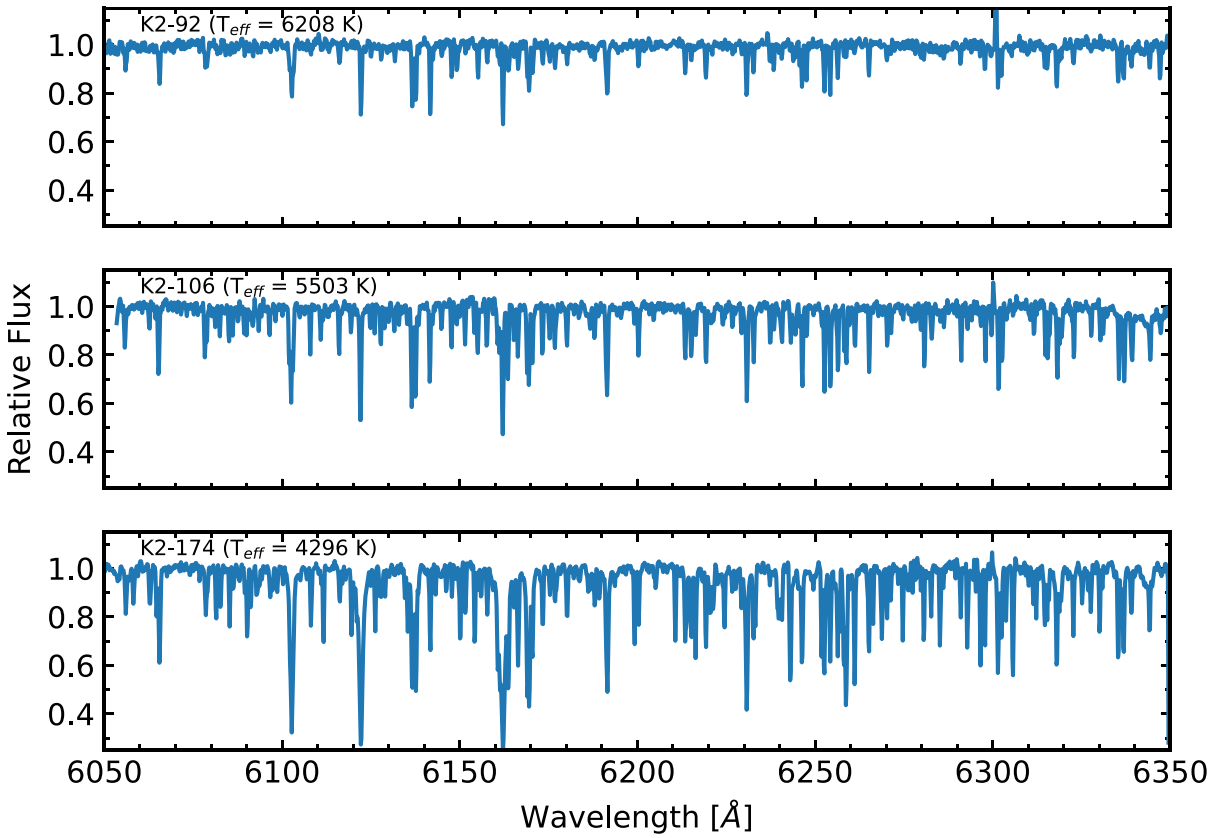


**Figure 1.** Examples of reduced Hydra spectra; the top, middle, and lower panels correspond to the target stars K2-92 ($T_{\rm eff}$ = 6208K; F dwarf), K2-106 ($T_{\rm eff}$ = 5503K; G dwarf), and K2-174 ($T_{\rm eff}$ = 4296K; K dwarf), respectively. The increasing spectral-line absorption from spectral type F to G to K is clear, which arise from both a larger number of lines plus increasing line absorption.

The Hydra spectra were reduced using routines in IRAF.[14] - Briefly, we trimmed and overscan-subtracted the individual frames. The bias frames were combined into a master bias and then this was subtracted from the rest of the images. Cosmic rays from object frames were removed using L. A. Cosmic, an IRAF script developed by van Dokkum (2001). After aperture extraction, the 1D spectra were flat fielded and wavelength calibrated. Finally, to remove the telluric lines between 6270 and 6300 Å we used the spectrum of a rapidly rotating B-type star. The continuum normalization of all spectra was done with the IRAF task continuum and a spline fit. Figure 1 displays the continuum-normalized spectra showing the entire wavelength range (6050 to 6350 Å) covered by the analyzed Hydra spectra. The three stars presented in the different panels of the figure were selected to showcase the change in spectral features due to different effective temperatures. The top panel shows a hotter star with $T_{\rm eff}$ = 6208 K (K2-92), the middle panel a star with $T_{\rm eff}$ = 5503 K (K2-106), and the bottom panel a cooler star with $T_{\rm eff}$ = 4296 K (K2-174). The effective temperatures in the panels are those from this study.

The sample studied here contains 115 stars and the targets were selected based on observability, and with an emphasis on G and K spectral types (Section 5). Our prime program was to target K2 stars but due to observing constraints Kepler 1 targets were also observed. The total number of K2 stars analyzed is 81 (69 stars with confirmed planets and 12 stars with candidate planets) and it includes stars from campaigns C0, C1, C3−C6, C8, and C10 (some stars from C5 were also observed in C16 and C18). Our sample includes 33 stars identified as Kepler, KOIs, or KIC, plus two asteroids observed as solar proxies (Astraea and Phartenopen). We also observed a solar twin (HIP 81512), which was analyzed previously by Ramirez et al. (2009, 2013), as a comparison star. The quality of the spectra in this analysis are good and suitable for a precise spectroscopic analysis with most of the spectra having a signal-to-noise ratio (S/N) of ∼100, while about 10% of the spectra have 50 < S/N < 100. The S/N were estimated in spectral regions between ∼6068–6075 Å.

In our sample there are seven stars that have been flagged as eclipsing binaries: KOI-6 by Slawson et al. (2011), EPIC 202126847 by LaCourse et al. (2015), EPIC 210754505 by Barros et al. (2016), EPIC 201569483, EPIC 202071289, EPIC 202086968, and K2-10 by Armstrong et al. (2015). In order to evaluate if there is evidence of a companion star in the observed spectra, all seven stars have been inspected carefully, finding no trace of contamination by a second set of spectral lines from a companion, although some small level (∼1%–2%) effect may still be present. In any case, these stars do not enter into the calculation of any planetary radii, except for K2-10. We note, that the exoplanet archive classifies K2-10 as a confirmed planet-host based on the following studies: Kruse et al. (2019), Van Eylen et al. (2016), Vanderburg et al. (2016), Montet et al. (2015), Barros et al. (2016), and Crossfield et al. (2016). We also note that Lester et al. (2021) and Howell et al. (2021), have shown that in binary systems,

[14] IRAF is distributed by the National Optical Astronomy Observatory, which is operated by the Association of Universities for Research in Astronomy, Inc., under a cooperative agreement with the National Science Foundation.

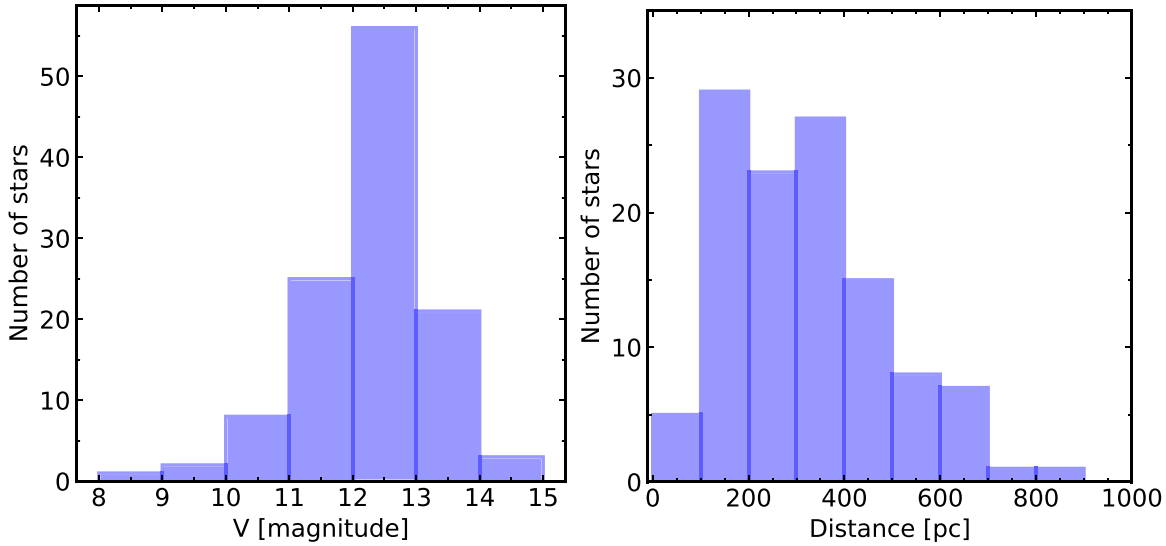


**Figure 2.** The distributions of $V$ magnitudes and distances for the sample stars. Distances were taken from Bailer-Jones et al. (2021), using Gaia EDR3 data, with $V$ magnitudes from the NASA Exoplanet Archive.

**Table 1**
Main Sample Data

| ID | Host Name | UT Date | R.A. | Decl. | $V$ (mag) | Exposure (s) | S/N |
|---|---|---|---|---|---|---|---|
| EPIC201403446 | K2-46 | 2018 Mar 30 | 11:37:03.92 | −00:54:26.10 | 12.03 | 2 × 1800 | 135 |
| EPIC211355342 | K2-181 | 2018 Mar 30 | 08:30:12.97 | 10:54:37.04 | 12.75 | 3 × 1800 | 95 |
| EPIC201736247 | K2-15 | 2016 Mar 16 | 11:52:26.59 | 04:15:17.10 | 14.76 | 2 × 1800 | 50 |
| … | … | … | … | … | … | … | |

(This table is available in its entirety in machine-readable form.)

smaller planets ($R < 2\,R_{\oplus}$) are not detected as the companion "third-light" would fill in their shallow transit.

In addition to systems that have been identified as eclipsing binaries, eight of the Kepler 1 targets here have been found to have nearby companion stars lying less than 1″ away from the primary star. These stars were taken from Furlan et al. (2017) and are: Kepler-132, KOI-1119, Kepler-1040, Kepler-396, Kepler-1339, Kepler-1505, Kepler-1525, and Kepler-1542. The reported separations range from 0.04″ to 0.88″ and in all cases the companion was fainter than the primary. Using values of Δmagnitudes from Furlan et al. (2017) (mostly ΔK-magnitudes), convolved with a 1″ seeing-disk, it is found that the expected contaminations, in all but one target, are small, with estimated flux contaminations of 0.3%–4.4%. The one primary target with a very close (0.″04) companion having nearly the same brightness is Kepler-1505 (Δmagnitude(562) = 0.00 ± 0.15 and Δmagnitude(880) = 0.16 ± 0.15; Furlan et al. 2017) and, at an estimated distance of 488 pc, the projected sky separation would be ∼20 au. Composite spectra that are not properly modeled can lead to uncertainties in the derived stellar parameters (Furlan & Howell 2017). Due to likely significant contamination of the spectrum of Kepler-1505 from its companion, this star was removed from the sample.

The main observational data, such as identifiers, observation dates, positions, $V$ magnitudes (taken from NASA Exoplanet Archive), exposure time per spectrum, and S/Ns of the reduced spectra are presented in Table 1.

Histograms with $V$ magnitudes and distances for our sample are presented in the left and right panels of Figure 2, respectively. The $V$-magnitude distribution of the observed targets peaks at $V \sim 12.5$ and goes as faint as $V \sim 15$. The target distances shown in the right panel of Figure 2 were estimated by Bailer-Jones et al. (2021) using the parallaxes and $G$-magnitude and $G_{BP}$–$G_{RP}$ color from Gaia EDR3. The studied sample is dominated by stars whose distances are less than 600 pc, with the distance distribution having a peak at approximately 300 pc.

## 3. Analysis

### 3.1. Spectroscopic Stellar Parameters

The spectroscopic analysis employed here assumes local thermodynamic equilibrium (LTE) and uses 1D plane parallel model atmospheres from the Kurucz ATLAS9 ODFNEW grid (Castelli & Kurucz 2003). Stellar spectroscopic parameters, namely the effective temperature ($T_{\rm eff}$), surface gravity (log $g$), iron abundance ($A$(Fe)[15]), and microturbulent velocity ($\xi$) were derived using a standard spectroscopic methodology which is based on measurements of the equivalent widths (EWs) of selected iron lines (Fe I and Fe II lines).

The adopted line list in this study was taken from Ghezzi et al. (2018), Meléndez et al. (2014), and Friel et al. (2003) and within the Hydra spectral window, a list of 25 Fe I lines and 5 Fe II lines was selected for analysis. The EWs of the selected

[15] $A(X) = \log(N(X)/N(H)) + 12.0$.

**Table 2**
Iron Line List

| λ (Å) | Species | χ (eV) | log *gf* | References |
|---|---|---|---|---|
| 6056.004 | Fe I | 4.733 | −0.558 | G18 |
| 6085.257 | Fe I | 2.759 | −2.908 | G18 |
| 6094.374 | Fe I | 4.650 | −1.650 | F03 |
| 6096.664 | Fe I | 3.984 | −1.861 | G18 |
| 6098.243 | Fe I | 4.559 | −1.825 | G18 |
| 6100.271 | Fe I | 4.559 | −2.201 | K14 |
| 6127.906 | Fe I | 4.143 | −1.503 | G18 |
| 6151.617 | Fe I | 2.176 | −3.357 | G18 |
| 6157.727 | Fe I | 4.076 | −1.257 | G18 |
| 6165.359 | Fe I | 4.143 | −1.487 | G18 |
| 6173.334 | Fe I | 2.223 | −2.938 | G18 |
| 6187.989 | Fe I | 3.943 | −1.724 | G18 |
| 6200.312 | Fe I | 2.608 | −2.457 | G18 |
| 6213.429 | Fe I | 2.223 | −2.650 | G18 |
| 6219.280 | Fe I | 2.198 | −2.549 | G18 |
| 6226.734 | Fe I | 3.884 | −2.143 | G18 |
| 6229.230 | Fe I | 2.850 | −3.040 | F03 |
| 6232.640 | Fe I | 3.654 | −1.232 | G18 |
| 6252.555 | Fe I | 2.404 | −1.687 | M14 |
| 6265.132 | Fe I | 2.176 | −2.633 | G18 |
| 6270.225 | Fe I | 2.858 | −2.540 | M14 |
| 6322.690 | Fe I | 2.590 | −2.250 | F03 |
| 6335.329 | Fe I | 2.198 | −2.423 | G18 |
| 6336.824 | Fe I | 3.686 | −0.856 | BK94 |
| 6344.150 | Fe I | 2.430 | −2.970 | F03 |
| 6084.102 | Fe II | 3.199 | −3.840 | G18 |
| 6113.319 | Fe II | 3.221 | −4.155 | G18 |
| 6149.246 | Fe II | 3.889 | −2.789 | G18 |
| 6238.386 | Fe II | 3.889 | −2.634 | G18 |
| 6247.557 | Fe II | 3.892 | −2.427 | G18 |

**Note.** The sources for the log *gf* values are given in the last column. G18: Ghezzi et al. (2018), M14: Meléndez et al. (2014), F03: Friel et al. (2003), K14: Kurucz (2014), and BK94: Bard & Kock (1994).

lines were measured using the ARES code v2 (Sousa et al. 2015). In Table 2 we present the Fe I and Fe II lines, the excitation potential energies $\chi$, the oscillator strengths (log *gf*), and the respective references for the latter.

Three conditions were required for obtaining a consistent solution for $T_{\rm eff}$, log $g$, and $\xi$ for the stars. To obtain $T_{\rm eff}$, the excitation equilibrium was required, or, removing trends between $A$(Fe I) and the excitation potential ($\chi$), of the lines. To obtain log $g$, the ionization equilibrium was required, or, requiring that the average abundances of the Fe I ($A$(Fe I)) and Fe II ($A$(Fe II)) lines are equal. By minimizing the slope (<0.005) of the relationship between $A$(Fe I) and the logarithm of the reduced EWs (log(EW/$\lambda$ )), the microturbulent velocity, $\xi$, is obtained. Finally, the iron abundances were consistent with the input model metallicities.

In order to analyze a relatively large number of stars in a homogeneous and efficient way, we used the automated stellar parameter and metallicity code named `qoyllur-quipu` (or $q^2$).[16] This is a Python code developed by Ramirez et al. (2014). Briefly, $q^2$ uses an input iron line list and measured EWs, along with the 2019 version of the abundance analysis code MOOG (Sneden 1973), to compute the iron abundances, effective temperatures, and surface gravities. The iterative process starts by interpolating a model atmosphere calculated assuming given values for $T_{\rm eff}$, log $g$, and metallicity and then the values of $T_{\rm eff}$, log $g$, and $A$(Fe) are increased or decreased iteratively to minimize the slopes of the relationships, and until obtaining a final adjusted value for the spectroscopic parameters of each star. Figure 3 shows an example of the iterated solution for the sample star HIP 81512, obtained for $T_{\rm eff} = 5752$ K, log $g = 4.34$, and $\xi = 1.06$ km s$^{-1}$, with the mean metallictity for this star represented by the solid blue line.

Table 3 presents the derived effective temperatures, surface gravities, metallicities, and microturbulent velocities for all stars in our sample, as well as the stellar radii and masses (see Section 3.3). We note that for a few stars having no measurable Fe II lines in their spectra, or having only one measurable Fe II line with a large uncertainty in the EW, the asteroseismic log $g$, if available, was adopted and used in the derivation of the effective temperature and microturbulence from the Fe I lines. Alternatively, when an asteroseismic log $g$ was also not available, the Fe I lines were used to estimate the parameters by varying log $g$ in steps of 0.05 dex and finding the log $g$ value that produced the most consistent solution in terms of the scatter in the Fe abundances from the individual lines.

### 3.2. Solar Proxies and a Solar Twin as Benchmarks

As benchmarks to our methodology and analysis techniques, we also analyzed solar-proxy spectra obtained with the Hydra spectrograph for reflected solar light from two asteroids, Astraea and Parthenope, as well as the well-studied solar twin HIP 81512 as a benchmark. Results are presented in Table 4. The parameters and metallicities obtained for the solar-proxy Astraea ($T_{\rm eff} = 5778$ K, log $g = 4.34$, $A$(Fe) = 7.51, and $\xi = 1.16$ km s$^{-1}$) and for Parthenope ($T_{\rm eff} = 5770$ K, log $g = 4.40$, $A$(Fe) = 7.54, and $\xi = 1.06$ km s$^{-1}$) are in excellent agreement with the solar parameters, indicating that our methodology does not harbor strong biases for solar-type stars. We note, however, that the mean metallicity for the solar proxies of $A$(Fe) =7.52 is slightly more metal-rich than the Asplund et al. (2021) ($A(\rm Fe)_\odot = 7.46$) scale, although it is in good agreement with the Magg et al. (2022) ($A(\rm Fe)_\odot = 7.50$) scale. We also note excellent agreement with the stellar parameters derived in the high-precision analysis of the solar twin HIP 81512 by Ramirez et al. (2009) and Ramirez et al. (2013); the latter studies are based on the analysis of high-resolution spectra ($R = \lambda/\Delta\lambda \simeq 60,000$) obtained with the Robert G. Tull coudé spectrograph on the 2.7 m Harlan J. Smith telescope and measurements of 128 Fe I and 16 Fe II lines, obtaining $T_{\rm eff} = 5755 \pm 32$ K, log $g = 4.43 \pm 0.04$ dex, and $A$(Fe) =7.40 ± 0.04 dex. These comparisons with benchmark spectra can serve as validations for the technique adopted in this study for the analysis of Hydra spectra covering 6050 −6350 Å and the Fe I/Fe II line list from Table 2.

### 3.3. Stellar Masses and Radii and Planetary Radii

Fundamental stellar properties, such as stellar radius, age, or mass, can be estimated by comparing the positions of stars in a color–magnitude diagram with theoretical isochrones. Gaia DR3 (Gaia Collaboration et al. 2021) currently provides high-precision parallaxes that can be used to determine the absolute magnitudes of large numbers of stars.

Different codes that are available to the community, such as `PARAM` (Girardi et al. 2000; da Silva et al. 2006;

[16] https://github.com/astroChasqui/q2

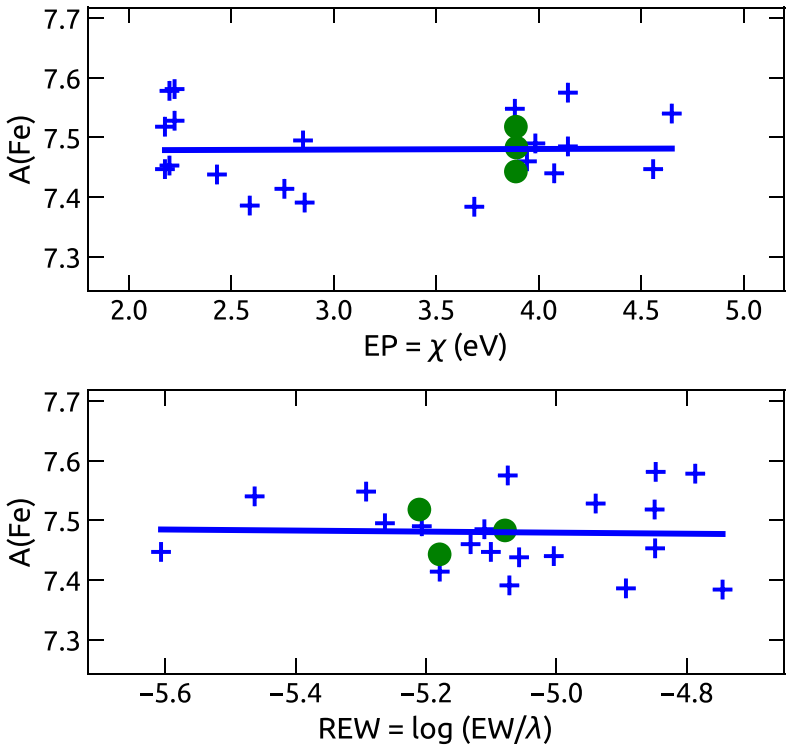


**Figure 3.** An example of the applied methodology to the solar twin HIP 81512. The top panel shows the iron abundance of the Fe I lines (blue crosses) as a function of excitation potential ($\chi$), which defines the effective temperature of the star. The Fe II transitions are shown as green circles. The bottom panel illustrates the Fe I abundance as a function of the reduced EW (REW) of the Fe lines, which defines the microturbulent velocity parameter.

Rodrigues et al. 2014, 2017), or `isochrones` (Morton 2015), have been developed as interfaces to find best fits to various isochrones, such as MESA Isochrones & Stellar Tracks (MIST; Choi et al. 2016; Dotter 2016), and several works have adopted similar methodologies to obtain stellar masses and radii (e.g., Johnson et al. 2017; Mayo et al. 2018; Wittenmyer et al. 2020).

In this work, stellar masses and radii were computed using the isochrone method via the $q^2$ code (`qoyllur-quipu`; Ramirez et al. 2014), which determines stellar mass, age, luminosity, and radius, using a grid of Yonsei–Yale isochrones (Yi et al. 2001). Briefly, to determine which isochrones best represent a particular set of observed stellar parameters (spectroscopic $T_{\rm eff}$ and [Fe/H] from this work, along with the $M_V$ absolute magnitude derived from the parallax), probability distributions of those parameters are determined and matched to the isochrones, assuming that the errors in the observed stellar parameters ($\delta\ T_{\rm eff}$, $\delta M_V$, and $\delta$ [Fe/H]) have Gaussian probability distributions. For more details see Ramirez et al. (2013) and Ramirez et al. (2014). Isochrone-derived masses and radii of the sample stars are shown in Table 3. For five stars, instead of using $M_V$, we used the log $g$ values to compute the stellar radii and the latter are flagged with an "$a$" in Table 3. In particular, we opted for using log $g$ when there was a range of $V$ magnitudes reported for a star, which was the case, for example, for two of the eclipsing binaries in our sample. We note that the stellar masses in these cases were estimated in the same way as the other stars using $Y^2$ isochrones.

Planetary radii were then obtained using the derived stellar radii and the value of the transit depth ($\Delta F$), which is the fraction of stellar flux lost at the minimum of the planetary transit, given by the equation from Seager & Mallen-Ornelas (2003):

$$R_{\rm pl} = 109.1979 \times \sqrt{\Delta F \times 10^{-6}} \times R_{\rm star}, \quad (1)$$

where the radius of the planet is in Earth radii.

We note that in this study, only values of $\Delta F$ from confirmed planets were used; we did not consider planets classified as planet candidates and false positives (according to the Kepler 1 and K2 notes in the NASA Exoplanet Archive). Most of the planetary transit depths of the K2 stars were from Kruse et al. (2019) (for 66 confirmed planets); for planets not cataloged by Kruse et al. (2019) we used values from Vanderburg et al. (2016), Pope et al. (2016), Barros et al. (2016), Rizzuto et al. (2017), and Livingston et al. (2018). We note that for K2-100 we noticed that the $\Delta F$ from Kruse et al. (2019) was discrepant when compared to other literature sources (e.g., Livingston et al. 2018; Stefansson et al. 2018; Mann et al. 2017; Libralato et al. 2016; Pope et al. 2016) and in this study we adopted the transit depth from Livingston et al. (2018). The transit depth of the planets of Kepler 1 stars were from Thompson et al. (2018) (for 56 confirmed planets). The $\Delta F$ values are provided in the Table 6.

### 3.4. Uncertainties in the Derived Parameters

The formal errors adopted for the stellar parameters $T_{\rm eff}$, log $g$, and $\xi$ were computed using $q^2$, which follows the error analysis discussed by Epstein et al. (2010) and Bensby et al. (2014). Errors in the iron abundances, $A$(Fe I) and $A$(Fe II), were obtained by combining errors estimated from the EW measurements with the stellar parameter uncertainties. The

**Table 3**
Stellar Parameters, Radii, and Masses

| ID | $T_{\rm eff}$ (K) | $\delta T_{\rm eff}$ (K) | log $g$ (dex) | $\delta$log $g$ (dex) | $A$(Fe) (dex) | $\delta A$(Fe) (dex) | $\xi$ (km s$^{-1}$) | $\delta \xi$ (km s$^{-1}$) | $R_{\rm star}$ ($R_\odot$) | $\delta R_{\rm star}$ ($R_\odot$) | $M_{\rm star}$ ($M_\odot$) | $\delta M_{\rm star}$ ($M_\odot$) |
|---|---|---|---|---|---|---|---|---|---|---|---|---|
| EPIC 201166680 | 6051 | 289 | 4.01 | 0.49 | 7.39 | 0.11 | 1.45 | 0.37 | 1.45 | 0.16 | 1.09 | 0.06 |
| EPIC 201211526 | 5717 | 176 | 4.13 | 0.39 | 7.21 | 0.08 | 1.07 | 0.17 | 0.92 | 0.03 | 0.89 | 0.04 |
| EPIC 201257461 | 4945 | 160 | 2.95 | 0.82 | 7.41 | 0.11 | 1.67 | 0.18 | 5.48 | 0.40 | 1.25 | 0.22 |
| … | … | … | … | … | … | … | … | … | … | … | … | … |

**Note.** (*) Asteroseismic log $g$; (**) no measurable Fe II lines; (*a*) $R_{\rm star}$ computed using log $g$ values. This table is published in its entirety in the machine-readable format. A portion is shown here for guidance regarding its form and content.

(This table is available in its entirety in machine-readable form.)

**Table 4**
Stellar Parameters of the Solar Proxies

| ID | $T_{\rm eff}$ (K) | log $g$ (dex) | $A$(Fe) (dex) | $\xi$ (km s$^{-1}$) |
|---|---|---|---|---|
| Astraea | 5778 ± 160 | 4.34 ± 0.33 | 7.51 ± 0.09 | 1.16 ± 0.14 |
| Parthenope | 5770 ± 158 | 4.40 ± 0.36 | 7.54 ± 0.09 | 1.06 ± 0.24 |
| HIP 81512 | 5752 ± 113 | 4.34 ± 0.33 | 7.48 ± 0.07 | 1.06 ± 0.10 |

**Note.** $A(\mathrm{Fe})_\odot = 7.46 \pm 0.04$ (Asplund et al. 2021); $A(\mathrm{Fe})_\odot = 7.52 \pm 0.06$ dex (Magg et al. 2022).

**Table 5**
Error Budget

| Parameter | Median Uncertainty |
|---|---|
| $T_{\rm eff}$ | 154 K |
| log $g$ | 0.36 dex |
| $A$(Fe) | 0.09 dex |
| $V$ | 0.07 mag |
| plx | 0.02 mas |
| $M_{\rm star}$ | 0.04 $M_\odot$ |
| $R_{\rm star}$ | 4.15 % |
| $\Delta$F | 3.35 % |
| $R_{\rm pl}$ | 4.44 % |

individual errors of these parameters are presented in Tables 3 and 4.

The median errors in the stellar parameters derived in this study are reported in Table 5: $\delta T_{\rm eff} = 154$ K, $\delta$log $g = 0.36$ dex, $\delta A(\mathrm{Fe}) = 0.09$ dex, and $\delta\xi = 0.24$ km s$^{-1}$. We note that these are somewhat larger than the typical values from analyses of high-resolution spectra ($R \sim 60{,}000$) in the literature (e.g., Ramirez et al. 2014; Martinez et al. 2019; Ghezzi et al. 2021). Larger errors here are to be expected given that the Hydra spectra have lower resolution ($R \sim 18{,}500$) and smaller wavelength coverage, which results in having a smaller number measurable Fe I lines (25) and Fe II lines (5).

Since the stellar masses and radii and planetary radii of our sample were derived from other parameters, we considered the individual contributions of the errors in each one of the parameters to estimate the error budget (similar to the discussions by Fulton & Petigura 2018; Martinez et al. 2019). The internal precisions (median errors) in the derived effective temperatures and metallicities were discussed above. The error in the $V$ magnitude contributes ∼1% to the stellar radius error, when taking 0.07 mag to be the median error in $V$ magnitude for our stars. The contribution due to errors in the parallaxes corresponds to a median error of 0.02 mas and represents a 0.45% error in the stellar mass and radius.

The stellar radii uncertainty and the transit depth ($\Delta F$) errors have a direct impact on the determination of planetary radii errors. The median internal uncertainty in our derived stellar radii distribution is 4.2%; we adopted the transit depth values $\Delta F$ and respective errors from Kruse et al. (2019) and Thompson et al. (2018), which, for the planets in our sample, result in a 3.4% internal precision in $\Delta F$. Finally, these uncertainties lead to a 4.4% internal precision for the $R_{\rm pl}$ error budget. A summary of the contributions to the error budgets in the $R_{\rm star}$ and $R_{\rm pl}$ determinations is presented in Table 5. To assess possible differences in the choice of isochrones we adopted the Darmouth isochrones instead of the Yonsei–Yale ones and found no signicant differences in the derived stellar radii and masses. As an example, for the star Kepler-62 we find $R_{\rm star} = 0.659 \pm 0.018\ R_\odot$ and $M_{\rm star} = 0.711 \pm 0.024\ M_\odot$ (using Dartmouth isochrones), while the result in this study is the same but just with a slightly higher uncertainty in the mass: $R_{\rm star} = 0.659 \pm 0.018\ R_\odot$ and $M_{\rm star} = 0.711 \pm 0.026\ M_\odot$ (using Yonsei–Yale isochrones).

### 3.5. Possible Impact of Magnetic Activity on Stellar Parameter Determination

In addition to the various sources of uncertainty discussed in the previous subsection, stellar magnetic activity can also affect the determinations of $T_{\rm eff}$, $\xi$, and [Fe/H], as shown by Flores et al. (2016), Yana Galarza et al. (2019), and Spina et al.(2020).

Three stars in our sample had activity indices reported by Brown et al. (2022), who compiled a database of chromospheric activity measurements and surface-averaged large-scale magnetic-field measurements for a sample of FGK main-sequence stars. These stars are K2-229, EPIC 202089657, and Kepler-409, with log $R'_{\rm HK} = -4.73$, $-4.75$, and $-4.82$, respectively, keeping in mind that the Sun has a value of log $R'_{\rm HK} = -5.02$, which varies by about ±0.01 dex over the Solar activity cycle (Lorenzo-Oliveira et al. 2018).

Stellar magnetic activity effects have been quantified by Spina et al. (2020) via the log $R_{\rm HK}$ index, based on a stellar parameter analysis that relies on relations between the Fe I excitation equilibria and the Fe I reduced EWs (EW/$\lambda$), both as functions of the Fe I abundance, in addition to the ionization balance of Fe I and Fe II. These constraints provide the values of $T_{\rm eff}$, log $g$, $\xi$, and [Fe/H], and this is the technique used in our study. The impact that stellar activity has on the derivations of the specific stellar parameters using Fe I and Fe II lines is found to be the greatest for $T_{\rm eff}$, $\xi$, and [Fe/H], with almost no effect on log $g$ (as illustrated in Figure 3 of Spina et al. 2020). In rough numbers (from Figure 4 of Spina et al. 2020), $R_{\rm HK} \sim$ –4.25 leads to a lower value of $T_{\rm eff}$ by ∼100 K, while log

$R_{HK} \sim -4.40$ causes a metallicity change of [Fe/H] = −0.05, and a value of log $R_{HK} \sim$ −4.35 would lead to a derived microturbulent velocity that is too large by ∼0.3 km s$^{-1}$. A much lower activity level of log $R_{HK} \sim -4.7$–4.8, as measured, for example, for the three target stars mentioned above, would cause an unmeasurable change in the effective temperature, a metallicity change of −0.02 dex, and would lead to a microturbulent velocity change of ∼0.05 km s$^{-1}$. All of these variations are well within the uncertainties in our analysis. These are also in line with the results of Lorenzo-Oliveira et al. (2018) who, for the young solar twin HIP 36515 (log $R_{HK} \sim$ −4.70), the stellar parameters derived over its six year activity cycle find a scatter in $T_{eff}$ of ±10 K, ±0.01 in [Fe/H], and ±0.07 km s$^{-1}$ in microturbulent velocity. It is possible, however, that other stars in our sample may have higher levels of activity, although such high activity levels would suggest ages <1 Gyr (Lorenzo-Oliveira et al. 2018) or that the stars are members of close binary systems (Oláh 2007).

As part of an analysis of the young active solar twin HIP 36515 (age ∼ 0.4 Gyr), Yana Galarza et al. (2019) established a list of Fe I and Fe II lines that are sensitive to stellar magnetic activity. Among the lines in our line list that were identified as sensitive to magnetic fields are Fe I 6173 Å, 6200 Å, 6213 Å, 6219 Å, 6252 Å, 6265 Å, and 6270 Å (Table 2) and these have both large Landé factors, coupled with large EWs (through a combination of log *gf* values and excitation potentials). None of our Fe II lines were identified as sensitive to stellar magnetic activity.

We investigated the impact that the inclusion of "sensitive" Fe I lines has on the derivation of stellar parameters by removing these sensitive lines and rederiving the parameters for a selected sample of 15 stars. This subsample contains the three stars with measured values of log $R_{HK}$ mentioned above, plus five stars in our sample with approximate ages from $q^2$ of <4 Gyr (K2-223, K2-44, Kepler-1339, KOI-6, and KOI-293), and two stars (K2-100 and K2-101) which are members of the young (650 ± 70 Myr; Martin et al. 2018) open cluster M 44. We also added the stars K2-186, K2-34, Kepler-139, Kepler-1445, and Kepler-396, as these have measured flares with energies $>10^{34}$ erg along with log $R_{H\alpha} > -4.4$ in Su et al. (2022), who determined the $R_{H\alpha}$ activity index and flare energy using LAMOST spectra and light curves of stars observed by Kepler 1 and K2.

Figure 4 provides comparisons between the stellar parameters derived in this study (without taking into consideration the possible effects of magnetic fields in the measured Fe I lines) and those obtained including only those Fe I lines that were deemed as insensitive to magnetic fields. The median and median absolute deviation (MAD) values of the differences for each stellar parameter are included in each panel of the figure. The upper left panel shows that the differences in the effective temperatures are less than ∼50 K for most stars, with only two stars, K2-44 and Kepler-1445, having larger differences of $\Delta T_{eff}$ ("Non-sensitive"—"This Work") = −112 K and −142 K, respectively. This result suggests that the differences in the effective temperatures are not significant and, in general, fall within the range of our uncertainties (see Table 5). In the case of log *g* (top right panel), all stars have differences less than 0.09 dex, with the exceptions of K2-44 and Kepler-409 having differences of −0.2 and −0.15 dex, respectively. Given the uncertainties in log *g*, all differences are well within the estimated median uncertainty of 0.36 dex. A similar result is found for values of [Fe/H] (lower left panel), as the median uncertainty in [Fe/H] in this study is 0.09 dex (Table 5), with the largest metallicity difference found being −0.118 for Kepler-1445. According to Spina et al. (2020), magnetic activity is expected to result in an increase in microturbulent velocities for log $R_{HK} > -5.0$, or in active young stars (ages < 4–5 Gyr). The median difference found for the microturbulent velocity parameter is −0.01 and the MAD is 0.06 km s$^{-1}$ (Figure 4), indicating that there is no significant evidence that magnetic activity is measurably affecting the microturbulent velocities in this analysis.

In summary, the stellar parameters derived without the use of the magnetically sensitive lines are within the uncertainties when compared to the parameters from this study that include some Fe I lines that are deemed as lines sensitive to the effects of magnetic fields and activity. This result suggests that the final stellar parameters derived for this sample of stars have not been perturbed significantly by strong magnetic activity.

## 4. Results and Comparisons with the Literature

### 4.1. Effective Temperatures and Surface Gravities

In general, there are more results available for Kepler 1 mission targets than for K2. Several studies in the literature (Petigura et al. 2017; Brewer & Fischer 2018; Martinez et al. 2019; Ghezzi et al. 2021) analyzed the CKS (Petigura et al. 2017) but used different analysis techniques. The stellar parameters obtained by Petigura et al. (2017) were derived using synthetic spectra and the codes `SpecMatch` and `SME@XSEDE`; Brewer & Fischer (2018) derived the stellar parameters also using spectral synthesis and the Spectroscopy Made Easy (SME; Piskunov & Valenti 2017) code, while Martinez et al. (2019) and Ghezzi et al. (2021) adopted a methodology that was based on the classical spectroscopic EW method and used the code MOOG (Sneden 1973). Concerning results for K2 targets, in particular, Petigura et al. (2018a), using the same methodology of Petigura et al. (2017), analyzed a sample of 141 K2 candidate planet-host stars, while Wittenmyer et al. (2020) analyzed a sample of 129 K2 planet candidate host stars whose spectra were observed by the K2-HERMES program (Wittenmyer et al. 2018; Sharma et al. 2019; Clark et al. 2022) in the Galactic Archeology with HERMES (GALAH; Buder et al. 2021) survey. In addition, results for a large number of both Kepler 1 and K2 targets were obtained by the low-resolution optical spectroscopic LAMOST survey (Cui et al. 2012; Zong et al. 2018), as well as the high-resolution spectroscopic near-infrared APOGEE survey (Majewski et al. 2017; see also Wilson et al. 2018).

Comparisons of our $T_{eff}$ values with those from the studies mentioned above are shown in the different panels of Figure 5; for each case, the median differences "Other Work–This Work" are given in the top left of each panel, along with the corresponding MADs; in all panels the gray diamonds correspond to Kepler 1 stars, while the blue circles correspond to K2 stars. From the medians and MADs in Figure 5 we can conclude that there is overall good agreement between our effective temperatures and those from the APOGEE and LAMOST surveys, as well as those available from the literature. The mean of the median differences is small, $\Delta T_{eff} \sim -45$ K and the MADs are all below 70 K, except for the comparison with the GALAH results, where MAD = 119 K (Wittenmyer et al. 2020) and

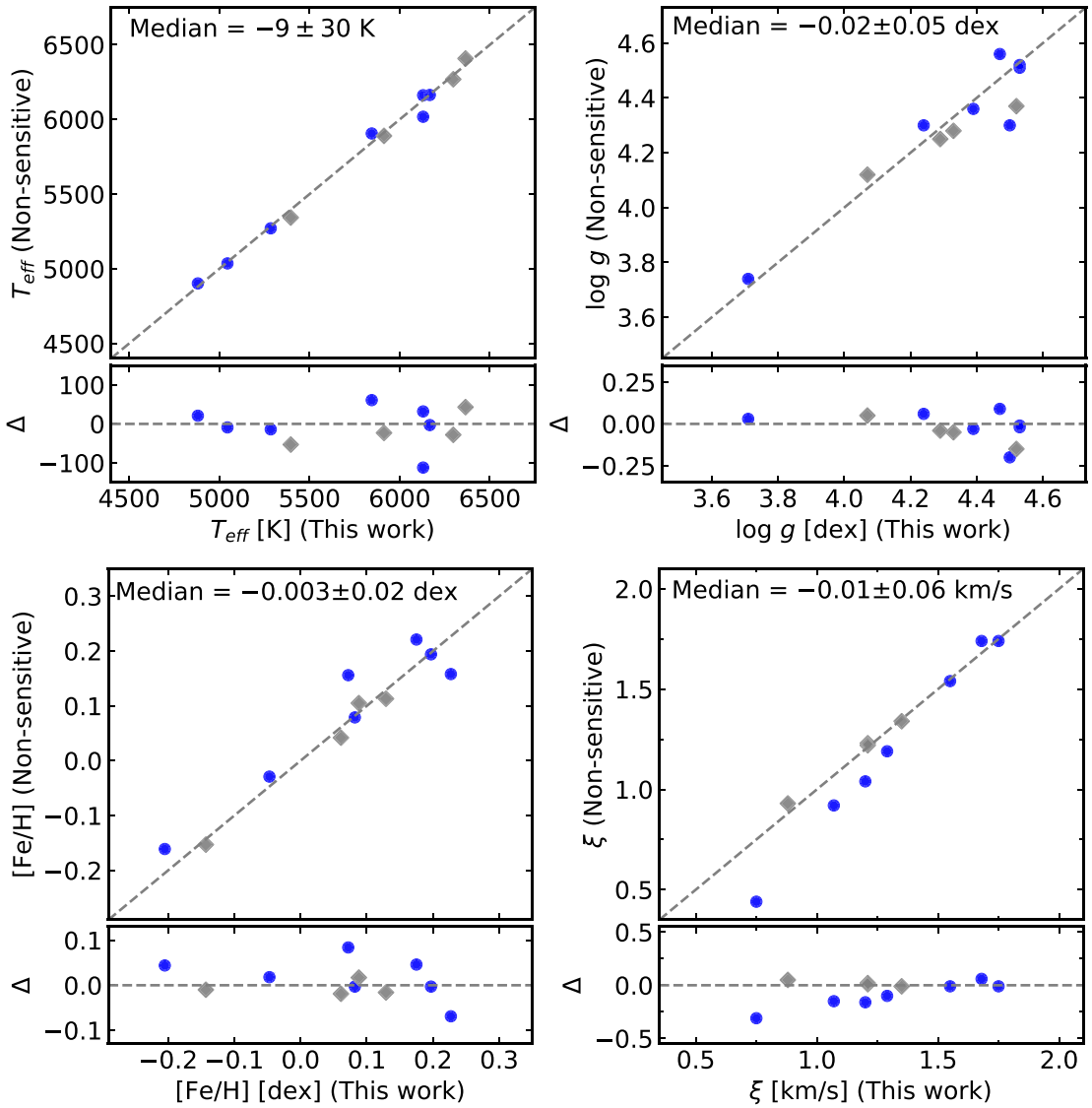


**Figure 4.** Comparison between the effective temperatures, surface gravities, metallicities, and microturbulent velocities derived in this work with stellar parameters that were rederived using only the subset of the Fe I lines that are deemed as insensitive to the effects of stellar activity ("Non-sensitive"). The bottom panels present the difference, Δ, between the stellar parameters for "Non-sensitive—This work." The blue circles represent K2 stars and gray diamonds Kepler 1 stars. The selected targets include host stars that exhibit flare activity (flares with energies $> 10^{34}$ erg) along with log $R_{H\alpha} > -4.4$, three stars with a measured chromospheric Ca II index of log $R_{HK}$ ∼−4.7–4.8, five stars that have estimated ages <4 Gyr, and two stars that are members of the young open cluster M 44.

114 K (GALAH). Overall our $T_{\rm eff}$ scale is just slightly hotter than the other scales, except for the comparison with Petigura et al. (2018a; K2 targets median difference = 8 K) and Martinez et al. (2019; median difference = 0 K).

Comparisons of the surface gravities derived here—from Fe I and Fe II ionization balance—with those from the works discussed above are shown in Figure 6 (as in Figure 5, the median differences ("Other Work"—"This Work") ± MAD are given in each panel). The median log $g$ differences for all studies and the surveys are surprisingly small (see Section 4.1.1) given the different analysis methodologies and line lists, all <0.06 dex, except for Petigura et al. (2018a) that has a mean log $g$ difference of 0.12 dex. In all comparisons the MAD values are smaller or equal to 0.14 dex, which is smaller than typical uncetainties in log $g$ values.

#### 4.1.1. Asteroseismic versus Spectroscopic Surface Gravities

The stellar parameters derived here ($T_{\rm eff}$, log $g$, $\xi$, and [Fe/H]) are based on an analysis of a sample of Fe I and Fe II lines, where correlations between parameters in such a spectroscopic analysis can lead to systematic errors, especially in the derived values for log $g$; for example, Fe I lines are typically stronger than Fe II lines, leading to potential correlations between the microturbulent velocity and log $g$. Accurate surface gravities can thus be one of the more difficult parameters to constrain via spectroscopy, especially if the Fe II lines are few in number and weak. In order to investigate possible systematic offsets in the log $g$ values derived in this study, we compare our results with those computed via asteroseismology, where the surface gravity can be derived with quite good precision (Pinsonneault et al. 2018).

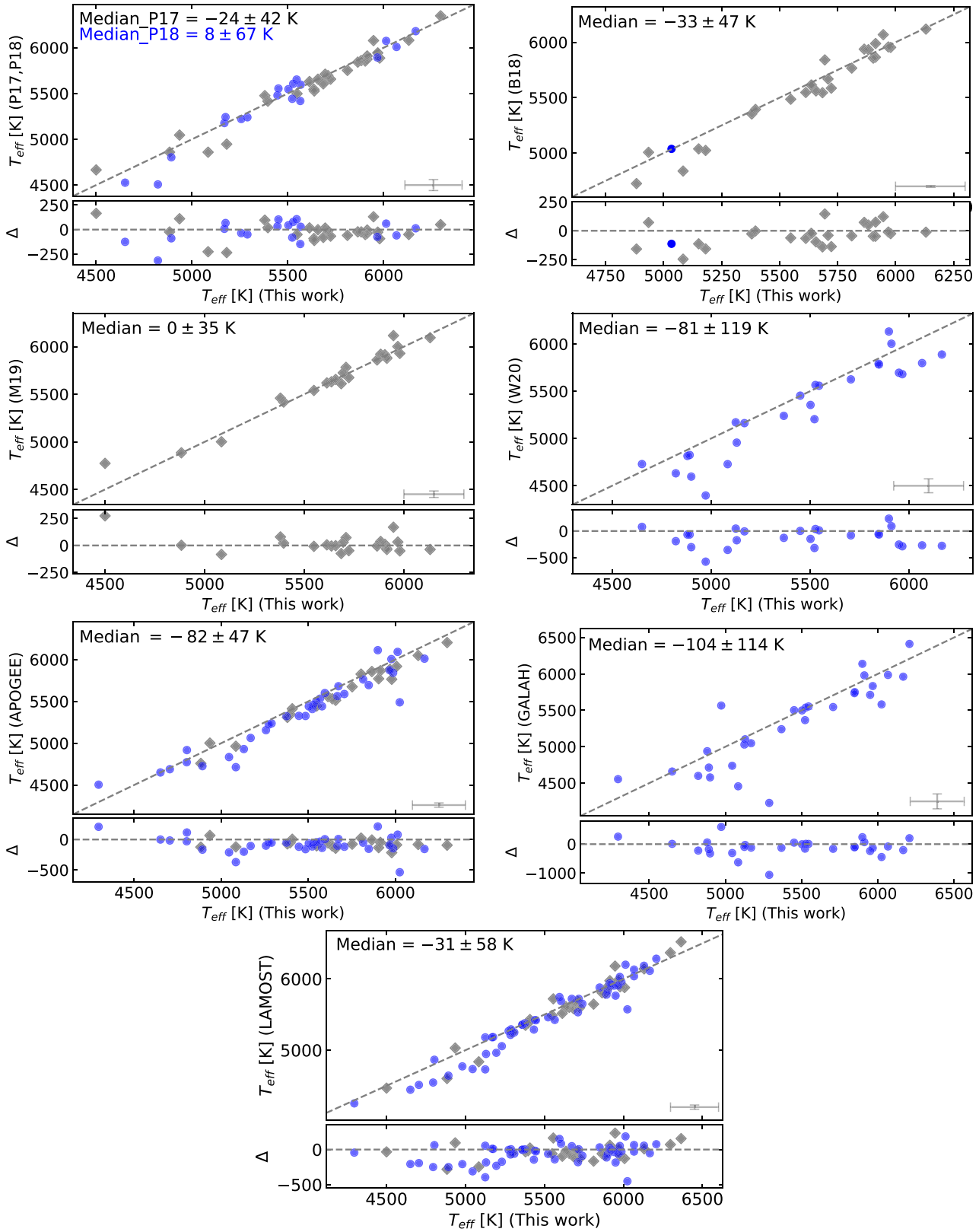


**Figure 5.** Comparisons of the effective temperatures in this study with those from Petigura et al. (2017, 2018a; P17 and P18, respectively), Brewer & Fischer (2018; B18), Martinez et al. (2019; M19), Wittenmyer et al. (2020; W20), APOGEE DR17, GALAH DR3, and LAMOST DR5. K2 stars are blue circles and Kepler 1 stars are gray diamonds. The bottom subpanels show the difference between "Other Work–This Work" (Δ). The median differences between the parameters and the corresponding MAD are indicated in each case. The black dashed lines represent equality.

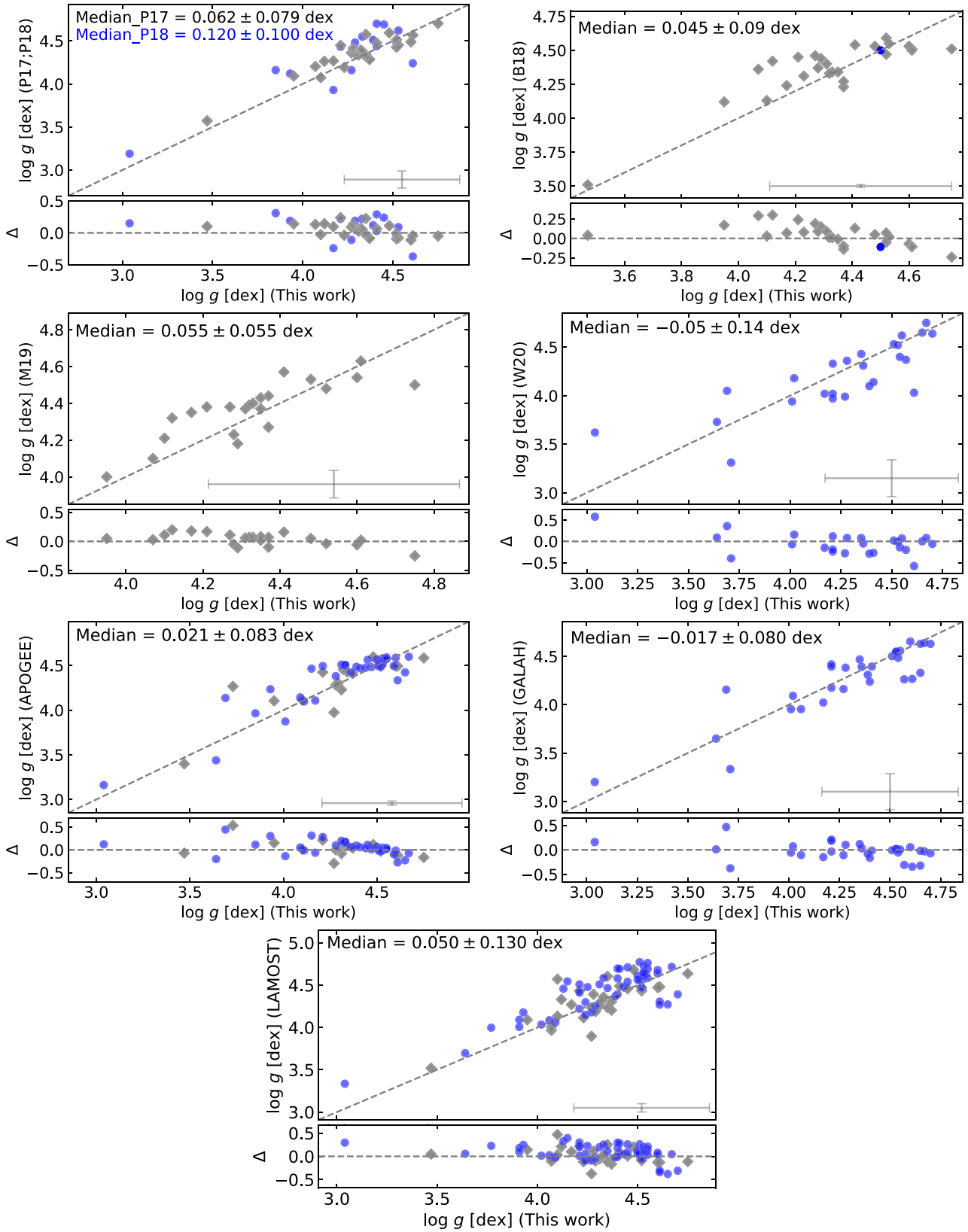


**Figure 6.** Comparison of the log $g$ values derived in this work and Petigura et al. (2017, 2018a; P17 and P18, respectively), Brewer & Fischer (2018; B18), Martinez et al. (2019; M19), Wittenmyer et al. (2020; W20), APOGEE DR17, GALAH DR3, and LAMOST DR5 for K2 stars (blue circle) and Kepler 1 stars (gray diamond). The median differences between the parameters and the corresponding MAD are indicated in each case. The black dashed lines represent equality. Each bottom subpanel plots the difference, Δ, between "Other Work–This Work."

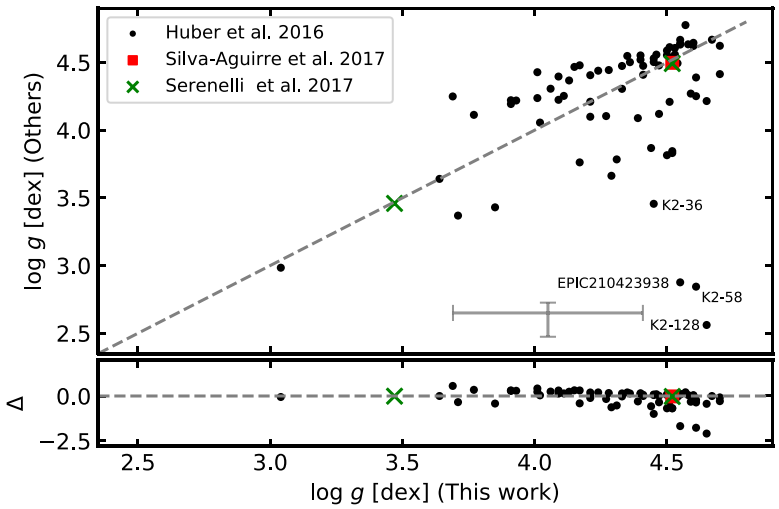


**Figure 7.** Comparisons of spectroscopic surface gravities derived in this work with asteroseismic surface gravities from Huber et al. (2016), Aguirre et al. (2017), and Serenelli et al. (2017). The four most discrepant values of stellar log $g$ between this work and Huber et al. (2016) are labeled and these are discussed in the text. The bottom panel shows the differences between "Other Work–This Work." Median uncertainty error bars are presented.

For such a comparison, we collected in Figure 7 asteroseismology results for 83 stars from Huber et al. (2016), Aguirre et al. (2017), and Serenelli et al. (2017). In order to compute surface gravities via asteroseismology, Huber et al. (2016) and Serenelli et al. (2017) used the $T_{\rm eff}$ and [Fe/H] from the APOGEE survey (DR13), while Aguirre et al. (2017) adopted $T_{\rm eff}$ and [Fe/H] from several literature sources. Most of the stars in common with this study are from Huber et al. (2016); the log $g$ values from that study show no significant offsets and are in good agreement when compared to ours, with a median log $g$ difference ("Huber et al. 2016–This Work") $= 0.033 \pm 0.164$ dex. However, there are four stars for which the log $g$ differences are $>1$ dex. These four discrepent stars (which are labeled in Figure 7) have asteroseismic gravities that would indicate that they are giant or subgiant stars, whereas other studies have derived surface gravities that suggest that these stars are dwarfs as discussed below:

1. K2-36: this star was analyzed individually by Damasso et al. (2019) using high-resolution spectra from HARPS-N, with stellar parameters derived using the spectroscopic technique and finding log $g$ values of 4.73, 4.60, and 4.57 with EWs, Atmospheric Stellar Parameters from Cross-Correlation Functions (CCFpams), and Stellar Parameter Classification (SPC; Buchhave et al. 2014), respectively. Using `SME` and `SpecMatch` with HIRES spectra, Sinukoff et al. (2016), Brewer et al. (2016), and Crossfield et al. (2016) derived log $g = 4.65$, 4.55, and 4.60, respectively. Finally, using SPC in Tillinghast Reflector Echelle Spectrograph (TRES) spectra, Vanderburg et al. (2016) derived log $g = 4.70$. Our result (log $g = 4.45$) is $\sim$0.1–0.3 dex lower than these studies, although all of these results indicate that K2-36 is a dwarf.
2. K2-58: using `SpecMatch` and `SME` with HIRES spectra, Crossfield et al. (2016) and Brewer & Fischer (2018) derived log $g = 4.52$ and 4.50, respectively. Using `SPC` with TRES spectra, Vanderburg et al. (2016) derived log $g = 4.54$, with these values being consistent with our log $g = 4.50$ dex, pointing to K2-58 as being a dwarf.
3. K2-128: using `SPC` with TRES spectra, Crossfield et al. (2018) and Mayo et al. (2018) derived log $g = 4.70$; while this result is 0.20 dex larger than our log $g$, taken together, these studies point to K2-128 as being a dwarf.
4. EPIC 210423938: for this star, the log $g$ value obtained by Mayo et al. (2018) is 4.69. Stassun et al. (2019) determined that log $g = 4.55$ from its stellar radius and mass. Considering our result (log $g = 4.55$ dex), we identify EPIC 210423938 as a dwarf.

In summary, spectroscopic studies have found the four stars discussed above to have dwarf-star surface gravities. In addition, this status is confirmed from their DR3 Gaia parallaxes and distances, with distances to K2-36 of 109 pc, K2-58 of 182 pc, K2-128 of 114 pc, and EPIC 210423938 of 149 pc, resulting in absolute Gaia or V magnitudes of $M_V = 6.5$, $M_G = 5.8$, $M_V = 7.3$, and $M_V = 7.1$, respectively. These absolute magnitudes confirm them as K dwarfs. Without considering the four discrepant stars discussed above, we find median log $g$ differences with Huber et al. (2016) $= -0.049 \pm 0.136$. We note that for the few stars in common with Aguirre et al. (2017) and Serenelli et al. (2017), there is excellent agreement.

### 4.2. Metallicities

Figure 8 summarizes a comparison of the metallicities for K2 stars (blue circles) and Kepler 1 stars (gray diamonds) derived in this work with those derived in other studies and surveys. The metallicities from the literature were obtained either via spectrum synthesis methods (Petigura et al. 2017, 2018a; Brewer & Fischer 2018; Wittenmyer et al. 2020), (Buder et al. 2021; GALAH), (Jonsson et al. 2020; APOGEE), (Zong et al. 2018; LAMOST) or were based on EW measurements of Fe I and Fe II lines (Ghezzi et al. 2021). For Kepler 1 stars in common with Petigura et al. (2017), the median metallicity difference is $0.040 \pm 0.034$ dex, while with Brewer & Fischer (2018) it is $0.024 \pm 0.064$ dex. There are 22 stars in common with Ghezzi et al. (2021), with a median difference of $0.017 \pm 0.037$ dex. The K2 stars in common with Petigura et al. (2018a) have a median difference of $0.021 \pm 0.052$ dex, and for those in common with Wittenmyer et al. (2020) the

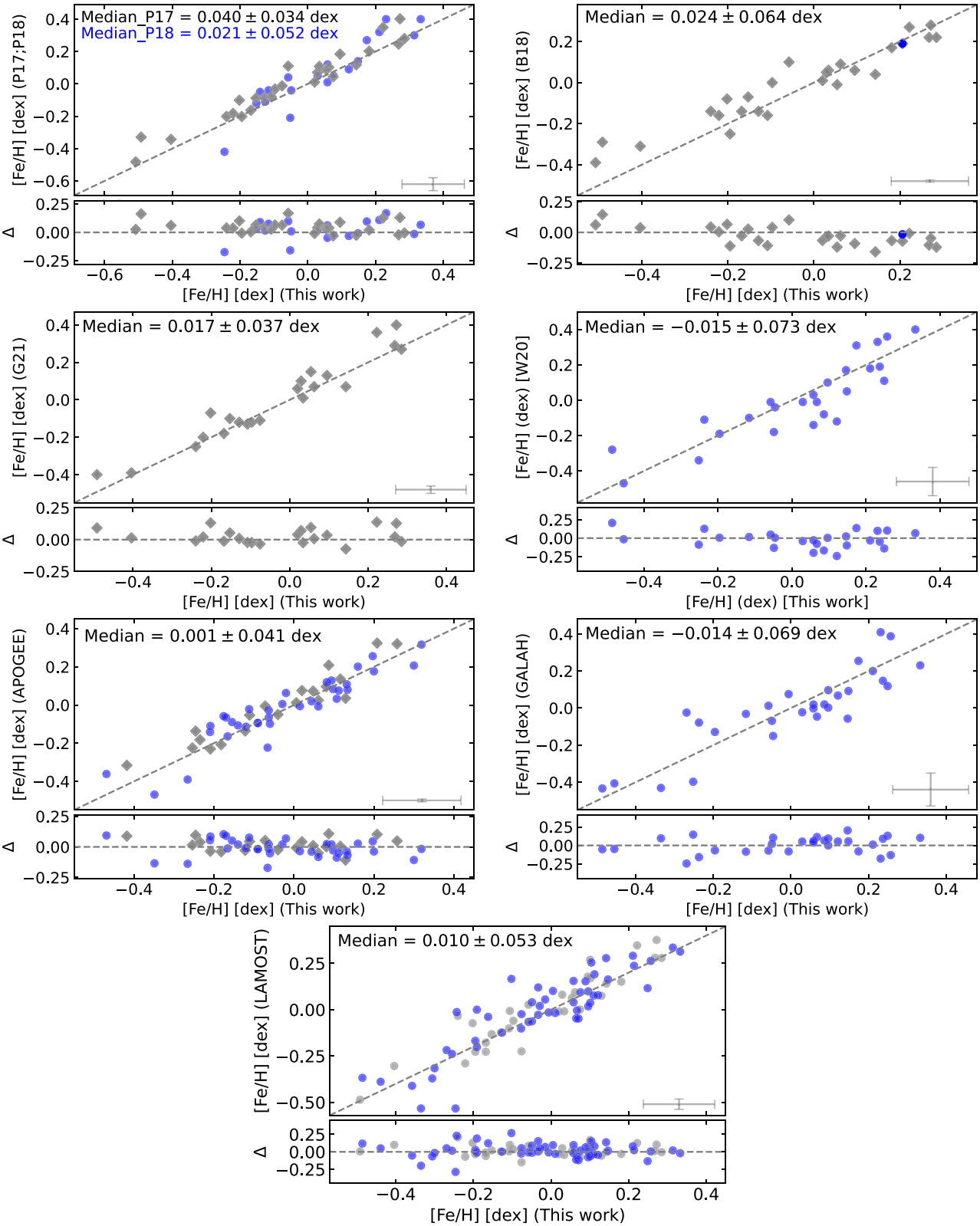


**Figure 8.** Comparisons of metallicities derived in this work with results from Petigura et al. (2017, 2018a; P17 and P18, respectively), Brewer & Fischer (2018; B18), Ghezzi et al. (2021; G21), Wittenmyer et al. (2020; W20), APOGEE DR17, GALAH DR3, and LAMOST DR5, for K2 stars (blue circles) and Kepler 1 stars (gray diamonds). The median differences between the parameters and the corresponding MAD scatters are indicated in each case. The black dashed lines represents equality. The bottom subpanels show the differences between "Other Work–This Work."

median [Fe/H] difference is $-0.015 \pm 0.073$ dex. Comparison of the metallicities with the spectroscopic surveys also finds excellent agreement: $0.001 \pm 0.041$ dex for APOGEE DR17, while with GALAH DR3 it is $-0.014 \pm 0.069$ dex. Finally, the median difference for stars in common with LAMOST DR5 is $0.010 \pm 0.053$ dex.

Overall, the metallicity comparisons in Figure 8 indicate good consistency between our results and the other metallicity scales, with median metallicity differences in all cases being smaller than ∼0.04 dex and MAD less than 0.07 dex. Save for a few outliers, the scatter in the [Fe/H] differences are well within the expected uncertainties.

### 4.3. Stellar Radii and Masses

A number of studies in the literature obtained stellar radii and, in some instances, also masses, for Kepler 1 targets using different combinations of codes, models, and parameters. Johnson et al. (2017) used the isochrone method, stellar parameters from Petigura et al. (2017), and Dartmouth Stellar Evolution Program (DSEP) models (Dotter et al. 2008); Fulton & Petigura (2018), computed stellar radii using Gaia DR2 inverted parallaxes, and Martinez et al. (2019) used their stellar parameters, combined with the Gaia DR2 distances from Bailer-Jones et al. (2018). The large Gaia–Kepler stellar properties catalog by Berger et al. (2020b) combined isochrones, Gaia DR2 parallaxes, and spectroscopic metallicities using the `isoclassify` (Huber et al. 2017) package, while Hardegree-Ullman et al. (2020) used stellar parameters from LAMOST and derived K2 stellar radii from the Stefan–Boltzmann law and stellar masses from stellar radii. Via asteroseismology, Huber et al. (2016) also derived the stellar masses and radii of K2 stars using $T_{\rm eff}$ and [Fe/H] from APOGEE DR14, while Mayo et al. (2018) used the `isochrone` package (Morton 2015), which requires the effective temperature, surface gravity, and metallicity as input parameters (these parameters were derived using the spectral synthesis method described by Mayo et al. 2018).

Comparisons of our derived radii (Section 3.3) with those in the six studies mentioned above are shown in the left and right panels of Figure 9, respectively for K2 and Kepler 1 targets. Please note the different scales for the $x$- and $y$- axes in the different panels. First, when considering the median radius differences "Other works–This work," overall, there is not a clear bias in any direction. Overall, all results from the literature present similar levels of consistency relative to ours. We note, however, the presence of the four significant outliers of Huber et al. (2016) for which their radii are much larger than ours (the log $g$ values for these cases are also very discrepant as discussed in Section 4.1.1 and shown in Figure 7), which when removed improve the consistency relative to our results ($0.029 \pm 0.082\ R_{\odot}$).

For example, for the most discrepant case (K2-128), the stellar radius of Huber et al. (2016) would be roughly 15 times larger than ours, which would imply a correspondingly larger planet radius. For the comparisons with Berger et al. (2020b), Mayo et al. (2018), and Martinez et al. (2019), the median differences are $\Delta R_{\rm star} < -0.01\ R_{\odot}$, noting again the presence of outliers. In the comparison with Mayo et al. (2018), in particular, the outliers are mostly for radii larger than $\sim 1.5\ R_{\odot}$, with a tendency that our radii are larger. For the comparisons with Hardegree-Ullman et al. (2020) and Johnson et al. (2017), the systematics go in the opposite direction, with median $\Delta R_{\rm star} \sim 0.03\ R_{\odot}$. In all comparisons, the MADs are less than $0.05\ R_{\odot}$, except for Johnson et al. (2017) that is slightly larger ($0.07\ R_{\odot}$), while Huber et al. (2016) has a much larger MAD of $0.08\ R_{\odot}$.

Moving on to discuss the stellar masses derived in this study, comparisons with other results are shown in Figure 10. The mass scale from Mayo et al. (2018) has a median difference (and MAD) that are very small when compared to ours, indicating overall good agreement. We note, however, that for stars more massive than $M_{\rm star} \sim 1.1\ M_{\odot}$, there is significantly more scatter, while for stars with $M < 1.1\ M_{\odot}$ we find a median mass difference of $0.026 \pm 0.020\ M_{\odot}$. The mass comparisons for the Kepler 1 stars (Johnson et al. 2017; Berger et al. 2020a; right panels of Figure 10), indicate even smaller offsets, where, the median mass differences are less than 3% and the MADs are $\Delta M_{\rm star} \sim 0.03\ M_{\odot}$, although there are also outliers in these comparisons. The median difference for stars with less than 1 $M_{\odot}$ are $-0.009 \pm 0.025\ M_{\odot}$ and $0.003 \pm 0.021\ M_{\odot}$ for Johnson et al. (2017) and Berger et al. (2020a), respectively. The mass scale of Hardegree-Ullman et al. (2020), on the other hand, has a larger systematic offset when compared to ours, being overall more massive than our scale by ∼8.2%; the latter comparison also shows some scatter with an rms value of 0.22 and a MAD of $0.111\ M_{\odot}$, which is the largest in Figure 10.

Asteroseismic masses are, in principle, the most accurate masses presented in Figure 10, having the smallest expected uncertainties (Pinsonneault et al. 2018). When compared to our results, there is a clear systematic difference between the mean mass of Huber et al. (2016) and ours, with our masses being smaller than the asteroseismic ones in the median by ∼3%. We note for example, the significant outlier that appears as much more massive ($M_{\rm star} = 1.2\ M_{\odot}$) when compared to our mass value ($M_{\rm star} \sim 0.7\ M_{\odot}$) and again refer to the discussion in Section 4.1.1. As in the comparison with Mayo et al. (2018), there is also more scatter for stars with masses larger than 1.1 $M_{\odot}$.

### 4.4. Planetary Radii

The radii of exoplanets orbiting Kepler 1 and K2 host stars have been derived in several studies in the literature and these are compared with our results in the different panels of Figure 11. Here, the planetary radii were computed using Equation (1), which combines our derived stellar radii with transit depth values available in the literature (Section 3.3), and these are presented in Table 6, which contains the star identifications, the planet names, transit depths, and planetary radii along with the error in $R_{\rm pl}$.

For K2, we compare planetary radii with those of Petigura et al. (2018a), Hardegree-Ullman et al. (2020), Kruse et al. (2019), Mayo et al. (2018), Vanderburg et al. (2016), and Crossfield et al. (2016). Overall, the results in Figure 11 indicate that our planetary radii for K2 hosts are, on the median, larger than in the other K2 works, except for Crossfield et al. (2016); however, the median differences in the planetary radii ("Other Work–This Work") are small, with median systematic differences (("Other Work–This Work")/"This Work") of 0.2% for Crossfield et al. (2016), ∼2% for Kruse et al. (2019), ∼3% for Hardegree-Ullman et al. (2020) and Vanderburg et al. (2016), and ∼4% for Mayo et al. (2018). Although the median differences are, in some cases insignificant (at the level of 0%–2%), or small (at the level of 3%–4%), there are some outliers with larger

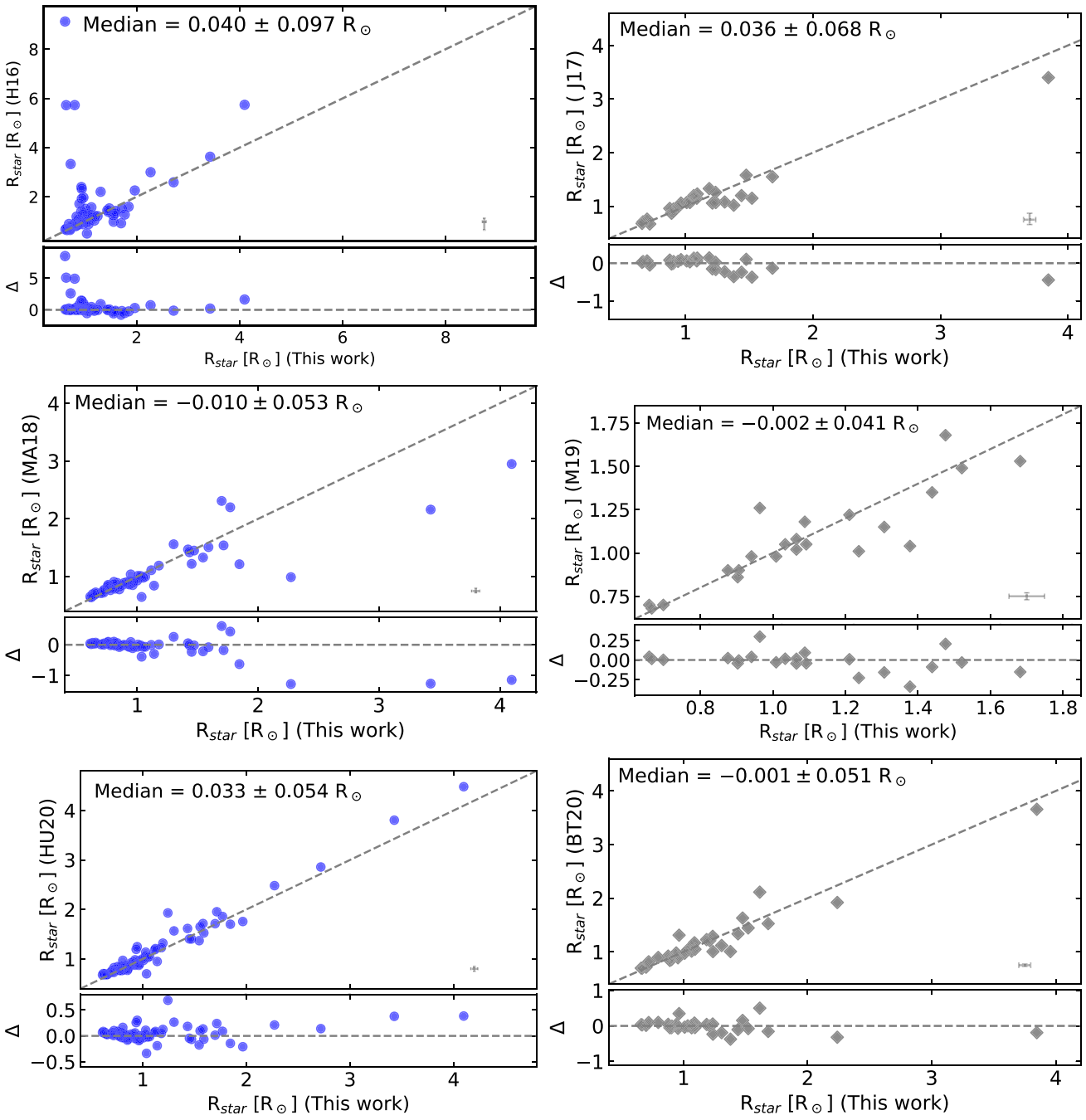


**Figure 9.** Comparisons of the stellar radii derived in this work with stellar radii from Huber et al. (2016; H16), Mayo et al. (2018; MA18) and Hardegree-Ullman et al. (2020; HU20) for K2 stars (left panels), and Johnson et al. (2017; J17), Martinez et al. (2019; M19) and Berger et al. (2020a; BT20) for Kepler 1 stars (right panels). The four most discrepant radii between this study and Huber et al. (2016) are discussed in the text. Each bottom subpanel shows the difference, $\Delta$ = "Other Work–This Work."

discrepancies in some regimes, as is the case of the comparison with Vanderburg et al. (2016) that reveals larger offsets, in particular for planets with radii larger than $\sim$2.5 $R_\oplus$. The comparison with Petigura et al. (2018a) finds larger median differences with our derived planetary radii of $\sim$6% larger.

In this comparison (top left panel), there is one significant outlier in the small planet regime, planet K2-183d, for which we find $R_{\rm pl} = 3.1$ $R_\oplus$, while Petigura et al. (2018a) find $R_{\rm pl} = 17.4$ $R_\oplus$. Our result is better agreement with the planet radius reported by Livingston et al. (2018) ($R_{\rm pl} = 2.9 R_\oplus$) and Mayo et al. (2018) ($R_{\rm pl} = 2.5$ $R_\oplus$), as well as by Hardegree-Ullman et al. (2020) ($R_{\rm pl} = 5.1$ $R_\oplus$) and Kruse et al. 2019) ($R_{\rm pl} = 5.2$ $R_\oplus$). We also note that the difference in the effective temperature between Petigura et al. (2018a) and our result is $\Delta T_{\rm eff} = -81$ K and that if we used Petigura et al. (2018a) $R_{\rm pl}/R_{\rm star}$ value we would obtain $R_{\rm pl} = 17.56$ $R_\oplus$, which is in much closer agreement with Petigura et al. (2018a), indicating that the difference in transit depth is responsible for a large part of the difference in $R_{\rm pl}$.

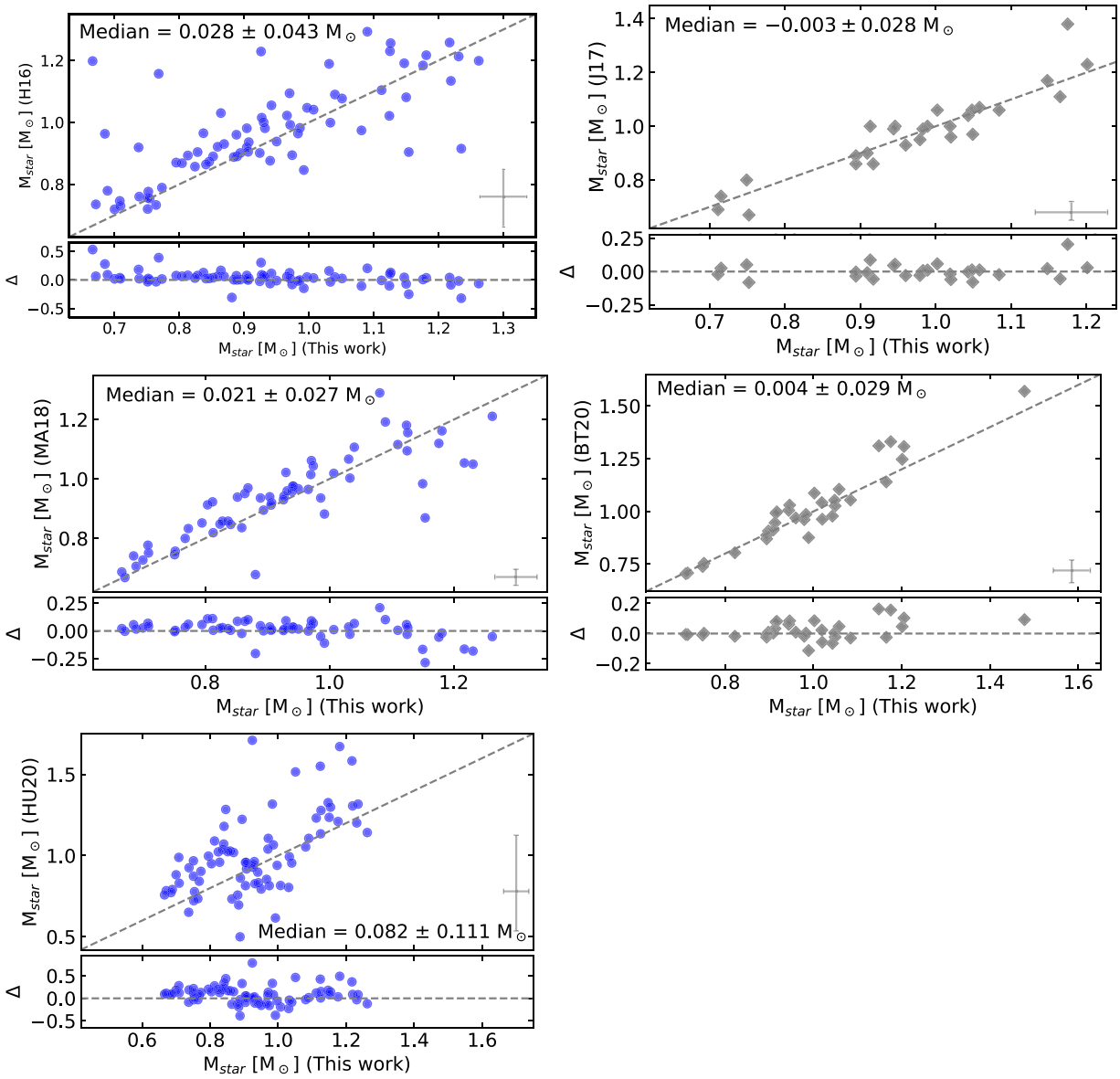


**Figure 10.** Comparisons between the derived stellar masses in this study with those from Huber et al. (2016; H16), Mayo et al. (2018; MA18) and Hardegree-Ullman et al. (2020; HU20) for K2 stars (left panels), and Johnson et al. (2017; J17) and Berger et al. (2020a; BT20) for Kepler 1 stars (right panels). The bottom subpanels show the differences, Δ, between "Other Work–This Work."

For the Kepler 1 planets studied here, the radii of Petigura et al. (2022) and Fulton & Petigura (2018) show the largest offsets relative to our results, with a median systematic difference of 8%–9%, again with our planetary radius scale being larger. For Martinez et al. (2019), there is a much smaller systematic shift in the planetary radii relative to ours of ∼1%, and also having the smallest MAD of all comparisons, indicating that the scales for planetary radii are very consistent in both studies.

One aspect to keep in mind is the fact that the various studies discussed here may have employed different transit depths. Some studies, such as ours, use literature values, while others derive their own. For planets in common, we should note that we used the transit depths from Kruse et al. (2019) and these were also used by Hardegree-Ullman et al. (2020), while Vanderburg et al. (2016), Crossfield et al. (2016), Mayo et al. (2018), and Petigura et al. (2018a) derived their own transit depths. For the Kepler 1 planets, we used the transit depths from Thompson et al. (2018), which are also used by Martinez et al. (2019) and Petigura et al. (2022), while the transit depths of Fulton & Petigura (2018) come from Mullally et al. (2015).

## 5. Discussion

The stellar parameters obtained for the 115 stars analyzed in this study, along with those for the solar proxies Astraea and Parthenope, are summarized in Figure 12 as a Kiel diagram, with log $g$ plotted as a function of $T_{\rm eff}$ and the stars shown as filled circles color-coded by their iron abundance; the color bar represents the metallicities. Results for the solar proxies are shown as black stars. The dashed lines are the Yonsei–Yale isochrones (Yi et al. 2001, 2003;

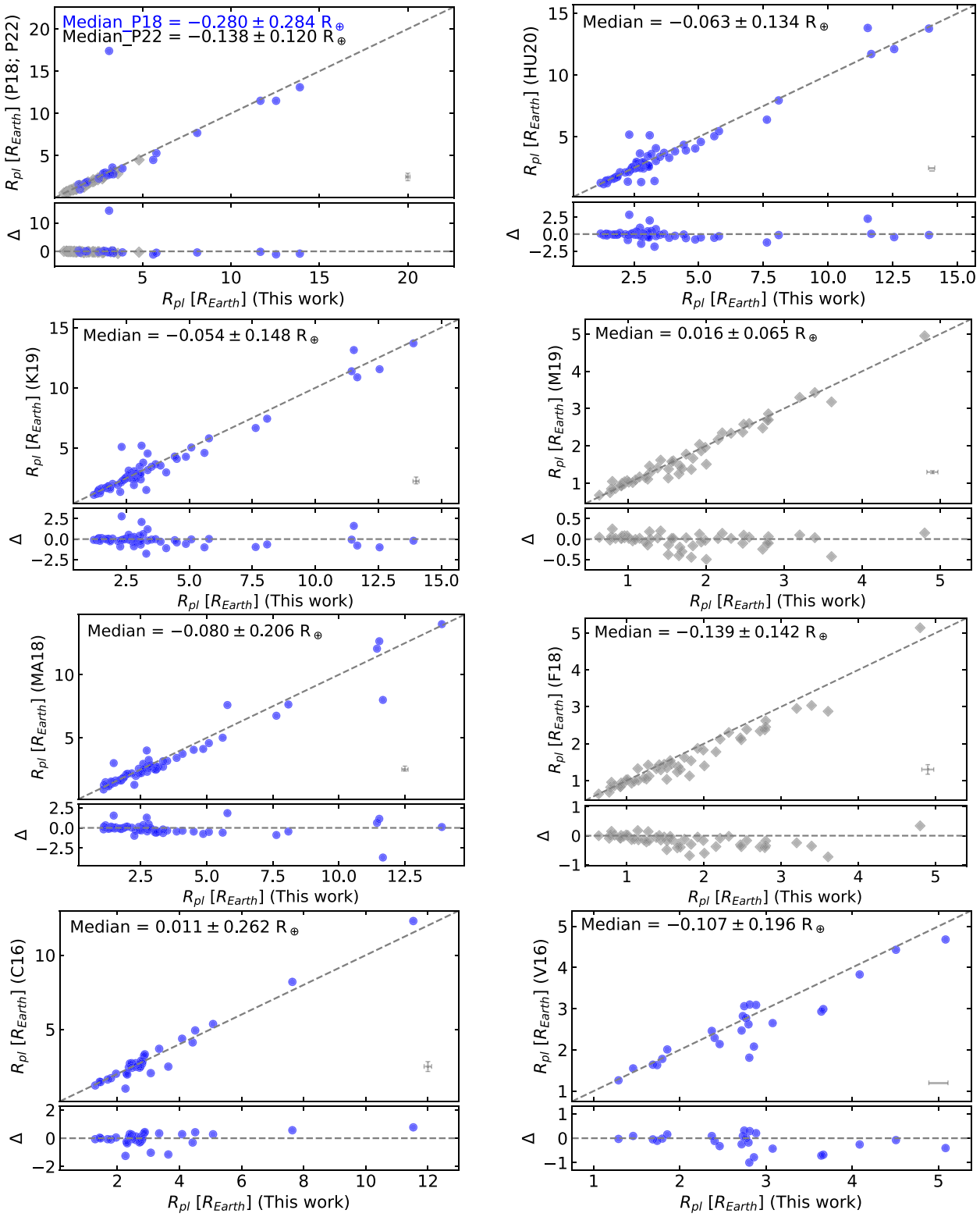


**Figure 11.** Comparison of the derived planetary radii with the literature values. Blue circles represent the planets of K2 host stars and gray diamonds of Kepler 1 host stars; beginning in the top left panel and preceeding clockwise, the comparisons are with Petigura et al. (2018a, 2022; P18 and P22, respectively), Hardegree-Ullman et al. (2020; HU20), Kruse et al. (2019; K19), Martinez et al. (2019; M19), Mayo et al. (2018; MA18), Fulton & Petigura (2018; F18), Crossfield et al. (2016; C16), and Vanderburg et al. (2016; V16). The bottom subpanels present the differences, Δ, of "Other Work–This Work."

Demarque et al. 2004; Han et al. 2009) corresponding to an age of 4.6 Gyr and metallicities between −0.6 and 0.2 dex, with steps of 0.2 dex. As can be seen from the locations of the points in this diagram, most of the stars in our sample are on, or near, the main sequence, but there are also a small number of stars that are clearly evolved.

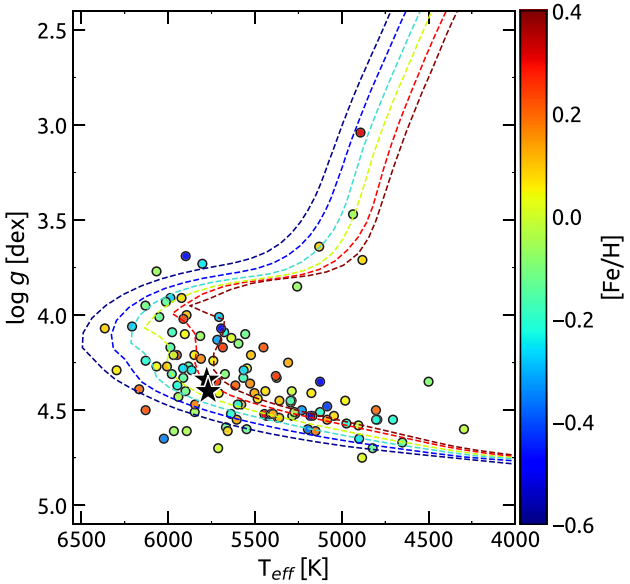


**Figure 12.** Kiel diagram for the sample stars. Dashed lines represent 4.6 Gyr old stellar evolution tracks from Yonsei–Yale isochrones for different metallicities: −0.6, −0.4, −0.2, 0.0, 0.2, and 0.4 dex. The colors of circles represent different metallicities as shown by the color bar.

**Table 6**
Planetary Radii

| Star ID | Planet Name | $\Delta F$ (ppm) | $R_{\rm pl}$ ($R_\oplus$) | $\delta R_{\rm pl}$ ($R_\oplus$) |
|---|---|---|---|---|
| EPIC201577035 | K2-10 b | 1691.0 | 4.09 | 0.14 |
| EPIC211990866 | K2-100 b | 122.5 | 1.36 | 0.04 |
| EPIC211913977 | K2-101 b | 749.0 | 2.17 | 0.08 |
| EPIC211970147 | K2-102 b | 200.0 | 1.09 | 0.09 |
| EPIC211525389 | K2-105 b | 1338.0 | 3.86 | 0.14 |
| EPIC220674823 | EPIC220674823 b | 284.7 | 1.78 | 0.06 |
| EPIC220674823 | EPIC220674823 c | 903.0 | 3.17 | 0.10 |
| EPIC211736671 | K2-108 b | 973.0 | 5.78 | 0.45 |
| EPIC201596316 | K2-11 b | 916.0 | 2.72 | 0.11 |
| … | … | … | … | |

**Note.** Transit depths ($\Delta F$) are collected from Kruse et al. (2019) and where available for K2 planets, while for Kepler 1 planets they are from Thompson et al. (2018). This table is published in its entirety in the machine-readable format. A portion is shown here for guidance regarding its form and content.

(This table is available in its entirety in machine-readable form.)

Focusing initially on our results for the K2 sample, Figure 13 uses histograms to illustrate the distributions of effective temperature and surface gravity in the top left and right panels, respectively. Our target selection was biased, as it avoided M dwarfs, and most of the K2 stars in this sample have effective temperatures between ∼4800—6000 K, with a peak at roughly $T_{\rm eff} \sim 5500$ K (median = 5503 K; MAD = 346 K). The log $g$ distribution of the K2 stars in this study is dominated by stars having values between log $g \sim 4.2$ and 4.6, with a median log $g = 4.41$ (MAD = 0.14; 16th percentile = −0.36; 84th percentile = 0.14).

The bottom panels of Figure 13 show the distributions of the derived stellar masses (left bottom panel) and radii (right bottom panel) for the K2 targets. The median of the mass distribution of the K2 sample studied here is just below the solar value of $M_{\rm star} = 0.93 \pm 0.11\ M_\odot$, with all K2 stars having masses between $M_{\rm star} = 0.6$–$1.3\ M_\odot$. This is a narrower mass range than that found for the 2956 Kepler hosts by Berger et al. (2020a), which covers $M_{\rm star} = 0.5$–$1.7\ M_\odot$, noting however that their median stellar mass ($M_{\rm star} = 0.99 \pm 0.2\ M_\odot$) is just slightly larger than our K2 sample. The K2 C5 sample of Zink et al. (2020) has a similar median mass of $M_{\rm star} = 0.92^{+0.34}_{-0.18}\ M_\odot$, but which extends over a much larger range in mass, from ∼0.1 to 2.5 $M_\odot$.

The stellar radii distribution of the studied K2 sample (shown in the right bottom panel of Figure 13), has a median radius of $R_{\rm star} = 0.94\ R_\odot$ (16th percentile = −0.22; 84th percentile = 0.59), with very few stars in our sample having radii larger than $R_{\rm star} > 2\ R_\odot$. An investigation of the mass–radius relation indicates that the four stars in our K2 sample having radii $R_{\rm star} > 2\ R_\odot$ and log $g$ values smaller than 3.8 all have masses larger than 1.1 $M_\odot$, indicating that they have evolved away from the main sequence over realisitic timescales (∼7 − 8 Gyr for 1.1 $M_\odot$).

In Figure 14 we show the metallicity distributions on the left panel, along with the cumulative distribution functions on the right panel for the K2 sample (shown in blue) and the CKS sample analyzed by Ghezzi et al. (2021) (shown in red). The metallicity distribution of our K2 sample covers the range between [Fe/H] = −0.5 to 0.3 (iron abundances roughly between $7.00 < A(\rm Fe) < 7.80$), with ∼12% of stars being more metal-poor than [Fe/H] = −0.2. The median (±MAD) metallicity of the distribution is [Fe/H] = −0.03 ± 0.14 dex ($A$(Fe) = 7.49 ± 0.14 dex) and this value is very close to the metallicity obtained here for the solar-proxy asteroids ($A$(Fe) >= 7.52), and also in good agreement with the solar Fe abundance of Magg et al. (2022) (see Section 3.2). Overall the range in metallicity of our K2 sample overlaps roughly with that of the Galactic thin disk, although the K2 sample is slightly more metal-poor. The comparison with the metallicity distribution of the CKS sample of Ghezzi et al. (2021) also indicates that our K2 sample is more metal-poor, which is in line with the finding of Ghezzi et al. (2021) that the CKS metallicity distribution was akin to the metallicity distribution function (MDF) of the solar neighborhood based on stellar samples with Galactocentric distances between 7 kpc < Rg < 9 kpc from the APOGEE and GALAH surveys (Hayden et al. 2015, 2020); the metallicity distribution of APOGEE red giants is also shown as the black curve in Figure 14 for comparison. We can see that the distribution of both the K2 sample and the Ghezzi et al. (2021) CKS sample have a peak at [Fe/H] = 0.1 dex that is not well matched by the metallicity distribution of red giants in APOGEE. Compared to APOGEE, the K2 sample is relatively more metal-poor, not extending to [Fe/H] = 0.4, having fewer stars in the metal-rich end, and a more significant number of stars in the [Fe/H] = −0.2 bin than the APOGEE distribution. The median metallicity of the CKS sample is [Fe/H] = 0.06 ± 0.14 (Ghezzi et al. 2021), or, [Fe/H] = 0.04 ± 0.11 (Petigura et al. 2017); the K2 sample studied here is more metal-poor by −0.09 dex in the median, but we note that it is not as metal-poor as the K2 Campaign 5 sample analyzed by Zink et al. (2020), which has an approximately Gaussian distribution with a median [Fe/H] = −0.14 ± 0.18.

### 5.1. Planetary Radii and the Radius Gap

The final distribution of planetary radii derived from the Hydra spectra of K2 host stars contains 85 confirmed planets

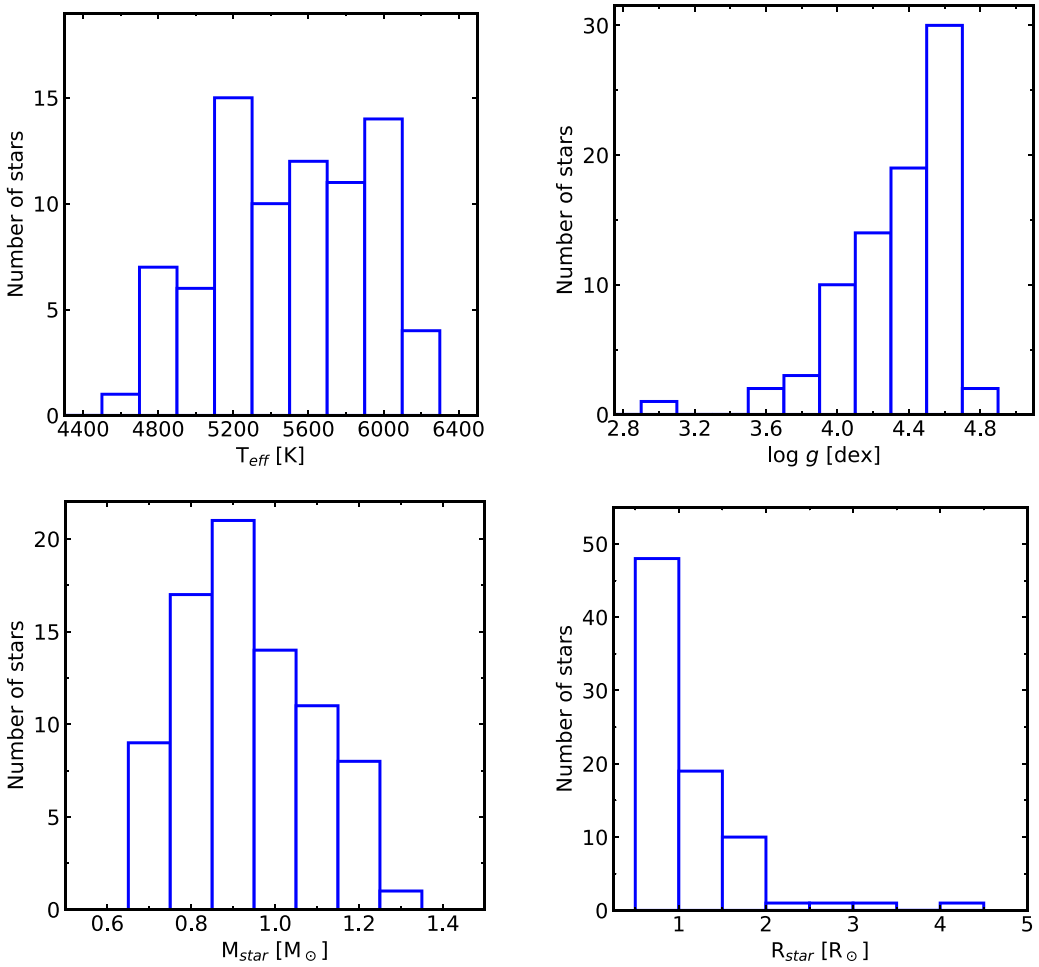


**Figure 13.** Effective temperature, surface gravity, mass, and radius distributions for the K2 stellar sample.

orbiting 69 stars. Although this sample is relatively small, the results presented here are derived using an independent methodology that relies on an analysis of a carefully selected set of Fe I and Fe II lines, which are used to determine fundamental host-star parameters ($T_{\rm eff}$, log $g$, and [Fe/H]), and thus represent a useful addition to the growing number of independently derived K2 planetary radii. Figure 15 (top panel) presents a histogram of K2 planetary radii that result from the derived stellar radii combined with available transit depth catalogs. The 85 planets plotted in Figure 15 reveal a distinct and well-defined radius valley that spans $R_{\rm pl} \sim 1.6{-}2.2\ R_{\oplus}$, with a minimun near 1.9 $R_{\oplus}$. Figure 15 includes all planetary orbital periods which, for this sample, range from P $\sim$ 0.5 days up to 53 days and it should be noted that, due to the differing observing techniques between Kepler 1 and K2, the sample studied here is biased toward shorter orbital periods when compared to Kepler 1 periods, e.g., the CKS sample. Nevertheless, the K2 radius valley observed in this sample, with a minimum at $R_{\rm pl} \sim 1.9\ R_{\oplus}$, is very similar to the results derived from the CKS sample from several studies (e.g., Fulton et al. 2017; Berger et al. 2018; Fulton & Petigura 2018; Van Eylen et al. 2018; Martinez et al. 2019).

The bottom panel of Figure 15 provides a comparison of radii derived for the CKS sample (all Kepler 1 planets) from Martinez et al. (2019; their Figure 11(d)). Comparing the top and bottom panels of Figure 15 illustrates the similarity in the location of the radius valley between the K2 and Kepler 1 samples. Although the Kepler 1 field focused on a single pointing, encompassing a limited Galactic longitude and latitude (l $\sim$70°–8°, b $\sim$10°–20°), the K2 fields were constrained by the ecliptic plane and thus ranged over a broader range of Galactic longitudes and latitudes. The similarity in the position of the radius valley suggests it to be a ubiquitous phenomenon among short-period planets across a broad range of Galactocentric distances in the thin and thick disk populations; Zink et al. (2021) arrived at this conclusion after their analysis of planetary radii in the K2 Campaign fields 1−8 and 10−18.

With the similarity in the position of the radius valley between the K2 and Kepler 1 samples (Mayo et al. 2018; Hardegree-Ullman et al. 2020; Zink et al. 2021), we next investigate planet radius as a function of orbital period, with Figure 16 plotting our planet sample in a period–radius plane. The top panel includes all planets (our full sample) in the different orbital periods, with the K2 planets plotted as black filled circles and the Kepler 1 planets plotted as open diamonds; blue symbols represent the median and MADs of the planetary radii and orbital period distributions for each planet size domain: super-Earths ($R_{\rm pl} \leqslant 2\ R_{\oplus}$; square), sub-Neptunes ($2\ R_{\oplus} < R_{\rm pl} \leqslant 4.4\ R_{\oplus}$; circle), sub-Saturns ($4.4\ R_{\oplus} < R_{\rm pl} \leqslant 8\ R_{\oplus}$; triangle), and Jupiters ($8\ R_{\oplus} < R_{\rm pl} \leqslant 20\ R_{\oplus}$; star). These median values are overall similar to those for the

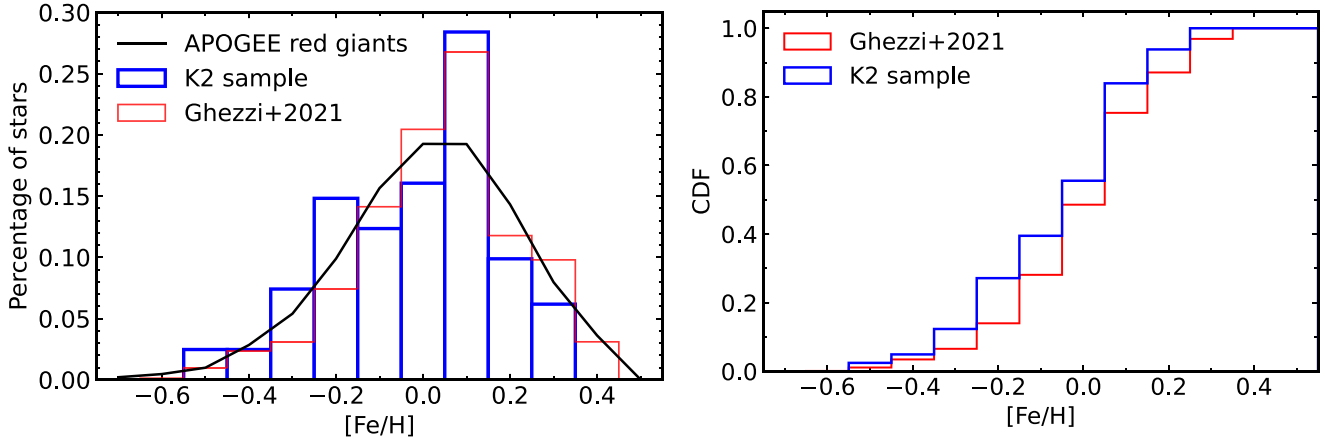


**Figure 14.** Iron abundance distributions (left panel) and cumulative distribution functions (right panel) for different samples of stars. The left panel presents the K2 sample studied here, shown as the blue histogram, and the CKS sample of Ghezzi et al. (2021) is shown in red, while the [Fe/H] distribution for the red giant stars in the local Milky Way disk from the APOGEE survey is shown as the black curve. The cumulative distribution functions for the K2 sample here and the CKS sample of Ghezzi et al. (2021) are compared in the right panel. Both panels show that the K2 sample studied here is slightly more metal-poor than both the CKS sample and the local disk.

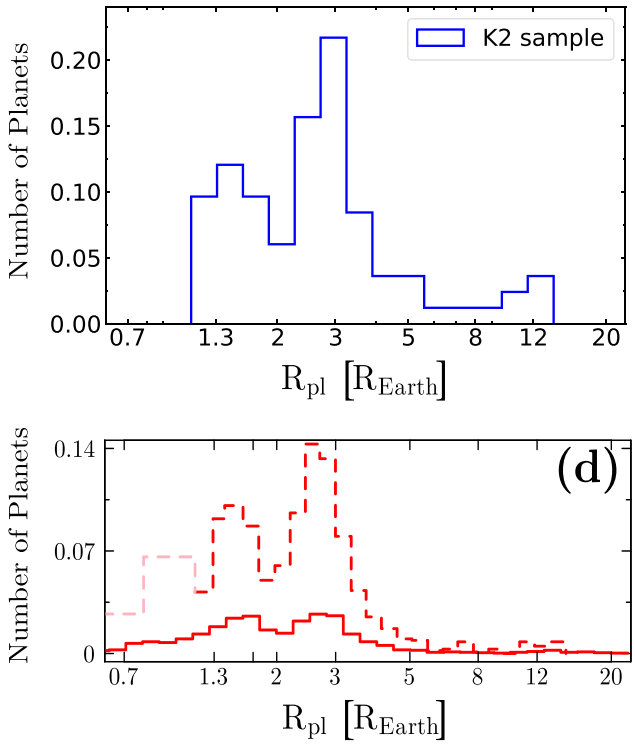


**Figure 15.** The top panel shows the planetary radius distribution for the K2 planet sample studied here, while the bottom panel shows the distribution of the CKS planet sample studied by Martinez et al. (2019), as shown in their Figure 11 panel (d). The red filled line histogram represents their sample and the red dashed line distribution takes into account completeness corrections. The location of the gap in the K2 (top panel) and CKS (bottom panel) radius distributions is approximately the same: $R_{gap} \sim 2\ R_{\oplus}$.

CKS sample of Martinez et al. (2019), but here we adopt the limit of 4.4 $R_{\oplus}$ for the transition between sub-Neptunes and sub-Saturns, as discussed by Ghezzi et al. (2021).

Planetary radii $<4\ R_{\oplus}$ are shown in the bottom panels, where the bottom left panel plots only the sample of K2 planets, while in the bottom right panel includes all K2 planets and those Kepler 1 planets having orbital periods less than 100 days. In both plots the slope of the radius valley is shown as a blue line (we used the slope of −0.11 from Martinez et al. 2019). Although we do not fit a trend of the position of the radius gap, $R_{gap}$, as a function of orbital period ($P$) to the 139 planets in our sample, the planetary radii that result from the stellar parameters derived here are consistent with the relation of the radius valley following a power law of the form $R_{gap} \propto P^{-0.11}$, as shown in the bottom panels of Figure 16.

### 5.2. Planetary Radius, Orbital Period, and Stellar Metallicity

The distribution of host-star metallicity as a function of planetary radius is shown in the left panel of Figure 17. The 85 K2 planets in this study are the solid black circles and the Kepler 1 planets are the gray open diamonds. The blue symbols represent the median (±MAD) metallicities of the K2 planet hosts dividing the sample in the same planet size domains as in Figure 16: super-Earths, sub-Neptunes, sub-Saturns, and Jupiters. Although the K2 planet sample size is small, we find that, in general, the metallicities of the K2 planet hosts increase with planetary radius, but the increase in metallicity is seen in particular for the transition between the small (super-Earth and sub-Neptune) and large (sub-Neptune and sub-Saturn) planet regimes, a result that is similar to what has been found in previous studies of Kepler planets in the literature (Petigura et al. 2018b; Narang et al. 2018; Ghezzi et al. 2021; see also Beauge & Nesvorny 2013).

As mentioned in the introduction, previous works have investigated correlations between host-star metallicity and planet orbital period distributions, concluding that small and hot planets with orbital periods $P \lesssim 8$–10 days appear preferentially around metal-rich stars (e.g., Mulders et al. 2016; Wilson et al. 2018). The right panel of Figure 17 shows the host-star metallicity as a function of the planet orbital period for our studied sample (symbols are the same as in the left panel). The horizontal dashed lines represent the mean metallicities for those K2 planets having orbital periods below and above 10 days, and the 10 day boundary is marked as a dashed vertical line. We find that the median host-star metallicity for planets with $P < 10$ days is slightly metal-rich, $0.059 \pm 0.122$ dex, while the median host-star metallicity for planets with $P > 10$ days is slightly metal-poor, $-0.060 \pm 0.106$ dex. Our K2 sample has mostly small planets and only some large planets. If we restrict the sample to that having only planets with $R_{pl} < 4.4\ R_{\oplus}$, we obtain a similar behavior, with a median

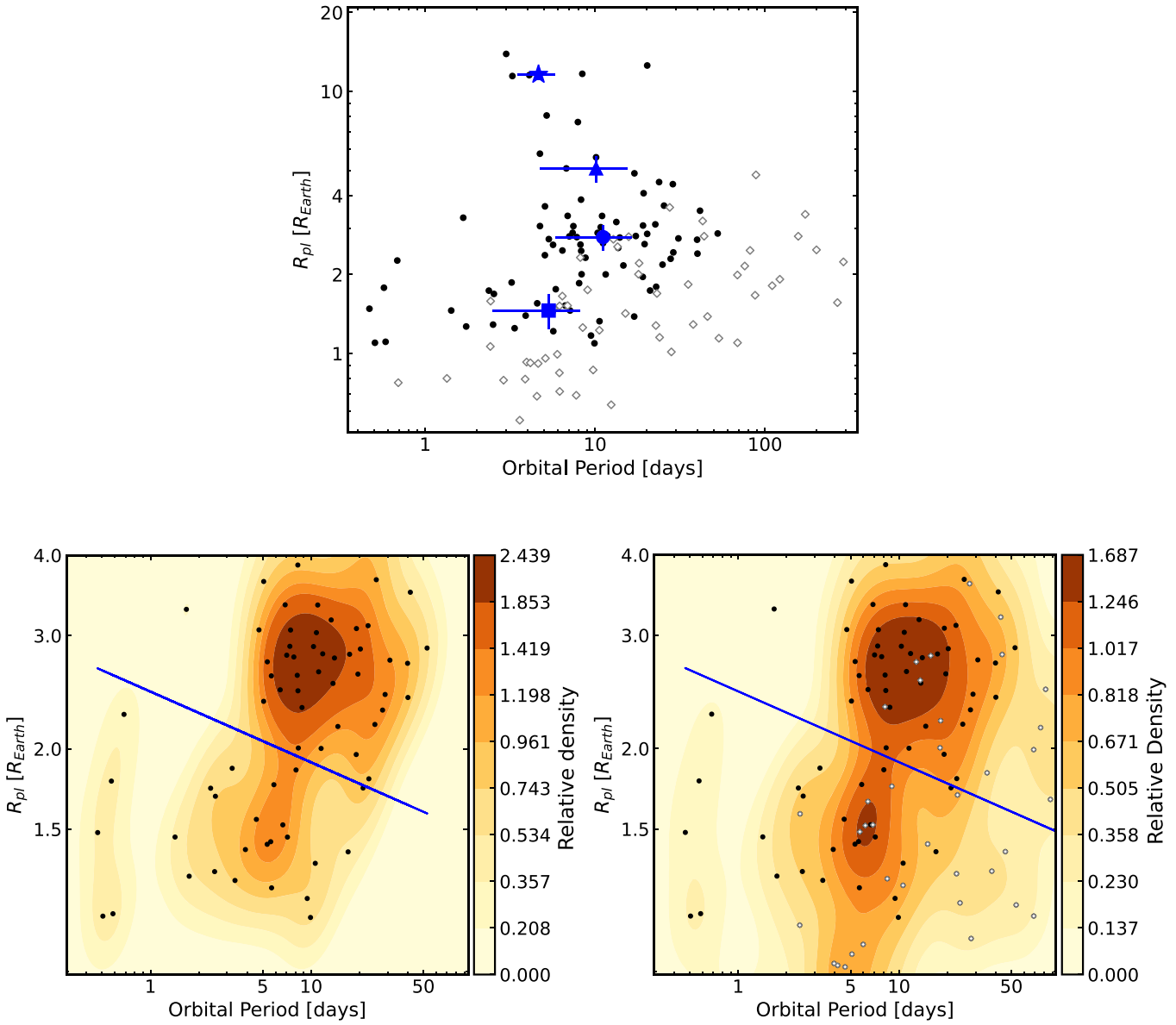


**Figure 16.** Planetary radius as a function of planetary orbital period. The top panel shows our sample of K2 planets (filled black circles) and Kepler 1 planets (open diamonds). The blue symbols are the median values of $R_{pl}$ vs. orbital period for the Jupiters ($8\ R_\oplus < R_{pl} \leqslant 20\ R_\oplus$), sub-Saturns ($4.4\ R_\oplus < R_{pl} \leqslant 8\ R_\oplus$), sub-Neptunes ($2\ R_\oplus < R_{pl} \leqslant 4.4\ R_\oplus$), and super-Earths ($R_{pl} \leqslant 2\ R_\oplus$). The bottom left panel shows the K2 planets in our sample with $<4\ R_\oplus$ and in the bottom right panel we show the same but with the addition of the Kepler 1 planets in our sample. The slope of the radius valley vs. orbital period derived by Martinez et al. (2019) for the CKS sample is also shown for comparison purposes only. The color bar shows the relative density of detected planets in the $P$–$R_{pl}$ plane using a Gaussian kernel density estimation (KDE).

metallicity of $0.051 \pm 0.124$ for $P < 10$ days and $-0.051 \pm 0.090$ for planets with $P > 10$ days. We note that adopting a boundary at $R_{pl} = 8.3\ R_\oplus$, as found by Wilson et al. (2018), gives similar metallicity differences between the two orbital period regimes. Summarizing the results obtained here for the K2 host-star metallicities and orbital planetary periods are in line with what was found previously for Kepler 1 systems.

## 6. Summary and Conclusions

We present effective temperatures, surface gravities, metallicities, and microturbulent velocities for 81 planet-hosting K2 stars based on a homogeneous spectroscopic analysis using a uniform set of high-resolution spectra from the WIYN/Hydra spectrograph covering a spectral window between 6050 and 6350 Å. Additionally, stellar parameters are presented for 33 planet-hosting Kepler 1 stars.

The calculations were done in LTE and we used Kurucz model atmospheres. The stellar parameters and metallicities were derived from measurements of the EWs of Fe I and Fe II lines and from requiring excitation and ionization balance, in addition to requiring the independence of the Fe line abundances with the EWs. Such a methodology has the advantage of directly estimating the microturbulent velocity, which is a needed parameter for an abundance analysis, and being independent of fitting for the projected rotation velocity ($v \sin i$), macroturbulent velocity and the instrumental profile.

The limited wavelength coverage of the Hydra spectra combined with a resolving power ($R = \lambda/\Delta\lambda = 18{,}500$) that is

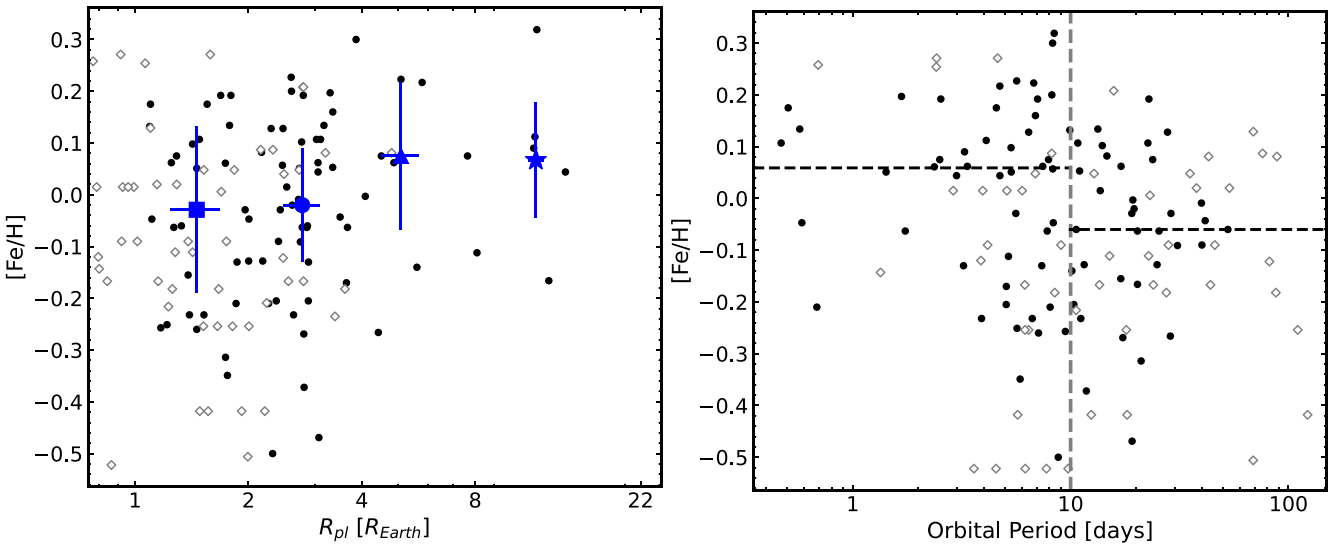


**Figure 17.** Host-star metallicities as a function of the planetary radius (left panel) and orbital period (right panel). K2 planets are shown as black filled circles and Kepler 1 planets as open diamonds. Left panel: the blue symbols are the median host-star metallicities for super-Earths (square), sub-Neptunes (circle), sub-Saturns (triangle), and Jupiters (star). Right panel: the horizontal dashed lines are the median host-star metallicities for planets having orbital periods smaller and larger than 10 days.

lower than that typically found in single-object high-resolution spectrographs, demanded a systematic and careful selection of unblended Fe I and Fe II lines combined with a "boutique" analysis of a benchmark solar twin to assess the reliability of the individual line results. The methodology and line list were then validated via the analysis of two solar-proxy spectra (obtained with the Hydra spectrograph) of the asteroids Astraea and Parthenope, which resulted in effective temperatures, surface gravity values, and metallicities that are similar to cannonical values in the literature for the Sun (Asplund et al. 2021; Magg et al. 2022).

Once the line list was vetted, the spectral analysis was done semiautomatically using the code $q^2$ (Ramirez et al. 2014) that interpolates atmospheric models, computes iron abundances, and their corresponding errors. Additional stellar properties, such as stellar masses and radii, were also computed using the $q^2$ package, where the input parameters were the derived effective temperatures and metallicities, along with $V$ magnitudes, parallaxes from Gaia EDR3, and their corresponding uncertainties and isochrones from Yonsei–Yale (Demarque et al. 2004; Han et al. 2009)

The analyzed K2 stellar sample has distributions of effective temperature, surface gravity, and metallicity that fall mostly between $T_{\rm eff} \sim 4800$–$6200$ K, log $g$ ~3.7–4.6, and [Fe/H] ~$-0.5$ – 0.3 dex, respectively. These stars all have distances (Bailer-Jones et al. 2021) within ~900 pc of the Sun, with most of them having stellar radii between 1 and 2 $R_{\odot}$, and only a few stars having radii between 2 and 4 $R_{\odot}$; their masses vary mostly between $\sim M_{\rm star} = 0.7$–$1.2$ $M_{\odot}$.

Stellar radii and transit depth values are needed to constrain planetary radii, which is a crucial parameter necessary to unveil planetary composition. Most of the transit depth values for K2 planets here were from Kruse et al. (2019), and the internal precision achieved in the derived planetary radii in this work is 4.44%.

The results derived here for $T_{\rm eff}$, log $g$, $A$(Fe), $R_{\rm star}$, $M_{\rm star}$, and $R_{\rm pl}$ were compared to, and found to be in general agreement with, results obtained in several literature studies that were based on high-resolution spectra and asteroseismology for Kepler 1 stars, as well as results obtained through photometry, spectrum synthesis, and asteroseismology for K2 stars. More specifically, comparisons between our results and those in spectroscopic studies and surveys for both $T_{\rm eff}$ and log $g$, find agreement within ~100 K and <0.1 dex, respectively. A closer inspection reveals consistent offsets in the sense that the effective temperatures derived here are hotter and the surface gravities slightly lower, with median differences taken over all studies ("Other Work–This Work") of $\langle \Delta T_{\rm eff} \rangle = -37 \pm 38$ K and $\langle \Delta \log g \rangle = 0.05 \pm 0.04$ dex.

The possible impact that magnetic stellar activity might have on the derived stellar parameters was investigated by removing Fe I lines that were found to be the most sensitive to Zeeman broadening/enhancement. A subset of 15 stars that were deemed likely to be active were reanalyzed using these less magnetically sensitive Fe I lines. No significant differences, beyond the expected uncertainties, were found between the results from an analysis that included magnetically sensitive lines when compared to the analysis which excluded such lines. Based on this exercise, we do not find evidence that the stellar parameters presented here have been biased significantly by underlying stellar activity.

The relations between planet radius and orbital period and metallicity in our small K2 planet sample confirm previous results in the literature for Kepler 1 planets (Mulders et al. 2016; Petigura et al. 2018b; Narang et al. 2018; Wilson et al. 2018; Ghezzi et al. 2021). Overall, the metallicity of K2 planet hosts increases with planetary radius; this increase in metallicity is seen in particular for the transition between the small (<4.4 $R_{\oplus}$) and large (>4.4 $R_{\oplus}$) planet regimes. The median K2 host-star metallicity for planets with orbital periods < 10 days is slightly metal-rich, while the median host-star metallicity for planets with $P$ > 10 days is slightly metal-poor. When we restrict the sample to that having only planets with $R_{\rm pl} < 4.4$ $R_{\oplus}$, we obtain a similar behavior.

Previous studies deriving precise values for planetary radii (Fulton et al. 2017; Petigura et al. 2017; Van Eylen et al. 2018; Martinez et al. 2019) have uncovered signatures, such as the radius gap, and the slope in the radius gap with orbital period,

which would not be apparent when uncertainties in stellar parameters are higher. The distribution of K2 planetary radii resulting from the stellar parameters derived here reveals a well-defined radius gap, with a minimum at $R_{\rm pl} \sim 1.9\ R_{\oplus}$. This gap falls at the same radius value as found for planets orbiting stars found by Kepler 1; the similarity between differing samples of exoplanet-hosting stars inhabiting larger swathes of volume across the galaxy points to the radius gap as a common feature of short-period ($P < 100$ days) exoplanetary systems. Such a conclusion concerning K2 planetary radii was also reached by Zink et al. (2020).

Although the number of K2 planetary radii derived here is relatively small, the radius gap as a function of orbital period defined by this sample is in agreement with the decreasing value of $R_{\rm pl}$ with increasing orbital period ($P$) found in previous studies of Kepler 1 planets (e.g., Van Eylen et al. 2018; Martinez et al. 2019), where the minimum of the radius gap follows a trend of $R_{\rm gap} \propto P^{-0.11}$.

This study adds to the list of K2 hosts with stellar parameters from high-resolution spectra, which is crucial for the field of exoplanet studies.

We thank the referee for detailed comments that helped improve the paper. We thank Ivan Ramirez for his support regarding the use and handling of the `qoyllur-quipu` code. V.L-T. acknowledges the financial support from Coordenação de Aperfeiçoamento de Pessoal de Nível Superior (CAPES). S. C.S was supported by David Delo Research Professor and Dana Foundation grants from the University of Tampa. This work is based on observations at Kitt Peak National Observatory at NSF's NOIRLab (NOIRLab Prop. ID 2019A-0334; PI: V. Smith), which is managed by the Association of Universities for Research in Astronomy (AURA) under a cooperative agreement with the National Science Foundation. The authors are honored to be permitted to conduct astronomical research on Iolkam Du'ag (Kitt Peak), a mountain with particular significance to the Tohono O'odham. Data presented were obtained at the WIYN Observatory, operated by NOIRLab, under the NN-EXPLORE partnership of the National Aeronautics and Space Administration and the National Science Foundation. This work was supported by a NASA WIYN PI Data Award, administered by the NASA Exoplanet Science Institute. This research has made use of the NASA Exoplanet Archive, which is operated by the California Institute of Technology, under contract with NASA under the Exoplanet Exploration Program. K.C. and V.S. acknowledge that their work here is supported, in part, by the National Science Foundation through NSF grant No. AST-2009507.

## ORCID iDs

V. Loaiza-Tacuri https://orcid.org/0000-0003-0506-8269
Katia Cunha https://orcid.org/0000-0001-6476-0576
Verne V. Smith https://orcid.org/0000-0002-0134-2024
Luan Ghezzi https://orcid.org/0000-0002-9089-0136
Simon C. Schuler https://orcid.org/0000-0001-7203-8014
Steve B. Howell https://orcid.org/0000-0002-2532-2853

## References

Adibekyan, V. 2019, Geosc, 9, 105
Adibekyan, V., Santos, N. C., Figueira, P., et al. 2015, A&A, 581, L2
Adibekyan, V. Z., Figueira, P., Santos, N. C., et al. 2013, A&A, 560, A51
Armstrong, D. J., Kirk, J., Lam, K. W. F., et al. 2015, A&A, 579, A19
Asplund, M., Amarsi, A. M., & Grevesse, N. 2021, A&A, 653, A141
Aguirre, V. S., Lund, M. N., Antia, H. M., et al. 2017, ApJ, 835, 173
Bailer-Jones, C. A. L., Rybizki, J., Fouesneau, M., Demleitner, M., & Andrae, R. 2021, AJ, 161, 147
Bailer-Jones, C. A. L., Rybizki, J., Fouesneau, M., Mantelet, G., & Andrae, R. 2018, AJ, 156, 58
Bard, A., & Kock, M. 1994, A&A, 282, 1014
Barros, S. C. C., Demangeon, O., & Deleuil, M. 2016, A&A, 594, A100
Batalha, N. M., Rowe, J. F., Bryson, S. T., et al. 2013, ApJS, 204, 24
Beauge, C., & Nesvorny, D. 2013, ApJ, 763, 12
Bensby, T., Feltzing, S., & Oey, M. S. 2014, A&A, 562, A71
Berger, T. A., Huber, D., Gaidos, E., & van Saders, J. L. 2018, ApJ, 866, 99
Berger, T. A., Huber, D., Gaidos, E., van Saders, J. L., & Weiss, L. M. 2020a, AJ, 160, 108
Berger, T. A., Huber, D., van Saders, J. L., et al. 2020b, AJ, 159, 280
Borucki, W. J. 2016, RPPh, 79, 036901
Borucki, W. J., Koch, D., Basri, G., et al. 2010, Sci, 327, 977
Boyajian, T. S., von Braun, K., van Belle, G., et al. 2013, ApJ, 771, 40
Brewer, J. M., & Fischer, D. A. 2018, ApJS, 237, 38
Brewer, J. M., Fischer, D. A., Valenti, J. A., & Piskunov, N. 2016, ApJS, 225, 32
Brown, E. L., Jeffers, S. V., Marsden, S. C., et al. 2022, MNRAS, 514, 4300
Buchhave, L. A., Bizzarro, M., Latham, D. W., et al. 2014, Natur, 509, 593
Buchhave, L. A., & Latham, D. W. 2015, ApJ, 808, 187
Buchhave, L. A., Latham, D. W., Johansen, A., et al. 2012, Natur, 486, 375
Buder, S., Sharma, S., Kos, J., et al. 2021, MNRAS, 506, 150
Castelli, F., & Kurucz, R. L. 2003, in IAU Symp. 210, Modelling of Stellar Atmospheres, ed. N. Piskunov, W. W. Weiss, & D. F. Gray (San Francisco, CA: ASP), A20
Choi, J., Dotter, A., Conroy, C., et al. 2016, ApJ, 823, 102
Clark, J. T., Wright, D. J., Wittenmyer, R. A., et al. 2022, MNRAS, 510, 2041
Cloutier, R., & Menou, K. 2020, AJ, 159, 211
Crossfield, I. J. M., Ciardi, D. R., Petigura, E. A., et al. 2016, ApJS, 226, 7
Crossfield, I. J. M., Guerrero, N., David, T., et al. 2018, ApJS, 239, 5
Cui, X.-Q., Zhao, Y.-H., Chu, Y.-Q., et al. 2012, RAA, 12, 1197
da Silva, L., Girardi, L., Pasquini, L., et al. 2006, A&A, 458, 609
Damasso, M., Zeng, L., Malavolta, L., et al. 2019, A&A, 624, A38
Dawson, R. I., Chiang, E., & Lee, E. J. 2015, MNRAS, 453, 1471
Deleuil, M., Barge, P., Defay, C., et al. 2000, in ASP Conf. Ser. 219, Disks, Planetesimals, and Planets, ed. C. Garzón et al. (San Francisco, CA: ASP), 656
Deleuil, M., Aigrain, S., Moutou, C., et al. 2018, A&A, 619, A97
Demarque, P., Woo, J.-H., Kim, Y.-C., & Yi, S. K. 2004, ApJS, 155, 667
Dong, S., Xie, J.-W., Zhou, J.-L., Zheng, Z., & Luo, A. 2018, PNAS, 115, 266
Dotter, A. 2016, ApJS, 222, 8
Dotter, A., Chaboyer, B., Jevremovic, D., et al. 2008, ApJS, 178, 89
Epstein, C. R., Johnson, J. A., Dong, S., et al. 2010, ApJ, 709, 447
Everett, M. E., Howell, S. B., Silva, D. R., & Szkody, P. 2013, ApJ, 771, 107
Fischer, D. A., & Valenti, J. 2005, ApJ, 622, 1102
Flores, M., Gonzalez, J. F., Jaque Arancibia, M., Buccino, A., & Saffe, C. 2016, A&A, 589, A135
Friel, E. D., Jacobson, H. R., Barrett, E., et al. 2003, AJ, 126, 2372
Fulton, B. J., & Petigura, E. A. 2018, AJ, 156, 264
Fulton, B. J., Petigura, E. A., Howard, A. W., et al. 2017, AJ, 154, 109
Furlan, E., & Howell, S. B. 2017, AJ, 154, 66
Furlan, E., Ciardi, D. R., Everett, M. E., et al. 2017, AJ, 153, 71
Gaia Collaboration, Brown, A. G. A., Vallenari, A., et al. 2021, A&A, 649, A1
Gaudi, B. S. 2013, AAS Meeting, 221, 310.03
Ghezzi, L., Cunha, K., Schuler, S. C., & Smith, V. V. 2010, ApJ, 725, 721
Ghezzi, L., Martinez, C. F., Wilson, R. F., et al. 2021, ApJ, 920, 19
Ghezzi, L., Montet, B. T., & Johnson, J. A. 2018, ApJ, 860, 109
Ginzburg, S., Schlichting, H. E., & Sari, R. 2016, ApJ, 825, 29
Ginzburg, S., Schlichting, H. E., & Sari, R. 2018, MNRAS, 476, 759
Girardi, L., Bressan, A., Bertelli, G., & Chiosi, C. 2000, A&AS, 141, 371
Gonzalez, G. 1997, MNRAS, 285, 403
Gupta, A., & Schlichting, H. E. 2019, MNRAS, 487, 24
Han, S. I., Kim, Y. C., Lee, Y. W., et al. 2009, Globular Clusters—Guides to Galaxies. Eso Astrophysics Symp., ed. T. Richter & S. Larsen (Berlin: Springer), 33
Hardegree-Ullman, K. K., Zink, J. K., Christiansen, J. L., et al. 2020, ApJS, 247, 28
Hayden, M. R., Bovy, J., Holtzman, J. A., et al. 2015, ApJ, 808, 132
Hayden, M. R., Bland-Hawthorn, J., Sharma, S., et al. 2020, MNRAS, 493, 2952
Howell, S. B., Matson, R. A., Ciardi, D. R., et al. 2021, AJ, 161, 164
Howell, S. B., Sobeck, C., Haas, M., et al. 2014, PASP, 126, 398

Huber, D., Bryson, S. T., Haas, M. R., et al. 2016, ApJS, 224, 2
Huber, D., Zinn, J., Bojsen-Hansen, M., et al. 2017, ApJ, 844, 102
Ida, S., & Lin, D. N. C. 2004a, ApJ, 604, 388
Ida, S., & Lin, D. N. C. 2004b, ApJ, 616, 567
Ida, S., & Lin, D. N. C. 2005, ApJ, 626, 1045
Johnson, J. A., Petigura, E. A., Fulton, B. J., et al. 2017, AJ, 154, 108
Jonsson, H., Holtzman, J. A., Prieto, C. A., et al. 2020, AJ, 160, 120
Koch, D. G., Borucki, W. J., Basri, G., et al. 2010, ApJL, 713, L79
Kruse, E., Agol, E., Luger, R., & Foreman-Mackey, D. 2019, ApJS, 244, 11
Kurucz, R. L. 2014, in Determination of Atmospheric Parameters of B-, A-, F- and G-Type Stars, ed. E. Niemczura, B. Smalley, & W. Pych (Berlin: Springer), 63
LaCourse, D. M., Jek, K. J., Jacobs, T. L., et al. 2015, MNRAS, 452, 3561
Lester, K. V., Matson, R. A., Howell, S. B., et al. 2021, AJ, 162, 75
Libralato, M., Nardiello, D., Bedin, L. R., et al. 2016, MNRAS, 463, 1780
Livingston, J. H., Crossfield, I. J. M., Petigura, E. A., et al. 2018, AJ, 156, 277
Lopez, E. D., & Fortney, J. J. 2013, ApJ, 776, 2
Lorenzo-Oliveira, D., Freitas, F. C., Melendez, J., et al. 2018, A&A, 619, A73
Magg, E., Bergemann, M., Serenelli, A., et al. 2022, A&A, 661, A140
Majewski, S. R., Schiavon, R. P., Frinchaboy, P. M., et al. 2017, AJ, 154, 94
Mann, A. W., Gaidos, E., Vanderburg, A., et al. 2017, AJ, 153, 64
Martin, E. L., Lodieu, N., Pavlenko, Y., & Bejar, V. J. S. 2018, ApJ, 856, 40
Martinez, C. F., Cunha, K., Ghezzi, L., & Smith, V. V. 2019, ApJ, 875, 29
Mayo, A. W., Vanderburg, A., Latham, D. W., et al. 2018, AJ, 155, 136
Meléndez, J., Ramírez, I., Karakas, A. a. I., et al. 2014, ApJ, 791, 14
Montet, B. T., Morton, T. D., Foreman-Mackey, D., et al. 2015, ApJ, 809, 25
Mordasini, C., Alibert, Y., Benz, W., Klahr, H., & Henning, T. 2012, A&A, 541, A97
Mordasini, C., Molliere, P., Dittkrist, K.-M., Jin, S., & Alibert, Y. 2015, IJAsB, 14, 201
Morton, T. D. 2015, isochrones: Stellar model grid package, Astrophysics Source Code Library, ascl:1503.010
Mulders, G. D., Pascucci, I., Apai, D., Frasca, A., & Molenda-Zakowicz, J. 2016, AJ, 152, 187
Mullally, F., Coughlin, J. L., Thompson, S. E., et al. 2015, ApJS, 217, 31
Narang, M., Manoj, P., Furlan, E., et al. 2018, AJ, 156, 221
Nayakshin, S. 2010, MNRAS, 408, L36
Oláh, Katalin 2007, in IAU Symp. 240, Binary Stars as Critical Tools & Tests in Contemporary Astrophysics, ed. W. I. Hartkopf, P. Harmanec, & E. F. Guinan (Cambridge: Cambridge Univ. Press), 442
Owen, J. E., & Murray-Clay, R. 2018, MNRAS, 480, 2206
Owen, J. E., & Wu, Y. 2013, ApJ, 775, 105
Petigura, E. A., Crossfield, I. J. M., Isaacson, H., et al. 2018a, AJ, 155, 21
Petigura, E. A., Howard, A. W., Marcy, G. W., et al. 2017, AJ, 154, 107
Petigura, E. A., Marcy, G. W., Winn, J. N., et al. 2018b, AJ, 155, 89
Petigura, E. A., Rogers, J. G., Isaacson, H., et al. 2022, AJ, 163, 179
Pinsonneault, M. H., Elsworth, Y. P., Tayar, J., et al. 2018, ApJS, 239, 32
Piskunov, N., & Valenti, J. A. 2017, A&A, 597, A16
Pope, B. J. S., Parviainen, H., & Aigrain, S. 2016, MNRAS, 461, 3399
Ramirez, I., Allende Prieto, C., & Lambert, D. L. 2013, ApJ, 764, 78
Ramirez, I., Melendez, J., & Asplund, M. 2009, A&A, 508, L17
Ramirez, I., Melendez, J., Bean, J., et al. 2014, A&A, 572, A48
Ricker, G. R., Winn, J. N., Vanderspek, R., et al. 2015, JATIS, 1, 014003
Rizzuto, A. C., Mann, A. W., Vanderburg, A., Kraus, A. L., & Covey, K. R. 2017, AJ, 154, 224
Rodrigues, T. S., Bossini, D., Miglio, A., et al. 2017, MNRAS, 467, 1433
Rodrigues, T. S., Girardi, L., Miglio, A., et al. 2014, MNRAS, 445, 2758
Santos, N. C., Israelian, G., & Mayor, M. 2004, A&A, 415, 1153
Schuler, S. C., Vaz, Z. A., Katime Santrich, O. o. J., et al. 2015, ApJ, 815, 5
Seager, S., & Mallen-Ornelas, G. 2003, ApJ, 585, 1038
Serenelli, A., Johnson, J., Huber, D., et al. 2017, ApJS, 233, 23
Sharma, S., Stello, D., Bland-Hawthorn, J., et al. 2019, MNRAS, 490, 5335
Sinukoff, E., Howard, A. W., Petigura, E. A., et al. 2016, ApJ, 827, 78
Slawson, R. W., Prsa, A., Welsh, W. F., et al. 2011, AJ, 142, 160
Sneden, C. A. 1973, PhD thesis, The University of Texas at Austin
Sousa, S. G., Santos, N. C., Adibekyan, V., Delgado-Mena, E., & Israelian, G. 2015, A&A, 577, A67
Sousa, S. G., Santos, N. C., Israelian, G., Mayor, M., & Udry, S. 2011, A&A, 533, A141
Sousa, S. G., Santos, N. C., Mayor, M., et al. 2008, yCat, 348, 70373
Spina, L., Nordlander, T., Casey, A. R., et al. 2020, ApJ, 895, 52
Stassun, K. G., Oelkers, R. J., Paegert, M., et al. 2019, AJ, 158, 138
Stefansson, G., Li, Y., Mahadevan, S., et al. 2018, AJ, 156, 266
Su, T., Zhang, L.-y., Long, L., et al. 2022, ApJS, 261, 26
Thompson, S. E., Coughlin, J. L., Hoffman, K., et al. 2018, ApJS, 235, 38
van Dokkum, P. G. 2001, PASP, 113, 1420
Van Eylen, V., Agentoft, C., Lundkvist, M. S., et al. 2018, MNRAS, 479, 4786
Van Eylen, V., Albrecht, S., Gandolfi, D., et al. 2016, AJ, 152, 143
Van Eylen, V., Astudillo-Defru, N., Bonfils, X., et al. 2021, MNRAS, 507, 2154
Vanderburg, A., Latham, D. W., Buchhave, L. A., et al. 2016, ApJS, 222, 14
Venturini, J., Guilera, O. M., Haldemann, J., Ronco, M. P., & Mordasini, C. 2020, A&A, 643, L1
Wang, J., & Fischer, D. A. 2015, AJ, 149, 14
Weiss, L. M., Isaacson, H. T., Marcy, G. W., et al. 2018, AJ, 156, 254
Wilson, R. F., Teske, J., Majewski, S. R., et al. 2018, AJ, 155, 68
Wittenmyer, R. A., Sharma, S., Stello, D., et al. 2018, AJ, 155, 84
Wittenmyer, R. A., Clark, J. T., Sharma, S., et al. 2020, MNRAS, 496, 851
Yana Galarza, J., Meléndez, J., Lorenzo-Oliveira, D., et al. 2019, MNRAS, 490, L86
Yi, S., Demarque, P., Kim, Y.-C., et al. 2001, ApJS, 136, 417
Yi, S. K., Kim, Y.-C., & Demarque, P. 2003, ApJS, 144, 259
Zhu, W., Wang, J., & Huang, C. 2016, ApJ, 832, 196
Zink, J. K., Hardegree-Ullman, K. K., Christiansen, J. L., et al. 2020, AJ, 160, 94
Zink, J. K., Hardegree-Ullman, K. K., Christiansen, J. L., et al. 2021, AJ, 162, 259
Zong, W., Fu, J.-N., Cat, P. D., et al. 2018, ApJS, 238, 30

# Capítulo 3

# Caracterização Estelar e uma Análise da Atividade Cromosférica de uma Amostra de Estrelas K2 Hospedeiras de Planetas

Neste capítulo, apresentamos o artigo submetido para publicação à revista *AAS Journals*: "Stellar Characterization and a Chromospheric Activity Analysis of a K2 Sample of Planet-Hosting Stars". Este trabalho aborda a caracterização estelar e uma análise da atividade cromosférica de uma amostra de estrelas K2, hospedeiras de planetas de tipos espectrais F, G e K. A amostra é composta por estrelas observadas pela missão estendida Kepler (K2) durante as campanhas C0 – C8, cujos espectros ópticos foram obtidos pelo programa *California Planet Search* (CPS), que utilizou o espectrógrafo HIRES no telescópio Keck I de 10 metros do Observatório Keck. Esses espectros foram observados durante campanhas observacionais realizadas após agosto de 2004, com os CCDs atualizados do HIRES, abrangendo um intervalo de comprimento de onda de $\lambda$3640 Å até $\lambda$7990 Å, que inclui as linhas Ca II H e K que são sensíveis a atividade estelar.

Os parâmetros estelares (temperatura efetiva, gravidade superficial, metalicidade e velocidade de microturbulência) de 86 estrelas foram determinados seguindo a mesma metodologia do artigo apresentado no capítulo 2, que utiliza o método espectroscópico clássico, baseado nos equilíbrios de excitação e ionização das linhas do Fe I e Fe II. Nesta análise, utilizamos a lista de linhas de YANA GALARZA *et al.* (2019) , que está baseada na lista de MELÉNDEZ *et al.* (2014). As larguras equivalentes das linhas de ferro foram determinadas usando o código ARES (SOUSA *et al.*, 2015). Os cálculos foram feitos assumindo o equilíbrio termodinâmico local (LTE) e utilizamos o modelo de atmosferas plano-paralelos da grade ATLAS9 ODFNEW de Kurucz (CASTELLI e KURUCZ, 2003). As massas e raios estelares também foram determinados a partir do método de isócronas.

Determinamos também os raios de 73 planetas confirmados, com uma incerteza interna mediana de 3,4%, cuja distribuição mostrou o já conhecido vale do raio para planetas menores ($R_{pl} < 4$ R$_\oplus$).

Analisamos a atividade cromosférica a partir do índice $S_{HK}$, que foi determinado para 144 estrelas a partir de 542 espectros, os quais foram obtidos do ExoFop (*Exoplanet Follow-up Observing Program*, AKESON e CHRISTIANSEN (2019)). Com o objetivo de analisarmos a maior quantidade possível de espectros por estrela, obtivemos também espectros do arquivo público do Keck (*Keck Observatory Archives*, KOA). A contribuição fotosférica foi removida usando a metodologia de NOYES *et al.* (1984) e aplicando as correções bolométricas de RUTTEN (1984) para estrelas de sequência principal e estrelas evoluídas, e assim determinamos o índice $R'_{HK}$. Na seção 5.1.2, analisamos a relação entre a atividade estelar e a rotação das estrelas. À medida que uma estrela evolui, perde momento angular devido à perda de massa ao longo do tempo e à interação dos campos magnéticos com os ventos estelares. Isso resulta na diminuição da velocidade de rotação e na atividade estelar. É fundamental ressaltar neste contexto a ligação entre a velocidade de rotação e o processo físico do dínamo estelar, no qual os campos magnéticos são gerados pela convecção. Nossas medidas de atividade estelar mostraram que temos mais estrelas com índice $S_{HK} < 0,2$ e poucas estrelas com valores entre 2 e 3. Adicionalmente, nossa amostra indica a presença da lacuna de Vaughan-Preston.

Na Seção 3.1 apresentamos uma seção adicional apresentando comparações adicionais (não incluídas nos artigo publicado) entre parâmetros estelares determinados nos diferentes estudos da literatura e os determinados neste trabalho.

Draft version January 12, 2024
Typeset using LaTeX **modern** style in AASTeX631

# Stellar Characterization and a Chromospheric Activity Analysis of a K2 Sample of Planet-Hosting Stars

V. Loaiza-Tacuri [1], Katia Cunha [1,2], Verne V. Smith [3], F. Quispe-Huaynasi,[1] Ellen Almeida,[1] Luan Ghezzi,[4] and Jorge Melendez[5]

[1] *Observatório Nacional, Rua General José Cristino, 77, 20921-400 São Cristóvão, Rio de Janeiro, RJ, Brazil*

[2] *Steward Observatory, University of Arizona, 933 North Cherry Avenue, Tucson, AZ 85721, USA*

[3] *NSF's NOIRLab, 950 North Cherry Avenue, Tucson, AZ 85719, USA*

[4] *Universidade Federal do Rio de Janeiro, Observatório do Valongo, Ladeira do Pedro Antônio, 43, Rio de Janeiro, RJ 20080-090, Brazil*

[5] *Instituto de Astronomia, Geofísica e Ciências Atmosféricas, Universidade de São Paulo, Rua do Matão 1226, São Paulo 05508-090, Brazil*

## ABSTRACT

Effective temperatures, surface gravities, and metallicities were derived for 86 stars observed by the K2 mission using equivalent width measurements of Fe I and Fe II lines. Calculations were carried out in LTE using Kurucz model atmospheres. Stellar masses and radii were derived by combining the stellar parameters with Gaia DR3 parallaxes, V-magnitudes, and isochrones. The derived stellar and planetary radii have median internal precision of 2.6%, and 3.4%, respectively. The radius gap near $R_{planet} \sim 1.9 R_{\oplus}$ was detected in this K2 sample. Chromospheric activity was measured from the Ca II H and K lines using the $S_{HK}$ index for 144 K2 stars. Values of $\log R'_{HK}$ were investigated as a function of stellar rotational period ($P_{rot}$) and we found that chromospheric activity decreases with increasing $P_{rot}$, although there is a large scatter in $\log R'_{HK}$ ($\sim$0.5) for a given $P_{rot}$. Activity levels in this sample reveal a paucity of F & G dwarfs with intermediate activity levels (Vaughan-Preston gap). The effect that stellar activity might have on the derivation of stellar parameters was investigated by including magnetically-sensitive Fe I lines in the analysis and we find no significant differences between parameters with and without magnetically-sensitive lines, although the more active stars ($\log R'_{HK} > -5.0$) exhibit a larger scatter in the differences in $T_{eff}$ and [Fe/H].

*Keywords:* (stars:) planetary systems — stars: fundamental parameters — techniques: spectroscopic, parallaxes

Corresponding author: Verónica Loaiza Tacuri
vtacuri@on.br

## 1. INTRODUCTION

Currently there are ∼5500 confirmed exoplanets (NASA Exoplanet Archive) orbiting more than 4250 host stars, with the majority of detections resulting from planetary transits, the largest number of which were observed by the Kepler mission (Borucki et al. 2010; Koch et al. 2010; Borucki 2016) and the extended Kepler mission, known as K2 (Howell et al. 2014), as well as the CoRoT mission (Deleuil et al. 2000, 2018). The growing number of exoplanets has led to numerous studies whose main goals have been the characterization of planet-hosting stars and the planets orbiting them. Results from these studies have revealed fascinating patterns, such as the correlation between stellar metallicity and the frequency of giant planets (Gonzalez 1997; Fischer & Valenti 2005; Ghezzi et al. 2018, and subsequent studies), the absence of planets having sizes between the super-Earth and sub-Neptune regimes (Fulton et al. 2017; Fulton & Petigura 2018), known as the radius valley, and a slope in the value of the radius valley as a function of planetary orbital period (Van Eylen et al. 2018; Martinez et al. 2019, among others); such conclusions provide constraints on planetary formation theories (e.g. Ida & Lin 2004a,b, 2005; Nayakshin 2010; Mordasini et al. 2012, 2015; Owen & Murray-Clay 2018; Venturini et al. 2020). The discovery of a planet-radius valley and its change as a function of orbital period was made possible thanks to high-precision spectroscopic methods used to determine the parameters and physical properties (effective temperature, $T_{\rm eff}$, surface gravity, as log g, and metallicity, [Fe/H]) of the planet-hosting stars. The derived planetary radii depend most strongly on the radii of their host-stars coupled with the transit depths, with the stellar radii derived from the stellar parameters, thus precise stellar characterization is critical to the derivation of precise planetary radii.

An additional stellar parameter that can impact derived stellar and planetary radii is magnetic activity on the host star (Yana Galarza et al. 2019; Spina et al. 2020), as it can influence the characterization of the host star and, thus, the planets orbiting it. This influence arises from the connections between planetary properties, such as radius and mass, and those of their parent stars. The intensity of stellar magnetic activity can manifest itself in features such as spots and flares, or chromospheric UV, X-ray, and radio emission (Han et al. 2023). Emission lines such as the cores of Ca II H and K, Mg II, H-$\alpha$, the IR triplet of Ca II, and others are commonly used as indicators of chromospheric activity (or chromospheric emission). Among these indicators, the Ca II H ($\lambda$3968Å) and K ($\lambda$3934Å) lines, which originate in the photosphere, are commonly used as they are sensitive to chromospheric activity, which itself is associated with magnetic fields (Leighton 1959; Skumanich et al. 1975). When a star has an active chromosphere, the cores of these very strong Ca II absorption lines undergo reversals, due to the chromospheric temperature increase, and become core emission features which appear in sharp constrast to the deep photospheric absorption, making them excellent diagnostic tools for assessing chromospheric activity.

In this study we derive stellar parameters for a sample of planet-hosting stars discovered by the K2 mission via a quantitative high-resolution spectroscopic analysis based on a set of carefully vetted Fe I and Fe II lines. As part of the analysis, we also derive chromospheric activity levels by using the Ca II H and K lines and investigate the impact that stellar activity might have on spectroscopically-derived stellar parameters.

This paper is organized as follows: Section 2 provides details on the observations and data reduction. Section 3 discusses the methodology used to derive key stellar parameters and uncertainties, including effective temperatures, surface gravities, metallicities, stellar masses, radii, and planetary radii. In Section 4 we explain the approach used to assess stellar activity using the calcium H and K lines and in Sections 5 and 6 present discussions and conclusions, respectively.

## 2. DATA

The sample consists of host-stars observed by the Kepler extended mission (K2) during the C0 – C8 campaigns. The optical spectra of these stars were obtained from the California Planet Search (CPS) program, which used the HIgh Resolution Echelle Spectrometer (HIRES; Vogt et al. 1994) on the Keck I 10m telescope. These spectra were observed during observational campaigns carried out after August 2004, with the updated HIRES CCDs, and cover the wavelength range from $\lambda$3640Å-7990Å, which includes the Ca II H and K lines.

Reduced HIRES spectra for a sample of 144 stars (one spectrum per star) were obtained from ExoFop[1]. These spectra were carefully inspected and 86 of them had signal-to-noise high enough in order to be analyzed for the derivation of stellar parameters and metallicities (Section 3). As it was of interest to have as many observations as possible per star to study stellar activity, 725 spectra were obtained from the Keck Observatory Archives (KOA)[2], which were then used to measure the Ca II H and K lines located in the blue spectral region (Section 4). Observational data, such as identifiers, positions, B and V magnitudes (taken from the EPIC catalog and the NASA Exoplanet Archive), and K2 observational campaigns information of the sample stars are given in Table 1.

**Table 1**. Sample K2 Stars

| ID | Host Name | R.A. (deg) | Decl. (deg) | B (mag) | V (mag) | Camp |
|---|---|---|---|---|---|---|
| EPIC211319617 | K2-180 | 126.463933 | 10.246968 | 13.334 | 12.601 | C5 |
| EPIC211331236 | K2-117 | 133.855682 | 10.469131 | 16.137 | 14.655 | C5 |

**Table 1** *continued on next page*

[1] https://exofop.ipac.caltech.edu/tess/
[2] https://nexsci.caltech.edu/archives/koa/

**Table 1** *(continued)*

| ID | Host Name | R.A. (deg) | Decl. (deg) | B (mag) | V (mag) | Camp |
|---|---|---|---|---|---|---|
| EPIC211342524 | ··· | 128.098694 | 10.677239 | 13.052 | 12.422 | C5 |
| EPIC211351816 | K2-97 | 127.762836 | 10.847586 | 13.770 | 12.611 | C5 |
| EPIC211355342 | K2-181 | 127.554034 | 10.910294 | 13.494 | 12.749 | C5 |
| ... | ... | ... | ... | ... | ... | ... |

NOTE—This table is published in its entirety in the machine readable format. A portion is shown here for guidance regarding its form and content.

## 3. STELLAR PARAMETERS

The spectroscopic stellar parameters of effective temperature ($T_{\rm eff}$), surface gravity ($\log g$), iron abundance (A(Fe)[3]), and microturbulent velocity ($\xi$), were derived by enforcing the excitation/ionization balances of a selected set of Fe I and Fe II equivalent widths. The analysis assumes local thermodynamic equilibrium (LTE) and uses 1-D plane parallel model atmospheres from the Kurucz ATLAS9 ODFNEW grid (Castelli & Kurucz 2003).

The line list used in this study was adopted from Yana Galarza et al. (2019), which is based on the line list of Meléndez et al. (2014); it contains 61 Fe I and 13 Fe II lines. Yana Galarza et al. (2019) provide a critical discussion of which Fe I and Fe II lines are most sensitive, along with those that are not sensitive, to magnetic activity through the combination of magnetic susceptibility, as measured by the Landé g-factor ($g_L$), and the line strength, as measured by the equivalent width. Table 2 lists the wavelengths of the Fe I (species=26.0) and Fe II (species=26.1) lines along with their excitation potentials, log gf values (both solar and from laboratory), and whether the line is classified as magnetically sensitive (Y) or not (N) by Yana Galarza et al. (2019). The equivalent widths of the lines in this list were measured using the ARES code v2 (Sousa et al. 2015). In this section we only consider in the analysis Fe lines which are deemed as insensitive to stellar activity. (An analysis including sensitive lines will be discussed in Section 5.1.4).

The spectroscopic methodology adopted here is similar to that used in our previous study of K2 targets (Loaiza-Tacuri et al. 2023), which used an automated code for the determinations of stellar parameters and metallicities named `qoyllur-quipu`[4] or $q^2$ (Ramírez et al. 2014). Briefly, $q^2$ uses an input iron line list and measured equivalent widths in combination with the 2019 version of the abundance analysis code MOOG (Sneden 1973) to compute iron abundances, effective temperatures, surface gravities and metallicities. The iterative process begins with an interpolated model atmosphere calculated for assumed values of $T_{\rm eff}$, $\log g$, and metallicity. Values of $T_{\rm eff}$ / $\log g$

[3] A(X)=log(N(X)/N(H))+12.0
[4] https://github.com/astroChasqui/q2

/ A(Fe) are adjusted iteratively (increased or decreased) to minimize trends A(Fe I) and A(Fe II) as functions of $T_{eff}$, log g, and $\xi$ until a solution is found for a final adjusted set of spectroscopic parameters of each star.

As a test to our methodology we analyzed solar-proxy spectra obtained with the HIRES spectrograph, focusing on reflected solar light from the asteroid Iris. The parameters and metallicities obtained for the solar proxy Iris were: $T_{eff} = 5744 \pm 33$ K, log g $= 4.52 \pm 0.05$, A(Fe) $= 7.39 \pm 0.02$, and $\xi = 1.12 \pm 0.13$ km.s$^{-1}$); these are in general agreement with the solar parameters, indicating that our methodology does not likely have strong biases for solar-type stars. We note, however, that the mean metallicity for the solar proxies of A(Fe) = 7.39 is slightly more metal-poor than the Asplund et al. (2021) $(A(Fe)_{\odot} = 7.46)$ scale, keeping in mind that they obtain A(Fe) $< 7.40$ when they analyze in 1D.

The derived effective temperatures, surface gravities, metallicities, and microturbulent velocities for all analyzed stars are presented in Table 3. We show the stellar parameters of $T_{eff}$ and log g for the K2 stars in this study in the Kiel diagram presented in Figure 1. The target stars are shown as filled circles color-coded by their log $R'_{HK}$ index (which will be derived in Section 4) as indicated by the color bar. We also show two Yonsei-Yale isochrones (Yi et al. 2001, 2003; Demarque et al. 2004; Han et al. 2009) corresponding to 4.6 and 10 Gyr as dashed gray lines. The majority of the stars in this study are on the main sequence, with a small number of them having lower values of log g which are indicative of evolved stars. The black dashed line in Figure 1 represents the adopted division between main-sequence and evolved stars. Here we use the same division between main sequence and subgiants and giants that was adopted in Gomes da Silva et al. (2021) which is from Ciardi et al. (2011).

Comparisons of the derived stellar parameters with results from the literature find, in general, reasonable agreement. There is good agreement between our values of $T_{eff}$s with those from the works of Petigura et al. (2018) and Mayo et al. (2018), as well as the DR17 APOGEE (Majewski et al. 2017) and the DR3 GALAH (Buder et al. 2021) surveys. Comparisons of the different temperature scales find median values of $T_{eff}$ ("Other Work" - "This Work") and MADs (Median Absolute Deviations) of: +22 ± 71 and +35 ± 74 K for the two first studies, and -16 ± 51 and -51 ± 64 K for the two surveys, respectively. The comparison with $T_{eff}$s from the Gaia survey (Gaia Collaboration et al. 2016, 2023) and the DR8 LAMOST survey (Cui et al. 2012) reveals slightly more significant systematic differences and MADs of -59 ± 115 and -63 ± 91 K, respectively.

Our values of log g also generally agree, within the uncertainties, with those from the mentioned works/surveys, with median differences in log g from $\sim -0.04$ to $-0.01$ dex and MAD values from ± 0.13 to ± 0.18. For Mayo et al. (2018) and LAMOST, however, we find higher systematic differences of $+0.16 \pm 0.12$ and $-0.08 \pm 0.17$ dex, respectively. Finally, our log g values overall compare well with those based on asteroseismology for K2 stars from Huber et al. (2016): median log g difference (±

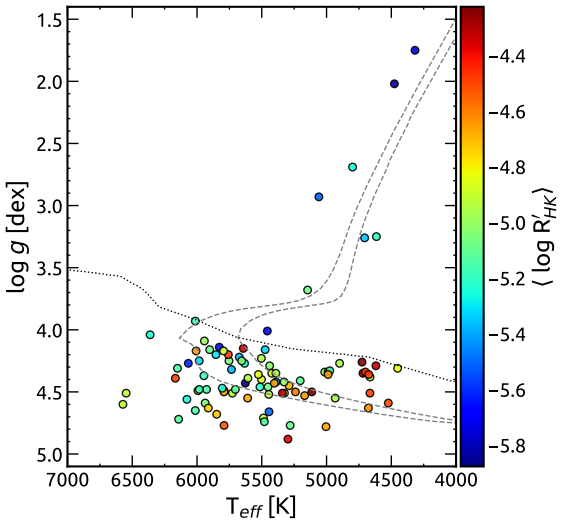


**Figure 1.** Kiel diagram for the sample stars. The gray dashed lines represent solar metallicity 4.6 and 10 Gyr old stellar evolution tracks from Yonsei-Yale. The colors of the circles indicate stellar activity as measured by the log $R'_{HK}$ indicator (Section 4) and corresponding to the color bar. The main sequence stars and the evolved stars are separated by the black dashed line.

MAD) of -0.02 ± 0.19 dex. But we note that there are four stars with significant differences, with this work finding them to be dwarfs (log g varying between 4.3 to 4.8 with uncertainties between 0.08 and 0.2), while Huber et al. (2016) find them to be more evolved (log g varying between 2.7 to 3.7 with uncertainties from 0.07 to 0.53 dex). These are: EPIC 220481411, EPIC 211413752, EPIC 212012119, and EPIC 212782836, which are nearby stars with distances of approximately 114, 321, 123, and 184 pc, and absolute V-magnitudes of 7.04, 6.39, 6.69, and 5.79, respectively, placing them as K-dwarf stars and more in line with our log values. (See also discussion in Section 3.1 of differences in the derived radii with Huber et al. (2016)).

**Table 2**. Iron Line List

| $\lambda$ (Å) | Species | $\chi$ (eV) | log $gf$ | *Sensitive* |
|---|---|---|---|---|
| 4088.560 | 26.0 | 3.640 | -1.720 | Y |
| 4091.560 | 26.0 | 2.830 | -2.310 | Y |
| 4365.896 | 26.0 | 2.990 | -2.250 | N |

NOTE—The complete table is available in machine-readable format. Here, a portion is provided for reference regarding its format and content. Lines with (Y) are sensitive to activity. Lines with (N) are not sensitive. Lines marked with (*) were excluded from the analysis of stellar parameters for all stars because their equivalent widths exceeded 120 mÅ.

**Table 3.** Stellar Parameters

| ID | $\langle S_{HK} \rangle$ | $\sigma$ | $\langle \log R'_{HK} \rangle$ | $\sigma$ | # Sp | $T_{eff}$ (K) | log g (dex) | A(Fe) (dex) | $\xi$ (km.s$^{-1}$) | $R_{star}$ ($R_\odot$) | $M_{star}$ ($M_\odot$) |
|---|---|---|---|---|---|---|---|---|---|---|---|
| EPIC211319617 | 0.166 | 0.019 | -5.024 | 0.123 | 15 | $5281 \pm 54$ | $4.77 \pm 0.15$ | $6.82 \pm 0.03$ | $0.89 \pm 0.29$ | $0.68 \pm 0.01$ | $0.73 \pm 0.02$ |
| EPIC211331236 | 2.488 | ... | -4.648 | ... | 1 | ... | ... | ... | ... | ... | ... |
| EPIC211342524 | 0.259 | ... | -4.571 | ... | 1 | $6007 \pm 163$ | $4.17 \pm 0.28$ | $7.08 \pm 0.11$ | $2.53 \pm 1.64$ | $1.61 \pm 0.11$ | $1.06 \pm 0.05$ |
| EPIC211351816 | 0.110 | 0.023 | -5.374 | 0.108 | 7 | $4706 \pm 74$ | $3.26 \pm 0.22$ | $7.62 \pm 0.07$ | $1.44 \pm 0.14$ | $3.64 \pm 0.14$ | $1.05 \pm 0.08$ |
| EPIC211355342 | 0.149 | 0.017 | -5.139 | 0.138 | 9 | $5514 \pm 23$ | $4.46 \pm 0.06$ | $7.62 \pm 0.03$ | $1.02 \pm 0.14$ | $0.99 \pm 0.02$ | $0.97 \pm 0.02$ |
| ... | ... | ... | ... | ... | ... | ... | ... | ... | ... | ... | |

Note—This table is published in its entirety in the machine readable format. A portion is shown here for guidance regarding its form and content.

### 3.1. *Stellar Masses & Radii*

We calculated the stellar masses and radii using the isochrone method, which involves estimating these fundamental parameters by comparing the positions of stars in a $T_{eff}$ - $M_V$ diagram with theoretical isochrones. To perform this analysis, we used the $q^2$ code, which derives stellar mass, radius, luminosity, and age based on a grid of Yonsei-Yale isochrones (Yi et al. 2001, 2003). The required input parameters are $T_{eff}$ and [Fe/H], determined spectroscopically in this work, and the absolute magnitude ($M_V$) derived using the parallax measurements obtained from Gaia DR3 data (Gaia Collaboration et al. 2021). We corrected all V-magnitudes for extinction using $A_V$ values calculated from IRSA/Galactic Dust Reddening and Extinction[5] (Schlafly & Finkbeiner 2011). The probability distributions of stellar mass, radius, age and luminosity are determined and matched to the isochrones using as weights the distances between the values of the input parameters, which are normalized by their errors (we refer to Ramírez et al. 2013; Ramírez et al. 2014, for more details). In Table 3 are shown the isochrone-derived masses and radii of the sample stars.

The distributions of stellar masses and radii for our sample are displayed in Figure 2, revealing that the majority of the sample stars have stellar radii $< 2$ $R_\odot$ and masses $< 1.2$ $M_\odot$. The median radius of the distribution is 0.996 $R_\odot$ (16th percentile = 0.745; 84th percentile = 1.384) and median mass is 0.970 $M_\odot$ (16th percentile = 0.793; 84th percentile = 1.075).

The stellar masses and radii obtained here using the isochrone method are compared with results from asteroseismology from Huber et al. (2016) in Figure 3, with stellar radii shown on the left panel and masses on the right panel. Overall the derived radii and masses compare well with Huber et al. (2016), with a small systematic difference, except for a few clear outliers. The median ($\pm$ MAD) of the differences between the stellar radii from Huber et al. (2016) minus ours is $0.027 \pm 0.149$ $R_\odot$. We note,

[5] https://irsa.ipac.caltech.edu/applications/DUST/

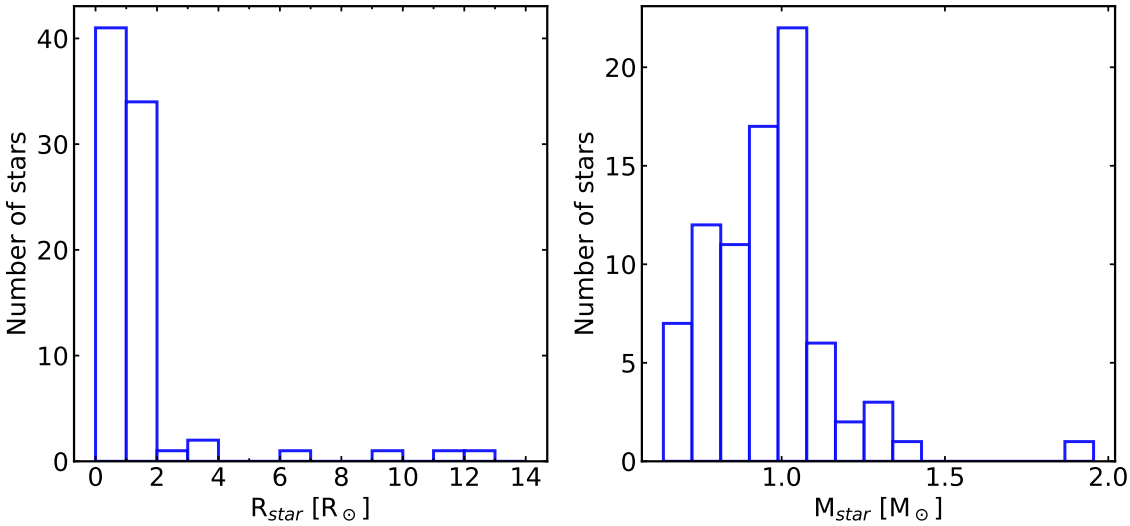


**Figure 2.** Mass and radius distributions for the sample stars.

however, that there seems to be a slight trend for the more evolved stars having radii roughly larger than 5 $R_\odot$. Concerning the masses, a small systematic difference is found between our stellar mass determinations and those of Huber et al. (2016) (see right panel Figure 3). Our masses are smaller than those from asteroseismology with a small median (± MAD) of the differences of 0.04 ± 0.07 $M_\odot$.

One of the outliers in the radius comparison with Huber et al. (2016) is particularly significant - star EPIC 215346008, for which we obtained a stellar radius of 11.9 ± 0.496 $R_\odot$ which is about 3 times smaller than the one in Huber et al. (2016) of 36.6 $R_\odot$, but the latter has an extremely large uncertainty of +86.878 −8.192 $R_\odot$. This star is also reported in Petigura et al. (2018) as having 12.3 $R_\odot$, which is more similar to ours, while in Hardegree-Ullman et al. (2020), who obtained radius from Stefan-Boltzmann law using stellar parameters from the LAMOST survey, this star has 24.2 $R_\odot$. Finally, we note that in Gaia DR3 the radius for this star is 29.53 $R_\odot$ and it has a very large error of +28.288 −30.523 $R_\odot$. Another star with a large difference in radius in this comparison is EPIC 220481411, for which we obtain 0.645 ± 0.029 $R_\odot$, while Huber et al. (2016) obtain 6.924 ± 4.716 $R_\odot$. Other results in the literature also find radii in better agreement with our result: Livingston et al. (2018, 0.69 $R_\odot$), Persson et al. (2018, 0.72 $R_\odot$), Mayo et al. (2018, 0.67 $R_\odot$), Petigura et al. (2018, 0.71 $R_\odot$), and Kruse et al. (2019, 0.64 $R_\odot$). EPIC 220481411 is a nearby star with a well-determined parallax from Gaia DR3 of $\pi$=8.69 mas, with a distance of ∼115 pc and, with an apparent V-magnitude of 12.48, the absolute V-magnitude is $M_V$=7.15, placing this star squarely in the realm of the K-dwarfs, where a sub-solar radius is expected, giving confidence to our derived radius.

Concerning the mass comparison, the most significant outlier in Figure 3 is the star EPIC 220503133, for which we find ∼1.90 ± 0.43 $M_\odot$, while the asteroseismic result

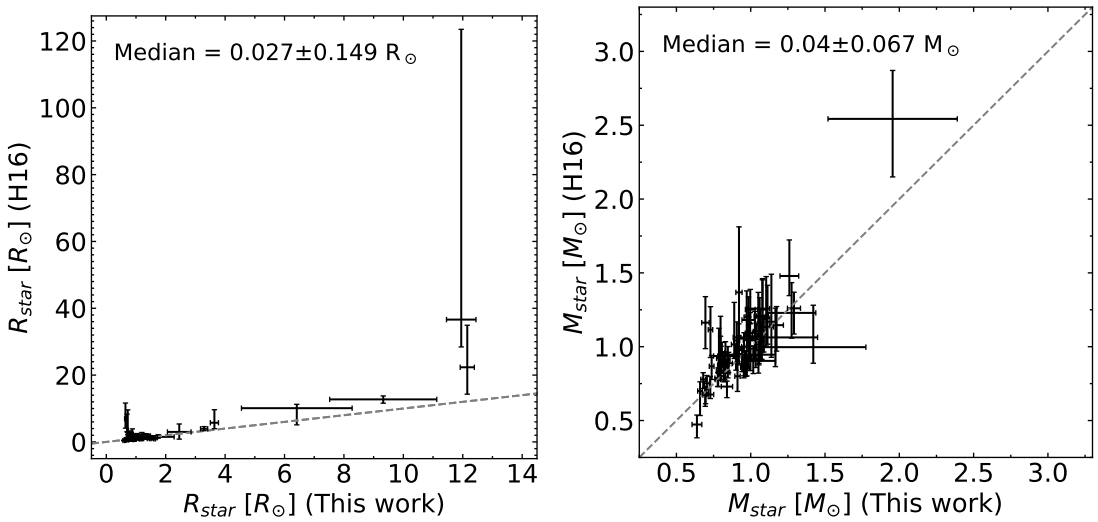


**Figure 3.** Comparisons of the stellar radii and masses in this study with those determined through asteroseismology by Huber et al. (2016, H16). The median differences ('Other Work - This Work') between the parameters and the corresponding MAD are indicated in each case.

from Huber et al. (2016) is $\sim$ 2.50 +0.33 −0.39 $M_\odot$, with results not overlapping within the errorbars.

### 3.2. *Planetary Radii*

The planetary radii were determined using the inferred stellar radii and the transit depth ($\Delta F$), which represents the fraction of stellar flux lost during the planet's transit minimum, given by Seager & Mallén-Ornelas (2003):

$$R_{pl} = 109.1979 \times \sqrt{\Delta F \times 10^{-6}} \times R_{star}, \quad (1)$$

where the planet's radius is given in terms of Earth radii.

For our analysis, we considered only the $\Delta F$ values of confirmed planets. All candidates or false positives, according to the NASA Exoplanet Archive notes, were excluded from our planet sample. The $\Delta F$ values were obtained from Kruse et al. (2019), Barros et al. (2016), Pope et al. (2016), and Christiansen et al. (2017), and these values, along with the planetary radii, are listed in Table 4. The comparison between the radii of exoplanets orbiting K2 host stars determined here and those in Loaiza-Tacuri et al. (2023), Hardegree-Ullman et al. (2020), Kruse et al. (2019), Petigura et al. (2018), and Mayo et al. (2018) is shown in Figure 4. In general, the median differences in planetary radii ("Other Work – This Work") are small, varying between $\sim -0.3$ and $\sim 0$; more specifically corresponding to 6% difference for Kruse et al. (2019), 6.5% for Hardegree-Ullman et al. (2020), 10.4 % for (Petigura et al. 2018), 9.9 % for Mayo et al. (2018), and 1.9 % for Loaiza-Tacuri et al. (2023).

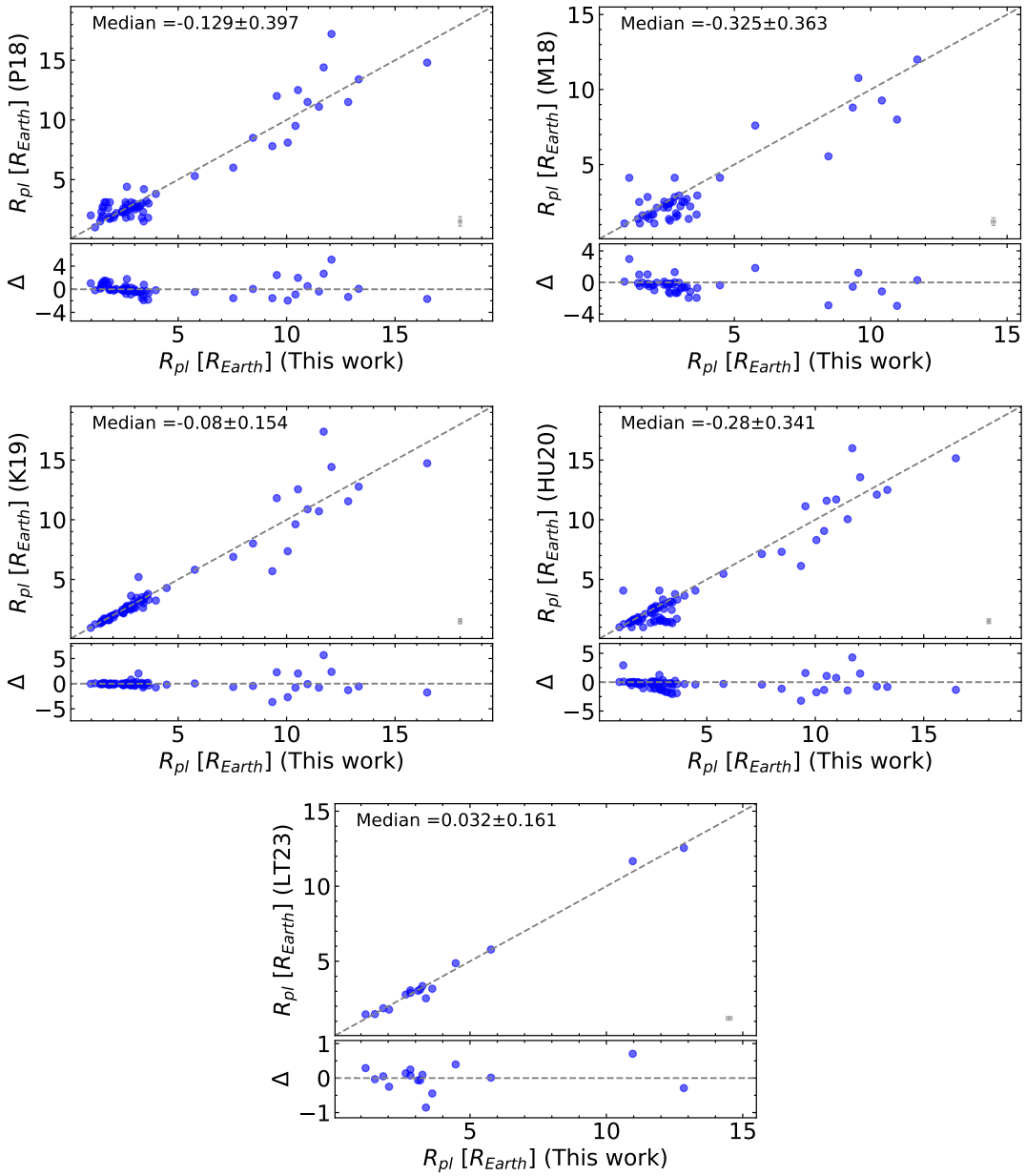


**Figure 4.** Comparisons of the planetary radii in this study with those from Petigura et al. (2018, P18,), Mayo et al. (2018, M18), Kruse et al. (2019, K19), Hardegree-Ullman et al. (2020, HU20), and Loaiza-Tacuri et al. (2023, LT23). The bottom sub-panels show the difference between 'Other Work - This Work' ($\Delta$). The median differences between the parameters and the corresponding MAD are indicated in each case. The black dashed lines represent equality.

### 3.2.1. *Planetary Radii and the Radius Gap*

Figure 5 shows the distribution of planetary radii for our sample of 73 confirmed planets orbiting 50 K2 stars. Not unexpectedly, there is a dearth of planets around $R_{gap} \sim 2\ R_{\oplus}$ for the smaller planets in the sample ($R_{pl} < 4\ R_{\oplus}$). Similarly to what was found in our previous study of K2 targets based on Hydra spectra (Loaiza-Tacuri

**Table 4.** Planetary Radii

| Star ID | Planet Name | $\Delta F$ (ppm) | $R_{pl}$ ($R_\oplus$) | $\delta R_{pl}$ ($R_\oplus$) |
|---|---|---|---|---|
| EPIC211319617 | K2-180 b | 1189.0 | 2.64 | 0.05 |
| EPIC211351816 | K2-97 b | 680.0 | 10.97 | 0.49 |
| EPIC211355342 | K2-181 b | 828.0 | 3.26 | 0.08 |
| EPIC211413752 | K2-268 b | 398.0 | 1.60 | 0.08 |
| EPIC211413752 | K2-268 c | 1239.0 | 2.83 | 0.07 |
| EPIC211413752 | K2-268 d | 531.0 | 1.85 | 0.06 |
| ... | ... | ... | ... | |

Note—Transit depth ($\Delta F$) collected from Kruse et al. (2019), Pope et al. (2016), Barros et al. (2016), and Christiansen et al. (2017) for K2 planets. This table is published in its entirety in the machine readable format. A portion is shown here for guidance regarding its form and content.

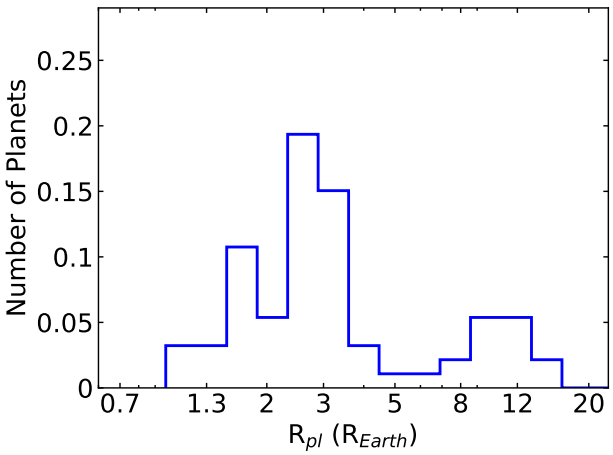


**Figure 5.** The planetary radius distribution for the K2 planet sample. The location of the gap in the planetary radius distributions is approximately at $R_{gap} \sim 2\ R_\oplus$.

et al. 2023) and with a similar number of confirmed planets, our methodology for determining stellar radii and, from them, planetary radii allowed for the identification of the radius gap, also known as the Fulton gap (Fulton et al. 2017). This well known feature has been widely confirmed in various studies using the Kepler sample (Berger et al. 2018; Fulton & Petigura 2018; Van Eylen et al. 2018; Martinez et al. 2019) and the fact that our results depict the gap attests to the high quality and precision achieved by our spectroscopic analysis. The error budget in the derived radii are discussed in the section below.

### 3.3. *Uncertainties in the Derived Parameters*

The formal errors adopted for the stellar parameters $T_{eff}$, log $g$, and $\xi$ were computed using $q^2$, which follows the error analysis discussed in Epstein et al. (2010) and Bensby

**Table 5.** Error budget

| Parameter | Median Uncertainty |
|---|---|
| $T_{eff}$ | 44 K |
| log $g$ | 0.11 dex |
| A(Fe) | 0.03 dex |
| V | 0.03 mag |
| plx | 0.02 mas |
| $M_{star}$ | 0.02 $M_{\odot}$ |
| $R_{star}$ | 2.56 % |
| $\Delta F$ | 2.57 % |
| $R_{pl}$ | 3.35 % |

et al. (2014). Errors in the iron abundances, A(Fe I) and A(Fe II), were obtained by combining errors estimated from the equivalent-width measurements with stellar parameter uncertainties. The individual errors of these parameters are presented in Table 3.

The median errors in the stellar parameters derived in this study are reported in Table 5: $\delta T_{eff}$ = 44 K, $\delta$logg = 0.11 dex, $\delta$A(Fe) = 0.03 dex, and $\delta\xi$ = 0.18 km.s$^{-1}$. Following a similar approach to that employed by Loaiza-Tacuri et al. (2023), we have taken into account the contributions of individual errors in determining the error budget for derived parameters, such as $M_{star}$, $R_{star}$, and $R_{pl}$. It's important to note that the error in the V magnitude contributes about 0.25 % to the error in the stellar radius, assuming a median error of 0.03 mag for the V magnitudes of our stars. In addition, errors in parallaxes, with a median error of 0.02 mas, result in a 0.66 % error in both stellar mass and radius. The uncertainties in stellar radii and transit depth errors ($\Delta F$) have a direct influence on the determination of planetary radius errors. The median internal uncertainty in our derived stellar radius distribution is 4.6 %. For the transit depth values ($\Delta F$) and their associated errors, we adopted data from Kruse et al. (2019), Barros et al. (2016), and Christiansen et al. (2017), resulting in an internal transit depth precision of 2.6 % for the planets in our sample. Ultimately, these combined uncertainties contribute to an internal precision of 3.4 % in the error budget for the radius of the planets ($R_{pl}$). Table 5 summarizes the error budgets for our $R_{star}$ and $R_{pl}$ determinations.

## 4. MEASUREMENTS OF THE CALCIUM H AND K LINES

The Ca II H and K lines are useful diagnostics of chromospheric activity due to the sensitivity of their line cores to chromospheric temperature inversions, which are related to magnetic activity (Leighton 1959). Quantitative Ca II H and K activity levels can be expressed using the S-index, also known as the Mount Wilson index (Vaughan et al. 1978, $S_{MW}$). The S-index is defined as a ratio of fluxes measured in

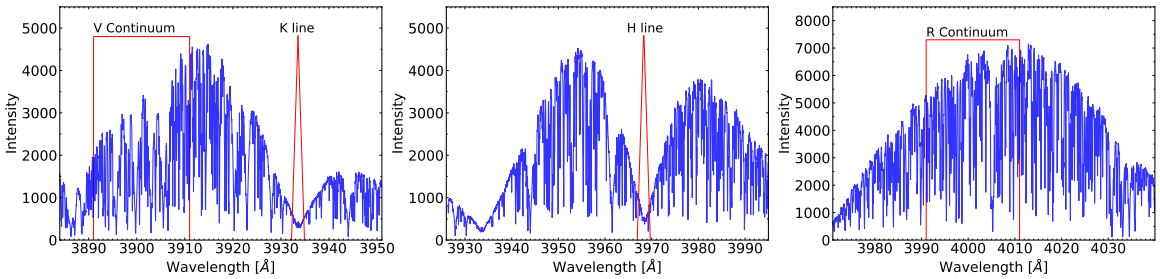


**Figure 6.** Keck HIRES spectra of the star EPIC220383386 showing the three echelle orders containing the calcium H and K lines and pseudo-continuum at V and R.

the H and K line cores and fluxes in nearby pseudo-continuum passbands, which are labeled R and V. In this study these fluxes were measured following the procedure described in Isaacson & Fischer (2010) and using the IRAF[6] task `sbands`. Fluxes in the H and K line cores were measured using a triangular bandpasses (full width at half maximum of 1.09 Å) centered at $\lambda$3968.47 Å and $\lambda$3933.67 Å, respectively, while the pseudo-continuum R and V fluxes were measured using rectangular bandpasses of 20 Å, centered at $\lambda$3901 Å and $\lambda$4001 Å, respectively.

Isaacson & Fischer (2010) provide a defining equation for the $S_{HK}$-index from HIRES spectra of

$$S_{HK} = 32.510\frac{(H + 1.45K)}{(R + 25V)} + 0.021 \quad (2)$$

where the coefficient for V was set in order to bring the mean fluxes in the R and V continuum bandpasses to approximately the same levels. Our use of this equation led to unrealistically small values of $S_{HK}$ for our HIRES spectra. Following the discussion in Isaacson & Fischer (2010), we investigated what V-coefficient would bring the measured R and V mean-fluxes to approximately the same levels in our HIRES spectra (see Figure 6), and found a mean V-coefficient from all spectra of 2.28, with a small scatter. The computation of $S_{HK}$ used a unique V-coefficent for each spectrum such that the R and V mean fluxes were equal.

We measured the $S_{HK}$ index in a total of 725 spectra from 144 K2 stars, noting that for 40 of our targets there were two or more spectra available in the Keck Archive, with the other stars having only one HIRES observation. The measured $S_{HK}$ index for the stars are presented in Table 3, noting that for those stars having more than one observation, the values in the table are the mean (and standard deviation) of the $S_{HK}$ measurements. The $S_{HK}$ indices for our K2 sample will the discussed in Section 5 and validated from comparisons with the literature below.

We opted to place our $S_{HK}$ measurements from archival spectra onto the commonly used Mt. Wilson scale via a comparison for stars in common with the following

[6] Image Reduction and Analysis Facility (IRAF) is distributed by the National Optical Astronomy Observatory, which is operated by the Association of Universities for Research in Astronomy, Inc., under a cooperative agreement with the National Science Foundation.

studies, all of which have transformed their respective $S_{HK}$ values onto the Mt. Wilson scale: Chahal et al. (2023), who used LAMOST spectra, Brown et al. (2022), who used spectra from NARVAL and ESPaDOnS, Gomes da Silva et al. (2021), Mayo et al. (2018), and Isaacson & Fischer (2010) who used spectra from HARPS, TRES, and HIRES, respectively. The comparisons are shown in Figure 7, with the largest number of stars in common being Chahal et al. (2023), where the median of the differences (and MAD) between $S_{HK}$("Chahal - This Work") are $-0.033 \pm 0.052$, respectively. These are small differences and the overall comparisons with Chahal et al. (2023), as well as for the other studies, are good. The solid red line in Figure 7 is the least squares fit of $S_{HK}$(This Work) as a function of $S_{HK}$(Other), while the dashed line is a one-to-one line. The fitted slope of m=1.10 and the intercept of b=0.00 results in differences between the fitted line and the one-to-one line that are so small we chose not to apply any transformation to our $S_{HK}$ measurements. This close correspondence with the Mt. Wilson scale also indicates that the equation given in Isaacson & Fischer (2010), with a V-flux coefficient adjusted to the values for each spectrum, yields values of $S_{HK}$ that are close to the Mt. Wilson system. We note that the star highlighted in parentheses in Figure 7 (EPIC 212069861) is a M0-dwarf, one of the most active stars in our sample. The $S_{HK}$ measurement for this star in this study was derived from a single available Keck HIRES spectrum observed on November 11, 2016. Given the very large difference in the $S_{HK}$ measurements for this star, it is likely that its activity level has varied significantly between the measurements here ($S_{HK} = 2.37$) and in Chahal et al. (2023) ($S_{HK}$=1.43382 $\pm$ 0.06749). This star has not been included in the best fit slope shown in Figure 7.

### 4.1. *Conversion from S-index to* $R'_{HK}$

The equation for the S-index includes terms with flux contributions from both the chromosphere plus the basal photosphere, which are referred to as $R'_{HK}$ and $R_{phot}$, respectively. In order to isolate and measure chromospheric activity in stars with different effective temperatures, it is necessary to subtract the photospheric contribution by considering the dependence of the R and V fluxes on the effective temperature. We adopted the method described in Noyes et al. (1984), taking

$$R'_{HK} = R_{HK} - R_{phot} = 1.34 \times 10^{-4} C_{cf} S_{HK} - R_{phot}, \tag{3}$$

where the photospheric contribution, $R_{phot}$, and the temperature dependent bolometric correction factor, $C_{cf}$, are modeled as polynomial functions of $(B-V)$:

$$logR_{phot} = -4.898 + 1.918(B-V)^2 - 2.893(B-V)^3. \tag{4}$$

Since our sample includes FGK dwarfs and some evolved stars, we applied the bolometric corrections proposed by Rutten (1984), defined for $0.3 \leq (B-V) \leq 1.7$. For main sequence stars, taken as those stars falling below the black dashed line in Figure

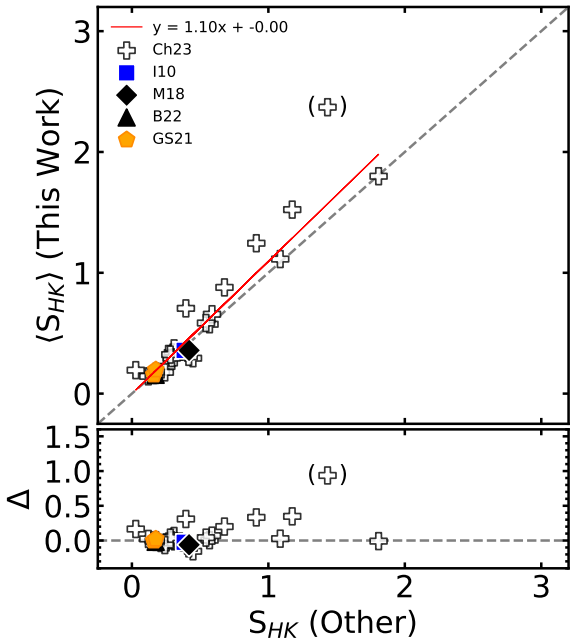


**Figure 7.** Comparison of the derived S-indices for stars in common with other studies in the literature. The crosses correspond to Chahal et al. (2023, Ch23), open circles to Zhang et al. (2022, Z22), triangles to Brown et al. (2022, B22), pentagon to Gomes da Silva et al. (2021, GS21), diamond to Mayo et al. (2018, M18), and square to Isaacson & Fischer (2010, I10). The gray dashed line in the upper panel represents equality, while the red solid line represents the best fit between our results and the literature.

1, we used:

$$logC_{cf} = 0.25(B-V)^3 - 1.33(B-V)^2 + 0.43(B-V) + 0.24, \quad (5)$$

while for evolved stars we used:

$$logC_{cf} = -0.066(B-V)^3 - 0.25(B-V)^2 - 0.49(B-V) + 0.45. \quad (6)$$

Finally, $R'_{HK}$ in Equation 3 depends only on $B-V$, and the applicability of this relations is no longer limited only to late-F to early-K dwarfs. The mean $\log R'_{HK}$ obtained for our sample stars are presented in Table 3.

## 5. DISCUSSION

### 5.1. *Stellar Activity of the Sample K2 Targets*

In Section 4 we discussed the derivation of the $S_{HK}$ index, and in the left panel of Figure 8 we show the distribution of the derived indices for our sample of K2 stars. Most of the K2 targets in this study have $S_{HK} < 0.2$, with the median of the distribution of $S_{HK} = 0.178$ (16th percentile 0.134; 84th percentile = 0.577). There are, however, a few stars in our sample that have $S_{HK} \sim 2-3$, signifying high levels of activity. The range of $S_{HK}$-index values measured in this sample are similar to those presented in the large compilation of Mt. Wilson measurements from Duncan et al.

(1991). In the right panel of Figure 8 we show the $S_{HK}$ index distribution obtained for the star in our sample having the largest number of available HIRES spectra, EPIC 220725186. The $S_{HK}$-index determinations for this star were based on 211 HIRES spectra collected over a period of six years (from July 10 2016 to January 19, 2022). The distribution of the $S_{HK}$ indices for this star is peaked, having a mean $S_{HK}$-index of $0.154 \pm 0.021$ (median of $0.158 \pm 0.009$), which indicates small stellar variability and its mean $S_{HK}$-index is similar to the peak of the $S_{HK}$-index distribution of our K2 sample.

It is useful for our discussion to note the S-index of the Sun within the distribution of $S_{HK}$-index values shown in the left panel of Figure 8. Egeland et al. (2017) used solar observations from both Mt. Wilson and Sacramento Peak to place the Sun on the Mt. Wilson $S_{HK}$-index scale. Over solar cycles 15-24, Egeland et al. (2017) find a mean S-index of $\langle S \rangle = 0.1694 \pm 0.0020$, and at solar minima (the quiet Sun) to be $\langle S_{min} \rangle = 0.1621 \pm 0.0008$. The variations in the S-index over the solar cycle were found to have a mean full amplitude of $\langle \Delta S_{cyc} \rangle = 0.0145 \pm 0.0012$. Lorenzo-Oliveira et al. (2018) used ESO/HARPS spectra to measure the solar S-index from reflected light of solar system objects, in the same Mount-Wilson scale as that used for their sample of solar twins observed through the same spectrograph, and found an average solar activity of $\langle S_{MW} \rangle = 0.17$. Using a correlation between activity and sunspots, they estimated an average S-index for the solar cycles 15 - 24 of $\langle S_{MW} \rangle = 0.1696 \pm 0.0025$, in perfect agreement with the same cycles analyzed by (Egeland et al. 2017). Since most of the stars in our sample have only one, or a few observations, our $S_{HK}$ measurements present a "snapshot" of chromospheric activity over the sample of stars which were caught in random phases over their respective activity cycles and, thus, we are not in a position to discuss individual stellar magnetic cycles nor rotational period coverage. Nonetheless, our results yield a distribution of $S_{HK}$ values sampled at random over a population of FGK stars and we now discuss some characteristics of this sample.

#### 5.1.1. $S_{HK}$ *vs.* $B$-$V$

Figure 9 shows the $S_{HK}$ for the K2 targets measured here as a function of their $(B-V)_0$ color. Both Isaacson & Fischer (2010) and Boro Saikia et al. (2018) observed an increase in the S-index for $B-V$ colors ranging from $\sim 1.0$ to 1.4 in a sample of $\sim 2600$ and $\sim 4400$ main-sequence stars, respectively. The lower envelope increase of $S_{HK}$ with increasing $(B-V)_0$ is due primarily to the decreasing flux in the V and R continuum fluxes in cooler stars relative to the fluxes in the Ca II H and K lines (e.g., Isaacson & Fischer 2010). In this study of 144 K2 stars within the same range in $(B-V)_0$, our results for S-index vs $(B-V)_0$ shown in the figure also exhibit a similar pattern for $(B-V) < 1.4$, as the S-index begins to increase roughly at $(B-V)_0 \sim 0.8$. The general agreement is made clearer in comparison with the orange dashed line in the figure, which represents the polynomial fit, taken from Isaacson & Fischer (2010), and traces the lower envelope of their distribution.

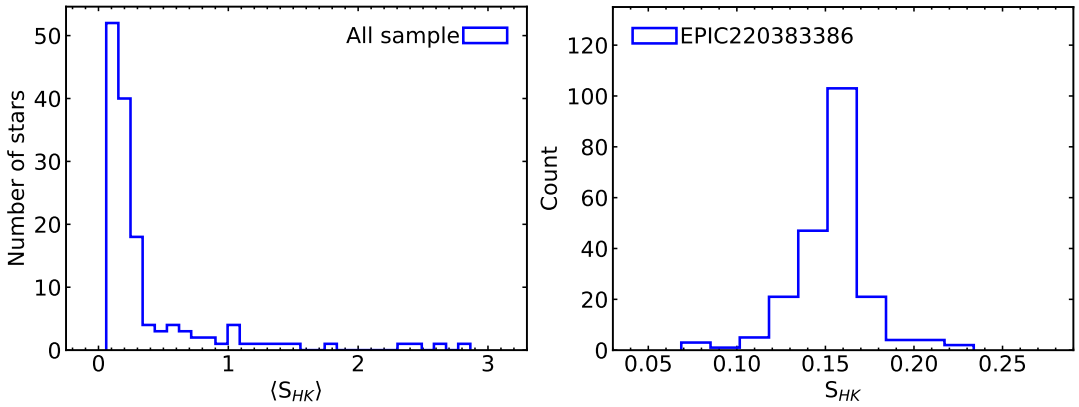


**Figure 8.** Left panel: the distribution of the mean $S_{HK}$ ($\langle S_{HK} \rangle$) obtained for 111 K2 stars in our sample. Right panel: the $S_{HK}$ index distribution for the star EPIC 220383386; this is the star in our sample with the largest number of HIRES spectra available: 211 spectra between July 10, 2016, and January 19, 2022.

In our sample the lower activity limit remains approximately constant for $(B-V)_0$ $\lesssim$0.9, while for redder colors in the range of $0.9 \lesssim (B-V)_0 \lesssim 1.4$, the lower limit of the S-index exhibits a smooth increase, from $S_{HK}$ ∼0.2 at $(B-V)_0 = 0.9$ up to $S_{HK}$ ∼0.8 at $(B-V)_0 = 1.4$, and begins to decrease for $(B-V)_0 \gtrsim 1.4$. Notably, throughout this entire range, the highest levels of activity, or the fraction of active stars, increase sharply towards redder values of $(B-V)_0$ (later spectral types). For colors of $(B-V)_0 < 0.9$ there are only 8 stars out of 30 stars with $S_{HK} > 0.4$ (roughly twice the value of the lower envelope), while in the range of $(B-V)_0 \sim 0.9$ to 1.2 there are 14 stars out of 22 that exhibit $S_{HK}$ values that are more than twice the lower envelope.

### 5.1.2. $R'_{HK}$ *and Stellar Rotation*

As a star evolves it loses angular momentum, resulting in lower stellar rotational velocities, which is accompanied by a decrease in stellar activity (Skumanich 1972). In order to analyze the behavior of the activity index $R'_{HK}$ in relation to $v$ sin $i$ and stellar rotational period, we collected $v$ sin $i$ measurements for our sample stars from the DR17 APOGEE survey (Majewski et al. 2017) and Petigura et al. (2018). The $v$ sin $i$ sample is a mixture of Keck/HIRES spectra, with R ∼ 60,000, and APOGEE spectra, with R ∼ 22,400, providing theoretical lower limits to $v$ sin $i$ detections of roughly $\sim 2-3$ km-s$^{-1}$. The rotational periods for the sample were taken from Reinhold & Hekker (2020), de Leon et al. (2021), and Rampalli et al. (2021), however rotational periods were available for only 44 sample stars. In Figure 10 we plot $v$ sin $i$ versus rotational period for those stars that have both measurements available, using different symbols for stars as a function of their spectral types and also identify the $v$ sin $i$ measurement source as either from APOGEE or Petigura et al. (2018). There is an expected increase in $v$ sin $i$ as the rotational period decreases and the star having

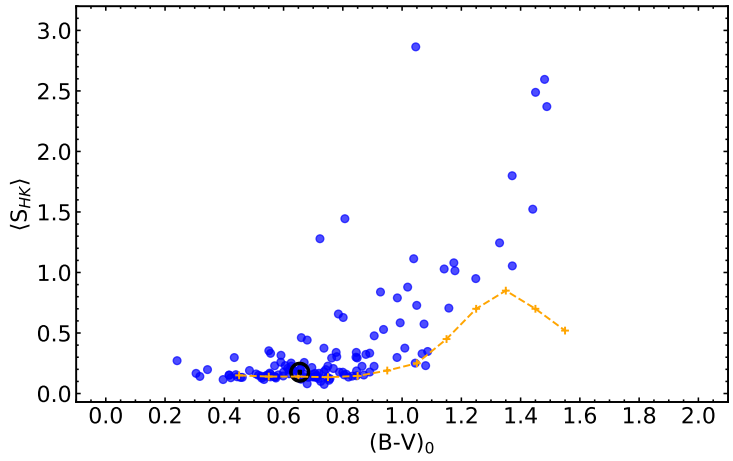


**Figure 9.** Mean $S_{HK}$ indices as a function of the $B-V_0$ color for the main sequence stars in our K2 sample. The solar symbol represents the solar value at $<S_{HK}>$=0.176 (Mamajek & Hillenbrand 2008), lying close to the dashed orange line taken from Isaacson & Fischer (2010).

the highest $v$ sin $i$ in this sample ($v$ sin $i$ = 13.6 km/s) has a measured rotational period of less than 5 days. These independent measurements are self-consistent: a G-dwarf having an approximate radius of 1 $R_\odot$ and a rotational period of ∼4.5 days would have an equatorial rotational velocity of ∼12 km-s$^{-1}$. We can identify a floor in the $v$ sin $i$ at around 2−3 km-s$^{-1}$ which is likely due to the loss in sensitivity given the intrinsic broadening in stellar spectra due to microturbulence and macroturbulence..

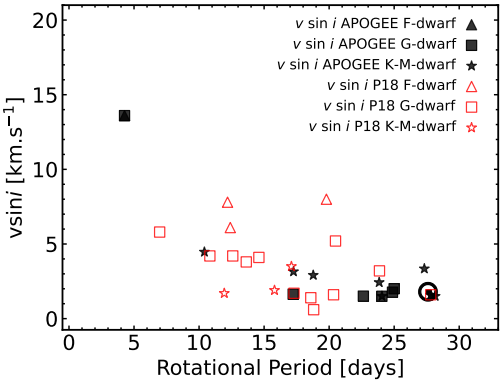


**Figure 10.** Projected rotation velocities ($v$ sin $i$) and measured rotation periods for those stars in our sample having the two measurements available in the literature. The different symbols segregate the stars according to their spectral types.

The top left panel of Figure 11 shows $\langle \log R'_{HK} \rangle$ versus the rotational period for the 44 stars in our sample with measured rotational periods available in the literature, as discussed earlier in this section. The distribution of stars with measured rotational periods for our sample is skewed towards higher levels of activity, with only two stars having $\langle \log R'_{HK} \rangle < -5.10$. This is likely due to more active stars having stellar surface features, such as spots, that can be detected via K2 photometry. Nevertheless,

there is a trend in this sub-sample, as illustrated by the red running median and black running mean lines, in which the distribution of $\langle \log R'_{HK} \rangle$ values remains nearly flat at longer rotational periods (P $\sim 14-30$ days) and then increases for lower rotational periods (higher rotational velocities). Our results agree well with measurements of $\langle \log R'_{HK} \rangle$ versus rotational period for a sample of planet-hosting stars in the Kepler prime field by Morris et al. (2017). As a reference, a period of 12 days for a solar-radius star would have an equatorial rotational velocity of $\sim 4-5$ km-s$^{-1}$.

To further investigate trends between rotation and activity, we derived P/sin $i$ from the $v$ sin $i$ values and these are shown in the top right panel of Figure 11, noting that those stars with measured rotational periods have been excluded from this figure. The stars with very large values of P/sin $i > 80$ days are evolved stars (see Figure 1), with the main sequence stars having P/sin i$\lesssim$40 days, keeping in mind that these periods are upper limits, with typical expected inclination effects of $\sim$0-40% for half of the sample. Unlike the upper left panel of this figure, with measured photometric periods, this sample exhibits the full range of activity levels and with large scatter in log $R'_{HK}$ at a given value of P/sin $i$. Within this scatter, however, both the lower and upper envelopes define increasing log $R'_{HK}$ with decreasing P/sin $i$ and the points from the upper left panel are contained within the high activity region of the envelope. Although there is not a simple relation in the upper panels of Figure 11, the general trend is that stars show more activity for low values of P/sin $i$ with a steep rise in $\langle \log R'_{HK} \rangle$ beginning at approximately $P$ sin $i \sim$ 30–40 days. The stars with P/sin $i$ higher than this threshold all show very low levels of activity at log $R'_{HK} \sim -5.5$. The lack of a simple relation between log $R'_{HK}$ as a function $P_{rot}$ is also found by Böhm-Vitense (2007) in a study of 25 G and K dwarfs which display large scatter in log $R'_{HK}$ at a given rotational period, with the suggestion of two sequences that Böhm-Vitense (2007) labels as active (A) and inactive (I), although some stars are found in-between the two sequences. Similar results are found by Metcalfe & van Saders (2017) in a sample of $\sim$50 FGK dwarfs. The results from both Böhm-Vitense (2007) and Metcalfe & van Saders (2017) overlap closely our results as presented in the top panels of Figure 11, over the rotational period range of $\sim$5-45 days. To better illustrate this comparison, the approximate envelope in log $R'_{HK}$ versus $P_{rot}$ found by Metcalfe & van Saders (2017) in their Figure 2 is outlined by the solid lines in the top right panel of Figure 11, while the dashed lines follow the respective Inactive and Active sequences from Böhm-Vitense (2007) in her Figure 8. These two earlier studies, along with the results presented here, point to a complex interplay between stellar rotational period and chromospheric activity that is likely a function of both stellar mass and age.

The bottom panels of Figure 11 present the literature $v$ sin $i$ measurements along with their corresponding log $R'_{HK}$ values derived in this study, with the left panel showing all stars, while the right panel has an expanded scale showing $v$ sin $i$ values up to 20 km-s$^{-1}$. Given that the $v$ sin $i$ values represent lower limits to the true

rotational velocities, stars with low values of $v$ sin $i$ < 3 km-s$^{-1}$ (the approximate floor in detection limit from Figure 10) are composed of a mixture of slowly rotating stars and rapidly rotating stars that are viewed at small inclination angles. Stars with higher values of $v$ sin $i$ can be considered as bone fide rapid rotators. As shown in the right bottom panel of Figure 11, the stars with $v$ sin $i$ < 3 km-s$^{-1}$, which are a mixture of slow and rapid rotators, exhibit a large range in log $R'_{HK}$ and contain 20 stars having high activity levels of log $R'_{HK} \geq -4.75$, or 14.3% being in the high activity group. As discussed above, it is likely that a fraction of the stars in this sub-sample are fast rotators viewed at small inclination angles. There remain five stars with $v$ sin $i$ >10 km-s$^{-1}$ and this sub-sample rapid rotators contains a larger fraction of 83% (5 out of 6) active stars, with log $R'_{HK} \geq -4.75$, supporting the general result that rapidly rotating stars tend to have higher levels of chromospheric activity.

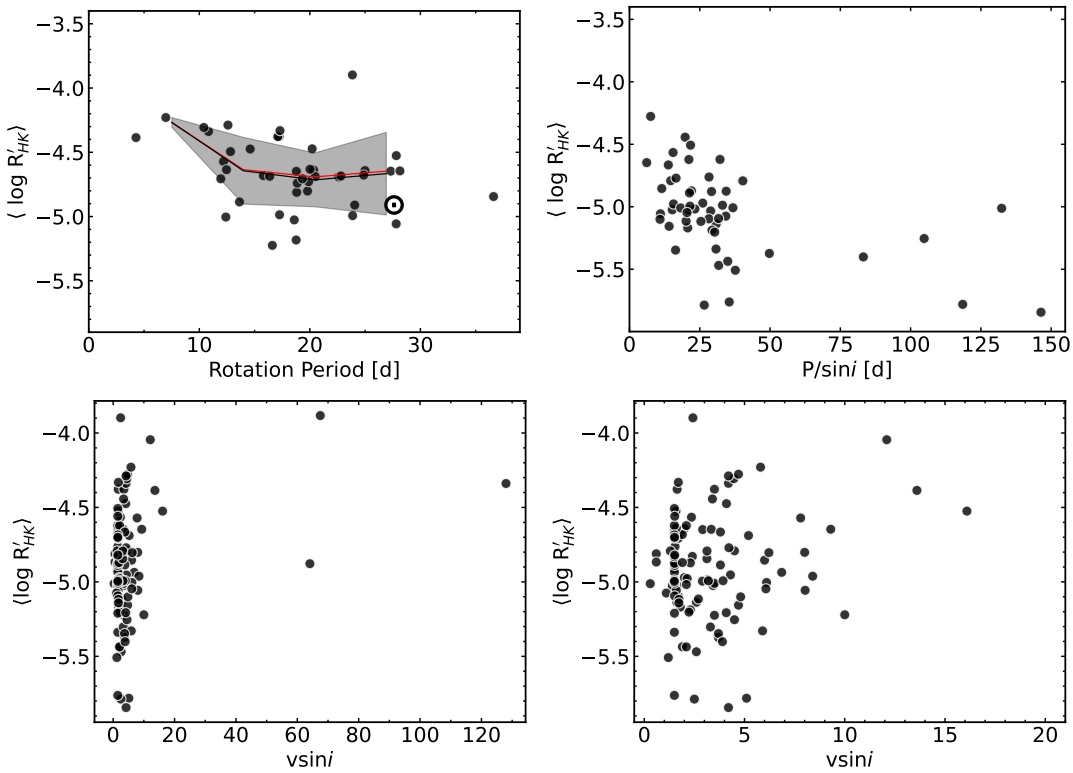


**Figure 11.** Top right panel: Top right panel shows mean log $R'_{HK}$ index as a function of rotational period. The red line represents the running median and the black line the running mean, the gray area is the standard deviation. Bottom panels: mean log $R'_{HK}$ index as a function of rotational projected velocity ($v$ sin $i$).

### 5.1.3. *The Vaughan-Preston gap*

Vaughan & Preston (1980) used the Ca II H and K lines to map chromospheric activity in 486 field stars in the solar neighborhood as part of the Mount Wilson project (Wilson 1968; Duncan et al. 1991; Baliunas et al. 1995). They found that in

this sample there was a lack of F- and G-type stars with intermediate activity levels, which has been labeled the "Vaughan-Preston gap", with this gap spanning a range in $(B-V)_0$ roughly between 0.4 and 1.1 and values of $S_{HK}$ between 0.2 to 0.7. A lack of stars in this regime was later confirmed by Henry et al. (1996) from an analysis of 800 stars observed with the Coude' spectrograph on the 1.5 m Telescope at CTIO and more recently by Gomes da Silva et al. (2021) from analysis of HARPS spectra of 1674 FGK stars. Boro Saikia et al. (2018) also investigated stellar activity in a large sample of cool stars using results collected from various surveys in the literature and concluded that the Vaughan-Preston gap may not be a significant feature.

The top panel of Figure 12 shows the distribution of the mean values of log $R'_{HK}$ for our sample of main sequence stars and reveals a gap, or valley, with a depth of ∼35% of the main peak, at the approximate location of the Vaughan-Preston gap (shown as the vertical lines), with boundaries as defined in Boro Saikia et al. (2018)). This boundary delineates a bimodal distribution around the gap. In the middle panel of the figure we show the log $R'_{HK}$ distribution only for the sub-sample of F and G-type dwarfs, using for this selection a threshold of $T_{eff} > 5000$ K. This distribution is also bi-modal but it is noted that the peak at the side of the gap corresponding to active stars is smaller when compared to the distribution shown in the top panel. The bi-modality of our FG-dwarf distribution is highlighted by the double-Gaussian fit (shown in red) to the histogram of observed values, with Gaussian means of log $R'_{HK} = -5.035$ and $-4.574$, respectively. Gomes da Silva et al. (2021) also noted bimodal distributions in the values of log $R'_{HK}$ for their sample of F and G dwarfs with means close to -4.95 and -4.50 for the inactive and active stars, respectively, which are very close to ours. That study, with a much larger number of stars, found a similar distribution to ours, with a similarly smaller peak on the active side of the gap when compared to the non-active side. Since Gomes da Silva et al. (2021) had a much larger sample than the one we present here, they also carried out three, four, and five component Gaussian fits to their results, finding that three and four component models yield somewhat better fits to their results; our sample is not large enough to support more than a two-component model. Gomes da Silva et al. (2021) also found that the K-dwarfs in their sample had a different distribution of log $R'_{HK}$ than the F and G dwarfs and exhibited three distinct peaks, with no Vaughan-Preston gap. Although our sample is dominated by F and G dwarfs, having only 26 K dwarfs, in the bottom panel of Figure 12 we present the log $R'_{HK}$ distribution of the K dwarfs. Given the small number of stars in this sub-sample it is hard to conclude that we also see three peaks in the distribution of K dwarfs, although the region of the Vaughan-Preston gap shows a reduced number of stars with the obvious caveat that we have very few K-dwarfs in our sample. One feature of the distribution of these stars is that they all have log $R'_{HK} > -5$, none of them belonging to the "inactive stars" category.

#### 5.1.4. *The Impact of Including Activity Sensitive Lines in the Analysis*

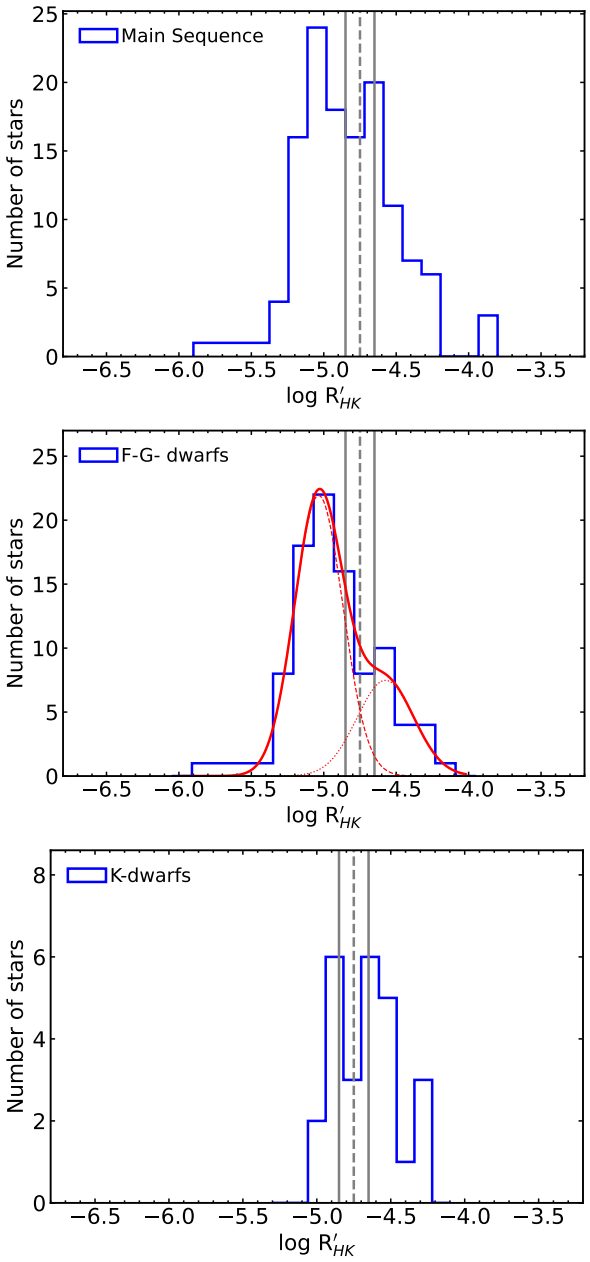


**Figure 12.** Top panel: the distribution of log $R'_{HK}$ for the main sequence stars in our K2 sample. Middle panel: the distribution of log $R'_{HK}$ for the F-G- type dwarfs in our sample. The red solid curve is the double-Gaussian fit to the distribution with means of log $R'_{HK} = -5.035$ and $-4.574$. Bottom panel: the distribution of log $R'_{HK}$ for the K-type dwarfs in our sample.The region of the Vaughn-Preston gap is marked by the gray solid lines in all panels.

In Section 3 we described our derivation of stellar parameters that is based upon Fe I and Fe II lines and which relied only on lines deemed to be insensitive to stellar magnetic activity, as described in Yana Galarza et al. (2019). In this section we investigate possible differences between the stellar parameters derived without using activity-sensitive Fe lines (see Section 3) when compared to those derived with the

inclusion of a significant number of activity-sensitive Fe lines and check whether any differences in $\Delta T_{eff}$, $\Delta$[Fe/H], or $\Delta\xi$ correlate with log $R'_{HK}$. A number of recent studies using high-resolution spectra (R $\sim$ 115,000), such as those by Flores et al. (2016), Lorenzo-Oliveira et al. (2018), Yana Galarza et al. (2019), and Spina et al. (2020), have shown that stellar magnetic activity can affect determinations of $T_{eff}$, $\xi$, and [Fe/H] that are based upon an analysis using Fe I and Fe II lines. Figures 3 and 4 in Spina et al. (2020) show that there can be an enhancement in the strengths of certain magnetically sensitive Fe I lines in stars with log $R'_{HK} > -5.0$. As reported by Spina et al. (2020), the presence of stellar activity may lead to differences in the derived effective temperature, metallicity, and microturbulent velocity, but with no significant variations in the surface gravity determinations. In particular, they found a decrease in the effective temperatures for stars with log $R'_{HK} > -4.6$, while a decrease in [Fe/H] values begins at log $R'_{HK} \sim -5.0$, along with an increase in the microturbulent velocity. In addition, Yana Galarza et al. (2019) analyzed several observations of the solar twin star HIP 36515 and showed that the difference in the derived parameters computed with and without activity-sensitive lines varies depending on the phase of the stellar activity cycle. Here we will investigate the impact in the stellar parameter determinations from inclusion of an additional 49 Fe I lines and 2 Fe II lines that were found to be sensitive to stellar activity.

As shown in Figure 13 there are systematic differences between the results in the sense that the effective temperatures and metallicities derived including activity sensitive Fe lines are overall larger than those derived without sensitive lines. The mean differences ("non sensitive − sensitive") and standard deviations are: $-42 \pm 52$ K, $-0.028 \pm 0.043$, and $0.066 \pm 0.262$ km.s$^{-1}$ for $T_{eff}$, metallicity, and microturbulent velocity, respectively. However, these are small differences which are of the order of the uncertainties in the derived parameters (see Table 5), which leads us to conclude that, based on the sample of Fe I and Fe II lines used here, there is no evidence (beyond the uncertainties) of a clear correlation between $\Delta T_{eff}$, $\Delta$[Fe/H] and $\Delta\xi$ with log $R'_{HK}$. Furthermore, if we segregate this sample into 3 regimes in terms of stellar activity (from Henry et al. 1996) we find that the mean $T_{eff}$, [Fe/H] and $\xi$ differences for the sub-samples of very inactive, inactive, and active stars are respectively $-43$ K, $-0.026$ dex, 0.040 km.s$^{-1}$; $-38$ K, $-0.034$ dex, 0.088 km.s$^{-1}$; and $-44$ K, $-0.019$ dex, 0.022 km.s$^{-1}$, again not showing a clear signature with log $R'_{HK}$. The only signature to note is that the spread in $\Delta T_{eff}$ and $\Delta$[Fe/H] increases for log $R'_{HK} >\sim -5$. The 8 stars with the largest differences in $T_{eff}$ ($>\sim$110 K) all have log $R'_{HK}$ larger than $\sim -5.1$. This is also the case for the metallicity results shown in the middle panel of Figure 13: those stars with the largest variations in metallicity have log $R'_{HK}$ larger than $\sim -5$. In summary, very inactive stars display smaller spreads in $\Delta T_{eff}$ and $\Delta$[Fe/H] when compared to the more active stars.

## 6. SUMMARY AND CONCLUSIONS

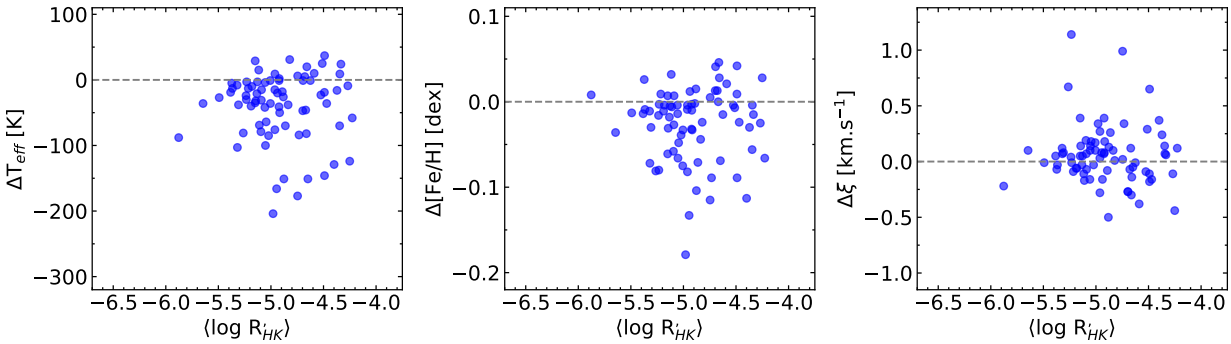


**Figure 13.** Differences ($\Delta$) between effective temperatures, metallicities and microturbulent velocities determined without including Fe lines which are sensitive to activity (This study) and those determined including a significant number of activity sensitive Fe lines, as a function the mean activity index log $R'_{HK}$ measured for the stars.

The results presented here were obtained through a spectroscopic analysis of a uniform set of high-resolution Keck I/HIRES spectra using a list of Fe I and Fe II lines, which yielded the fundamental stellar parameters of $T_{eff}$, log g, $\xi$, and [Fe/H], as well as stellar radii. The analysis employed the spectroscopic analysis code $q^2$ (Ramírez et al. 2014), which derives stellar parameters semi-automatically. The sample includes 86 K2 stars, of which 50 have confirmed planets; the derived values of stellar radii were used to determine planetary radii. The Fe I and Fe II lines used in the analysis were from Yana Galarza et al. (2019) and consists of some lines that are sensitive to magnetic fields, as well as some lines that are insensitive. Main results are summarized below.

• Our stellar radii were combined with transit depths to calculate planetary radii for 73 confirmed planets orbiting 50 K2 stars. Most of transit depths were obtained from Kruse et al. (2019), with additional transit depths from Barros et al. (2016), Pope et al. (2016), and Christiansen et al. (2017). The internal precision of the planetary radii achieved here was 3.4 % and the radius gap is detected in this sample of K2 planets, located at $R_{pl} \sim 1.9\ R_{\oplus}$.

• Stellar activity using the $S_{HK}$ index, which is defined by the fluxes of the Ca II H and K lines, was measured for 144 stars using spectra obtained from ExoFop and the KOA. The values of $S_{HK}$ were derived using the equation in Isaacson & Fischer (2010), with a V-flux coefficient fit to values obtained for each spectrum, and were found to fall closely on the Mt. Wilson scale. Our derived values of $S_{HK}$ as a function of $(B-V)_0$ follow the same trends as shown in Isaacson & Fischer (2010) and Boro Saikia et al. (2018). Photospheric contributions to $S_{HK}$ were subtracted to obtain values of log $R'_{HK}$ by using bolometric corrections from Rutten (1984) for main sequence and evolved stars.

• Our results for $\langle \log R'_{HK} \rangle$ as a function of rotational period for the K2 sample indicate that although activity, in general, decreases with increasing rotational period, there is a large scatter in the activity level for a given rotational period of ∼0.5 dex

in log $R'_{HK}$; such a result has been noted previously, e.g., Böhm-Vitense (2007) and Metcalfe & van Saders (2017), and points to a complex behavior in stellar activity that is related possibly to Rossby number (Metcalfe & van Saders 2017).

• In a previous study of chromospheric activity in a sample of solar-type stars, Vaughan & Preston (1980) found a lack of F- and G-type stars with a intermediate activity levels, now called the"Vaughan-Preston gap". This gap was confirmed by Henry et al. (1996) and Gomes da Silva et al. (2021) using a large sample of stars. Although we studied a much smaller sample of stars, our distribution of the mean values of log $R'_{HK}$ also reveal the presence of the Vaughan-Preston gap.

• The possible impact of stellar activity on the derivation of the stellar parameters $T_{eff}$, [Fe/H], and $\xi$ (surface gravity is not expected to be sensitive to stellar activity) was investigated by including magnetically sensitive Fe I lines in a separate spectroscopic analysis. We found systematic offsets between the two analyses with mean differences of "non sensitive – sensitive" of $\Delta T_{eff} = -42 \pm 52$ K, $\Delta$[Fe/H] $= -0.03 \pm 0.04$, and $\Delta\xi = +0.07 \pm 0.26$ km-s$^{-1}$. Although these systematic offsets are not significant and within the expected uncertainties, we note that the more active stars, with log $R'_{HK} > -5.0$, exhibit larger scatter in their distributions of $\Delta T_{eff}$ and $\Delta$[Fe/H] when compared to the quiet stars.

V. L-T. acknowledges the financial support from Coordenação de Aperfeiçoamento de Pessoal de Nível Superior (CAPES). This research has made use of the NASA Exoplanet Archive, which is operated by the California Institute of Technology, under contract with NASA under the Exoplanet Exploration Program.

## REFERENCES

Asplund, M., Amarsi, A. M., & Grevesse, N. 2021, A&A, 653, A141, doi: 10.1051/0004-6361/202140445

Baliunas, S. L., Donahue, R. A., Soon, W. H., et al. 1995, ApJ, 438, 269, doi: 10.1086/175072

Barros, S. C. C., Demangeon, O., & Deleuil, M. 2016, A&A, 594, A100, doi: 10.1051/0004-6361/201628902

Bensby, T., Feltzing, S., & Oey, M. S. 2014, A&A, 562, A71, doi: 10.1051/0004-6361/201322631

Berger, T. A., Huber, D., Gaidos, E., & van Saders, J. L. 2018, ApJ, 866, 99, doi: 10.3847/1538-4357/aada83

Böhm-Vitense, E. 2007, ApJ, 657, 486, doi: 10.1086/510482

Boro Saikia, S., Marvin, C. J., Jeffers, S. V., et al. 2018, A&A, 616, A108, doi: 10.1051/0004-6361/201629518

Borucki, W. J. 2016, Reports on Progress in Physics, 79, 036901, doi: 10.1088/0034-4885/79/3/036901

Borucki, W. J., Koch, D., Basri, G., et al. 2010, Science, 327, 977, doi: 10.1126/science.1185402

Brown, E. L., Jeffers, S. V., Marsden, S. C., et al. 2022, MNRAS, 514, 4300, doi: 10.1093/mnras/stac1291

Buder, S., Sharma, S., Kos, J., et al. 2021, MNRAS, 506, 150, doi: 10.1093/mnras/stab1242

Castelli, F., & Kurucz, R. L. 2003, in IAU Symposium, Vol. 210, Modelling of Stellar Atmospheres, ed. N. Piskunov, W. W. Weiss, & D. F. Gray, A20. https://arxiv.org/abs/astro-ph/0405087

Chahal, D., Kamath, D., de Grijs, R., Ventura, P., & Chen, X. 2023, MNRAS, 525, 4026, doi: 10.1093/mnras/stad2521

Christiansen, J. L., Vanderburg, A., Burt, J., et al. 2017, AJ, 154, 122, doi: 10.3847/1538-3881/aa832d

Ciardi, D. R., von Braun, K., Bryden, G., et al. 2011, AJ, 141, 108, doi: 10.1088/0004-6256/141/4/108

Cui, X.-Q., Zhao, Y.-H., Chu, Y.-Q., et al. 2012, Research in Astronomy and Astrophysics, 12, 1197, doi: 10.1088/1674-4527/12/9/003

de Leon, J. P., Livingston, J., Endl, M., et al. 2021, MNRAS, 508, 195, doi: 10.1093/mnras/stab2305

Deleuil, M., Barge, P., Defay, C., et al. 2000, in Astronomical Society of the Pacific Conference Series, Vol. 219, Disks, Planetesimals, and Planets, ed. G. Garzón, C. Eiroa, D. de Winter, & T. J. Mahoney, 656

Deleuil, M., Aigrain, S., Moutou, C., et al. 2018, A&A, 619, A97, doi: 10.1051/0004-6361/201731068

Demarque, P., Woo, J.-H., Kim, Y.-C., & Yi, S. K. 2004, ApJS, 155, 667, doi: 10.1086/424966

Duncan, D. K., Vaughan, A. H., Wilson, O. C., et al. 1991, ApJS, 76, 383, doi: 10.1086/191572

Egeland, R., Soon, W., Baliunas, S., et al. 2017, ApJ, 835, 25, doi: 10.3847/1538-4357/835/1/25

Epstein, C. R., Johnson, J. A., Dong, S., et al. 2010, ApJ, 709, 447, doi: 10.1088/0004-637X/709/1/447

Fischer, D. A., & Valenti, J. 2005, ApJ, 622, 1102, doi: 10.1086/428383

Flores, M., González, J. F., Jaque Arancibia, M., Buccino, A., & Saffe, C. 2016, A&A, 589, A135, doi: 10.1051/0004-6361/201628145
Fulton, B. J., & Petigura, E. A. 2018, AJ, 156, 264, doi: 10.3847/1538-3881/aae828
Fulton, B. J., Petigura, E. A., Howard, A. W., et al. 2017, AJ, 154, 109, doi: 10.3847/1538-3881/aa80eb
Gaia Collaboration, Prusti, T., de Bruijne, J. H. J., et al. 2016, A&A, 595, A1, doi: 10.1051/0004-6361/201629272
Gaia Collaboration, Brown, A. G. A., Vallenari, A., et al. 2021, A&A, 649, A1, doi: 10.1051/0004-6361/202039657
Gaia Collaboration, Vallenari, A., Brown, A. G. A., et al. 2023, A&A, 674, A1, doi: 10.1051/0004-6361/202243940
Ghezzi, L., Montet, B. T., & Johnson, J. A. 2018, ApJ, 860, 109, doi: 10.3847/1538-4357/aac37c
Gomes da Silva, J., Santos, N. C., Adibekyan, V., et al. 2021, A&A, 646, A77, doi: 10.1051/0004-6361/202039765
Gonzalez, G. 1997, MNRAS, 285, 403, doi: 10.1093/mnras/285.2.403
Han, H., Wang, S., Bai, Y., et al. 2023, ApJS, 264, 12, doi: 10.3847/1538-4365/ac9eac
Han, S. I., Kim, Y. C., Lee, Y. W., et al. 2009, in Globular Clusters - Guides to Galaxies, ed. T. Richtler & S. Larsen, 33, doi: 10.1007/978-3-540-76961-3_9
Hardegree-Ullman, K. K., Zink, J. K., Christiansen, J. L., et al. 2020, ApJS, 247, 28, doi: 10.3847/1538-4365/ab7230
Henry, T. J., Soderblom, D. R., Donahue, R. A., & Baliunas, S. L. 1996, AJ, 111, 439, doi: 10.1086/117796
Howell, S. B., Sobeck, C., Haas, M., et al. 2014, PASP, 126, 398, doi: 10.1086/676406
Huber, D., Bryson, S. T., Haas, M. R., et al. 2016, ApJS, 224, 2, doi: 10.3847/0067-0049/224/1/2
Ida, S., & Lin, D. N. C. 2004a, ApJ, 604, 388, doi: 10.1086/381724
—. 2004b, ApJ, 616, 567, doi: 10.1086/424830
—. 2005, ApJ, 626, 1045, doi: 10.1086/429953
Isaacson, H., & Fischer, D. 2010, ApJ, 725, 875, doi: 10.1088/0004-637X/725/1/875
Koch, D. G., Borucki, W. J., Basri, G., et al. 2010, ApJL, 713, L79, doi: 10.1088/2041-8205/713/2/L79
Kruse, E., Agol, E., Luger, R., & Foreman-Mackey, D. 2019, ApJS, 244, 11, doi: 10.3847/1538-4365/ab346b
Leighton, R. B. 1959, ApJ, 130, 366, doi: 10.1086/146727
Livingston, J. H., Crossfield, I. J. M., Petigura, E. A., et al. 2018, AJ, 156, 277, doi: 10.3847/1538-3881/aae778
Loaiza-Tacuri, V., Cunha, K., Smith, V. V., et al. 2023, ApJ, 946, 61, doi: 10.3847/1538-4357/acb137
Lorenzo-Oliveira, D., Freitas, F. C., Meléndez, J., et al. 2018, A&A, 619, A73, doi: 10.1051/0004-6361/201629294
Majewski, S. R., Schiavon, R. P., Frinchaboy, P. M., et al. 2017, AJ, 154, 94, doi: 10.3847/1538-3881/aa784d
Mamajek, E. E., & Hillenbrand, L. A. 2008, ApJ, 687, 1264, doi: 10.1086/591785
Martinez, C. F., Cunha, K., Ghezzi, L., & Smith, V. V. 2019, ApJ, 875, 29, doi: 10.3847/1538-4357/ab0d93
Mayo, A. W., Vanderburg, A., Latham, D. W., et al. 2018, AJ, 155, 136, doi: 10.3847/1538-3881/aaadff
Meléndez, J., Ramírez, I., Karakas, A. a. I., et al. 2014, ApJ, 791, 14, doi: 10.1088/0004-637X/791/1/14
Metcalfe, T. S., & van Saders, J. 2017, SoPh, 292, 126, doi: 10.1007/s11207-017-1157-5
Mordasini, C., Alibert, Y., Benz, W., Klahr, H., & Henning, T. 2012, A&A, 541, A97, doi: 10.1051/0004-6361/201117350
Mordasini, C., Mollière, P., Dittkrist, K. M., Jin, S., & Alibert, Y. 2015, International Journal of Astrobiology, 14, 201, doi: 10.1017/S1473550414000263

Morris, B. M., Hawley, S. L., Hebb, L., et al. 2017, ApJ, 848, 58, doi: 10.3847/1538-4357/aa8cca

Nayakshin, S. 2010, MNRAS, 408, L36, doi: 10.1111/j.1745-3933.2010.00923.x

Noyes, R. W., Hartmann, L. W., Baliunas, S. L., Duncan, D. K., & Vaughan, A. H. 1984, ApJ, 279, 763, doi: 10.1086/161945

Owen, J. E., & Murray-Clay, R. 2018, MNRAS, 480, 2206, doi: 10.1093/mnras/sty1943

Persson, C. M., Fridlund, M., Barragán, O., et al. 2018, A&A, 618, A33, doi: 10.1051/0004-6361/201832867

Petigura, E. A., Crossfield, I. J. M., Isaacson, H., et al. 2018, AJ, 155, 21, doi: 10.3847/1538-3881/aa9b83

Pope, B. J. S., Parviainen, H., & Aigrain, S. 2016, MNRAS, 461, 3399, doi: 10.1093/mnras/stw1373

Ramírez, I., Allende Prieto, C., & Lambert, D. L. 2013, ApJ, 764, 78, doi: 10.1088/0004-637X/764/1/78

Ramírez, I., Meléndez, J., Bean, J., et al. 2014, A&A, 572, A48, doi: 10.1051/0004-6361/201424244

Rampalli, R., Agüeros, M. A., Curtis, J. L., et al. 2021, ApJ, 921, 167, doi: 10.3847/1538-4357/ac0c1e

Reinhold, T., & Hekker, S. 2020, A&A, 635, A43, doi: 10.1051/0004-6361/201936887

Rutten, R. G. M. 1984, A&A, 130, 353

Schlafly, E. F., & Finkbeiner, D. P. 2011, The Astrophysical Journal, 737, 103, doi: 10.1088/0004-637X/737/2/103

Seager, S., & Mallén-Ornelas, G. 2003, ApJ, 585, 1038, doi: 10.1086/346105

Skumanich, A. 1972, ApJ, 171, 565, doi: 10.1086/151310

Skumanich, A., Smythe, C., & Frazier, E. N. 1975, ApJ, 200, 747, doi: 10.1086/153846

Sneden, C. A. 1973, PhD thesis, THE UNIVERSITY OF TEXAS AT AUSTIN.

Sousa, S. G., Santos, N. C., Adibekyan, V., Delgado-Mena, E., & Israelian, G. 2015, A&A, 577, A67, doi: 10.1051/0004-6361/201425463

Spina, L., Nordlander, T., Casey, A. R., et al. 2020, ApJ, 895, 52, doi: 10.3847/1538-4357/ab8bd7

Van Eylen, V., Agentoft, C., Lundkvist, M. S., et al. 2018, MNRAS, 479, 4786, doi: 10.1093/mnras/sty1783

Vaughan, A. H., & Preston, G. W. 1980, PASP, 92, 385, doi: 10.1086/130683

Vaughan, A. H., Preston, G. W., & Wilson, O. C. 1978, PASP, 90, 267, doi: 10.1086/130324

Venturini, J., Guilera, O. M., Haldemann, J., Ronco, M. P., & Mordasini, C. 2020, A&A, 643, L1, doi: 10.1051/0004-6361/202039141

Vogt, S. S., Allen, S. L., Bigelow, B. C., et al. 1994, in Proc. SPIE, Vol. 2198, Instrumentation in Astronomy VIII, ed. D. L. Crawford & E. R. Craine, 362, doi: 10.1117/12.176725

Wilson, O. C. 1968, ApJ, 153, 221, doi: 10.1086/149652

Yana Galarza, J., Meléndez, J., Lorenzo-Oliveira, D., et al. 2019, MNRAS, 490, L86, doi: 10.1093/mnrasl/slz153

Yi, S., Demarque, P., Kim, Y.-C., et al. 2001, ApJS, 136, 417, doi: 10.1086/321795

Yi, S. K., Kim, Y.-C., & Demarque, P. 2003, ApJS, 144, 259, doi: 10.1086/345101

Zhang, W., Zhang, J., He, H., et al. 2022, ApJS, 263, 12, doi: 10.3847/1538-4365/ac9406

## 3.1 Comparações com Resultados Prévios da Literatura

### 3.1.1 Temperaturas Efetivas e Gravidades Superficiais

Nesta seção apresentamos comparações entre os parâmetros estelares determinados nesta tese com aqueles obtidos por meio de síntese espectral nos trabalhos de PETIGURA *et al.* (2018a) e MAYO *et al.* (2018), utilizando espectros ópticos obtidos com os espectrógrafos HIRES e TRES, respectivamente. Além disso, comparamos nossos resultados com dados de levantamentos espectroscópicos, como os resultados de espectros ópticos de alvos do projeto K2 obtidos pelo programa K2-HERMES (CLARK *et al.*, 2022; SHARMA *et al.*, 2019; WITTENMYER *et al.*, 2018), como parte do levantamento *Galactic Archaeology with HERMES* (BUDER *et al.*, 2021, GALAH), o levantamento de baixa resolução LAMOST (CUI *et al.*, 2012), e o levantamento de alta resolução espectroscópica no infravermelho próximo APOGEE (ABDURRO'UF *et al.*, 2022; MAJEWSKI *et al.*, 2017; WILSON *et al.*, 2018). Também comparamos nossos resultados com os do levantamento Gaia (GAIA COLLABORATION *et al.*, 2016, 2023), obtidos fotometricamente e a partir de espectros de baixa resolução com o espectrógrafo RVS.

As comparações das temperaturas efetivas obtidas nesta tese com os estudos mencionados acima são mostradas nos diferentes painéis da Figura 3.1; para cada caso, as diferenças medianas "Outros Estudos" - "Este Estudo" são fornecidas no canto superior esquerdo de cada painel, junto com o correspondente desvio absoluto mediano (MAD, da sigla em inglês "*median absolute deviation*"). Na Figura 3.2 apresentamos comparações com os mesmos estudos da literatura, porém, vale ressaltar que neste caso as temperaturas efetivas que apresentamos foram determinadas usando uma outra lista de linhas adicionando as linhas de ferro sensíveis à atividade estelar. No geral, observamos uma boa concordância entre nossas temperaturas efetivas e aquelas de MAYO *et al.* (2018) e PETIGURA *et al.* (2018a), APOGEE e GALAH com base nas medianas e MAD na Figura 3.1. Enquanto para Gaia e LAMOST, as medianas e MADs são $-59 \pm 115$ e $-63 \pm 91$ K, respectivamente. Uma situação semelhante é mostrada na Figura 3.2, mas as medianas para MAYO *et al.* (2018) e PETIGURA *et al.* (2018a) aumentam, enquanto as medianas para APOGEE, GALAH, LAMOST e Gaia diminuem.

As comparações de nossas gravidades superficiais, determinadas nesta tese com aquelas dos trabalhos discutidos acima são apresentadas na Figura 3.3. As diferenças medianas das gravidades superficiais ("Outros Estudos" - "Este Estudo") $\pm$ MAD são fornecidas em cada painel. As medianas indicam não haver diferenças sistemáticas significativas entre os resultados, já que em todos os casos a mediana das diferenças é menor que 0,15, enquanto que os valores de MAD ficam todos abaixo de 0,18 dex. Conforme para a temperatura efetiva, também apresentamos comparações para valores de log $g$ calculados

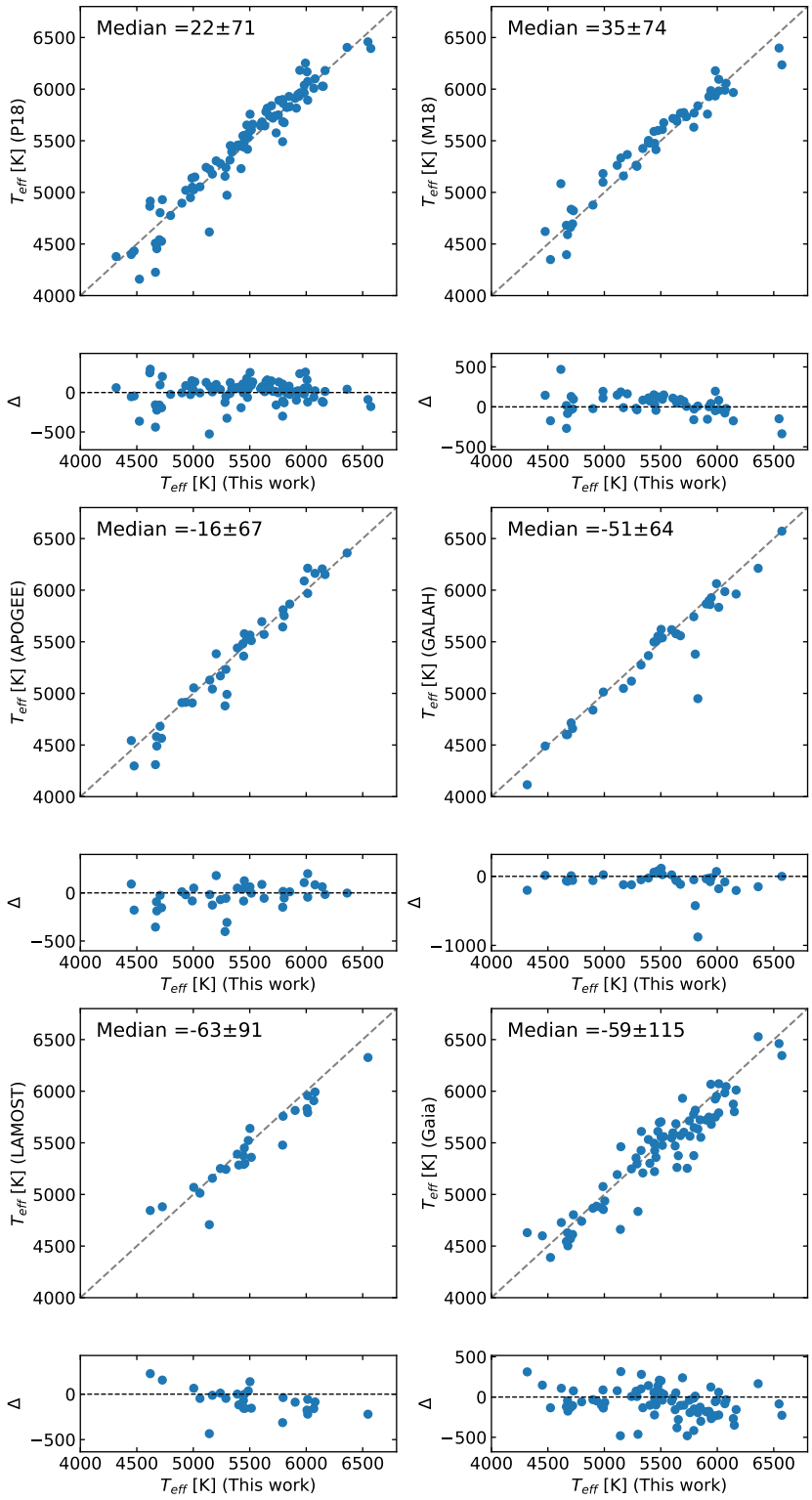


**Figura 3.1** – Comparações das temperaturas efetivas determinadas neste estudo, considerando as linhas de ferro não sensíveis à atividade estelar, com aquelas de PETIGURA *et al.* (2018a), MAYO *et al.* (M18, 2018), e dos levantamentos APOGEE DR17, GALAH DR3 e LAMOST DR8. Os sub-painéis inferiores mostram a diferença entre "Outros Estudos - Este Estudo" (Δ). As diferenças medianas entre os parâmetros e os correspondentes desvios absolutos medianos (MAD) são indicados em cada caso. As linhas tracejadas pretas representam a igualdade.

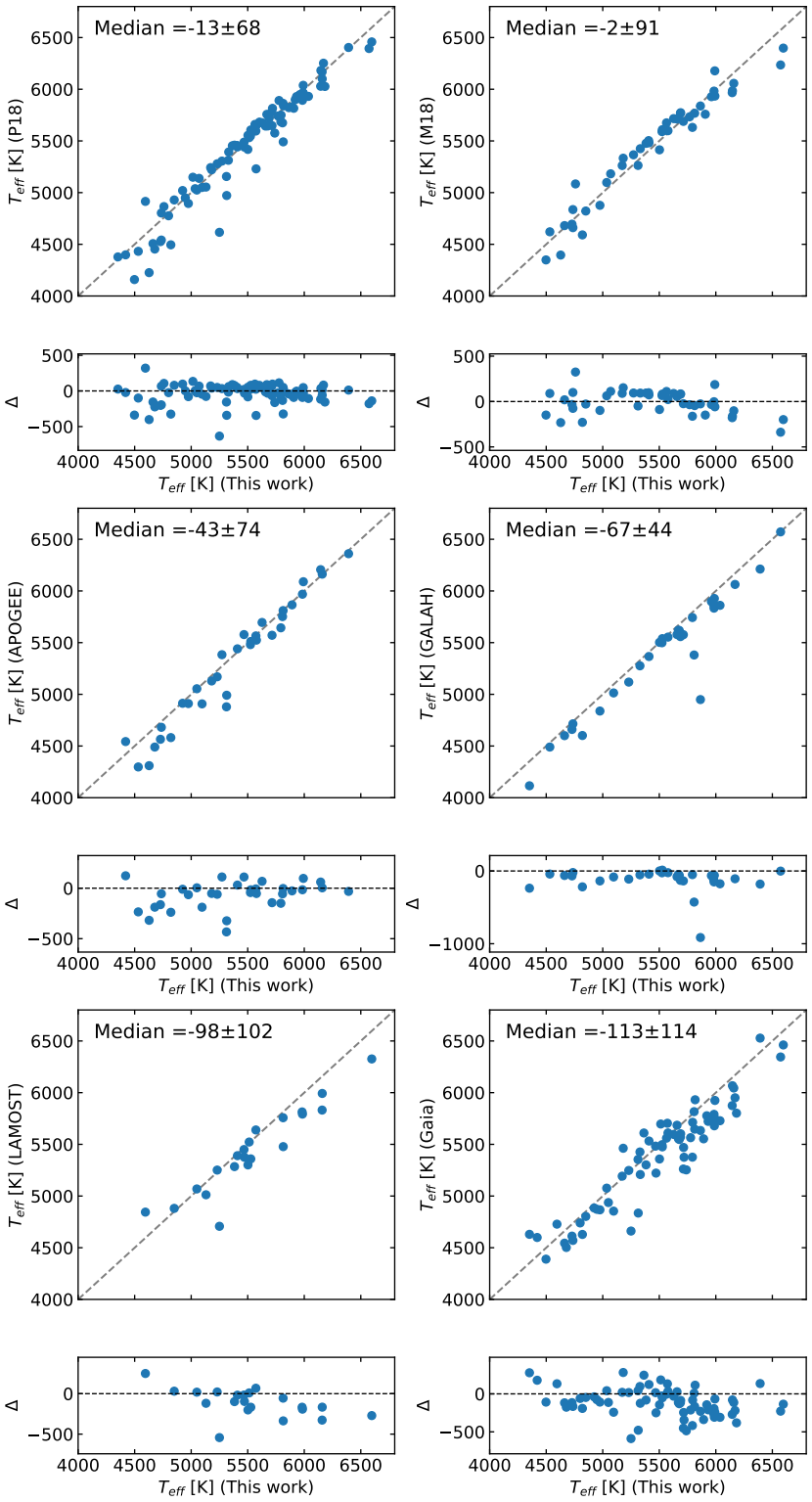


**Figura 3.2** – Comparações das temperaturas efetivas determinadas neste estudo adicionando as linhas de ferro sensíveis à atividade estelar com aquelas de PETIGURA *et al.* (2018a), MAYO *et al.* (M18, 2018), e dos levantamentos APOGEE DR17, GALAH DR3 e LAMOST DR8. Os sub-painéis inferiores mostram a diferença entre "Outros Estudos - Este Estudo" (Δ). As diferenças medianas entre os parâmetros e os correspondentes desvios absolutos medianos (MAD) são indicadas em cada caso. As linhas tracejadas pretas representam a igualdade.

usando uma lista de linhas modificada, incluindo linhas de Fe que são sensíveis à atividade estelar. Neste caso, as medianas das diferenças (mostradas na Figura 3.4) apresentam um pouco mais de diferença sistemática com os trabalhos da literatura, porém, mesmo assim a diferença em log g não é muito significativa, exceto para o caso da comparação com LAMOST que tem mediana da diferença de -0,22 (MAD=0,163).

#### 3.1.1.1 Gravidades Superficiais Espectroscópicas versus Asterosísmicas

Neste estudo, determinamos os parâmetros estelares ($T_{\rm eff}$, log $g$, $\xi$, [Fe/H]) com base na análise de uma lista de linhas de Fe I e Fe II. As correlações entre parâmetros nessa análise espectroscópica podem levar a erros sistemáticos, especialmente quando os valores de log $g$ são determinados. Um exemplo disso é que as linhas de Fe I são geralmente mais intensas do que as linhas de Fe II, levando a potenciais correlações entre a velocidade de microturbulência e log $g$. As gravidades superficiais precisas podem ser um dos parâmetros mais difíceis de serem restritos via espectroscopia, especialmente quando as linhas de Fe II forem poucas e fracas. Para investigar possíveis desvios sistemáticos nos valores de log $g$ derivados neste estudo, comparamos nossos resultados com aqueles calculados por meio da asterosismologia, onde a gravidade superficial pode ser derivada com boa precisão (PINSONNEAULT *et al.*, 2018). Para fazer essa comparação, coletamos as gravidades superficiais da asterosismologia das estrelas do projeto K2 de HUBER *et al.* (2016).

No painel esquerdo da Figura 3.5, comparamos os resultados obtidos neste estudo com os determinados em HUBER *et al.* (2016). A mediana das diferenças no log $g$ é $-0,015 \pm 0,187$ dex. Temos poucas estrelas com uma maior dispersão; essas estrelas são: EPIC 220481411, EPIC 211413752, EPIC 212012119 e EPIC 212782836, que são estrelas próximas com distâncias de aproximadamente 114, 321, 123, e 184 pc, e magnitudes absolutas de 7,04, 6,39, 6,69 e 5,79, respectivamente, sendo elas estrelas anãs-K e concordando com nossos resultados de gravidade superficial. No painel direito da Figura 3.5, apresentamos, como mencionado anteriormente, uma comparação das gravidades superficiais obtidas, agora incluindo as linhas de ferro sensíveis à atividade estelar. A mediana das diferenças apresenta uma pequena diferença sistemática de $-0,111 \pm 0,174$ dex (as estrelas que têm a maior dispersão são as mesmas identificadas anteriormente).

### 3.1.2 Metalicidades

Nos estudos de PETIGURA *et al.* (2018a) e MAYO *et al.* (2018), bem como nos levantamentos espectroscópicos APOGEE, GALAH, LAMOST e Gaia, as abundâncias de ferro foram determinadas por meio da síntese espectral. Nesta tese, as abundâncias de ferro foram avaliadas com base no equilíbrio de excitação e ionização das linhas de Fe I e Fe II.

Na Figura 3.6, apresentamos as comparações entre nossos resultados e os mesmos estudos mencionados nas sub-seções anteriores. A diferenças medianas em todos as com-

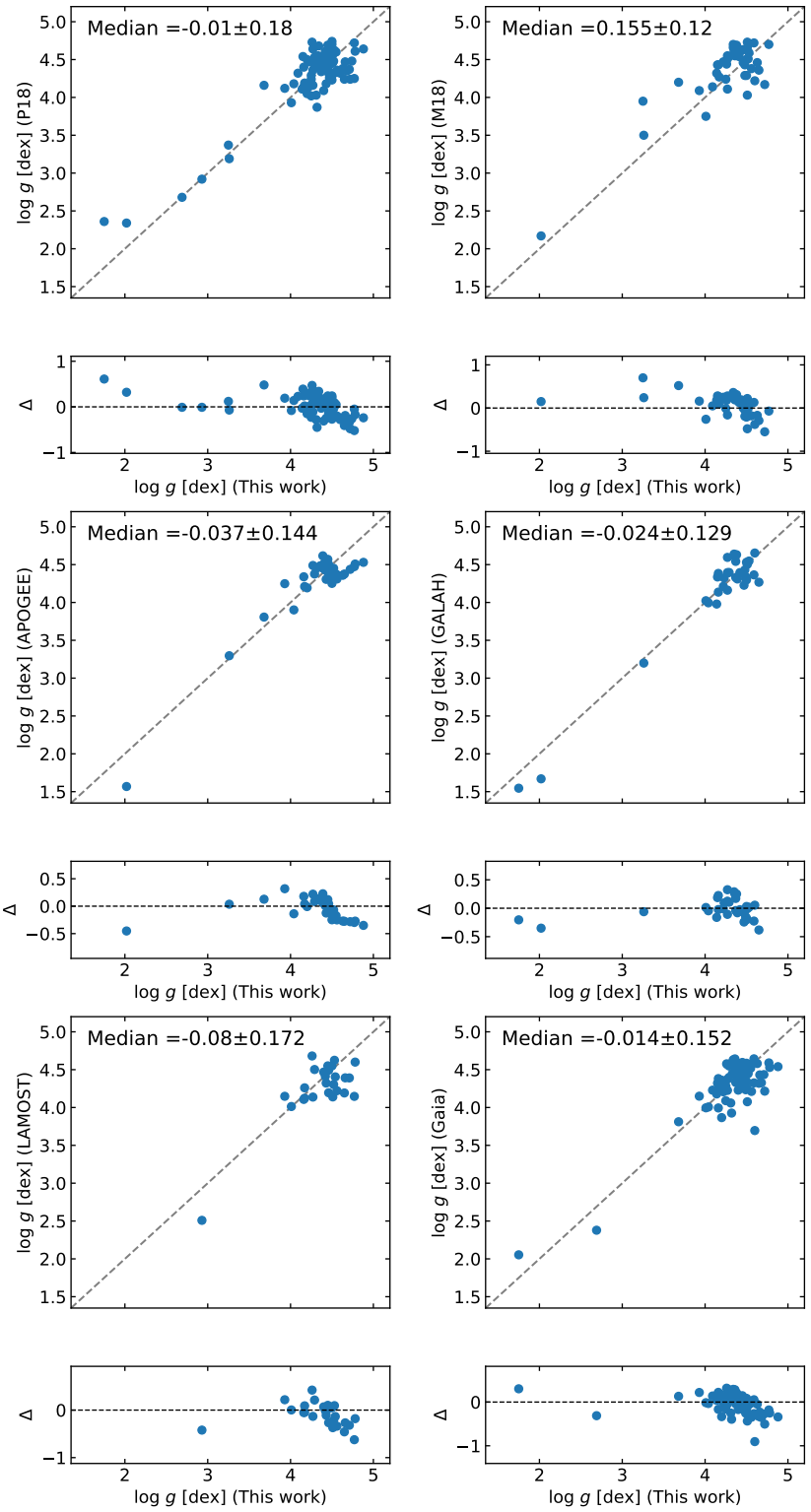


**Figura 3.3** – Comparações das gravidades superficiais derivadas neste estudo com aquelas de PETIGURA *et al.* (2018a), MAYO *et al.* (M18, 2018), e dos levantamentos APOGEE DR17, GALAH DR3 e LAMOST DR8. Os subpainéis inferiores mostram a diferença entre "Outros Estudos - Este Estudo" ($\Delta$). As diferenças medianas entre os parâmetros e os correspondentes desvios absolutos medianos (MAD) são indicadas em cada caso. As linhas tracejadas pretas representam a igualdade.

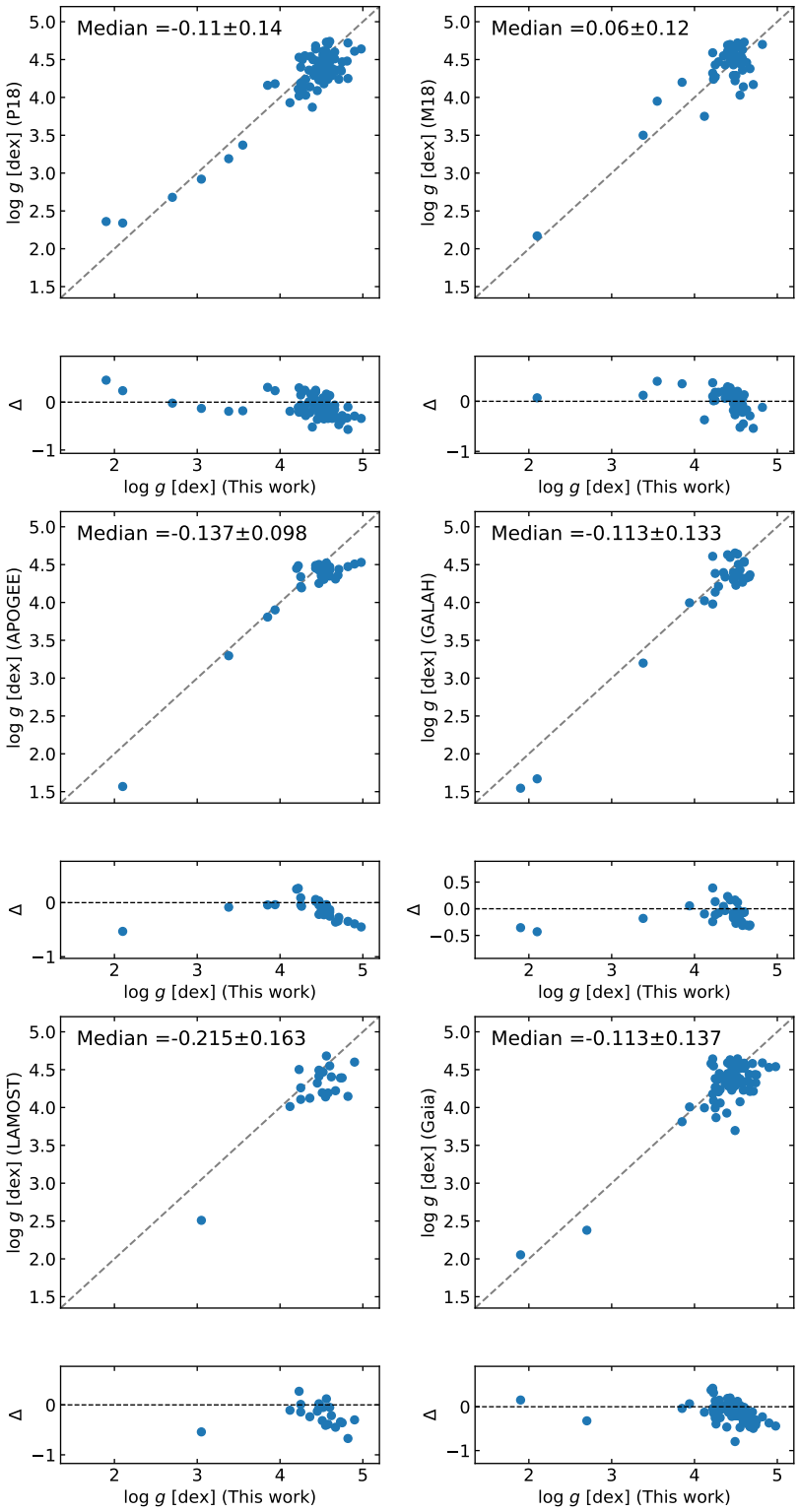


**Figura 3.4** – Comparações das gravidades superficiais deste estudo (adicionando linhas de ferro sensíveis à atividade estelar) com aquelas de PETIGURA *et al.* (2018a), MAYO *et al.* (M18, 2018), e dos levantamentos APOGEE DR17, GALAH DR3 e LAMOST DR8. Os sub-painéis inferiores mostram a diferença entre "Outros Estudos - Este Estudo" ($\Delta$). As diferenças medianas entre os parâmetros e os correspondentes desvios absolutos medianos (MAD) são indicadas em cada caso. As linhas tracejadas pretas representam a igualdade.

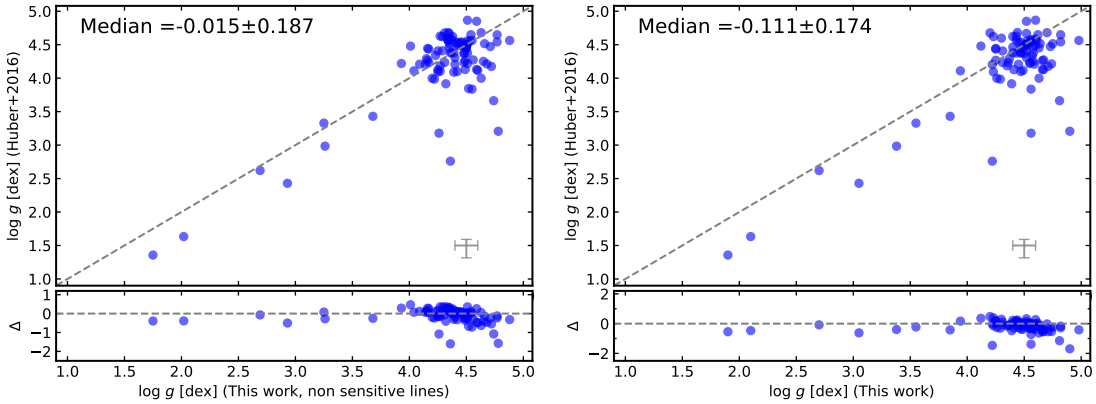


**Figura 3.5** – Comparação das gravidades superficiais espectroscópicas determinadas neste estudo com aquelas derivadas por meio de asterosismologia (HUBER *et al.*, 2016). O painel inferior apresenta as diferenças entre os resultados de "Huber+2016 - Este Estudo", acompanhadas das barras de erro médio das incertezas. No painel esquerdo mostramos a comparação entre nossos resultados, obtidos sem considerar as linhas de ferro sensíveis à atividade estelar, e os resultados da asterosismologia. O painel direito destaca a comparação entre nossos resultados, incluindo as linhas de ferro sensíveis à atividades estelar, e os resultados asterosismológicos.

parações são menores que 0,08 dex. Mais especificamente, em relação a PETIGURA *et al.* (2018a) é de $0,074 \pm 0,049$ dex, enquanto em comparação com MAYO *et al.* (2018), essa diferença é de $0,058 \pm 0,079$ dex. A análise dos resultados de levantamentos espectroscópicos, como APOGEE DR17, GALAH DR3 e LAMOST DR8, revela igualmente um bom acordo, com diferenças medianas de $0,028 \pm 0,053$, $0,022 \pm 0,064$ e $-0,036 \pm 0,050$ dex, respectivamente. Notavelmente, a única diferença sistemática um pouco maior aparece com Gaia RVS DR3: $-0,109 \pm 0,160$ dex.

Ao considerarmos a inclusão das linhas de ferro sensíveis à atividade, mostradas na Figura 3.7, não observamos diferenças significativas nas medianas das diferenças dos resultados e nos Desvios Absolutos Médios (MADs) na maioria dos casos. A maior discrepância ocorre de novo com Gaia RVS ($-0,129 \pm 0,175$).

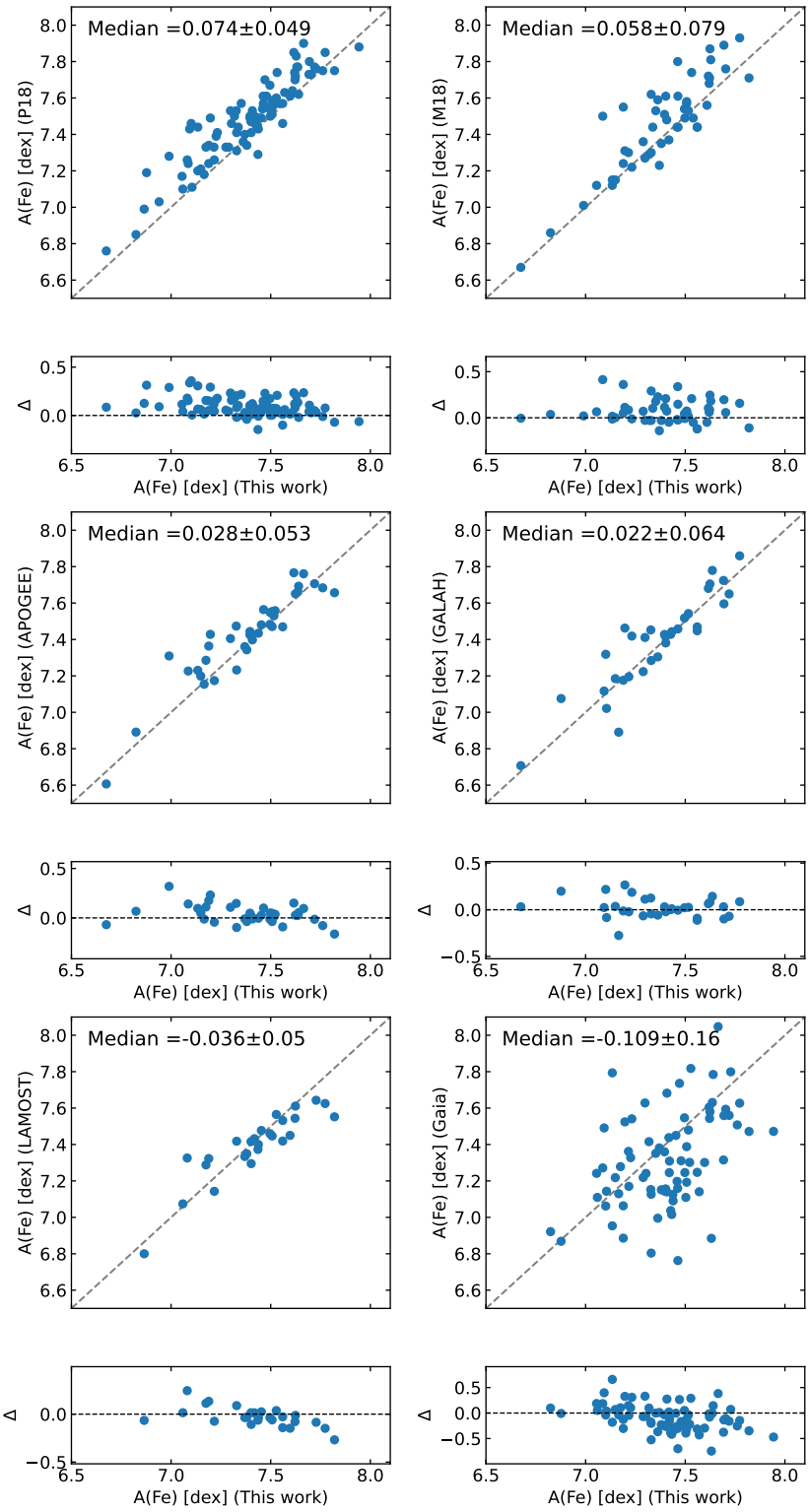


**Figura 3.6** – Comparação das metalicidades deste estudo com metalicidades obtidas por estudos anteriores de PETIGURA *et al.* (P18, 2018a), MAYO *et al.* (M18, 2018), e dos levantamentos APOGEE DR17, GALAH DR3 e LAMOST DR8. Os sub-painéis inferiores mostram as diferenças ($\Delta$) entre os resultados de "Outros Estudos" e "Este Estudo", com medianas e MADs indicados. Linhas tracejadas pretas denotam igualdade.

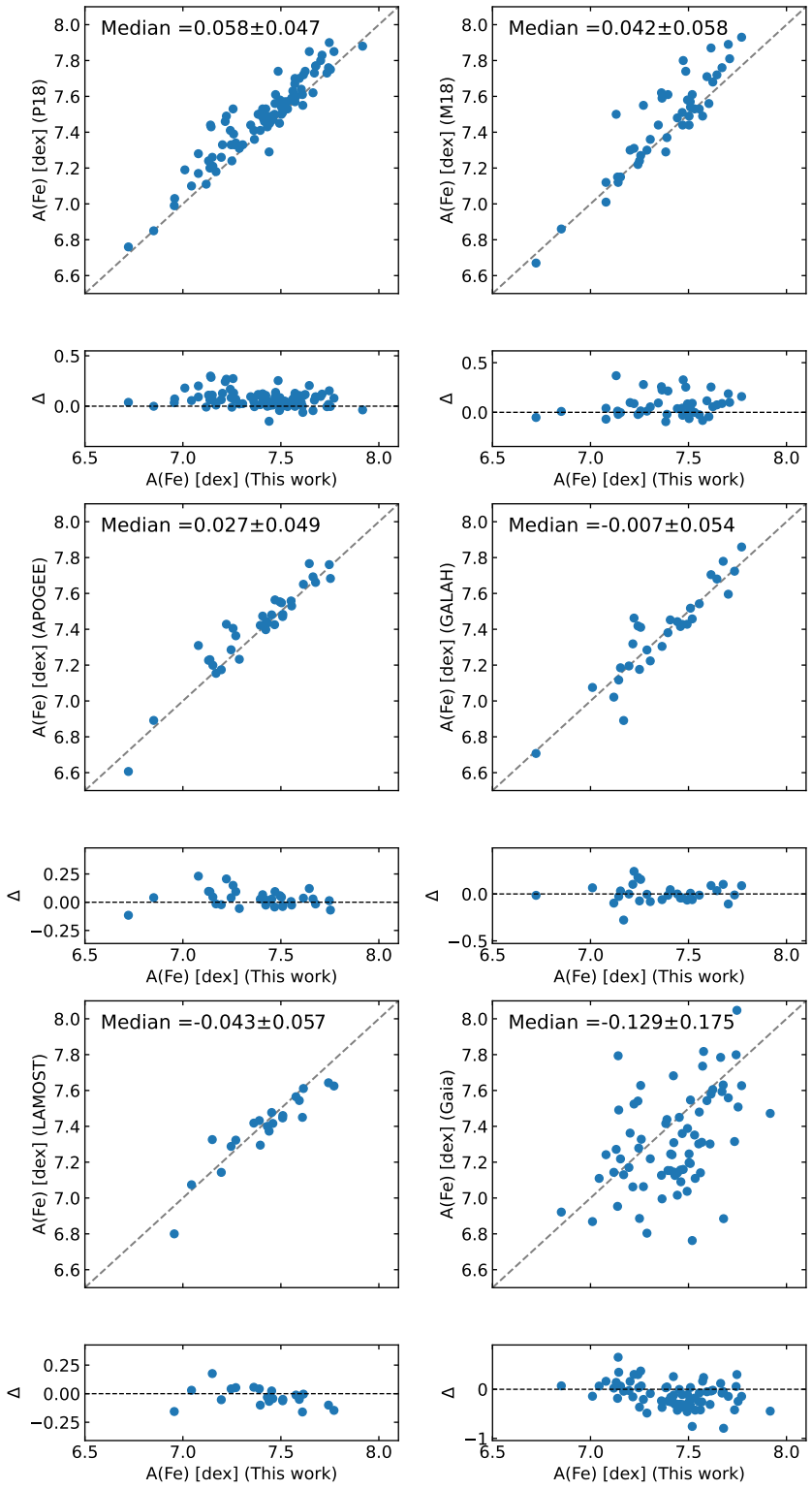


**Figura 3.7** – Comparação das metalicidades determinadas neste estudo ao incluir as linhas de ferro sensíveis à atividade estelar, em relação às metalicidades obtidas de estudos anteriores de PETIGURA *et al.* (P18, 2018a), MAYO *et al.* (M18, 2018), e dos levantamentos APOGEE DR17, GALAH DR3 e LAMOST DR8. Os sub-painéis inferiores mostram as diferenças entre os resultados de "Outros Estudos - Este Estudo" ($\Delta$), com as medianas e os respectivos MADs indicados em cada caso. Linhas tracejadas pretas representam a igualdade.

# Capítulo 4

# Análise Espectroscópica de Estrelas Gigantes Vermelhas do Aglomerado Aberto NGC 6705

Este capítulo apresenta o artigo publicado na revista *Monthly Notices of the Royal Astronomical Society*: "Chemical abundances of the young inner-disc open cluster NGC 6705 observed by APOGEE: sodium-rich and not $\alpha$-enhanced"[1]. Este estudo apresenta uma análise espectroscópica quantitativa de onze estrelas gigantes vermelhas membros do aglomerado aberto NGC 6705, determinando as abundâncias dos elementos C, N, Na, Al, K, Ti, V, Cr, Mn, Fe, Co, Ni e Ce, bem como os elementos-$\alpha$: O, Mg, Si e Ca. A análise foi realizada em LTE, usando os modelos MARCS com geometria esférica com o programa de transferência radiativa Turbospectrum. Essa análise espectroscópica é baseada em espectros do APOGEE, que estão no infravermelho próximo entre aproximadamente 1,51 e 1,70 $\mu$m, mas utilizamos uma análise e metodologia independentes quando comparada com o *pipeline* de abundância APOGEE ASPCAP (GARCÍA PÉREZ *et al.*, 2016), especialmente na derivação dos parâmetros estelares, temperatura efetiva e gravidade superficial. Isso é devido às conhecidas discrepâncias sistemáticas nos valores de gravidade superficial para os resultados do ASPCAP, que são pós-calibrados (JÖNSSON *et al.*, 2020).

Devido à sua idade comparativamente jovem ($\sim$ 300 milhões de anos) e riqueza estelar em comparação com outros aglomerados abertos do disco galáctico, NGC 6705 contém uma amostra populosa de gigantes vermelhas com massas entre M $\sim 3,0 - 3,5$ M$_\odot$, que nos permitiu investigar a mistura estelar em intervalo de massa intermediária.

Nossos resultados indicaram que o aglomerado NGC 6705 é rico em metais, $\langle [Fe/H] \rangle = 0,13 \pm 0,04$, o que é esperado para um aglomerado jovem do disco interno da Galáxia. A abundância média dos elementos-$\alpha$ encontrada para as estrelas analisadas deste aglomerado não indicam que este apresente enriquecimento: $\langle [\alpha/Fe] \rangle =$

[1] https://doi.org/10.1093/mnras/stad2896

$-0,03 \pm 0,05$. As abundâncias derivadas de Na encontram-se aumentadas de [Na/Fe] = +0,29, indicando uma assinatura adicional da primeira dragagem (1DUP), em bom acordo com predicões de modelos de (LAGARDE *et al.*, 2012). Notando que a correção não-ETL para as abundâncias ETL derivadas é muito pequena $(-0,02)$.

Monthly Notices of the ROYAL ASTRONOMICAL SOCIETY

MNRAS **526,** 2378–2393 (2023) https://doi.org/10.1093/mnras/stad2896
Advance Access publication 2023 September 22

# Chemical abundances of the young inner-disc open cluster NGC 6705 observed by APOGEE: sodium-rich and not $\alpha$-enhanced

V. Loaiza-Tacuri [1]★ K. Cunha,[1,2,3] D. Souto,[4] V. V. Smith,[3,5] R. Guerço [1] C. Chiappini,[6] J. V. Sales-Silva,[1] D. Horta [7] C. Allende Prieto,[8] R. Beaton,[9] D. Bizyaev [10,11] S. Daflon,[1] P. Frinchaboy,[12] S. Hasselquist,[13] C. R. Hayes [14] J. A. Holtzman,[15] H. Jönsson,[16] S. R. Majewski,[17] S. Mészáros,[18,19] D. L. Nidever,[20] M. Pinsonneault [21] and G. Zasowski[22]

*Affiliations are listed at the end of the paper*

Accepted 2023 September 19. Received 2023 September 12; in original form 2023 June 20

## ABSTRACT

Previous results in the literature have found the young inner-disc open cluster NGC 6705 to be mildly $\alpha$-enhanced. We examined this possibility via an independent chemical abundance analysis for 11 red-giant members of NGC 6705. The analysis is based on near-infrared APOGEE spectra and relies on LTE calculations using spherical model atmospheres and radiative transfer. We find a mean cluster metallicity of [Fe/H] $= +0.13 \pm 0.04$, indicating that NGC 6705 is metal-rich, as may be expected for a young inner-disc cluster. The mean $\alpha$-element abundance relative to iron is $\langle[\alpha/\mathrm{Fe}]\rangle = -0.03 \pm 0.05$, which is not at odds with expectations from general Galactic abundance trends. NGC 6705 also provides important probes for studying stellar mixing, given its turn-off mass of $M \sim 3.3\,\mathrm{M}_{\odot}$. Its red giants have low $^{12}$C abundances ([$^{12}$C/Fe] $= -0.16$) and enhanced $^{14}$N abundances ([$^{14}$N/Fe] $= +0.51$), which are key signatures of the first dredge-up on the red giant branch. An additional signature of dredge-up was found in the Na abundances, which are enhanced by [Na/Fe] $= +0.29$, with a very small non-LTE correction. The $^{16}$O and Al abundances are found to be near-solar. All of the derived mixing-sensitive abundances are in agreement with stellar models of approximately $3.3\,\mathrm{M}_{\odot}$ evolving along the red giant branch and onto the red clump. As found in young open clusters with similar metallicities, NGC 6705 exhibits a mild excess in the s-process element cerium with [Ce/Fe] $= +0.13 \pm 0.07$.

**Key words:** stars: abundances – infrared: stars – Galaxy: inner disc – stars: giants – stars: open cluster.

## 1 INTRODUCTION

Open clusters are excellent probes of chemical evolution in the Milky Way disc, as their range in metallicity overlaps that of the disc field stars, while their locations extend from the inner disc to the outskirts of the Galaxy, and they have formed over an extended period of Galactic history. NGC 6705 (Messier 11, M11) is relatively star-rich, compact, and located in the inner disc at a Galactocentric distance of 6.5 kpc (Cantat-Gaudin et al. 2020). This open cluster is young, with a well-defined age from isochrone fitting of $316 \pm 50$ Myr (Cantat-Gaudin et al. 2014; Dias et al. 2021) and, given its youth, has probably not migrated very far from its birthplace, with an estimated birth radius between 6.8–7.5 kpc (Casamiquela et al. 2018).

NGC 6705 has been reported to be a metal-rich cluster, with [Fe/H] $\sim +0.1$–$0.17$ (e.g.; Gonzalez & Wallerstein 2000; Heiter et al. 2014; Magrini et al. 2017; Casamiquela et al. 2018), although recent works have also found it to have mean metallicities closer to solar (Casamiquela et al. 2021; Magrini et al. 2021; Randich et al. 2022). Another aspect of this open cluster is that previous studies in the literature (Tautvaišienė et al. 2015; Casamiquela et al. 2018) have found its stellar members to be moderately enhanced in $\alpha$-elements relative to iron ([$\alpha$/Fe] $\sim +0.1$ to $+0.2$), although it has an age of only a few hundred million years. Magrini et al. (2014) also found NGC 6705 to be mildly enhanced in $\alpha$-elements: $<[\alpha/\mathrm{Fe}]> = +0.08$, while the more recent study of Magrini et al. (2017) found that only [Mg/Fe], and not the other $\alpha$-elements, was enhanced (by $+0.1$ dex) in NGC 6705.

Youth and $\alpha$-enhancement together are not expected from simple chemical evolution modelling, as $\alpha$-elements, such as O, Mg, Si, and Ca are produced at early times, mainly in Type II Supernovae (formed by massive stars on short timescales); enrichment in the [$\alpha$/Fe] ratio generally indicates that a star formed from gas enriched by SN II before SN Ia had the time to contribute iron to the natal gas. Within the Galactic disc, there are two sequences defined by the $\alpha$-element abundances: the high- and the low-$\alpha$ sequences (e.g. Fuhrmann 1998; Reddy, Lambert & Allende Prieto 2006; Anders et al. 2014; Nidever et al. 2014; Hayes et al. 2018; Queiroz et al. 2020); the high-$\alpha$ sequence is older and corresponds to the thick disc (rich in $\alpha$-elements relative to its Fe content), while the thin disc population consists of stars with lower values of [$\alpha$/Fe].

There are, however, interesting results in the literature pointing to a population of young field stars with a high abundance ratio of $\alpha$-element-to-iron, which are unusual given their ages reported in the literature. Chiappini et al. (2015) discovered such young [$\alpha$/Fe]-enhanced stars in a sample of field stars observed by the SDSS APOGEE Survey (Majewski et al. 2017) having CoRoT asteroseismology (Baglin et al. 2006). CoRoT provided precise age

★ E-mail: vtacuri@on.br

estimation for field stars, resulting in the identification of a large number of young stars in the inner region of the Galactic disc that are rich in $\alpha$-elements ([$\alpha$/Fe] $\sim$ 0.1–0.3) and with a low abundance of iron-peak elements. Meanwhile, Martig et al. (2015) analysed a sample of 1639 red giants with astereoseismic ages from the APOGEE sample and observed by the Kepler mission (referred to as the APOKASC sample) to investigate the relationship between age and chemical abundances. As a result of their analysis, they identified fourteen stars enriched in $\alpha$-elements ([$\alpha$/Fe] $>$ 0.13) that were younger than 6 Gyr, and five stars with [$\alpha$/Fe] $\geq$ 0.20 are younger than 4 Gyr. Possible scenarios to explain this young, $\alpha$-enhanced population of stars include accretion of material from a binary companion or binary mergers (e.g. Izzard et al. 2018; Silva Aguirre et al. 2018; Hekker & Johnson 2019; Jofré et al. 2023), resulting in stars that would appear to be young, while actually being old. In addition, Miglio et al. (2021) found that stars with [$\alpha$/Fe] $>$ 0.1 from the Kepler field that appeared young were overmassive; this result supports the scenario that most of these stars have undergone an interaction with a companion.

Given its youth, coupled to the mild $\alpha$-enhancements found for NGC 6705 in the literature (Tautvaišienė et al. 2015; Casamiquela et al. 2018), along with the different signatures ($\alpha$-enhanced versus non $\alpha$-enhanced) obtained, for example, for Mg in comparison with other $\alpha$-elements (Magrini et al. 2017), and the relevance of finding a young $\alpha$-rich open cluster in the context of the young $\alpha$-enhanced field stars in the Galaxy (as discussed in Casamiquela et al. 2018), it becomes important to revisit the $\alpha$-abundances in NGC 6705 from a completely independent analysis, also keeping in mind that the results in the literature for NGC 6705 mentioned above are all from optical studies. All, except for Casamiquela et al. (2018), being based on the Gaia-ESO survey (GES; Gilmore et al. 2012, 2022; Randich et al. 2022).

In addition, due to its relative youth and stellar richness in comparison to other open clusters, NGC 6705 contains a populous sample of red giants in which to probe stellar mixing in the interesting mass range between $M \sim 3.0$–$3.5\,M_{\odot}$. Such intermediate-mass red giants can exhibit measurable chemical abundance changes due to deep mixing beyond the usual variations in $^{12}$C, $^{13}$C, and $^{14}$N observed in lower-mass red giants, to include possible changes in the $^{16}$O, or Na, or Al abundances. The red giants in NGC 6705 can provide an important observational test of stellar models. Smiljanic et al. (2016) studied Na and Al in low- and intermediate-mass clump giants, in particular in six open clusters from the Gaia ESO survey, and found both Na and Al to be enriched in NGC 6705. While their Na results for this cluster were in agreement with predictions from stellar evolution models, their Al abundances were above model predictions, as aluminium is not expected to be affected by mixing in the mass range of NGC 6705 giants (Lagarde et al. 2012).

In this study, we select a sample of red giant stars that are members of NGC 6705 in order to determine their stellar parameters and present a detailed analysis of the chemical abundances of their $\alpha$-elements (O, Mg, Si, Ca, and Ti), along with iron and the Fe-peak elements (V, Cr, Mn, Co, and Ni), elements sensitive to red giant mixing ($^{12}$C, $^{14}$N, Na, and Al), as well as the s-process element cerium. This spectroscopic analysis is based on APOGEE spectra, which are in the near-infrared, but uses an independent analysis and methodology when compared with the APOGEE abundance pipeline ASPCAP (García Pérez et al. 2016), particularly in the derivation of the stellar parameters effective temperature and surface gravity, and given the well-known systematic offsets in surface gravity values for the ASPCAP results, which are post-calibrated (Jönsson et al. 2020). This paper is organized as follows: in Section 2, we present the sample and the observations, while Section 3 describes the methodology to determine the stellar parameters, and Section 4 presents the individual abundance analysis of seventeen elements. In Section 5, we compared our results with literature results. Section 6 contains a discussion of the results, and Section 7 the conclusions.

## 2 OBSERVATION AND SAMPLE

### 2.1 APOGEE spectra

The Apache Point Observatory Galactic Evolution Experiment (APOGEE; Majewski et al. 2017) was one of the three surveys carried out as part of the Sloan Digital Sky Survey-IV (SDSS-IV; Blanton et al. 2017). APOGEE targeted the open cluster NGC 6705 as part of its OCCAM (Open Cluster Chemical Abundances and Mapping) campaign, which aimed to study the structure and chemical evolution of the Milky Way (Frinchaboy et al. 2013; Donor et al. 2018; Myers et al. 2022). The APOGEE spectra analysed in this study were obtained using a 300-fiber cryogenic spectrograph on the 2.5-m telescope at the Apache Point Observatory (New Mexico, USA; Gunn et al. 2006), and these have a resolution $R = \lambda/\Delta\lambda \sim 22\,500$ and spectral coverage from 1.51 to 1.69 μm (Wilson et al. 2010, 2019). Reduction of the APOGEE spectra, as well as the determination of the stellar radial velocities, were carried out by an automated data processing pipeline (Nidever et al. 2015), and the reduced spectra analysed here come from the publicly available 17th APOGEE data release (DR17; Abdurro'uf et al. 2022). The open cluster NGC 6705 was observed in APOGEE field 027–04, identified by location ID 4470 (Zasowski et al. 2013, 2017; Beaton et al. 2021). APOGEE targeted a total of 343 stars in this field, which were investigated here for cluster membership in the section below.

### 2.2 NGC 6705 membership

The open cluster NGC 6705 is located at Galactic coordinates $l = 27.304^{\circ}$ and $b = -2.773^{\circ}$ at an estimated distance of $\sim$1900–2200 pc (e.g. Cantat-Gaudin & Anders 2020; Dias et al. 2021; Hunt & Reffert 2023). The mean radial velocity of its cluster members, according to radial velocities from *Gaia* DR2, was estimated in Dias et al. (2021) to be $35.68 \pm 0.24\,\mathrm{km\,s^{-1}}$ and considering 357 stars Tarricq et al. (2021) found a mean radial velocity of $34.49 \pm 0.27\,\mathrm{km\,s^{-1}}$.

#### 2.2.1 *Membership according to HDBSCAN*

We used the PYTHON code HDBSCAN (Hierarchical Density-Based Spatial Clustering of Applications with Noise; Campello, Moulavi & Sander 2013) clustering algorithm to independently assess which stars from the observed APOGEE field 027–04 would be identified as members of the NGC 6705 open cluster. HDBSCAN is an unsupervised machine learning method, which does not require learning from labelled data to make predictions. More specifically, HDBSCAN is a density-based clustering algorithm that groups data points together based on their proximity and density.

HDBSCAN uses a number of input parameters that can be adjusted to control its clustering estimations. The main input parameters are: *min_cluster_size*, *min_samples*, *cluster_selection_epsilon*, and *alpha*. The parameter *min_cluster_size* sets the minimum number of points needed to define a distinct cluster; thus, any potential cluster that might contain fewer points would be labelled as noise (outliers). The *min_samples* parameter defines the minimum number of neighbouring points surrounding a given point for it to be considered as a core

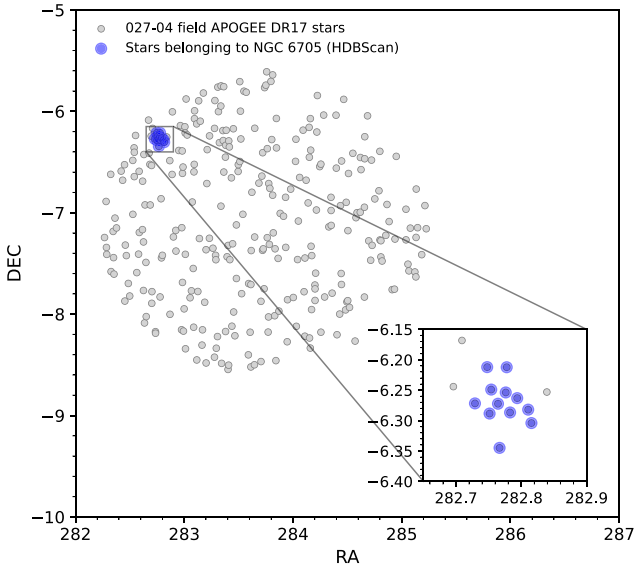


**Figure 1.** Declination (DEC) versus right ascension (RA) of stars from 027–04 field – APOGEE DR17. The stars highlighted in blue are the stars pointed out as members of the NGC 6705 cluster using the HDBSCAN code. The highlighted panel is a region zoom containing these stars.

point, while a minimum distance below which HDBSCAN will not further split a cluster is set by the parameter *cluster_selection_epsilon*. The parameter *alpha* controls the balance between condensed tree density and hierarchy depth. Higher values of *alpha* result in clusters that are more tightly bound within the hierarchy, while lower values allow clusters to be more easily split. For the APOGEE field 027–04, we used the following parameter values: *min_cluster_size* = *4*, *min_samples* = *3*, *cluster_selection_epsilon* = *0.0*, and *alpha* = *1.0*.

To search for cluster members within the observed stars in the APOGEE plate, we used three parameters: proper motions (pm RA and pm DEC) from *Gaia* DR3 (*Gaia* DR3; Gaia Collaboration 2021), distances from Bailer-Jones et al. (2021), and radial velocities from APOGEE DR17. As mentioned above, the APOGEE 027–04 field has 343 stars, however, not all of them have all three parameters available. Fig. 1 shows the RA-DEC space of the 307 stars analysed with the HDBSCAN code. From this group, twelve stars have been selected as cluster members according to our parameters, and these are shown as blue circles in Fig. 1. The results from HDBSCAN indicated that eleven of the stars had 100 per cent probability of being cluster members, while the star 2MASS J18510399-0620414 had a slightly lower probability (93 per cent) of belonging to the cluster.

### 2.2.2 *Other membership from the literature*

We also investigated which stars observed by APOGEE would be members of NGC 6705, according to other studies in the literature. Thirty one stars have been labelled as possible members of NGC 6705 in the most recent OCCAM study by (Myers et al. 2022) (their Table 3), and the upper right-hand panel of Fig. 2 shows the proper motions of these stars from *Gaia* DR3 (Gaia Collaboration 2021). Their APOGEE radial velocities are shown in the left-hand panel of Fig. 2 and it can be seen that these show a large variation in radial velocities, with RV values ranging mostly between $-30$–$90\,\mathrm{km\,s^{-1}}$. From this sample of 31 stars, Myers et al. (2022) used APOGEE radial velocities and metallicities, along with *Gaia* proper motions, to estimate membership probabilities to select a sample of twelve stars that were considered to be members of NGC 6705. In Fig. 2, the twelve member stars are depicted inside the red circle in the right-hand panel and within the red dashed lines in the left-hand panel.

We also verified which stars observed by APOGEE would be members of NGC 6705 according to the probabilities of membership provided by Cantat-Gaudin & Anders (2020). There are 1183 stars in that catalog with a probability of cluster membership larger or equal to 0.7. The cross-match of their member list with the APOGEE DR17 data base led to the identification of twelve stars in common. In addition, these same 12 stars are considered as members by Dias et al. (2021) and eleven of them are members according to Jackson et al. (2022).

In summary, we independently identified a sample of twelve bona fide stellar members of NGC 6705, and this membership is in agreement with the results from other independent studies in the literature. The NGC 6705 members are presented in Table 1, along with the star's 2MASS $J$, $H$, $K_s$ (Two Micron All Sky Survey; Cutri et al. 2003), and $V$ magnitudes taken from Cantat-Gaudin et al. (2014), Tautvaišienė et al. (2015), Casamiquela et al. (2016), and Zacharias et al. (2005), and *Gaia* magnitudes ($G$, $G_{BP}$, and $G_{RP}$) from *Gaia* DR3 (Gaia Collaboration et al. 2021).

Also included are the radial velocities (RV), along with the RV dispersions derived from individual APOGEE visits, and the signal-to-noise of the APOGEE spectra. We note that the star 2MASS J18510092-0614564 is deemed to be a binary given the scatter in the *Gaia* radial velocity measurements (*Gaia* DR3 $\mathrm{RV} = 37.45 \pm 11.37\,\mathrm{km\,s^{-1}}$) and will not be analysed in this study.

Finally, in the two lower panels of Fig. 2, we show the $(J - K_s)$ versus $J$ and $(G_{BP} - G_{RP})$ versus $G$ diagrams using 2MASS and *Gaia* DR3 photometry for the sample of twelve stars. The red line in both panels represents the PARSEC isochrone (Bressan et al. 2012) for the age and metallicity of NGC 6705 (0.316 Gyr and 0.10 dex, respectively). The location of the stars relative to the isochrones in the colour magnitude diagrams presented indicates that the selected members are probably red-clump stars, although they could also be on the red-giant branch.

## 3 STELLAR PARAMETERS

The determination of the abundances of chemical elements from stellar spectra relies on fundamental stellar atmospheric parameters, such as the effective temperature ($T_{\rm eff}$), surface gravity ($\log g$), microturbulence velocity ($\xi$), and metallicity ([Fe/H]). To derive these stellar parameters, we employed a methodology that is similar to the analysis presented in Souto et al. (2016).

Stellar effective temperatures were derived from the 2MASS (Two Micron All Sky Survey; Cutri et al. 2003) magnitudes $J$, $H$, and $K_s$, and the photometric calibrations of González Hernández & Bonifacio (2009) through the equation:

$$\theta_{\rm eff} = b_0 + b_1 X + b_2 X^2 + b_3 X[\mathrm{Fe/H}] + b_4[\mathrm{Fe/H}] + b_5[\mathrm{Fe/H}]^2, \quad (1)$$

where $T_{\rm eff} = 5040/\theta_{\rm eff}$, the values $X$ represent the colours $V - J$, $V - H$, $V - K_s$, and $J - K_s$, and the constants $b_0$, $b_1$, $b_2$, $b_3$, $b_4$, and $b_5$ for each photometric colour can be found in González Hernández & Bonifacio (2009). The adopted metallicity in this step was [Fe/H] = 0.10 dex (taken from Cantat-Gaudin et al. (2014)).

The reddening value adopted in this study was $E(B - V) = 0.4$ (Cantat-Gaudin et al. 2014) and reddening corrections were computed using the relations in Bilir et al. (2008). Table 2 lists

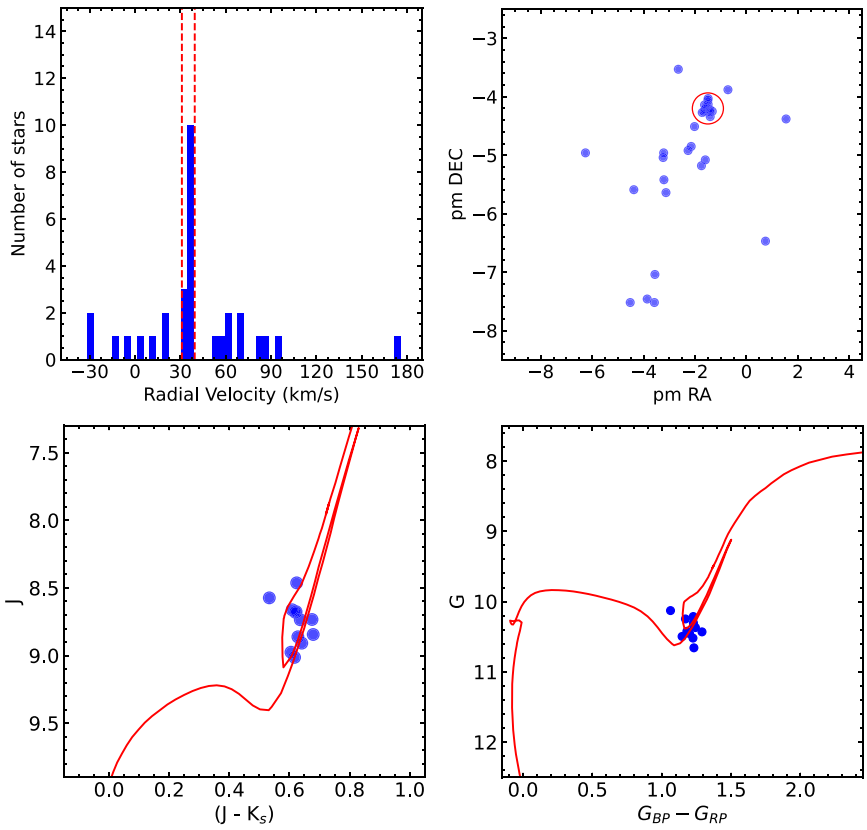


**Figure 2.** The upper left-hand panel displays the radial velocity distribution of stars in the 027–04 field, sourced from APOGEE DR17. The red dashed lines correspond to the radial velocity range determined for the cluster. In the upper right-hand panel, the *Gaia* DR3 proper motions of the targeted stars are presented. The blue dots inside the red circle signify stars within the radial velocity range determined for the cluster. The bottom panels depict the 2MASS ($J - K_s$) versuss $J$ and *Gaia* DR2 ($G_{BP} - G_{RP}$) versus $G$ diagrams. The red line in both cases represents the isochrones from Bressan et al. (2012).

**Table 1.** Member stars of NGC 6705.

| Star ID | $J$ (mag) | $H$ (mag) | $K$ (mag) | $V$ (mag) | $G$ (mag) | $G_{BP}$ (mag) | $G_{RP}$ (mag) | RV (km s$^{-1}$) | SNR |
|---|---|---|---|---|---|---|---|---|---|
| 2M18505494-0616182 | 9.199 | 8.498 | 8.318 | 11.860 | 11.338 | 12.131 | 10.467 | 35.019 ± 0.059 | 400 |
| 2M18510399-0620414 | 9.090 | 8.400 | 8.252 | 11.872 | 11.313 | 12.164 | 10.411 | 34.623 ± 0.018 | 467 |
| 2M18510661-0612442 | 9.035 | 8.406 | 8.213 | 11.720 | 11.184 | 11.997 | 10.306 | 33.761 ± 0.047 | 462 |
| 2M18511048-0615470 | 8.817 | 8.224 | 7.991 | 11.627 | 11.095 | 11.905 | 10.214 | 33.597 ± 0.019 | 488 |
| 2M18505944-0612435 | 9.330 | 8.722 | 8.523 | 11.872 | 11.378 | 12.138 | 10.528 | 34.710 ± 0.022 | 385 |
| 2M18510032-0617183 | 9.368 | 8.751 | 8.549 | 12.081 | 11.540 | 12.347 | 10.652 | 36.689 ± 0.050 | 396 |
| 2M18510341-0616202 | 9.216 | 8.579 | 8.386 | 11.801 | 11.305 | 12.087 | 10.443 | 37.108 ± 0.007 | 429 |
| 2M18510786-0617119 | 9.030 | 8.399 | 8.206 | 11.621 | 11.129 | 11.905 | 10.271 | 34.572 ± 0.019 | 359 |
| 2M18511452-0616551 | 9.263 | 8.620 | 8.420 | 11.923 | 11.402 | 12.209 | 10.521 | 36.307 ± 0.045 | 306 |
| 2M18510092-0614564 | 9.016 | 8.395 | 8.205 | 11.484 | 11.010 | 11.716 | 10.189 | 34.827 ± 0.509 | 466 |
| 2M18510626-0615134 | 8.928 | 8.379 | 8.193 | 11.627 | 11.222 | 12.030 | 10.337 | 35.116 ± 0.007 | 449 |
| 2M18511571-0618146 | 9.088 | 8.445 | 8.211 | 11.807 | 11.252 | 12.073 | 10.367 | 35.442 ± 0.024 | 475 |

the effective temperatures determined from each colour and the corresponding median effective temperatures (and median absolute deviation, MAD). The effective temperatures obtained from different colours agree quite well, with the MAD for most stars being less than 50 K, which is a typical uncertainty for effective temperature scales. We note also that these errors are similar to those found in Souto et al. (2016) for a sample of red-giants in the open cluster NGC 2420.

To determine the surface gravities for the targets, the fundamental relation (equation (2)) was used, with the following reference solar parameter values: log $g$ = 4.438 (cgs), $T_{\rm eff,\odot}$ = 5770 K, and a bolometric magnitude of $M_{\rm bol,\odot}$ = 4.75 (Prša et al. 2016). The effective temperatures used are the median effective temperatures listed in Table 2. Stellar masses were derived using the PARSEC isochrones (Bressan et al. 2012), which yield a mass of ∼3.3 $M_\odot$ for a cluster age of 0.316 Gyr (Cantat-Gaudin et al. 2018) and a metallicity of $[M/H] = +0.10$ dex. Absolute magnitudes were determined using the distance module $(m\text{-}M)_o = 11.38$ (Dias et al. 2021), along with bolometric corrections from Montegriffo et al. (1998):

$$\log g = \log g_\odot + \log\left(\frac{M_\star}{M_\odot}\right) + 4\log\left(\frac{T_\star}{T_\odot}\right) + 0.4(M_{\rm bol,\star} - M_{\rm bol,\odot}). \quad (2)$$

**Table 2.** Atmospheric parameters.

| Star ID | $T_{\rm eff}(V-J)$ (K) | $T_{\rm eff}(V-H)$ (K) | $T_{\rm eff}\,(V-K_s)$ (K) | $T_{\rm eff}\,(J-K_s)$ (K) | $\langle T_{\rm eff}\rangle$ (K) | log $g$ (cm s$^{-2}$) | [Fe/H] (dex) | $\xi$ (km s$^{-1}$) |
|---|---|---|---|---|---|---|---|---|
| 2M18505494-0616182 | 4735 | 4692 | 4715 | 4632 | 4704 ± 31 | 2.279 | 0.15 | 1.50 |
| 2M18510399-0620414 | 4599 | 4601 | 4651 | 4754 | 4626 ± 51 | 2.253 | 0.07 | 1.70 |
| 2M18510661-0612442 | 4707 | 4734 | 4745 | 4801 | 4739 ± 27 | 2.250 | 0.14 | 1.80 |
| 2M18511048-0615470 | 4570 | 4658 | 4638 | 4789 | 4648 ± 63 | 2.167 | 0.12 | 1.60 |
| 2M18505944-0612435 | 4882 | 4884 | 4885 | 4846 | 4883 ± 14 | 2.386 | 0.16 | 1.60 |
| 2M18510032-0617183 | 4675 | 4720 | 4723 | 4810 | 4722 ± 39 | 2.359 | 0.03 | 1.70 |
| 2M18510341-0616202 | 4827 | 4816 | 4825 | 4778 | 4821 ± 17 | 2.334 | 0.15 | 1.75 |
| 2M18510786-0617119 | 4819 | 4816 | 4825 | 4795 | 4818 ± 9 | 2.272 | 0.17 | 1.90 |
| 2M18511452-0616551 | 4736 | 4744 | 4748 | 4740 | 4742 ± 4 | 2.318 | 0.15 | 1.70 |
| 2M18510626-0615134 | 4691 | 4793 | 4808 | 5073 | 4800 ± 116 | 2.304 | 0.16 | 1.80 |
| 2M18511571-0618146 | 4668 | 4692 | 4670 | 4643 | 4669 ± 13 | 2.263 | 0.18 | 1.50 |

**Table 3.** Mean abundance differences of Na, Mg, K, and Ca (with STD) in Non-LTE and LTE.

| Element | $\langle\delta[X/H]\rangle$ (non-LTE–LTE) |
|---|---|
| Na | $-0.019 \pm 0.003$ |
| Mg | $-0.027 \pm 0.006$ |
| K | $+0.007 \pm 0.010$ |
| Ca | $-0.032 \pm 0.010$ |

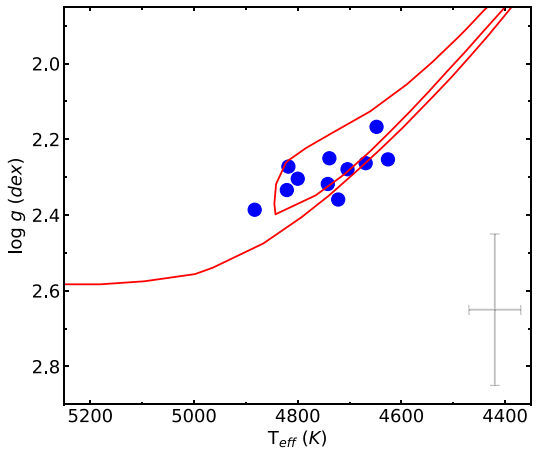


**Figure 3.** Kiel diagram. The red line in the plot represents the isochrone for metallicity of [Fe/H] = 0.13 dex and age of 0.316 Gyr. The isochrone was calculated using PARSEC (Bressan et al. 2012). Effective temperatures and surface gravities are the values determined in this work (see Table 2). A typical errorbar is shown in the bottom right of the figure.

The stellar parameters of our sample are presented in Fig. 3 as a Kiel diagram, where we also show as a red line a PARSEC isochrone (Bressan et al. 2012) computed for a metallicity of 0.13 dex and an age of 0.316 Gyr. The studied stars occupy a small range in parameter space close to the red clump, with the effective temperatures ranging between ∼4600–4900 K and surface gravities spanning from 2.2 to 2.4 dex. In Fig. 3, the stellar parameters seem to segregate, with four targets being hotter than 4800 K and more in line with them being on the red clump and seven targets cooler than 4800 K and falling closer to the RGB branch. However, given the uncertainties both in the stellar parameters and in the models, a secure distinction between red clump and RGB is difficult to make since we do not have information from asteroseismology.

## 4 ABUNDANCE ANALYSES AND METHODOLOGY

The chemical abundances for seventeen elements were calculated by comparing observed and synthetic spectra through the $\chi^2$-fitting method. Synthetic spectra were generated using MARCS model atmospheres (Gustafsson et al. 2008) and the Brussels Automatic Code for Characterizing High Accuracy Spectra (BACCHUS; Masseron, Merle & Hawkins 2016), which utilizes the radiative transfer code Turbospectrum (Alvarez & Plez 1998; Plez 2012). The APOGEE line list was adopted in the calculations of synthetic spectra (Smith et al. 2021).

We derived the stellar metallicities and microturbulent velocities using nine Fe I lines selected in the APOGEE region by Smith et al. (2013) and the methodology discussed in Souto et al. (2016). Briefly, the methodology consists of measuring the iron abundance of each Fe I line for different values of microturbulent velocities ($\xi$) using the spectrum synthesis method. The adopted values of microturbulent velocities were the ones that produced the smallest spread between the iron abundances of the individual lines.

The APOGEE spectra of red giant stars are characterized by the presence of numerous molecular features, predominantly spectral lines from CO, CN, and OH, making it an ideal tool for accurately determining the abundances of carbon, nitrogen, and oxygen. The molecular lines used for abundance determination are $^{12}C^{16}O$, $^{12}C^{14}N$, and $^{16}OH$, respectively, with the procedure to determine the C, N, and O abundances following the Smith et al. (2013) methodology. First, we derive the abundance of carbon from the molecular CO lines, then the oxygen abundance from the OH lines, and lastly, the nitrogen abundance from the CN lines.

The spectral range covered by APOGEE also contains atomic lines from many elements, including $\alpha$-elements, such as Mg, Si, Ca, and Ti, along with odd-Z elements, such as, Na, Al, and K, as well as the Fe-peak elements V, Cr, Mn, Fe, Co, and Ni, and the s-process element Ce. In this analysis, we analysed 73 spectral features that had been selected in the previous APOGEE studies of red giants of Smith et al. (2013), Cunha et al. (2015), and Souto et al. (2016) as abundance indicators: 9 Fe I lines, 4 CO lines, 9 CN lines, 2 Na I lines, 6 Mg I lines, 2 Al I lines, 7 Si I lines, 2 K I lines, 3 Ca I lines, 5 Ti I lines, 1 V I line, 1 Cr I line, 3 Mn lines, 1 Co I line, 7 Ni I lines, 7 Ce II lines, and 4 OH lines, noting that the latter are blended with CN at the studied range in parameter space. Table 4 contains the atomic and molecular line list used in the abundance analysis, the corresponding line-by-line abundances, the mean abundances, and standard deviations for each star, while in Table 5, we list the mean abundances, and standard deviation (STD) obtained for the

**Table 4.** Line-by-line elemental abundances.

| Element | λ (Å) | J18505494 −616182 | J18510399 −620414 | J18510661 −612442 | J18511048 −615470 | J18505944 −612435 | J18510032 −617183 | J18510341 −616202 | J18510786 −617119 | J18511452 −616551 | J18510626 −615134 | J18511571 −618146 |
|---|---|---|---|---|---|---|---|---|---|---|---|---|
| C from CO | 15580. | 8.42 | 8.33 | 8.41 | 8.45 | 8.51 | 8.33 | 8.49 | 8.51 | 8.43 | 8.45 | 8.43 |
| | 15977. | 8.48 | 8.29 | 8.46 | 8.33 | 8.45 | 8.24 | 8.44 | 8.55 | 8.39 | 8.40 | 8.44 |
| | 16186. | 8.47 | 8.35 | 8.55 | 8.42 | 8.54 | 8.32 | 8.51 | 8.60 | ... | 8.44 | 8.48 |
| | 16613. | 8.51 | 8.33 | 8.47 | 8.39 | 8.50 | 8.31 | 8.50 | 8.51 | 8.45 | 8.49 | 8.48 |
| ⟨*A*(C)⟩ | | 8.47 ± 0.03 | 8.32 ± 0.02 | 8.47 ± 0.05 | 8.40 ± 0.04 | 8.50 ± 0.03 | 8.30 ± 0.04 | 8.48 ± 0.03 | 8.54 ± 0.04 | 8.42 ± 0.02 | 8.45 ± 0.03 | 8.46 ± 0.02 |
| N from CN | 15260. | 8.43 | 8.59 | 8.50 | 8.52 | 8.46 | 8.49 | 8.49 | 8.46 | 8.43 | 8.52 | 8.40 |
| | 15322. | 8.47 | 8.60 | 8.49 | 8.56 | 8.50 | 8.46 | 8.53 | 8.53 | 8.49 | 8.53 | 8.39 |
| | 15397. | 8.60 | 8.63 | 8.59 | 8.51 | 8.58 | 8.50 | 8.59 | 8.69 | 8.50 | 8.51 | 8.42 |
| | 15332. | 8.50 | 8.54 | 8.49 | 8.56 | 8.55 | 8.57 | 8.55 | 8.54 | 8.49 | 8.53 | 8.45 |
| | 15410. | 8.41 | 8.58 | 8.42 | 8.42 | 8.46 | 8.46 | 8.46 | 8.49 | 8.45 | 8.52 | 8.37 |
| | 15447. | 8.42 | 8.63 | 8.48 | 8.55 | 8.53 | 8.51 | 8.52 | 8.55 | 8.56 | 8.52 | 8.48 |
| | 15466. | ... | ... | 8.28 | 8.40 | 8.42 | ... | 8.41 | 8.42 | 8.37 | 8.41 | 8.27 |
| | 15472. | 8.29 | 8.47 | 8.33 | 8.35 | 8.34 | 8.40 | ... | ... | 8.26 | 8.43 | 8.30 |
| | 15482. | 8.36 | 8.52 | 8.38 | 8.40 | 8.45 | 8.39 | 8.48 | 8.46 | 8.33 | 8.50 | 8.33 |
| ⟨*A*(N)⟩ | | 8.43 ± 0.09 | 8.57 ± 0.05 | 8.44 ± 0.09 | 8.47 ± 0.08 | 8.48 ± 0.07 | 8.47 ± 0.05 | 8.50 ± 0.05 | 8.52 ± 0.08 | 8.43 ± 0.09 | 8.50 ± 0.04 | 8.38 ± 0.07 |
| O from OH | 15280. | ... | 8.77 | 8.78 | 8.73 | 8.81 | ... | 8.86 | ... | ... | ... 8.83 | |
| | 15505. | 8.80 | 8.85 | 8.57 | 8.65 | 8.65 | 8.77 | 8.70 | 8.76 | 8.72 | 8.69 | 8.78 |
| | 15570. | ... | ... | ... | 8.87 | ... | ... | ... | ... | ... | ... | ... |
| | 16191. | ... | 8.71 | 8.75 | 8.68 | 8.77 | ... | 8.81 | 8.85 | ... | 8.85 | 8.69 |
| ⟨*A*(O)⟩ | | 8.80 | 8.78 ± 0.06 | 8.70 ± 0.09 | 8.73 ± 0.08 | 8.75 ± 0.07 | 8.77 | 8.79 ± 0.07 | 8.80 ± 0.05 | 8.72 | 8.77 ± 0.08 | 8.77 ± 0.06 |
| Fe I | 15194.492 | 7.72 | 7.50 | 7.69 | 7.61 | ... | 7.50 | 7.72 | ... | 7.67 | 7.75 | 7.64 |
| | 15207.526 | 7.58 | ... | 7.43 | 7.40 | ... | ... | ... | ... | 7.47 | 7.60 | ... |
| | 15395.718 | 7.64 | 7.51 | 7.62 | 7.64 | 7.59 | 7.52 | 7.49 | 7.58 | 7.66 | 7.64 | 7.71 |
| | 15490.339 | 7.65 | 7.53 | 7.61 | 7.53 | 7.50 | 7.42 | 7.59 | 7.54 | 7.53 | 7.58 | 7.61 |
| | 15648.51 | 7.64 | 7.69 | 7.65 | 7.63 | 7.73 | 7.56 | 7.69 | 7.59 | 7.69 | 7.64 | 7.65 |
| | 15964.867 | 7.50 | 7.42 | 7.62 | 7.58 | 7.56 | 7.48 | 7.63 | 7.65 | 7.60 | 7.60 | 7.65 |
| | 16040.657 | 7.54 | 7.46 | 7.54 | 7.56 | 7.58 | 7.46 | 7.48 | 7.62 | 7.52 | 7.55 | 7.56 |
| | 16153.247 | 7.53 | 7.49 | 7.52 | 7.60 | 7.61 | 7.45 | 7.54 | 7.68 | ... | 7.55 | 7.54 |
| | 16165.032 | 7.71 | 7.62 | 7.71 | 7.72 | 7.78 | ... | 7.71 | 7.72 | 7.77 | 7.65 | 7.76 |
| ⟨*A*(Fe)⟩ | | 7.61 ± 0.07 | 7.53 ± 0.08 | 7.60 ± 0.08 | 7.58 ± 0.08 | 7.62 ± 0.09 | 7.49 ± 0.04 | 7.61 ± 0.09 | 7.63 ± 0.06 | 7.61 ± 0.10 | 7.62 ± 0.06 | 7.64 ± 0.07 |
| Na I | 16373.853 | 6.67 | 6.67 | 6.62 | 6.55 | 6.65 | 6.49 | 6.60 | 6.67 | 6.64 | 6.61 | 6.62 |
| | 16388.858 | 6.74 | 6.73 | 6.66 | 6.62 | 6.72 | 6.55 | 6.65 | ... | 6.67 | 6.72 | 6.67 |
| ⟨*A*(Na)⟩ | | 6.71 ± 0.04 | 6.70 ± 0.03 | 6.64 ± 0.02 | 6.59 ± 0.04 | 6.68 ± 0.03 | 6.52 ± 0.03 | 6.63 ± 0.03 | 6.67 | 6.66 ± 0.02 | 6.67 ± 0.05 | 6.65 ± 0.03 |
| Mg I | 15740.716 | 7.75 | 7.60 | 7.67 | 7.61 | 7.72 | 7.51 | 7.63 | 7.63 | 7.70 | 7.57 | 7.68 |
| | 15748.9 | 7.72 | 7.63 | 7.63 | 7.52 | 7.65 | 7.51 | ... | 7.61 | 7.57 | 7.55 | 7.68 |
| | 15765.8 | 7.69 | 7.60 | 7.69 | 7.60 | 7.77 | 7.60 | 7.70 | 7.76 | 7.70 | 7.50 | 7.59 |
| | 15879.5 | 7.55 | 7.74 | 7.58 | 7.55 | 7.54 | 7.68 | 7.56 | 7.60 | 7.75 | 7.54 | 7.78 |
| | 15886.2 | 7.80 | 7.81 | 7.84 | 7.78 | ... | 7.78 | ... | ... | 7.86 | 7.73 | 7.82 |
| | 15954.477 | 7.71 | 7.72 | 7.75 | 7.68 | 7.77 | 7.63 | ... | 7.67 | 7.74 | 7.59 | 7.66 |
| ⟨*A* (Mg)⟩ | | 7.70 ± 0.08 | 7.68 ± 0.08 | 7.69 ± 0.08 | 7.62 ± 0.09 | 7.69 ± 0.09 | 7.62 ± 0.10 | 7.63 ± 0.06 | 7.65 ± 0.06 | 7.72 ± 0.09 | 7.58 ± 0.07 | 7.70 ± 0.07 |
| Al I | 16718.957 | 6.77 | 6.58 | 6.76 | 6.62 | ... | 6.53 | 6.70 | 6.68 | 6.71 | 6.65 | 6.72 |
| | 16763.359 | 6.72 | 6.58 | 6.66 | 6.50 | 6.49 | 6.45 | 6.60 | 6.55 | 6.65 | 6.61 | 6.64 |
| ⟨*A*(Al)⟩ | | 6.75 ± 0.02 | 6.58 ± 0.00 | 6.71 ± 0.05 | 6.56 ± 0.06 | 6.49 | 6.49 ± 0.04 | 6.65 ± 0.05 | 6.61 ± 0.06 | 6.68 ± 0.03 | 6.63 ± 0.02 | 6.68 ± 0.04 |
| Si I | 15361.161 | 7.68 | 7.75 | 7.78 | 7.75 | 7.68 | 7.73 | 7.59 | 7.58 | 7.78 | 7.74 | 7.80 |
| | 15376.831 | 7.89 | 7.83 | 7.83 | 7.85 | 7.80 | 7.75 | 7.84 | 7.78 | 7.86 | 7.87 | 7.92 |

**Table 4** – *continued*

| Element | λ (Å) | J18505494 −616182 | J18510399 −620414 | J18510661 −612442 | J18511048 −615470 | J18505944 −612435 | J18510032 −617183 | J18510341 −616202 | J18510786 −617119 | J18511452 −616551 | J18510626 −615134 | J18511571 −618146 |
|---|---|---|---|---|---|---|---|---|---|---|---|---|
| | 16060.009 | 7.56 | 7.48 | 7.45 | 7.45 | 7.56 | 7.45 | 7.47 | 7.44 | 7.57 | 7.50 | 7.61 |
| | 16094.787 | 7.79 | 7.60 | 7.71 | 7.61 | 7.68 | 7.48 | 7.63 | 7.70 | 7.76 | 7.80 | 7.85 |
| | 16215.67 | 7.73 | 7.52 | 7.71 | 7.58 | 7.64 | 7.48 | 7.60 | 7.73 | 7.74 | 7.60 | 7.67 |
| | 16680.77 | 7.70 | 7.63 | 7.78 | 7.61 | 7.73 | 7.55 | 7.63 | 7.73 | 7.77 | 7.70 | 7.73 |
| | 16828.159 | ... | 7.61 | 7.78 | 7.61 | 7.65 | 7.52 | 7.55 | 7.65 | 7.75 | 7.61 | 7.67 |
| ⟨*A*(Si)⟩ | | 7.73 ± 0.10 | 7.63 ± 0.11 | 7.72 ± 0.12 | 7.64 ± 0.12 | 7.68 ± 0.07 | 7.57 ± 0.11 | 7.62 ± 0.10 | 7.66 ± 0.11 | 7.75 ± 0.08 | 7.69 ± 0.12 | 7.75 ± 0.10 |
| K I | 15163.07 | 5.04 | 5.10 | 5.08 | 4.92 | 4.81 | 5.01 | 4.84 | 4.87 | ... | 5.07 | 5.10 |
| | 15168.38 | 5.04 | 5.04 | 5.03 | 4.88 | 4.90 | 5.01 | 4.95 | 4.90 | 4.95 | 4.93 | 5.04 |
| ⟨*A*(K)⟩ | | 5.04 ± 0.00 | 5.07 ± 0.03 | 5.06 ± 0.02 | 4.90 ± 0.02 | 4.86 ± 0.05 | 5.01 ± 0.00 | 4.90 ± 0.06 | 4.89 ± 0.02 | 4.95 | 5.00 ± 0.07 | 5.07 ± 0.03 |
| Ca I | 16150.763 | 6.55 | 6.33 | 6.43 | 6.42 | 6.47 | 6.30 | 6.40 | 6.50 | 6.57 | 6.42 | 6.39 |
| | 16155.236 | 6.61 | 6.40 | 6.52 | 6.45 | 6.51 | 6.36 | 6.50 | 6.51 | 6.59 | 6.50 | 6.45 |
| | 16157.364 | ... | 6.36 | 6.47 | 6.38 | 6.50 | 6.38 | 6.45 | 6.45 | 6.58 | 6.50 | 6.47 |
| ⟨*A*(Ca)⟩ | | 6.58 ± 0.03 | 6.36 ± 0.03 | 6.47 ± 0.04 | 6.42 ± 0.03 | 6.49 ± 0.02 | 6.35 ± 0.03 | 6.45 ± 0.04 | 6.49 ± 0.03 | 6.58 ± 0.01 | 6.47 ± 0.04 | 6.44 ± 0.03 |
| Ti I | 15543.756 | 5.22 | 4.92 | 5.01 | 4.90 | 5.09 | 4.77 | 4.98 | 5.09 | 5.08 | 5.11 | 5.04 |
| | 15602.842 | 5.28 | 5.02 | 5.17 | 4.94 | 5.23 | 5.01 | 5.20 | 5.25 | 5.14 | 5.28 | 5.13 |
| | 15698.979 | 5.16 | 4.94 | 5.03 | 4.80 | 4.98 | 4.79 | 4.92 | ... | 5.13 | 4.95 | 5.08 |
| | 15715.573 | 5.09 | 4.83 | ... | 4.68 | 4.96 | 4.75 | 4.92 | 4.92 | 4.88 | 4.95 | 4.95 |
| | 16635.161 | 5.19 | ... | ... | 4.83 | 4.84 | ... | ... | ... | 4.92 | ... | 4.93 |
| ⟨*A*(Ti)⟩ | | 5.19 ± 0.06 | 4.93 ± 0.07 | 5.07 ± 0.07 | 4.83 ± 0.09 | 5.02 ± 0.13 | 4.83 ± 0.10 | 5.01 ± 0.12 | 5.03 ± 0.13 | 5.03 ± 0.11 | 5.07 ± 0.14 | 5.03 ± 0.08 |
| V I | 5924.769 | 4.08 | 4.01 | 4.15 | 3.98 | 4.10 | 4.11 | 4.19 | 4.10 | 4.13 | 4.09 | 4.00 |
| ⟨*A*(V)⟩ | | 4.08 | 4.01 | 4.15 | 3.98 | 4.10 | 4.11 | 4.19 | 4.10 | 4.13 | 4.09 | 4.00 |
| Cr I | 15680.063 | 5.94 | 5.76 | 5.76 | 5.62 | 5.86 | 5.69 | 5.67 | 5.71 | 5.85 | 5.74 | 5.78 |
| ⟨*A*(Cr)⟩ | | 5.94 | 5.76 | 5.76 | 5.62 | 5.86 | 5.69 | 5.67 | 5.71 | 5.85 | 5.74 | 5.78 |
| Mn I | 15159. | 5.70 | 5.68 | 5.65 | 5.56 | 5.50 | 5.56 | 5.63 | 5.60 | 5.61 | 5.64 | 5.58 |
| | 15217. | 5.55 | ... | 5.48 | 5.35 | 5.42 | 5.33 | 5.40 | 5.43 | 5.45 | 5.56 | 5.47 |
| | 15262. | 5.70 | 5.59 | 5.67 | 5.50 | 5.55 | 5.48 | 5.53 | 5.50 | 5.61 | 5.68 | 5.70 |
| ⟨*A*(Mn)⟩ | | 5.65 ± 0.07 | 5.63 ± 0.04 | 5.60 ± 0.08 | 5.47 ± 0.09 | 5.49 ± 0.05 | 5.46 ± 0.09 | 5.52 ± 0.09 | 5.51 ± 0.07 | 5.56 ± 0.07 | 5.63 ± 0.05 | 5.58 ± 0.09 |
| Co I | 16757.7 | 5.11 | 5.06 | 5.12 | 4.94 | 5.10 | 4.97 | 5.08 | 5.15 | 5.07 | 5.07 | 5.04 |
| ⟨*A*(Co)⟩ | | 5.11 | 5.06 | 5.12 | 4.94 | 5.10 | 4.97 | 5.08 | 5.15 | 5.07 | 5.07 | 5.04 |
| Ni I | 15605.68 | 6.58 | 6.42 | 6.50 | 6.36 | 6.43 | 6.34 | 6.40 | 6.40 | 6.49 | 6.41 | 6.50 |
| | 15632.654 | 6.56 | 6.38 | 6.45 | 6.41 | 6.48 | 6.30 | 6.42 | 6.45 | 6.54 | 6.39 | 6.52 |
| | 16584.44 | 6.56 | 6.39 | 6.50 | 6.45 | 6.49 | 6.44 | 6.57 | 6.48 | 6.59 | 6.42 | 6.49 |
| | 16589.30 | 6.43 | 6.34 | 6.51 | 6.41 | 6.36 | 6.37 | 6.47 | 6.31 | 6.51 | 6.47 | 6.46 |
| | 16673.711 | ... | 6.28 | 6.30 | 6.37 | 6.27 | 6.30 | 6.37 | 6.31 | 6.32 | 6.35 | 6.29 |
| | 16815.471 | 6.51 | 6.46 | 6.40 | 6.28 | 6.37 | 6.39 | 6.40 | 6.37 | 6.32 | 6.51 | 6.43 |
| | 16818.76 | ... | 6.54 | 6.58 | 6.43 | 6.51 | 6.52 | 6.48 | 6.34 | 6.56 | ... | 6.55 |
| ⟨*A*(Ni)⟩ | | 6.53 ± 0.05 | 6.40 ± 0.08 | 6.46 ± 0.08 | 6.39 ± 0.05 | 6.41 ± 0.08 | 6.38 ± 0.07 | 6.45 ± 0.06 | 6.38 ± 0.06 | 6.48 ± 0.10 | 6.43 ± 0.05 | 6.46 ± 0.08 |
| Ce II | 15784.786 | 1.86 | 1.79 | 1.72 | 1.79 | 1.82 | 1.82 | 1.80 | ... | 1.82 | 1.84 | 1.79 |
| | 15958.39 | 1.90 | ... | ... | 1.89 | ... | 1.84 | ... | 2.05 | ... | 1.72 | 1.87 |
| | 15977.12 | 1.83 | ... | 1.81 | ... | ... | ... | ... | ... | 1.75 | 1.72 | ... |
| | 16327.32 | ... | ... | ... | ... | ... | ... | 1.70 | ... | ... | ... | ... |
| | 16376.46 | 1.78 | 1.91 | 1.91 | 1.85 | 1.93 | 1.80 | 1.80 | 1.90 | ... | ... | 1.96 |
| | 16595.233 | 1.97 | 1.75 | 1.82 | ... | 1.84 | ... | 1.77 | 1.92 | 1.74 | 1.90 | 1.69 |
| | 16722.6 | ... | 1.98 | ... | 2.03 | 1.96 | 1.92 | ... | 2.06 | ... | ... | 2.00 |
| ⟨*A*(Ce)⟩ | – | 1.87 ± 0.06 | 1.86 ± 0.09 | 1.81 ± 0.07 | 1.89 ± 0.09 | 1.89 ± 0.06 | 1.84 ± 0.05 | 1.77 ± 0.04 | 1.98 ± 0.07 | 1.77 ± 0.04 | 1.80 ± 0.08 | 1.86 ± 0.11 |

**Table 5.** Mean NGC 6705 abundances.

| Element | $\langle A(X)\rangle$ | $\langle[X/H]\rangle$ | STD | $\sigma(X)$ |
|---|---|---|---|---|
| C | 8.44 | −0.02 | 0.07 | 0.057 |
| N | 8.47 | 0.64 | 0.05 | 0.085 |
| O | 8.76 | 0.07 | 0.03 | 0.132 |
| Fe | 7.59 | 0.13 | 0.04 | 0.035 |
| Na | 6.65 | 0.43 | 0.05 | 0.035 |
| Mg | 7.66 | 0.11 | 0.04 | 0.078 |
| Al | 6.62 | 0.19 | 0.08 | 0.055 |
| Si | 7.68 | 0.17 | 0.06 | 0.055 |
| K | 4.98 | −0.09 | 0.08 | 0.053 |
| Ca | 6.46 | 0.16 | 0.07 | 0.058 |
| Ti | 5.01 | 0.04 | 0.10 | 0.103 |
| V | 4.06 | 0.19 | 0.06 | 0.051 |
| Cr | 5.76 | 0.14 | 0.09 | 0.032 |
| Mn | 5.55 | 0.13 | 0.07 | 0.062 |
| Co | 5.06 | 0.12 | 0.06 | 0.067 |
| Ni | 6.43 | 0.23 | 0.05 | 0.044 |
| Ce | 1.85 | 0.27 | 0.06 | 0.101 |

cluster, along with mean [X/H] ratios relative to the Solar abundances (Asplund, Amarsi & Grevesse 2021).

### 4.1 Abundance sensitivities and uncertainties

Souto et al. (2016, their table 4) estimated abundance uncertainties due to changes in stellar parameters), $\sigma$, for all elements analysed here, except for Ce. The uncertainties were computed by using the quadrature sum of abundance changes obtained by varying, respectively, the effective temperature by +50 K, the surface gravity by +0.2 dex, the metallicity by +0.2 dex, and the microturbulent velocity by +0.2 km s$^{-1}$ (see also the discussion in, Smith et al. 2013; Souto et al. 2016). Here, we add the uncertainties calculated for cerium: the change in the Ce abundance due to a +50 K variation in $T_{\rm eff}$ is +0.06 dex, while for $\Delta$log g of +0.2 it is +0.06 dex, for $\Delta\xi$ of +0.2 km s$^{-1}$ it is −0.04 dex, and for $\Delta$[M/H] of +0.2 dex is +0.04 dex. Summing these abundance changes in quadrature, we obtain an uncertainty in the Ce abundance of 0.1 dex. Table 5 (last column) lists these estimated uncertainties for all elements.

The elemental abundances in this study were derived, in general (except for V, Cr, and Co), from more than one atomic or molecular line, with the spread in the individual line abundances for a given star used to evaluate the internal consistency between the different line measurements. The STDs of the mean abundances in Table 4 are, for some elements quite small, being less than 0.04–0.05 dex, such as for C and Ca, while for many of the elements it is ∼0.09–0.1 dex, such as for O, N, Al, Fe, and Mg, while, in a few cases, the STDs of the mean reach values of 0.12–0.15 dex in some stars, such as for Si, Ti, and Ce.

Finally, given that the members of NGC 6705 presumably formed as a single stellar population, and that they are not affected by diffusion effects as they are on RGB or red clump (Bertelli Motta et al. 2018; Gao et al. 2018; Souto et al. 2018), one can use the STDs of the mean elemental abundances in the cluster (Table 5) to also gauge internal uncertainties in the analysis. The elements with the smallest abundance scatter among the member stars analysed (STD $\leq$ 0.05 dex) are O, N, Na, Mg, Fe, and Ni. The elements C, Al, Si, K, Ca, V, Mn, Co, and Ce exhibit higher scatter, although still moderate, ranging from 0.06 to 0.08 dex. For Cr, the scatter is 0.09 dex (which can be related to the fact that this element has only one measurable weak line in the APOGEE window), while for Ti, we find a scatter of 0.10 dex. We note that the STD for the iron abundances (0.04 dex), for example, is comparable to that reported by Cunha et al. (2015) for the open cluster NGC 6791, and Souto et al. (2016) for NGC 2420, both of which used APOGEE spectra of red giants in their analyses.

### 4.2 Non-LTE corrections for Na, Mg, K, and Ca

Non-LTE corrections to the LTE Na, Mg, K, and Ca abundances derived in this study can be estimated from the LTE and non-LTE abundances taken from spectral libraries generated for APOGEE DR17. Such synthetic spectra were computed using the Synspec spectral synthesis code (Hubeny et al. 2021), the APOGEE line list (Smith et al. 2021), APOGEE MARCS models (Gustafsson et al. 2008), and in the case of non-LTE, adopting atomic models for Na, Mg, K, and Ca discussed in Osorio et al. (2020). Both the LTE and non-LTE abundances were calculated using the ASPCAP pipeline (García Pérez et al. 2016). The mean differences between the non-LTE and LTE abundance results for our sample stars are given in Table 3.

The mean abundance differences 'non-LTE–LTE' are quite small for all four elements. For sodium, magnesium, and calcium the corrections were found to be negative, indicating that the LTE abundances of these elements are slightly overestimated, but not significantly so, relative to the non-LTE abundances by −0.02, −0.03, and −0.03, respectively. The mean difference for potassium is positive but also insignificant, at +0.01. It's worth noting that these differences are within the uncertainties associated with the abundances of these elements (see Table 5) and non-LTE corrected abundances will not be considered in this study.

## 5 COMPARISONS WITH PREVIOUS RESULTS

### 5.1 Stellar parameters

As discussed previously, the derived stellar parameters in this study relied on photometric calibrations for the derivation of the effective temperature, and fundamental relations for the derivation of the surface gravity. In the following, we compare our parameters with those obtained from high-resolution spectroscopy in the literature.

Several of the more recent studies of the open cluster NGC 6705 presented results from the GES, such as Cantat-Gaudin et al. (2014, 25 stars), Tautvaišienė et al. (2015, 27 stars), Magrini et al. (2017, 15 stars), and Magrini et al. (2021, 71 stars), who used effective temperatures and surface gravities from different survey data releases: GES-viDR1-final, GESviDR2Final, GES-IDR4, and GES-iDR6, respectively. In addition to these studies, there are also results for the NGC 6705 stars studied here in GES-DR5 (latest data release). Another recent study in the literature by Casamiquela et al. (2018) analysed eight stellar members of NGC 6705 observed by the OCCASO survey (Casamiquela et al. 2016).

A comparison of the effective temperatures for stars in common between our work and the studies mentioned above is shown in the top left-hand panel of Fig. 4, while the top right-hand panel shows the ASPCAP pipeline (García Pérez et al. 2016) results from APOGEE DR17 and GES-DR5: residual differences as a function of the literature $T_{\rm eff}$ are shown at the bottom of the two panels. The median differences between the effective temperatures in 'This work – Others' (±MAD) are as follows: −42 ± 57 K for Cantat-Gaudin et al. (2014) (9 stars); 6 ± 41 K for Tautvaišienė et al. (2015) (10 stars); 29 ± 33 K for Magrini et al. (2017) (5 stars); −69 ± 14 K for Casamiquela et al. (2018) (3 stars); 57.5 ± 34.0 for Magrini et al. (2021) (8 stars). The comparison with results GES-DR5 finds $<\Delta T_{\rm eff}>$ = 61 ± 34 K (10 stars) and with ASPCAP APOGEE DR17 (uncalibrated) is 28 ± 55 K (11 stars). In general, all analyses

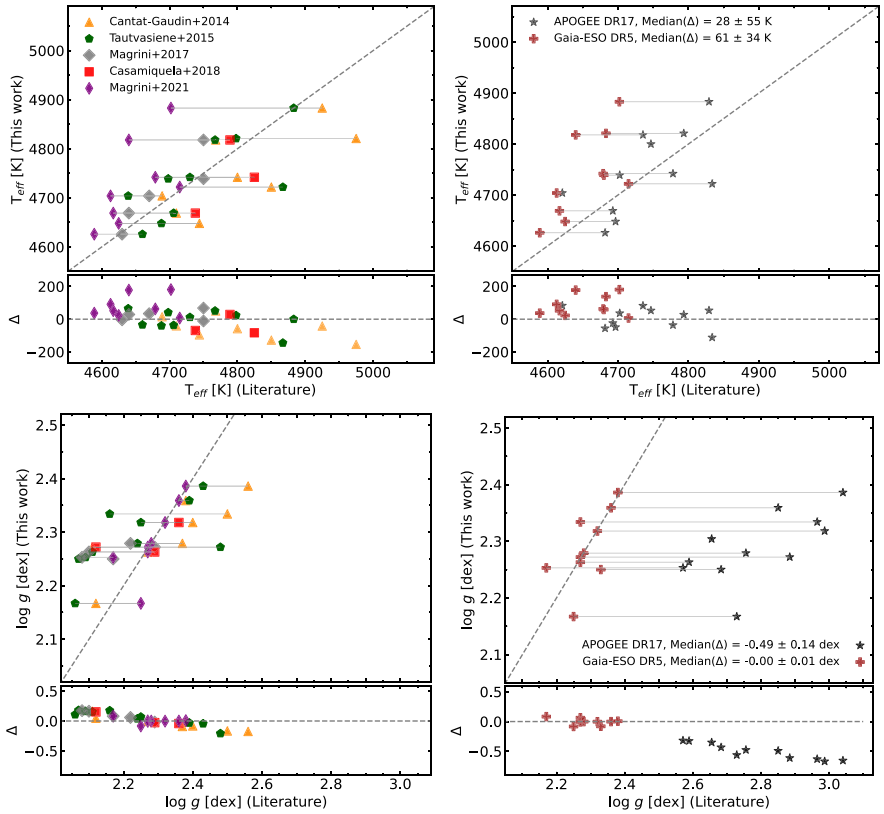


**Figure 4.** Comparison of the effective temperatures (top panels) and surface gravities (bottom panels) derived in this work with the literature results. The orange triangles show the comparison with Cantat-Gaudin et al. 2014, the green pentagons with Tautvaišienė et al. 2015, grey diamonds with Magrini et al. 2017, the red squares with Casamiquela et al. 2018, narrow purple diamonds with Magrini et al. 2021, black stars with APOGEE DR17 (non-calibrated), and the brown cross with GES DR5. Results for the same star are connected by the grey solid lines. The grey dashed lines represent equality. The lower panels show the differences, Δ, 'This work – Others' for effective temperatures and surface gravities, respectively.

yield consistent values of $T_{\rm eff}$ within typical uncertainties in effective temperature scales.

The two bottom panels of Fig. 4 are equivalent to the top panels, but the comparison is for surface gravities. The median differences (±MAD) in log $g$ between 'This Work – Others' (left bottom panel) are, respectively: $-0.06 \pm 0.05$ dex for (Cantat-Gaudin et al. 2014); $0.09 \pm 0.08$ dex for (Tautvaišienė et al. 2015), $0.08 \pm 0.08$ dex for (Magrini et al. 2017); and $-0.03 \pm 0.01$ dex for (Casamiquela et al. 2018). Although there is overall good agreement in these median log $g$ differences, which are well within the expected uncertainties for spectroscopically-determined values of log g (e.g. ∼0.2 dex), there are clear trends in the results, as can be seen from $\Delta\log g$ as a function of log g shown in the bottom subpanel. We generally find a smaller range in log $g$ values for the comparison sample than in the literature. However, our log $g$ values are in excellent agreement with GES-DR5: $\langle\Delta\log g\rangle = -0.0 \pm 0.01$ dex. APOGEE surface gravity results on the other hand, are known to have significant offsets (both for red giants and dwarfs) and this is clear from the bottom right-hand panel of Fig. 4. The range in log $g$ from APOGEE DR17 (ASPCAP derived values) varies roughly between 2.6 and 3.1 dex and the median differences in log $g$ values show systematics: $-0.49 \pm 0.14$ dex. APOGEE also provides post-calibrated log $g$ and in this case, the median log $g$ differences are improved: $-0.31 \pm 0.14$ dex.

### 5.2 Metallicities & other elemental abundances

There are several results for the metallicity of NGC 6705 in the literature. Metallicities derived spectroscopically, with values between +0.02 and +0.24 dex, are reported in studies by Gonzalez & Wallerstein (2000); Magrini et al. (2014); Tautvaišienė et al. (2015); Magrini et al. (2017); Casamiquela et al. (2018, 2021); Magrini et al. (2021). According to our results based on near-infrared spectroscopic analysis of a sample of eleven red giant stars, the mean metallicity of NGC 6705 is $\langle$[Fe/H]$\rangle = +0.13 \pm 0.04$ dex.

Fig. 5 shows violin distributions of the metallicity of NGC 6705 determined both in this study (white distribution) and other studies (grey distributions). The metallicity diagrams from this work, as well as Cantat-Gaudin et al. (2014), Tautvaišienė et al. (2015), Magrini et al. (2017), Casamiquela et al. (2018), and Magrini et al. (2021) are shown from top to bottom in chronological order. In general, our metallicity determination shows excellent agreement with Magrini et al. (2017) and Casamiquela et al. (2018) for their samples of 15 and 8 stars, with reported metallicities of [Fe/H] = $+0.12 \pm 0.05$ dex and [Fe/H] = $+0.17 \pm 0.04$ dex, respectively, or mean metallicity differences of +0.01 and −0.04 dex, respectively. However, the mean metallicity value determined here is somewhat larger than those reported by Tautvaišienė et al. (2015) in a sample of 27 stars ([Fe/H] = $0.00 \pm 0.05$ dex) and Magrini et al. (2021) using 71 stars ($0.02 \pm 0.05$ dex), with the latter study having used both high-resolution UVES and lower resolution GIRAFFE data.

In addition, an investigation into the differences between the metallicities of 'This work – Other' (±MAD) for stars in common between the studies, finds good agreement in some cases and systematic differences in others. There are no significant systematic differences when comparing with Casamiquela et al. (2018), Magrini et al.

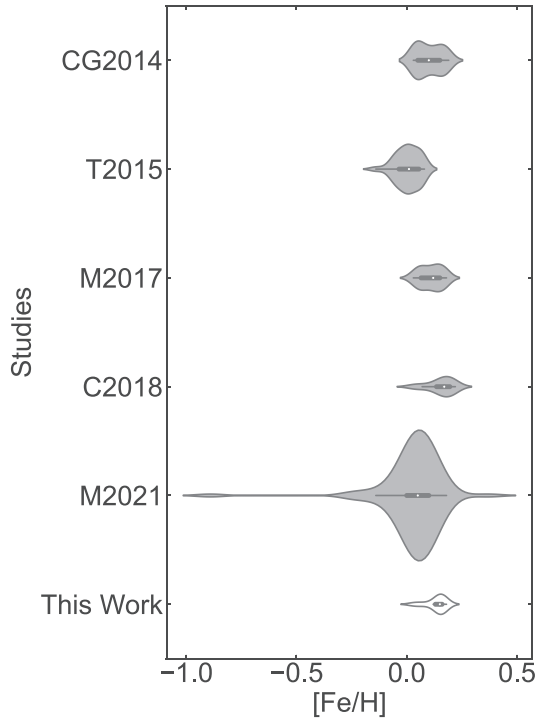


**Figure 5.** Metallicity distribution of NGC 6705 stars. The white distribution represents our [Fe/H] results, while the grey sequences show the literature [Fe/H] results: Cantat-Gaudin et al. (2014, CG2014), Tautvaišienė et al. (2015, T2015), Magrini et al. (2017, M2017), Casamiquela et al. (2018, C2018), and Magrini et al. (2021, M2021). White dots in the distribution indicate the median, while the thick bar represents the interquartile range, and the thin bar shows the 95 per cent confidence interval. Wider regions of the distribution represent a higher probability that a star will have that [Fe/H] value.

(2017), and Cantat-Gaudin et al. (2014), with median differences of 0.00 ± 0.01, 0.03 ± 0.02, and 0.03 ± 0.04 dex, respectively. The comparison with results from APOGEE DR17 is also very good: 0.04 ± 0.03 dex. On the other hand, there are larger differences between the metallicities of Tautvaišienė et al. (2015), Magrini et al. (2021), and GES DR5, for ten, eight and ten stars, with our metallicities being higher than theirs by 0.13 ± 0.04, 0.12 ± 0.04, and 0.12 ± 0.02 dex, respectively.

Besides metallicities, which are discussed above, we summarize in Table 6, the comparisons between the abundances of the other elements studied here with literature values, again exemplified as the median abundance differences (±MAD) [X/Fe] for 'This Work – Other Work' for stars in common with the studies of Cantat-Gaudin et al. (2014), Tautvaišienė et al. (2015), Magrini et al. (2017), Casamiquela et al. (2018), and the surveys APOGEE DR17 and GES-DR5. Most of the systematic differences between the results are less than or equal to 0.1 dex and this is not surprising given the different methodologies adopted in the various studies, but there are some cases with more significant discrepancies, such as, for example, oxygen having a median difference of −0.25 dex for Casamiquela et al. (2018) and −0.20 dex for GES-DR5, magnesium being different by −0.19 dex also for GES-DR5, or sodium having a −0.26 dex offset in comparison with Cantat-Gaudin et al. (2014). In addition, the MAD values for the majority of the cases are also typically small (<0.05 dex), with only one being larger than 0.1 dex.

## 6 DISCUSSION

### 6.1 C, N, O, Na, Al, and mixing in the red-giants of NGC 6705

NGC 6705 provides an important astrophysical laboratory in which to probe red-giant mixing in RGB and RC stars, as the masses of this cluster's red giants are $M \sim 3.3\,M_\odot$, well above the mass limit for stars that undergo the He-core flash ($M < 2.1\,M_\odot$ at solar metallicity, e.g. Karakas & Lattanzio 2014). As discussed in Section 3 and illustrated in Fig. 3, the red giants sampled here are likely a mixture of RGB and RC stars, with the interiors of the RGB stars consisting of an inert He core surrounded by a H-burning shell, while the RC stars have evolved beyond the RGB and are powered by core-He burning. Due to uncertainties in our derived values of $T_{\rm eff}$ and log $g$, assigning a classification to a red giant as either an RGB or RC star (without asteroseismic data) is uncertain, although based on their positions in the Kiel diagram in Fig. 3, it appears that those red giants with $T_{\rm eff} > 4750$–$4800$ K likely belong to the RC, while the cooler ones are evolving up the RGB. This classification criterion results in our sample dividing into four RC stars and seven RGB stars.

The luminosities of the RGB stars indicate that all have experienced the first dredge-up (as have the RC stars), which has contaminated their photospheres with matter that has undergone partial H-burning via the CN-cycle. This contamination is revealed through the abundances of carbon, both $^{12}$C and $^{13}$C (although carbon-13 will not be discussed here) and $^{14}$N. As a result of the first dredge-up, the surface $^{12}$C abundance will be lowered, while that of $^{14}$N will be increased significantly. As shown in Table 5, the average carbon and nitrogen abundances are $\langle A(^{12}\mathrm{C})\rangle = 8.44 \pm 0.07$ and $\langle A(^{14}\mathrm{N})\rangle = 8.47 \pm 0.05$, respectively. The solar abundances are $A(^{12}\mathrm{C}) = 8.46$ and $A(^{14}\mathrm{N}) = 7.83$, but with the average metallicity of NGC 6705 being [Fe/H] = +0.13, the average cluster red giant abundances of carbon and nitrogen with respect to iron are $[^{12}\mathrm{C/Fe}] = -0.16$ and $[^{14}\mathrm{N/Fe}] = +0.51$, in qualitative agreement with that expected from first dredge-up. Theoretical models of the 1st dredge-up and thermohaline mixing by Charbonnel & Lagarde (2010) predict $[^{12}\mathrm{C/Fe}] = -0.21$ and $[^{14}\mathrm{N/Fe}] = +0.47$ for stars with $M = 3\,M_\odot$ after dredge-up, which is in quantitative agreement with our results for the red giants in NGC 6705.

Fig. 6 presents a different way to view the 1st dredge-up, with the $^{14}$N-abundance plotted versus the $^{12}$C-abundance, and the observed red giants in NGC 6705 are divided into RGB (blue symbols) and RC (red symbols) stars, respectively. The smooth magenta curve represents a constant sum of the number abundances of carbon-12 and nitrogen-14, as the sum of these nuclei are conserved approximately during CN-cycle H-burning. This curve represents schematically the 1st dredge-up as a mixing curve. There are four stable nuclei involved in the CN-cycle: $^{12}$C, $^{13}$C, $^{14}$N, and $^{15}$N, of which carbon-13 and nitrogen-15 are considered minor species. In pure equilibrium CN-cycle matter, the value of $^{12}$C/$^{13}$C can be as small as 3.5, which would shift the upper part of the mixing curve in Fig. 6 to lower $^{12}$C abundances by ∼0.1 dex, however, the expected ratio in 3.3 $M_\odot$ RGB stars is 18–20 (Lagarde et al. 2012; McCormick et al. 2023), which would have a negligible effect on the mixing curve. Nitrogen-15 is an even more minor species, with typical 1st dredge-up values expected to be smaller than the solar value of $^{14}$N/$^{15}$N = 272 (Wannier et al. 1991), so this isotope can be neglected from our discussion.

The sum of N($^{12}$C) + N($^{14}$N) in Fig. 6 was taken as the average values from the RGB plus RC stars, and the initial individual carbon-12 and nitrogen-14 abundances were set assuming an initial solar ratio of N(C)/N(N) = 4.1 (Grevesse, Asplund & Sauval 2007). These two constraints lead to initial carbon and nitrogen abundances for

**Table 6.** Median abundance differences 'This Work – Other'.

| [X/Fe] | APOGEE DR17 (#11) | GES DR5 (#10) | CG2014 (#8) | T2015 (#10) | M2017 (#5) | C2018 (#3) | SS2022 (#9) |
|---|---|---|---|---|---|---|---|
| C | −0.18 ± 0.03 | −0.06 ± 0.04 | ... | −0.06 ± 0.03 | ... | ... | ... |
| N | 0.06 ± 0.03 | −0.05 ± 0.06 | ... | −0.12 ± 0.03 | ... | ... | ... |
| O | 0.03 ± 0.02 | −0.20 ± 0.03 | ... | −0.18 ± 0.08 | −0.03 ± 0.04 | −0.25 ± 0.07 | ... |
| Na | 0.11 ± 0.05 | 0.03 ± 0.10 | −0.26 ± 0.03 | ... | ... | ... | ... |
| Mg | 0.11 ± 0.03 | −0.19 ± 0.06 | −0.16 ± 0.04 | ... | −0.10 ± 0.04 | −0.14 ± 0.11 | ... |
| Si | 0.01 ± 0.03 | −0.04 ± 0.07 | 0.03 ± 0.02 | ... | 0.04 ± 0.04 | −0.05 ± 0.06 | ... |
| Ca | 0.04 ± 0.02 | 0.12 ± 0.09 | ... | ... | 0.11 ± 0.03 | −0.05 ± 0.10 | ... |
| Al | −0.00 ± 0.04 | −0.11 ± 0.05 | −0.15 ± 0.06 | ... | ... | ... | ... |
| K | −0.04 ± 0.06 | ... | ... | ... | ... | ... | ... |
| Ti | −0.06 ± 0.05 | −0.01 ± 0.10 | ... | ... | 0.05 ± 0.00 | −0.11 ± 0.01 | ... |
| V | 0.26 ± 0.03 | 0.05 ± 0.04 | ... | ... | 0.02 ± 0.01 | ... | ... |
| Cr | 0.03 ± 0.06 | 0.09 ± 0.10 | ... | ... | 0.15 ± 0.04 | ... | ... |
| Mn | 0.01 ± 0.06 | 0.07 ± 0.06 | ... | ... | ... | ... | ... |
| Co | −0.03 ± 0.04 | −0.05 ± 0.05 | ... | ... | ... | ... | ... |
| Ni | 0.10 ± 0.04 | 0.12 ± 0.05 | ... | ... | 0.12 ± 0.03 | ... | ... |
| Ce | 0.01 ± 0.07 | 0.05 ± 0.07 | ... | ... | ... | ... | −0.07 ± 0.02 |

*Note.* Our results are compared with: CG2014: Cantat-Gaudin et al. (2014); T2015: Tautvaišienė et al. (2015); M2017: Magrini et al. (2017); C2018: Casamiquela et al. (2018); SS2022: and Sales-Silva et al. (2022).

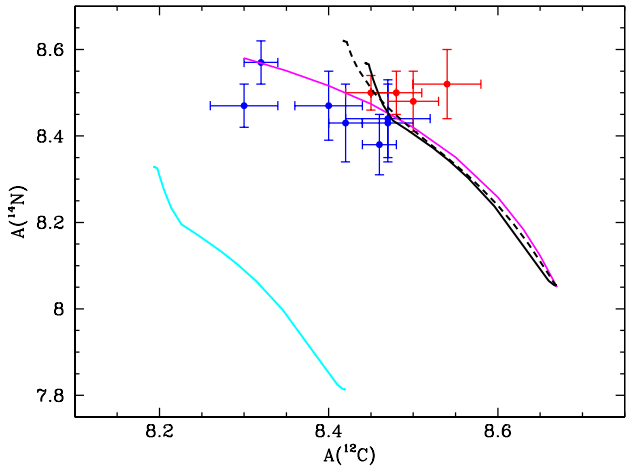


**Figure 6.** Carbon-12 and nitrogen-14 abundances for the NGC 6705 red giants are divided into RGB (blue symbols) and RC (red symbols) stars. The solid magenta curve is a 'mixing line' defined by a constant sum of $^{12}$C and $^{14}$N nuclei. A 3 $M_\odot$ solar-metallicity standard stellar model (i.e. no extra mixing) from Lagarde et al. (2012) is shown as a cyan curve, while the black curves represent solar metallicity models simply shifted by +0.22 dex in the initial $^{12}$C and $^{14}$N abundances to mimic the metallicity of NGC 6705, with the standard model shown by the solid line and a model that includes rotational and thermohaline mixing shown by the dashed line.

NGC 6705 of $A(^{12}C) = 8.67$ and $A(^{14}N) = 8.05$ and, with these initial abundance values, the mixing curve passes through the NGC 6705 RGB stars. One point to note from Fig. 6 is that the four RC stars, while having $^{14}$N abundances that are very similar to the RGB stars, exhibit $^{12}$C abundances that are slightly larger than the RGB sample. The average abundances of the two groups are $\langle A(^{12}C)\rangle = 8.41 \pm 0.07$ and $\langle A(^{14}N)\rangle = 8.46 \pm 0.05$ for the RGB stars and $\langle A(^{12}C)\rangle = 8.49 \pm 0.03$ and $\langle A(^{14}N)\rangle = 8.50 \pm 0.01$ for the RC stars, resulting in linear values for the C/N abundance ratios of $0.92 \pm 0.22$ and $0.99 \pm 0.07$ for the RGB and RC stars, respectively. A Kolmogorov–Smirnov test of the C/N ratios in the RGB and RC stars finds that they can be represented by a single population in C/N.

Models by Lagarde et al. (2012) for a 3 $M_\odot$ solar-metallicity star are also shown in Fig. 6 as a comparison to the simple mixing curve. As Lagarde et al. (2012) only presented solar-metallicity, or lower, models, we show their solar-metallicity model as the continuous cyan curve, which begins at an initial abundance of $A(^{12}C) = 8.43$ and $A(^{14}N) = 7.83$ and evolves from there. Since our discussion from above indicates that NGC 6705 is metal-rich relative to the Sun, the black curves in Fig. 6 represent solar-metallicity models from Lagarde et al. (2012) in which the initial $^{12}$C and $^{14}$N abundances are increased by +0.22 dex; the solid black curve is the standard model, while the dashed curve represents the model that includes rotational and thermohaline mixing. A quantitative comparison of models with observationally-derived abundance would demand consistent models; however, this straightforward test indicates that the 11 red giant members of NGC 6705 analysed here, at $M \sim 3.3\,M_\odot$, display unremarkable C and N abundances when compared to stellar models.

Moving up the periodic table past C and N, we investigate additional elemental abundances that are potentially sensitive to red giant mixing in the mass range of $M \sim 3$–$4\,M_\odot$ and focus on oxygen (as $^{16}$O), sodium, and aluminum. The red giants studied here have a mass of $\sim$3.3 $M_\odot$ and exhibit a significant overabundance of [Na/Fe] = +0.29 ± 0.04 dex. This confirms that giant stars with masses greater than 3 $M_\odot$ can have an overabundance of sodium, providing a strong indication that the sodium overabundance in these stars is caused by internal evolutionary processes, as suggested by Smiljanic et al. (2016). More specifically, we examine the behaviours of [Na/Fe], [Al/Fe], and [O/Fe] as functions of stellar mass in Fig. 7 and, in addition to NGC 6705, we consider the slightly more metal poor ([Fe/H] = −0.16) open cluster NGC 2420 ($M_{TO} = 1.6\,M_\odot$) with Na, Al, and O abundances taken from Souto et al. (2016), the open clusters NGC 4815 ($M_{TO} = 2.5\,M_\odot$), Berkeley 81 ($M_{TO} = 2.2\,M_\odot$), and Trumpler 20 ($M_{TO} = 1.8\,M_\odot$), for which Na and Al abundances and masses were taken from Smiljanic et al. (2016), while the oxygen abundances are from Magrini et al. (2017); the models from Lagarde et al. (2012), both standard as well as those including rotation, are also shown. The left-hand panel of Fig. 7 reveals an overabundance of sodium which increases with increasing red-giant mass, as predicted by the models. In the case of Al (middle panel of Fig. 7), we observe that the mean Al abundance of NGC 6705

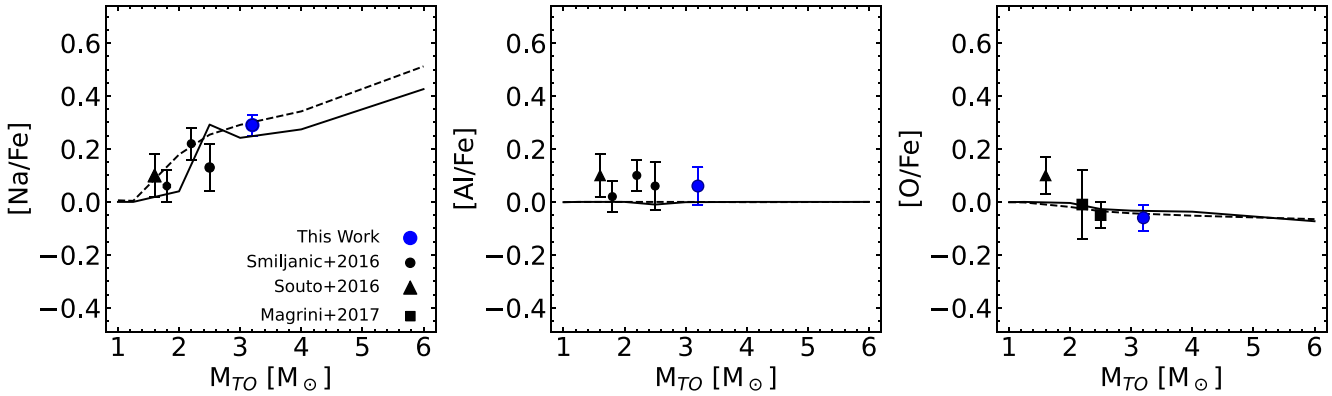


**Figure 7.** Mean cluster abundances of Na, Al, and O versus cluster turn-off mass. The blue circle corresponds to the abundances of NGC 6705 determined in this study, and the black circles correspond to mean Na and Al abundances of NGC 4815, Berkeley 81, and Trumpler 20 derived for giant stars in Smiljanic et al. (2016). Mean abundances of O are taken from Magrini et al. (2017) for NGC 4815 and Berkeley 81 (black squares). The black triangle correspond to mean Na, Al, and O abundances of NGC 2420 derived in Souto et al. (2016). The black solid and dashed lines correspond to the standard model and the model that includes rotational and thermohaline mixing, both from Lagarde et al. (2012), respectively.

determined here is slightly enhanced ([Al/Fe] $= +0.06 \pm 0.07$) but in agreement with the models within the uncertainties, with all clusters displaying a small (but not significant) offset from the models. In summary, we do not find that the [Al/Fe] abundance is enhanced in NGC 6705, unlike what was previously suggested in Smiljanic et al. (2016) for which the [Al/Fe] overabundance was +0.3. The right-hand panel of Fig. 7 shows [O/Fe] as a function of mass. According to the models of Lagarde et al. (2012), there is a small trend of decreasing oxygen with increasing stellar mass and our oxygen abundance for NGC 6705 is also in agreement with the models. Overall, the observed abundances of $^{12}$C, $^{14}$N, $^{16}$O, Na, and Al in the NGC 6705 red giants provide a benchmark for models of red giant mixing in intermediate-mass stars of $M \sim 3$–4 $M_\odot$ at near-solar metallicity.

### 6.2 Is the young open cluster NGC 6705 $\alpha$-enhanced?

As discussed in the introduction, one of the interesting recent results in the literature is the finding that there is a population of stars in the Galaxy that is young and enriched in [$\alpha$/Fe]; a result which was based on stellar ages obtained via CoRoT asteroseismology and chemical abundances taken from the APOGEE survey (Chiappini et al. 2015). Martig et al. (2015) also identified young $\alpha$-enhanced stars using independent age estimates inferred from Kepler asteroseismology. In simple terms, such population is unexpected because in principle a young star is formed from gas already enriched in Fe from SN Ia, having therefore a decreased [$\alpha$/Fe] ratio. However, these $\alpha$-enhanced stars that appear to be young may be products binary interactions/mergers (e.g. Izzard et al. 2018; Silva Aguirre et al. 2018; Hekker & Johnson 2019; Jofré et al. 2023), being actually old and having the expected $\alpha$-Fe content for their age. Moreover, Miglio et al. (2021) identified a sample of 400 red giant stars from the Kepler field (having asteroseismic data) that belong to the thick disc ([$\alpha$/Fe] $> +0.1$) and found that ~5 per cent of stars on the RGB were overmassive given the estimated age of the thick disc stars of ~11 Gyr ($M > 1.1$ $M_\odot$). This fraction of overmassive stars increased to ~18 per cent for red clump giants and Miglio et al. (2021) suggest that this result supports the idea that these stars increased their initial masses via interactions with a binary companion (either mass transfer or mergers) while evolving up the RGB.

In this context, the results in the literature finding the members of the young open cluster NGC 6705 to be $\alpha$-enhanced is puzzling. Casamiquela et al. (2018) studied a sample with eight stars members of the open cluster NGC 6705 from high-resolution optical spectra and found that they were enriched in $\alpha$-elements with an average of $\langle$[$\alpha$/Fe]$\rangle = +0.11 \pm 0.06$. Tautvaišienė et al. (2015) also studied NGC 6705 but focused only on the analysis of the elements carbon, nitrogen, and oxygen, which are involved in H-burning. They found that the mean oxygen abundance in their sample of 27 red giants was mildly enhanced, with $\langle$[O/Fe]$\rangle = 0.12 \pm 0.05$. Magrini et al. (2014, 2017) also found evidence of enhancements in some of the $\alpha$-elements in this cluster. Such results for an open cluster provided a possible connection with the young and $\alpha$-enhanced field stars in the Galaxy, which was examined in Casamiquela et al. (2018).

The main goal of this study was to do a detailed spectroscopic analysis of APOGEE spectra of NGC 6705 red-giants and, in particular, probe their $\alpha$-element abundances. Fig. 8 summarizes our results in the form of the [$\alpha$/Fe] versus [Fe/H] diagram for the five $\alpha$-elements studied: O, Mg, Si, Ca, and Ti. Each panel depicts the mean [$\alpha$/Fe] (represented by the red circles) and their corresponding STDs. The mean abundances obtained for the eleven studied red-giants are shown in each panel. On the solar scale, our sample exhibits on average a titanium-to-iron ratio ($\langle$[Ti/Fe]$\rangle = -0.10 \pm 0.08$), and an oxygen-to-iron ratio slightly below solar ($\langle$[O/Fe]$\rangle = -0.06 \pm 0.05$), while the mean calcium and silicon abundance ratios are marginally higher than solar scaled values, but not significantly so ($\langle$[Ca/Fe]$\rangle = +0.03 \pm 0.05$; $\langle$[Si/Fe]$\rangle = +0.03 \pm 0.04$). The magnesium abundance for the cluster is also not enhanced and has a mean value slightly below solar ($\langle$[Mg/Fe]$\rangle = -0.02 \pm 0.05$). All in all, our analysis does not find NGC 6705 to be $\alpha$-enhanced and this is corroborated by the average of the four $\alpha$-elements studied, which yields $\langle$[$\alpha$/Fe]$\rangle = -0.03 \pm 0.05$.

Given the location of NGC 6705 in the inner Galactic disc, it is also of interest to investigate whether the measured [$\alpha$/Fe] abundances for this open cluster are consistent with those of other open clusters residing in the inner galaxy, and how their $\alpha$-element abundance pattern contrasts with the galactic abundance gradients. The mean Fe abundances obtained here for NGC 6705 are in line with the gradients for [Fe/H] versus $R_{GC}$ presented in Fig. 4 of Myers et al. (2022). The five panels of Fig. 9 show the O, Mg, Si, Ca, and Ti over Fe ratios as a function of galactocentric distance ($R_{GC}$) for the open clusters

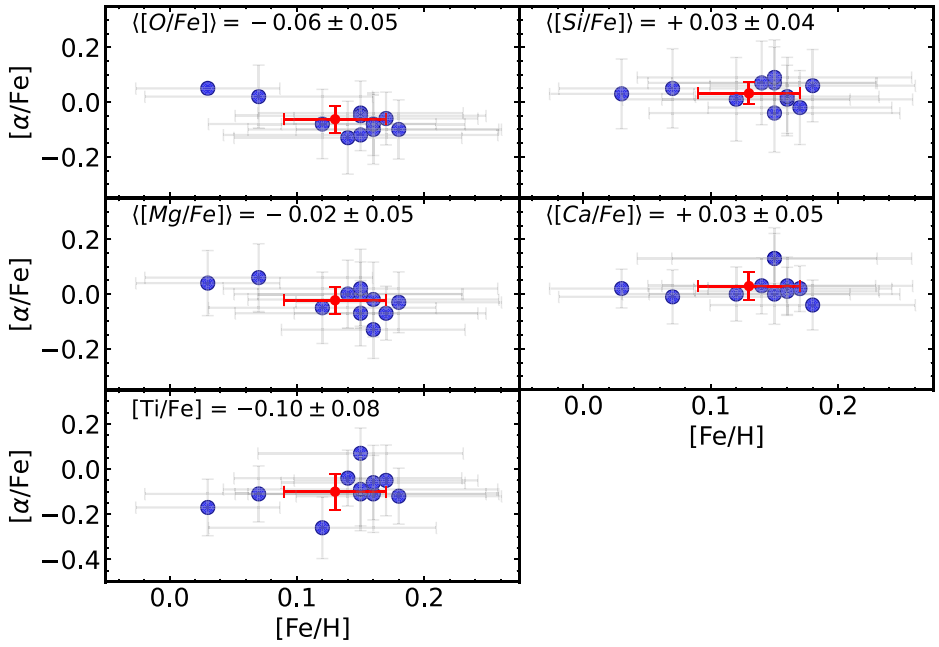


**Figure 8.** [α/Fe] versus [Fe/H] diagram for NGC 6705 stars. In each panel, the red circle indicates the mean abundance ratios of O, Mg, Si and Ca, and Ti as a function of mean metallicity, with the error bars representing the STD.

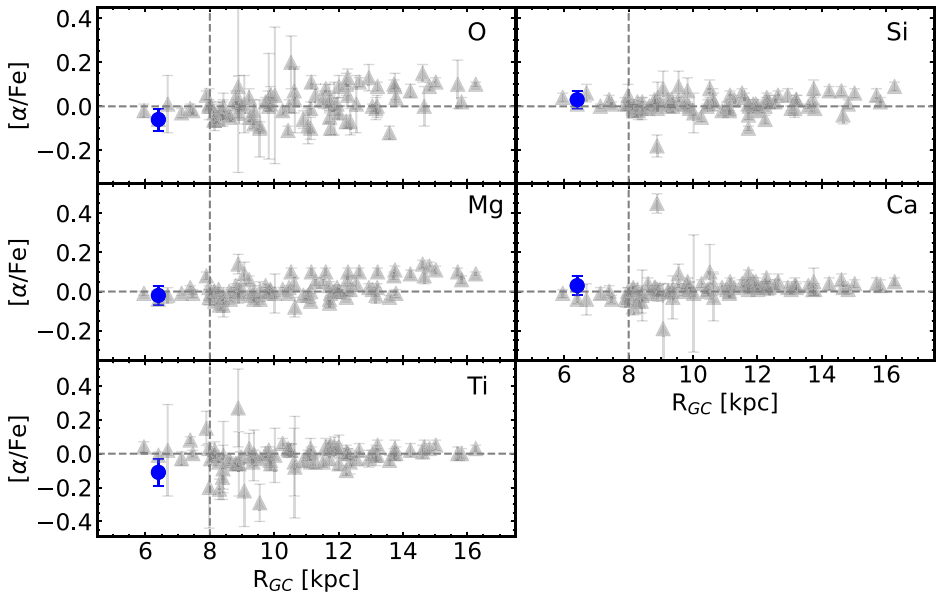


**Figure 9.** The plot shows the cluster mean abundances of [α/Fe] as a function of the cluster galactocentric distance (*x*-axis). The grey triangles represent the OCCAM data from Myers et al. 2022, while blue circles represent the results of this work.

from the OCCAM sample (Myers et al. 2022, grey triangles); our results for NGC 6705 are represented by the solid blue circles. The abundances in Myers et al. (2022) are calibrated abundances from DR17, and these were computed using the plane parallel radiative transfer code Synspec and in non-LTE for the elements Mg, Si, and Ca (Osorio et al. 2020). A simple inspection of Fig. 9 shows that the ratios for the five $\alpha$-elements in NGC 6705 are overall consistent with and do not fall above the results for the other open cluster in the OCCAM sample, and these seem to be in line also with the general trend of metallicity with $R_{GC}$ for the inner galaxy, with all open clusters in the inner galaxy having [$\alpha$/Fe] ratios roughly around the solar value.

### 6.3 Na, Al, K, V, Cr, Mn, Co, and Ce abundance patterns

The [X/Fe] versus [Fe/H] ratios for the other studied species besides CNO and $\alpha$-elements are presented as filled blue circles in Fig. 10, along with abundance results for Galactic field stars from five high-resolution optical studies in the literature (Chen et al. 2000; Adibekyan et al. 2012; Bensby, Feltzing & Oey 2014; Battistini &

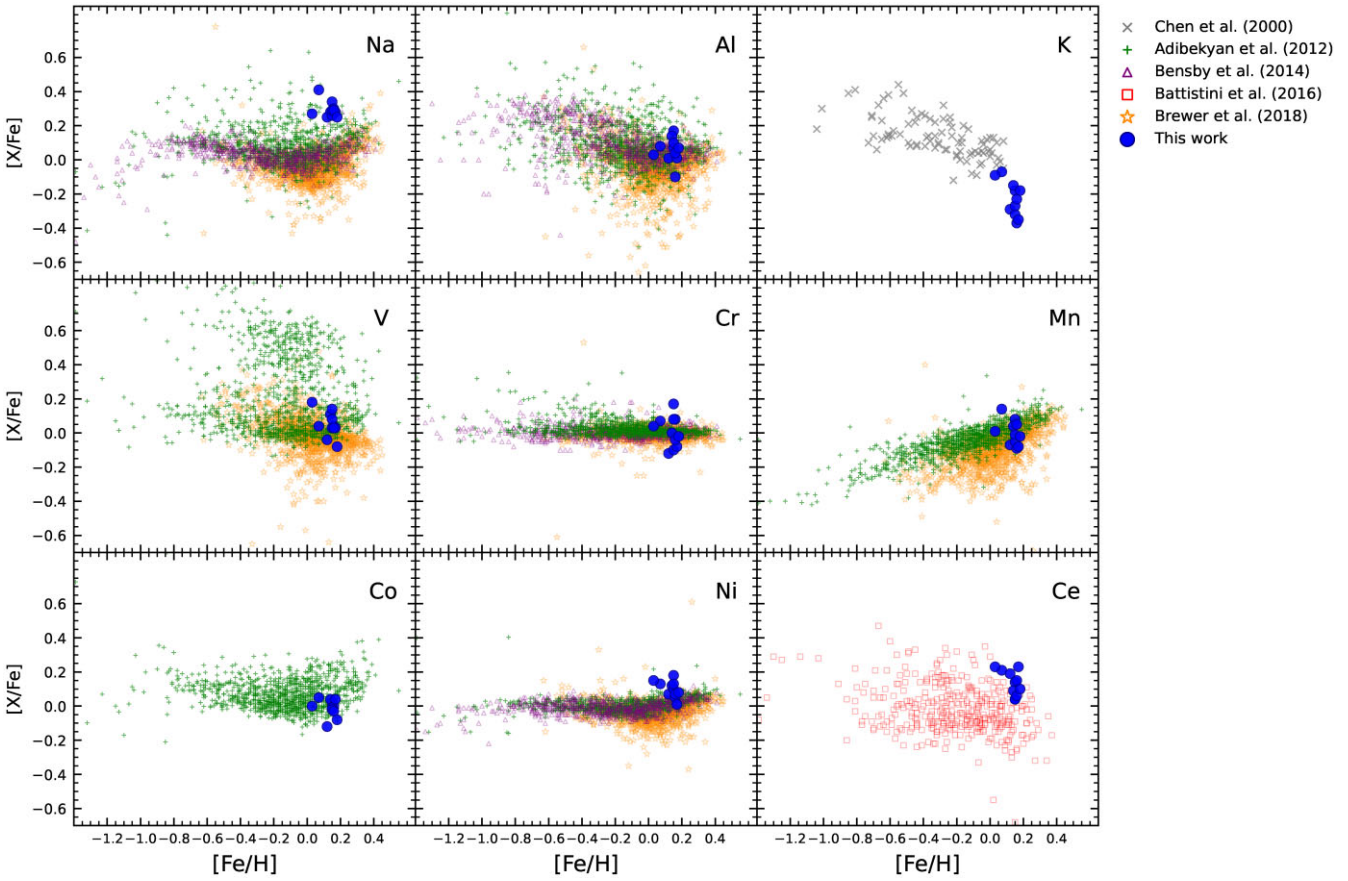


**Figure 10.** Galactic trends of [X/Fe] as a function of [Fe/H] for the stars in the open cluster NGC 6705 (blue circles). Field dwarf stars in the thin and thick disc are from Chen et al. (2000, grey xs), Adibekyan et al. (2012, green pluses), Bensby et al. (2014, purple triangles), Battistini & Bensby (2016, red squares), and Brewer & Fischer (2018, orange stars).

Bensby 2016; Brewer & Fischer 2018). The three top panels of Fig. 10 show the odd-Z elements Na, Al, and K. The derived Al abundances fall within the field star distribution at [Fe/H] $\sim +0.15$, while for sodium the abundances of NGC 6705 red-giants fall above the trend; this likely is a mixing signature, as discussed in Section 6.1. For K, the metallicity range probed for the field stars (Chen et al. 2000) stops at around solar [Fe/H], and the [K/Fe] values for NGC 6705 simply extend the downward trend of [K/Fe] versus [Fe/H]. For the Fe-peak elements V, Cr, Mn, and Co, our results also generally fall within the field star trends, noting, however, that there is more scatter in our Cr abundances when compared with the very thin (and flat) trend for the field stars obtained from the optical studies. For Ni, the derived abundances for some of the stars fall above the field star trend, the latter being also quite well defined according to the results in Bensby et al. (2014) and Adibekyan et al. (2012).

The only heavy element analysed from APOGEE spectra is the s-process element Ce, which is produced mainly in AGB stars (Cescutti & Matteucci 2022). The [Ce/Fe] versus [Fe/H] abundance pattern for the field stars from Battistini & Bensby (2016), shown as comparisons in Fig. 10, overall exhibits some scatter. The mean Ce abundance obtained for NGC 6705 red giants is enhanced, with $\langle$[Ce/Fe]$\rangle = +0.13 \pm 0.07$, falling in the upper envelope of the abundance distribution of field stars at [Fe/H] $> 0.0$. In addition, the observed [Ce/Fe] enhancement for NGC 6705 is in-line with previous findings that [Ce/Fe] ratios are a function of age (Casali et al. 2020). The observed chemical pattern resembles the enhancements in [Ce/Fe] observed in other young open clusters, which is larger than typical values of [Ce/Fe] in old open clusters with similar metallicities (see Fig. 6 in Sales-Silva et al. 2022).

## 7 CONCLUSIONS

NGC 6705 is a young open cluster that serves as an abundance benchmark for the inner Milky Way young stellar populations ($\sim$1–5 $\times$ $10^8$ yrs). The red giant members of this cluster are also good stellar samples in which to probe evolution along the RGB and RC in 3–4 $M_\odot$ metal-rich giants.

Previous works in the literature found this benchmark young open cluster to be $\alpha$-enhanced, a puzzling result as young stars are expected to be formed from material already enriched in Fe from SN Ia, which would result in low values of [$\alpha$/Fe]. The abundance patterns for NGC 6705 were discussed by Casamiquela et al. (2018) in the context of the population of young and $\alpha$-enhanced field stars found from CoRoT and Kepler data (Chiappini et al. 2015; Martig et al. 2015; Queiroz et al. 2023).

The population of young-$\alpha$-enhanced stars identified in the Galaxy, however, has now been shown to be old and to possibly result from binary mergers or mass transfer, as suggested by Izzard et al. (2018) and Hekker & Johnson (2019). This scenario was strengthened by the results of Miglio et al. (2021) from their analysis of old, thick-disc giants in the Kepler field that have been found to be overmassive, meaning that their initial birth masses were increased by mass transfer or mergers while evolving up the RGB.

The possibility that the young cluster NGC 6705 is $\alpha$-enhanced was further tested here based on the derived abundances of five $\alpha$-elements (O, Mg, Si, and Ca, and Ti), finding $\langle[\alpha/\mathrm{Fe}]\rangle = -0.025 \pm 0.051$), and indicating that NGC 6705 does not exhibit $\alpha$-enhancement. Our results are consistent with the expectation that the young open cluster NGC 6705 in the Galactic disc has solar-like values of the [$\alpha$/Fe] ratio.

This study presented a quantitative spectroscopic analysis of eleven red giant stars members of the open cluster NGC 6705, determining abundances of the elements C, N, Na, Al, K, Ti, V, Cr, Mn, Fe, Co, Ni, and Ce, as well as the $\alpha$-elements O, Mg, Si, and Ca. The analysis was carried out in LTE, using MARCS spherical model atmospheres with the spherical radiative transfer program Turbospectrum. The mean abundances obtained for the cluster are presented in Table 5.

Our results from the analysis of APOGEE NIR spectra for the NGC 6705 stars find an average metallicity of $\langle[\mathrm{Fe/H}]\rangle = +0.13 \pm 0.04$ dex, which is in agreement with the general trend of increasing metallicity with decreasing distance from the Galactic Centre. The ratios of the Fe-peak elements are found to track Galactic trends, as defined by field stars, with the mean values of [X/Fe] for V, Cr, Mn, Co, and Ni being +0.05, +0.01, 0.00, −0.01, and +0.10, respectively. The [Al/Fe] abundance ratios also fall within the distribution of field stars, while the [K/Fe] values appear to extend the downward trend of [K/Fe] versus [Fe/H]. Results for the s-process element cerium, with $\langle[\mathrm{Ce/Fe}]\rangle = +0.13$, are similar to the Ce abundances observed in other young open clusters with similar metallicities to NGC 6705 and consistent with an increase in the [Ce/Fe] ratio with decreasing age (Sales-Silva et al. 2022).

The red-giant members of NGC 6705 exhibit the low-$^{12}$C and enhanced-$^{14}$N abundance signature of 1st dredge-up on the RGB, with mean values of $[^{12}\mathrm{C/Fe}] = -0.16$ and $[^{14}\mathrm{N/Fe}] = +0.51$. These abundances are in quantitative agreement with 3–4.0 $\mathrm{M}_{\odot}$ stellar models from Lagarde et al. (2012). The sample here contains both candidate RGB (7) and RC (4) stars and a comparison of the $^{12}$C and $^{14}$N abundances between the two groups reveals no significant differences, indicating no measurable 'extra mixing' processes as these metal-rich 3.3 $\mathrm{M}_{\odot}$ stars evolve up the RGB and then onto the He-burning red clump. In addition to carbon-12 and nitrogen-14, oxygen, sodium, and aluminum abundances were compared to stellar models in order to test for deep mixing signatures. Sodium was found to be enhanced significantly with $[\mathrm{Na/Fe}] = +0.29 \pm 0.04$, in general agreement with stellar evolution model predictions from Lagarde et al. (2012) and in-line with what was previously concluded in Smiljanic et al. (2016). For aluminum, however, we find non-enhanced values of [Al/Fe] for NGC 6705, in contrast with what was found in the latter study. The values of [O/Fe] and [Al/Fe] for NGC 6705 were found to be roughly solar, within small uncertainties and a comparison to models by Lagarde et al. (2012) also finds agreement with our O and Al abundance results for stellar masses of 3.3 $\mathrm{M}_{\odot}$. Summarizing, at the masses of the NGC 6705 red giants, standard stellar evolution models agree well with the observationally-derived abundances of $^{12}$C, $^{14}$N, $^{16}$O, Na, and Al.

## ACKNOWLEDGEMENTS

We thank the referee for suggestions that improved the paper. VL-T acknowledges the financial support from Coordenação de Aperfeiçoamento de Pessoal de Nível Superior (CAPES). KC acknowledges that her work is supported, in part, by the National Science Foundation through NSF grant No. AST-2206543. DS thanks the National Council for Scientific and Technological Development – CNPq.

Funding for the Sloan Digital Sky Survey IV has been provided by the Alfred P. Sloan Foundation, the U.S. Department of Energy Office of Science, and the Participating Institutions. SDSS-IV acknowledges support and resources from the Center for High-Performance Computing at the University of Utah. The SDSS website is www.sdss.org. SDSS-IV is managed by the Astrophysical Research consortium for the Participating Institutions of the SDSS Collaboration including the Brazilian Participation Group, the Carnegie Institution for Science, Carnegie Mellon University, the Chilean Participation Group, the French Participation Group, Harvard-Smithsonian Center for Astrophysics, Instituto de Astrofísica de Canarias, The Johns Hopkins University, Kavli Institute for the Physics and Mathematics of the Universe (IPMU)/University of Tokyo, Lawrence Berkeley National Laboratory, Leibniz Institut für Astrophysik Potsdam (AIP), Max-Planck-Institut für Astronomie (MPIA Heidelberg), Max-Planck-Institut für Astrophysik (MPA Garching), Max-Planck-Institut für Extraterrestrische Physik (MPE), National Astronomical Observatory of China, New Mexico State University, New York University, University of Notre Dame, Observatório Nacional/MCTI, The Ohio State University, Pennsylvania State University, Shanghai Astronomical Observatory, United Kingdom Participation Group, Universidad Nacional Autónoma de México, University of Arizona, University of Colorado Boulder, University of Oxford, University of Portsmouth, University of Utah, University of Virginia, University of Washington, University of Wisconsin, Vanderbilt University, and Yale University.

*Facilities: Sloan, Gaia.*

Software: BACCHUS (Masseron et al. 2016), Turbospectrum (Alvarez & Plez 1998; Plez 2012; https://github.com/bertrandplez/Turbospectrum2019).

## DATA AVAILABILITY

The data underlying this article are available in the SDSS Data Release 17 for APOGEE (Abdurro'uf et al. 2022). These data can be accessed at the following links: https://www.sdss.org/dr17/irspec/(APOGEE).

## REFERENCES

Abdurro'uf et al., 2022, ApJS, 259, 35
Adibekyan V. Z., Sousa S. G., Santos N. C., Delgado Mena E., González Hernández J. I., Israelian G., Mayor M., Khachatryan G., 2012, A&A, 545, A32
Alvarez R., Plez B., 1998, A&A, 330, 1109
Anders F. et al., 2014, A&A, 564, A115
Asplund M., Amarsi A. M., Grevesse N., 2021, A&A, 653, A141
Baglin A., Auvergne M., Barge P., Deleuil M., Catala C., Michel E., Weiss W., Team COROT , 2006, in Fridlund M., Baglin A., Lochard J., Conroy L.eds, The CoRoT Mission Pre-Launch Status—Stellar Seismology and Planet Finding. 1306, ESA Special Publication, p.33
Bailer-Jones C. A. L., Rybizki J., Fouesneau M., Demleitner M., Andrae R., 2021, AJ, 161, 147
Battistini C., Bensby T., 2016, A&A, 586, A49
Beaton R. L. et al., 2021, AJ, 162, 302
Bensby T., Feltzing S., Oey M. S., 2014, A&A, 562, A71
Bertelli Motta C. et al., 2018, MNRAS, 478, 425
Bilir S., Ak S., Karaali S., Cabrera-Lavers A., Chonis T. S., Gaskell C. M., 2008, MNRAS, 384, 1178
Blanton M. R. et al., 2017, AJ, 154, 28
Bressan A., Marigo P., Girardí L., Salasnich B., Dal Cero C., Rubele S., Nanni A., 2012, MNRAS, 427, 127

Brewer J. M., Fischer D. A., 2018, ApJS, 237, 38
Campello R. J. G. B., Moulavi D., Sander J., 2013, in Pei J., Tseng V. S., Cao L., Motoda H., Xu G.eds, Advances in Knowledge Discovery and Data Mining. Springer Berlin Heidelberg, Berlin, Heidelberg, p. 160
Cantat-Gaudin T., Anders F., 2020, A&A, 633, A99
Cantat-Gaudin T. et al., 2014, A&A, 569, A17
Cantat-Gaudin T. et al., 2018, A&A, 618, A93
Cantat-Gaudin T. et al., 2020, A&A, 640, A1
Casali G. et al., 2020, A&A, 639, A127
Casamiquela L. et al., 2016, MNRAS, 458, 3150
Casamiquela L. et al., 2018, A&A, 610, A66
Casamiquela L. et al., 2021, A&A, 652, A25
Cescutti G., Matteucci F., 2022, Universe, 8, 173
Charbonnel C., Lagarde N., 2010, A&A, 522, A10
Chen Y. Q., Nissen P. E., Zhao G., Zhang H. W., Benoni T., 2000, A&AS, 141, 491
Chiappini C. et al., 2015, A&A, 576, L12
Cunha K. et al., 2015, ApJ, 798, L41
Cutri R. M. et al., 2003, 2MASS All Sky Catalog of point sources. available at: http://irsa.ipac.caltech.edu/applications/Gator/
Dias W. S., Monteiro H., Moitinho A., Lépine J. R. D., Carraro G., Paunzen E., Alessi B., Villela L., 2021, MNRAS, 504, 356
Donor J. et al., 2018, AJ, 156, 142
Frinchaboy P. M. et al., 2013, ApJ, 777, L1
Fuhrmann K., 1998, A&A, 338, 161
Gaia Collaboration, 2021, A&A, 649, A1
Gao X. et al., 2018, MNRAS, 481, 2666
García Pérez A. E. et al., 2016, AJ, 151, 144
Gilmore G. et al., 2012, The Messenger, 147, 25
Gilmore G. et al., 2022, A&A, 666, A120
Gonzalez G., Wallerstein G., 2000, PASP, 112, 1081
González Hernández J. I., Bonifacio P., 2009, A&A, 497, 497
Grevesse N., Asplund M., Sauval A. J., 2007, Space Sci. Rev., 130, 105
Gunn J. E. et al., 2006, AJ, 131, 2332
Gustafsson B., Edvardsson B., Eriksson K., Jørgensen U. G., Nordlund Å., Plez B., 2008, A&A, 486, 951
Hayes C. R. et al., 2018, ApJ, 852, 49
Heiter U., Soubiran C., Netopil M., Paunzen E., 2014, A&A, 561, A93
Hekker S., Johnson J. A., 2019, MNRAS, 487, 4343
Hubeny I., Allende Prieto C., Osorio Y., Lanz T., 2021, TLUSTY and SYNSPEC Users's Guide IV: Upgraded Versions 208 and 54. preprint(arXiv:2104.02829)
Hunt E. L., Reffert S., 2023, A&A, 673, A114
Izzard R. G., Preece H., Jofre P., Halabi G. M., Masseron T., Tout C. A., 2018, MNRAS, 473, 2984
Jackson R. J. et al., 2022, MNRAS, 509, 1664
Jofré P. et al., 2023, A&A, 671, A21
Jönsson H. et al., 2020, AJ, 160, 120
Karakas A. I., Lattanzio J. C., 2014, PASA, 31, e030
Lagarde N., Decressin T., Charbonnel C., Eggenberger P., Ekström S., Palacios A., 2012, A&A, 543, A108
Magrini L. et al., 2014, A&A, 563, A44
Magrini L. et al., 2017, A&A, 603, A2
Magrini L. et al., 2021, A&A, 651, A84
Majewski S. R. et al., 2017, AJ, 154, 94
Martig M. et al., 2015, MNRAS, 451, 2230
Masseron T., Merle T., Hawkins K., 2016, BACCHUS: Brussels Automatic Code for Characterizing High accUracy Spectra, Astrophysics Source Code Library, record(ascl:1605.004)
McCormick C. et al., 2023, MNRAS, 524, 4418
Miglio A. et al., 2021, A&A, 645, A85
Montegriffo P., Ferraro F. R., Origlia L., Fusi Pecci F., 1998, MNRAS, 297, 872
Myers N. et al., 2022, AJ, 164, 85
Nidever D. L. et al., 2014, ApJ, 796, 38
Nidever D. L. et al., 2015, AJ, 150, 173
Osorio Y., Allende Prieto C., Hubeny I., Mészáros S., Shetrone M., 2020, A&A, 637, A80


Plez B., 2012, Turbospectrum: Code for spectral synthesis, Astrophysics Source Code Library, record(ascl:1205.004)
Prša A. et al., 2016, AJ, 152, 41
Queiroz A. B. A. et al., 2020, A&A, 638, A76
Queiroz A. B. A. et al., 2023, A&A, 673, A155
Randich S. et al., 2022, A&A, 666, A121
Reddy B. E., Lambert D. L., Allende Prieto C., 2006, MNRAS, 367, 1329
Sales-Silva J. V. et al., 2022, ApJ, 926, 154
Silva Aguirre V. et al., 2018, MNRAS, 475, 5487
Smiljanic R. et al., 2016, A&A, 589, A115
Smith V. V. et al., 2013, ApJ, 765, 16
Smith V. V. et al., 2021, AJ, 161, 254
Souto D. et al., 2016, ApJ, 830, 35
Souto D. et al., 2018, ApJ, 857, 14
Tarricq Y. et al., 2021, A&A, 647, A19
Tautvaišienė G. et al., 2015, A&A, 573. A55
Wannier P. G., Andersson B. G., Olofsson H., Ukita N., Young K., 1991, ApJ, 380, 593
Wilson J. C. et al., 2010, SPIE, 7735, 77351C
Wilson J. C. et al., 2019, PASP, 131, 055001
Zacharias N., Monet D. G., Levine S. E., Urban S. E., Gaume R., Wycoff G. L., 2004, American Astronomical Society Meeting Abstracts, 205, 48
Zasowski G. et al., 2013, AJ, 146, 81
Zasowski G. et al., 2017, AJ, 154, 198

[1]*Observatório Nacional, Rua General José Cristino, 77, 20921-400 São Cristóvão, Rio de Janeiro, RJ, Brazil*
[2]*Steward Observatory, University of Arizona, 933 North Cherry Avenue, Tucson, AZ 85721-0065, USA*
[3]*Institut d'Astrophysique de Paris, UMR7095 CNRS, Sorbonne Université, 98bis Bd. Arago, F-75014 Paris, France*
[4]*Departamento de Física, Universidade Federal de Sergipe, Av. Marechal Rondon, S/N, 49000-000 São Cristóvão, SE, Brazil*
[5]*NSF's NOIRLab, 950 N. Cherry Ave. Tucson, AZ 85719, USA*
[6]*Leibniz-Institut für Astrophysik Potsdam (AIP), An der Sternwarte 16, D-14482 Potsdam, Germany*
[7]*Center for Computational Astrophysics, Flatiron Institute,162 Fifth Avenue, New York, NY 10010, USA*
[8]*Departamento de Astrofísica, Universidad de La Laguna, E-38206 La Laguna, Tenerife, Spain*
[9]*The Observatories of the Carnegie Institution for Science, 813 Santa Barbara Street, Pasadena, CA 91101, USA*
[10]*Apache Point Observatory and New Mexico State University, P.O. Box 59, Sunspot, NM 88349-0059, USA*
[11]*Sternberg Astronomical Institute, Moscow State University, 119234, Moscow, Russia*
[12]*Department of Physics & Astronomy, Texas Christian University, TCU Box 298840, Fort Worth, TX 76129, USA*
[13]*Space Telescope Science Institute, 3700 San Martin Drive, Baltimore, MD 21218, USA*
[14]*NRC Herzberg Astronomy and Astrophysics Research Centre, 5071 West Saanich Road, Victoria, B.C., Canada, V9E 2E7*
[15]*New Mexico State University, Las Cruces, NM 88003, USA*
[16]*Materials Science and Applied Mathematics, Malmö University, SE-205 06 Malmö, Sweden*
[17]*Department of Astronomy, University of Virginia, Charlottesville, VA 22904-4325, USA*
[18]*ELTE Eötvös Loránd University, Gothard Astrophysical Observatory, 9700 Szombathely, Szent Imre H. st. 112, Hungary*
[19]*MTA-ELTE Lendület 'Momentum' Milky Way Research Group, Hungary*
[20]*Department of Physics, Montana State University, P.O. Box 173840, Bozeman, MT 59717-3840*
[21]*Department of Astronomy, The Ohio State University, Columbus, OH 43210, USA*
[22]*Department of Physics and Astronomy, University of Utah, Salt Lake City, UT 84105, USA*

This paper has been typeset from a TEX/LATEX file prepared by the author.

# Capítulo 5

# Conclusões

Neste trabalho de tese apresentamos um estudo espectroscópico de uma amostra de estrelas do tipo F, G e K hospedeiras de exoplanetas observadas pela missão K2 usando espectros Hydra e HIRES. Uma segunda parte deste trabalho de tese consistiu em analisar estrelas gigantes vermelhas de tipo K pertencentes ao aglomerado jovem NGC 6705 usando espectros infravermelhos observados pelo levantamento APOGEE.

## 5.1 Estrelas K2

O estudo de estrelas hospedeiras de planetas que foram observadas pela missão K2 foi baseado em duas amostras de estrelas cuja analises foram apresentadas nos Capítulos 2 e 3. Para a primeira amostra de estrelas, os espectros foram obtidos com o espectrógrafo Hydra ($R = \Delta\lambda/\lambda \sim 18.500$) no telescópio WIYN de 3,5 m e estes cobrem um intervalo espectral de 6050 a 6350 Å, cujas campanhas observacionais ocorreram entre os anos 2015 e 2019. Para a segunda amostra de estrelas, espectros Echelle foram obtidos pelo programa *California Planet Search* (CPS, VALENTI e FISCHER, 2005) com o espectrógrafo HIRES ($R = \Delta\lambda/\lambda \sim 60.000$) no telescópio de 10 m Keck, e estes cobrem um intervalo espectral de $\sim$ 3600 até $\sim$ 8000 Å. Os principais resultados obtidos desta pesquisa foram:

- Determinamos os parâmetros estelares de 201 estrelas, sendo a primeira amostra composta de 81 estrelas K2 e 34 estrelas Kepler 1, e a segunda amostra composta de 86 estrelas K2. As duas amostras foram analisadas utilizando a mesma metodologia partir do método espectroscópico clássico, que está baseado nos equilíbrios de excitação e ionização das linhas do Fe I e Fe II. Construímos listas de linhas adequadas para as análise dos espectros que têm características diferentes. No caso da análise de espectros Hydra, a lista de linhas consistiu de 25 linhas de Fe I e 5 linhas de Fe II, enquanto que a lista de linhas usada para a análise de espectros HIRES contêm 61 linhas de Fe I e 13 linhas Fe II. Notando que esta lista não inclui as linhas que são sensíveis de acordo com YANA GALARZA *et al.* (2019). Os parâmetros

estelares obtidos para as estrelas da amostra Hydra, indicam temperaturas efetivas variando entre 4800 e 6000 K, com um pico em $\sim$ 5500 K; esta amostra é dominada por gravidades superficiais entre $\sim$ 4,2 e 4,6 dex. Para a amostra HIRES a maioria das estrelas K2 apresentam temperaturas efetivas entre 4500 e 6500 K, sendo que a maioria tem $T_{\rm eff} > 5000$ K, o que indica que temos mais estrelas do tipo espectral F e G, sendo que a maioria das estrelas desta amostra tem log $g$ entre $\sim$ 4,0 e 4,7 dex. Os diagramas de *Kiel* apresentados nas Figuras 12 do Capítulo 2 e 1 do Capítulo 3 mostram que temos um número reduzido estrelas evoluídas em ambas as amostras.

- As massas e raios estelares foram determinados a partir da combinação dos parâmetros espectroscópicos ($T_{\rm ef}$, [Fe/H], aqui determinados), a magnitude V (coletados do Nasa Exoplanet Archive) e a paralaxe (coletados da base de dados do Gaia DR3) através do método das isócronas e fazendo uso do código `qoyllur-quipu` (RAMÍREZ *et al.*, 2014). A mediana da distribuição da massa estelar da amostra Hydra é $M_\star = 0,93 \pm 0,11$ $M_\odot$ (com um intervalo entre 0,6 e 1,3 $M_\odot$) e da amostra HIRES é $M_\star = 0,97$ $M_\odot$ (percentil 16 = 0,793; percentil 84 = 1,075). Passando para o raio estelar para a amostra Hydra temos que a mediana da distribuição é $R_\star = 0.94$ $R_\odot$ (percentil 16 $=-0.22$; percentil 84 = 0.59) e na amostra HIRES 0.996 $R_\star$ (percentil 16 = 0.745; percentil 84 = 1.384), notando que temos poucas estrelas com raios estelares $> 2$ $R_\odot$ tanto nas amostras Hydra e HIRES.

- Combinando nossos raios estelares e as profundidades de trânsitos (obtidos de majoritariamente de KRUSE *et al.*, 2019 mas também de VANDERBURG *et al.* (2016), POPE *et al.* (2016), BARROS *et al.* (2016), RIZZUTO *et al.* (2017), LIVINGSTON *et al.* (2018), CHRISTIANSEN *et al.* (2017) e THOMPSON *et al.* (2018, para os planetas das estrelas Kepler), os raios de 83 planetas da amostra Hydra e 73 planetas da amostra HIRES, todos com condição de *planetas confirmados* segundo o NASA *Exoplanet Archive*, foram determinados usando a Equação 1, nos Capítulos 2 e 3, dada por SEAGER e MALLÉN-ORNELAS (2003). Os raios planetarios determinados nesta tese tem uma incerteza interna mediana de 4,4% para a amostra Hydra e 3,4% para a amostra HIRES, enquanto que nos parâmetros raios estelares e profundidades de trânsito, diretamente envolvidos na determinação dos raios planetários, temos uma incerteza mediana de 4,2% e 2,6% nos raios estelares, respectivamente, e 3,4% e 2,6% nas profundidades de trânsito, respectivamente.

- A distribuição dos raios planetários das amostras de planetas K2 Hydra e HIRES obtidos nesta tese é bimodal com mínimo em Rp $\sim 1,9$ $R_\oplus$, evidenciando o bem-conhecido "vale do raio" que é observado para a distribuição de planetas pequenos com raios planetários entre $R_{\rm pl} < 4$ $R_\oplus$. Este resultado, que aqui foi obtido para amostras contendo um número relativamente pequeno de exoplanetas quando comparado com os resultados da literatura obtidos para amostra de estrelas hospedeiras

de planetas Kepler (FULTON *et al.*, 2017; MARTINEZ *et al.*, 2019; VAN EYLEN *et al.*, 2018), demostra claramente que nossos parâmetros estelares determinados têm muito boa precisão. Notamos por exemplo, que os resultados de PETIGURA *et al.* (2018a) não encontraram o "vale do raio".

- Para amostra Hydra, a relação entre o raio do planeta, o período orbital e a metalicidade de exoplanetas K2 confirma resultados anteriores na literatura para exoplanetas Kepler. Em geral, a metalicidade das estrelas hospedeiras de planetas K2 aumenta com o raio planetário, sendo esse aumento mais evidente na transição entre os regimes de planetas pequenos ($< 4,4$ $R_\oplus$) e maiores ($> 4,4$ $R_\oplus$). A mediana da metalicidade das estrelas hospedeiras de planetas K2 com períodos orbitais $< 10$ dias é ligeiramente rica em metais, enquanto que a mediana da metalicidade das estrelas hospedeiras para planetas com P $> 10$ dias é ligeiramente pobre em metais. Ao restringir a amostra apenas para conter planetas com $R_{pl} < 4,4$ $R_\oplus$, observamos um comportamento similar.

- Para a amostra HIRES, dada a cobertura espectral estendida, pudemos estudar a atividade cromosférica a partir da análise das linhas ionizadas de cálcio II H ($\lambda$ 3968,47 Å) e K ($\lambda$ 3933,66 Å) medindo o índice $S_{HK}$. Este índice é definido na Equação 2 do Capítulo 3 com um ajuste do coeficiente de fluxo V para os valores obtidos em cada espectro. Nesta tese analisamos um total de 725 espectros, correspondentes a 144 estrelas K2. Os espectros analisados foram coletados tanto da base de dados ExoFop (*Exoplanet Follow-up Observing Program*, AKESON *et al.*, 2013) quanto da base de dados Keck (*Keck Observatory Archive*, KOA, TRAN *et al.*, 2015)). Notamos que para 40 estrelas da amostra havia mais de um espectro disponível na base de dados, o que permitiu investigar se houve variação na atividade estelar dessas estrelas.

- A distribuição obtida das medidas do índice $S_{HK}$ para as estrelas da amostra tem uma mediana de 0.178 (Percentil 16 = 0,134; Percentil 84 = 0,577), que é semelhante ao valor médio reportado para o Sol na literatura de $\langle S \rangle = 0,17$ (EGELAND *et al.*, 2017). Notando que a maioria das estrelas de nossa amostra apresenta nível de atividade menor do que o do Sol e que por outro lado, existem poucas estrelas com valores $S_{HK}$ entre 2 e 3, indicando níveis de atividade de 10 e 15 vezes o valor solar.

- Nossos resultados de $S_{HK}$ como função do $(B - V)$ seguem as mesmas tendências observadas nos trabalhos anteriores de ISAACSON e FISCHER (2010) e BORO SAIKIA *et al.* (2018). As estrelas analisadas apresentam níveis de atividade constante até $(B - V) \lesssim 0,9$, enquanto para cores mais avermelhadas na faixa de $0,9 \lesssim (B - V) \lesssim 1,4$, o limite inferior do índice S apresenta um aumento suave.

- Com o objetivo de remover a contribuição fotosférica ao índice $S_{HK}$ fizemos a conversão para o índice $R'_{HK}$ adotando o método de NOYES *et al.* (1984) e usando as calibrações bolométricas de RUTTEN (1984) para estrelas de sequencia principal e estrelas evoluídas. Nossos resultados para $\langle \log R'_{HK} \rangle$ como função do período de rotação para a amostra indicam que, embora a atividade, de maneira geral, diminua com o aumento do período de rotação, há uma grande dispersão nos níveis de atividade para um determinado período de rotação de ∼0,5 dex em $\log R'_{HK}$; tal resultado já foi observado anteriormente, por exemplo, por BÖHM-VITENSE (2007) e METCALFE e VAN SADERS (2017), e aponta para um comportamento complexo na atividade estelar que possivelmente está relacionado ao número de Rossby (METCALFE e VAN SADERS, 2017).

- Em um estudo seminal sobre a atividade cromosférica em uma amostra de estrelas do tipo solar, VAUGHAN *et al.* (1978) identificaram uma falta de estrelas dos tipos F e G com níveis intermediários de atividade, chamada de lacuna Vaughan-Preston. Essa lacuna foi confirmada mais recentemente pelos trabalhos de HENRY *et al.* (1996) e GOMES DA SILVA *et al.* (2021) usando uma grande amostra de estrelas. Embora tenhamos estudado uma amostra muito menor de estrelas, nossa distribuição dos valores médios de $\log R'_{HK}$ também revela a presença da lacuna Vaughan-Preston.

- Analisamos também o impacto na determinação de parâmetros estelares ao incluir linhas de ferro sensíveis à atividade estelar nas amostras Hydra e HIRES. No entanto, observamos pequenas diferenças que estão na ordem das incertezas dos parâmetros estelares tais como a temperatura efetiva, metalicidade e velocidade de microturbulência. O que nos leva a concluir que, com base nos dois conjuntos de resultados (com e sem linhas sensíveis) para as amostras Hydra e HIRES, não há evidências (além das incertezas) de uma correlação clara entre $\Delta T_{ef}$, $\Delta$[Fe/H] e $\Delta\xi$ com a atividade estelar ($\log R'_{HK}$).

## 5.2 NGC 6705

A segunda parte deste trabalho de tese consistiu na determinação das abundâncias químicas de 16 elementos em uma amostra de 11 estrelas gigantes vermelhas do aglomerado aberto do disco Galáctico NGC 6705. Analisamos espectros no infravermelho próximo obtidos do levantamento APOGEE DR17. A metodologia utilizada consistiu na análise dos espectros APOGEE utilizando a técnica de síntese espectral. Os espectros sintéticos foram calculados em equilíbrio termodinâmico local e em 1-D, utilizando modelos de atmosferas MARCS GUSTAFSSON *et al.* (2008). O código de transferência radiativa

adotado no cálculo foi o TurboSpectrum (ALVAREZ e PLEZ, 1998; PLEZ, 2012). Nossos principais resultados serão discutidos a seguir.

- As temperaturas efetivas das estrelas da amostra foram determinadas usando as calibrações fotométricas de GONZÁLEZ HERNÁNDEZ e BONIFACIO (2009) para as cores $(V-J)$, $(V-H)$, $(V-Ks)$ e $(J-Ks)$ (Equação 1 no Capítulo 4). Os valores de log $g$ foram determinados a partir de equações fundamentales (Equação 2 no Capítulo 4). Nossos resultados indicam que sete das estrelas pertencem ao ramo das gigantes vermelhas e enquanto que as outras quatro pertencem ao agrupamento vermelho.

- A metalicidade obtida para o aglomerado foi $\langle[\mathrm{Fe/H}]\rangle = +0,13 \pm 0,04$, esse resultado está de acordo com a tendência geral de aumento da metalicidade à medida que a distância em relação ao Centro Galáctico diminui.

- Nossos resultados indicam que as estrelas gigantes vermelhas de NGC 6705 apresentam baixas abundâncias de $^{12}$C ($\langle[^{12}\mathrm{C/Fe}]\rangle = -0,16$) e um enriquecimento de $^{14}$N ($\langle[^{14}\mathrm{N/Fe}]\rangle = +0,51$), tal assinatura química é consistente com o esperado na primeira dragagem. Em particular, as abundâncias de C and N obtidas encontram-se em concordância quantitativa com os modelos estelares de LAGARDE *et al.* (2012) para estrelas com massas entre 3 e 4 massas solares.

- Um resultado interessante que obtivemos com a análise detalhada das abundâncias de NGC 6705 foi referente ao elemento sódio que apresenta um enriquecimento significativo, com valor médio de abundâncias para as estrels estudadas de $\langle[\mathrm{Na/Fe}]\rangle = +0,29 \pm 0,04$. Notando que a correção não-ETL para as abundâncias derivadas em ETL de Na são muito pequenas $(-0,02)$. Já para o elemento Al não obtivemos abundâncias significativamente aumentadas neste aglomerado $\langle[\mathrm{Al/Fe}]\rangle = 0,06 \pm 0,07$. As abundâncias médias de Na e Al obtidas nesta tese encontram-se em excelente acordo com as previsões dos modelos de evolução estelar de LAGARDE *et al.* (2012). Resultados anteriores do levantamento Gaia ESO SMILJANIC *et al.* (2016) haviam encontrado tanto as abundâncias de Na quanto de Al altas para as estrelas gigantes vermelhas de NGC 6705, o que não podia ser facilmente explicado pelos modelos.

- A possibilidade de o aglomerado NGC 6705 apresentar enriquecimento em elementos-$\alpha$, conforme sugerido inicialmente por alguns resultados dos levantamento Gaia ESO e OCCASO (CASAMIQUELA *et al.*, 2018; TAUTVAIŠIENĖ *et al.*, 2015) foi examinada com base nas abundâncias derivadas de cinco elementos-$\alpha$: O, Mg, Si, Ca e Ti. A média da razões de abundância dos elementos-$\alpha$ em relação ao ferro obtida nesta tese de $\langle[\alpha/\mathrm{Fe}]\rangle = -0{,}025 \pm 0{,}051$ indica que o aglomerado jovem

NGC 6705 não apresenta enriquecimento em elementos-$\alpha$. Nossos resultados são consistentes com a expectativa de que o aglomerado aberto jovem NGC 6705 que é ligeiramente enriquecido em metais e localizado no disco Galáctico apresenta valores de [$\alpha$/Fe] não muito diferentes dos solares.

## 5.3 Perspectivas Futuras

Compreender a relação entre as propriedades dos exoplanetas e as características de suas estrelas hospedeiras é crucial para modelar as condições dos discos protoplanetários e, por extensão, os processos de formação planetária. A caracterização precisa das estrelas hospedeiras é, portanto, essencial tanto para a detecção de planetas quanto para a compreensão de suas propriedades. Embora existam muitos estudos focados nas estrelas observadas pela missão Kepler, ainda falta um estudo espectroscópico homogêneo que cubra toda a amostra de estrelas K2 com planetas confirmados. Como perspectiva futura, almejamos desenvolver um catálogo de parâmetros estelares, obtidos por meio de espectroscopia, juntamente com índices de atividade estelar para o maior número possível de estrelas K2 com planetas confirmados. Para alcançar esse objetivo, utilizaremos espectros de alta resolução (R $\sim$ 60.000) adquiridos com o espectrógrafo HIRES, disponíveis na base de dados ExoFOP.

A atividade magnética e os fenômenos a ela associados têm um papel crucial em estrelas com tipos espectrais de F médio a M. Dado que essas estrelas são o principal alvo das buscas por exoplanetas, é essencial entender como essa atividade afeta tanto a detecção desses planetas quanto a precisão na determinação de seus parâmetros. No que diz respeito à detecção de exoplanetas, o método mais suscetível à confusão devido à atividade estelar é o da velocidade radial. De acordo com Saar e Donahue (1997), manchas frias na superfície estelar podem causar variações no perfil das linhas espectrais, as quais podem ser erroneamente interpretadas como variações na velocidade radial dos planetas, fenômeno conhecido como "jitter" estelar. No futuro, pretendemos estudar o impacto do jitter estelar causado pela atividade estelar.

# Referências Bibliográficas


ABDURRO'UF, ACCETTA, K., AERTS, C., et al., 2022, "The Seventeenth Data Release of the Sloan Digital Sky Surveys: Complete Release of MaNGA, MaStar, and APOGEE-2 Data", Astrophys. J. Suppl., 259(2):35. doi: 10.3847/1538-4365/ac4414.

ADIBEKYAN, V. Z., FIGUEIRA, P., SANTOS, N. C., et al., 2013, "Orbital and physical properties of planets and their hosts: new insights on planet formation and evolution", Astron. Astrophys., 560:A51. doi: 10.1051/0004-6361/201322551.

ADIBEKYAN, V., 2019, "Heavy Metal Rules. I. Exoplanet Incidence and Metallicity", *Geosciences*, v. 9, n. 3 (fev.), pp. 105. doi: 10.3390/geosciences9030105.

ADIBEKYAN, V., DORN, C., SOUSA, S. G., et al., 2021, "A compositional link between rocky exoplanets and their host stars", *Science*, v. 374, n. 6565 (out.), pp. 330–332. doi: 10.1126/science.abg8794.

AKESON, R. L., CHEN, X., CIARDI, D., et al., 2013, "The NASA Exoplanet Archive: Data and Tools for Exoplanet Research", Publ. Astron. Soc. Pacific, v. 125, n. 930 (ago.), pp. 989. doi: 10.1086/672273.

AKESON, R., CHRISTIANSEN, J., 2019, "TESS Follow-up Observing Program Working Group (TFOP WG): The ExoFOP-TESS Website". In: *American Astronomical Society Meeting Abstracts #233*, v. 233, *American Astronomical Society Meeting Abstracts*, p. 140.09, jan.

ALVAREZ, R., PLEZ, B., 1998, "Near-infrared narrow-band photometry of M-giant and Mira stars: models meet observations", Astron. Astrophys., v. 330 (fev.), pp. 1109–1119. doi: 10.48550/arXiv.astro-ph/9710157.

ANDERS, E., GREVESSE, N., 1989, "Abundances of the elements: Meteoritic and solar", Geochim. Cosmochim. Acta, v. 53, n. 1 (jan.), pp. 197–214. doi: 10.1016/0016-7037(89)90286-X.

ASCHWANDEN, M. J., 2007, "CHAPTER 4 - The Sun". In: McFadden, L.-A., Weissman, P. R., Johnson, T. V. (Eds.), *Encyclopedia of the Solar System (Second*

*Edition)*, second edition ed., Academic Press, pp. 71–98, San Diego. ISBN: 978-0-12-088589-3. doi: https://doi.org/10.1016/B978-012088589-3/50008-6. Disponível em: <https://www.sciencedirect.com/science/article/pii/B9780120885893500086>.

ASPLUND, M., 2000, "Line formation in solar granulation. III. The photospheric Si and meteoritic Fe abundances", Astron. Astrophys., v. 359 (jul.), pp. 755–758. doi: 10.48550/arXiv.astro-ph/0005322.

ASPLUND, M., GREVESSE, N., SAUVAL, A. J., 2005, "The Solar Chemical Composition". In: *Cosmic Abundances as Records of Stellar Evolution and Nucleosynthesis*, v. 336, p. 25, set.

ASPLUND, M., AMARSI, A. M., GREVESSE, N., 2021, "The chemical make-up of the Sun: A 2020 vision", Astron. Astrophys., 653:A141. doi: 10.1051/0004-6361/202140445.

BALIUNAS, S. L., DONAHUE, R. A., SOON, W. H., et al., 1995, "Chromospheric Variations in Main-Sequence Stars. II." Astrophys. J., v. 438 (jan.), pp. 269. doi: 10.1086/175072.

BARROS, S. C. C., DEMANGEON, O., DELEUIL, M., 2016, "New planetary and eclipsing binary candidates from campaigns 1-6 of the K2 mission", Astron. Astrophys., 594:A100. doi: 10.1051/0004-6361/201628902.

BEAUGÉ, C., NESVORNÝ, D., 2013, "Emerging Trends in a Period-Radius Distribution of Close-in Planets", Astrophys. J., 763(1):12. doi: 10.1088/0004-637X/763/1/12.

BERGER, T. A., HUBER, D., GAIDOS, E., et al., 2020a, "The Gaia-Kepler Stellar Properties Catalog. II. Planet Radius Demographics as a Function of Stellar Mass and Age", Astron. J., 160(3):108. doi: 10.3847/1538-3881/aba18a.

BERGER, T. A., HUBER, D., VAN SADERS, J. L., et al., 2020b, "The Gaia-Kepler Stellar Properties Catalog. I. Homogeneous Fundamental Properties for 186,301 Kepler Stars", Astron. J., 159(6):280. doi: 10.3847/1538-3881/159/6/280.

BÖHM-VITENSE, E., 2007, "Chromospheric Activity in G and K Main-Sequence Stars, and What It Tells Us about Stellar Dynamos", Astrophys. J., v. 657, n. 1 (mar.), pp. 486–493. doi: 10.1086/510482.

BONIFACIO, P., CAFFAU, E., LUDWIG, H.-G., et al., 2011, "LTE Model Atmospheres: MARCS, ATLAS and CO5BOLD", *Proceedings of the International Astronomical Union*, v. 7, n. S282, pp. 213–220. doi: 10.1017/S1743921311027402.

BORO SAIKIA, S., MARVIN, C. J., JEFFERS, S. V., et al., 2018, "Chromospheric activity catalogue of 4454 cool stars. Questioning the active branch of stellar activity cycles", Astron. Astrophys., 616:A108. doi: 10.1051/0004-6361/201629518.

BORUCKI, W. J., 2016, "KEPLER Mission: development and overview", *Reports on Progress in Physics*, 79(3):036901. doi: 10.1088/0034-4885/79/3/036901.

BORUCKI, W. J., KOCH, D., BASRI, G., et al., 2010, "Kepler Planet-Detection Mission: Introduction and First Results", *Science*, v. 327 (fev.), pp. 977. doi: 10.1126/science.1185402.

BOSS, A. P., 1997, "Giant planet formation by gravitational instability." *Science*, v. 276 (jan.), pp. 1836–1839. doi: 10.1126/science.276.5320.1836.

BOYAJIAN, T. S., VON BRAUN, K., VAN BELLE, G., et al., 2013, "Stellar Diameters and Temperatures. III. Main-sequence A, F, G, and K Stars: Additional High-precision Measurements and Empirical Relations", Astrophys. J., 771(1):40. doi: 10.1088/0004-637X/771/1/40.

BREWER, J. M., FISCHER, D. A., 2018, "Spectral Properties of Cool Stars: Extended Abundance Analysis of Kepler Objects of Interest", Astrophys. J. Suppl., 237 (2):38. doi: 10.3847/1538-4365/aad501.

BROMM, V., COPPI, P. S., LARSON, R. B., 1999, "Forming the First Stars in the Universe: The Fragmentation of Primordial Gas", Astrophys. J. Lett., v. 527, n. 1 (dez.), pp. L5–L8. doi: 10.1086/312385.

BUCHHAVE, L. A., LATHAM, D. W., 2015, "The Metallicities of Stars with and without Transiting Planets", Astrophys. J., 808(2):187. doi: 10.1088/0004-637X/808/2/187.

BUCHHAVE, L. A., LATHAM, D. W., JOHANSEN, A., et al., 2012, "An abundance of small exoplanets around stars with a wide range of metallicities", Nature, v. 486, n. 7403 (jun.), pp. 375–377. doi: 10.1038/nature11121.

BUCHHAVE, L. A., BIZZARRO, M., LATHAM, D. W., et al., 2014, "Three regimes of extrasolar planet radius inferred from host star metallicities", Nature, v. 509, n. 7502 (maio), pp. 593–595. doi: 10.1038/nature13254.

BUDER, S., SHARMA, S., KOS, J., et al., 2021, "The GALAH+ survey: Third data release", Mon. Not, Roy. Astron. Soc., v. 506, n. 1 (set.), pp. 150–201. doi: 10.1093/mnras/stab1242.

CANTAT-GAUDIN, T., VALLENARI, A., ZAGGIA, S., et al., 2014, "VizieR Online Data Catalog: Gaia-ESO Survey: NGC6705 (Cantat-Gaudin+, 2014)", *VizieR Online Data Catalog*, v. 356 (jul.).

CANTAT-GAUDIN, T., ANDERS, F., CASTRO-GINARD, A., et al., 2020, "Painting a portrait of the Galactic disc with its stellar clusters", Astron. Astrophys., 640: A1. doi: 10.1051/0004-6361/202038192.

CANTIELLO, M., LANGER, N., 2010, "Thermohaline mixing in evolved low-mass stars", Astron. Astrophys., 521:A9. doi: 10.1051/0004-6361/201014305.

CARROLL, B. W., OSTLIE, D. A., 2017, *An introduction to modern astrophysics, Second Edition*.

CASAMIQUELA, L., CARRERA, R., BALAGUER-NÚÑEZ, L., et al., 2018, "NGC 6705 a young $\alpha$-enhanced open cluster from OCCASO data", Astron. Astrophys., 610:A66. doi: 10.1051/0004-6361/201732024.

CASTELLI, F., KURUCZ, R. L., 2004, "New Grids of ATLAS9 Model Atmospheres", *ArXiv e-prints*, art. astro-ph/0405087.

CASTELLI, F., KURUCZ, R. L., 2003, "New Grids of ATLAS9 Model Atmospheres". In: Piskunov, N., Weiss, W. W., Gray, D. F. (Eds.), *Modelling of Stellar Atmospheres*, v. 210, *IAU Symposium*, p. A20, jan.

CHANAMÉ, J., PINSONNEAULT, M., TERNDRUP, D. M., 2005, "Abundance Anomalies and Rotational Evolution of Low-Mass Red Giants: A Maximal Mixing Approach", Astrophys. J., v. 631, n. 1 (set.), pp. 540–571. doi: 10.1086/432410.

CHARBONNEL, C., LAGARDE, N., 2010, "Thermohaline instability and rotation-induced mixing. I. Low- and intermediate-mass solar metallicity stars up to the end of the AGB", Astron. Astrophys., 522:A10. doi: 10.1051/0004-6361/201014432.

CHARBONNEL, C., ZAHN, J. P., 2007, "Thermohaline mixing: a physical mechanism governing the photospheric composition of low-mass giants", Astron. Astrophys., v. 467, n. 1 (maio), pp. L15–L18. doi: 10.1051/0004-6361:20077274.

CHIAPPINI, C., 2001, "The Formation and Evolution of the Milky Way", *American Scientist*, v. 89, n. 6 (dez.), pp. 506. doi: 10.1511/2001.6.506.

CHRISTIANSEN, J. L., VANDERBURG, A., BURT, J., et al., 2017, "Three's Company: An Additional Non-transiting Super-Earth in the Bright HD 3167 System, and Masses for All Three Planets", Astron. J., 154(3):122. doi: 10.3847/1538-3881/aa832d.

CLARK, J. T., WRIGHT, D. J., WITTENMYER, R. A., et al., 2022, "The GALAH Survey: improving our understanding of confirmed and candidate planetary systems with large stellar surveys", Mon. Not, Roy. Astron. Soc., v. 510, n. 2 (fev.), pp. 2041–2060. doi: 10.1093/mnras/stab3498.

CUI, X.-Q., ZHAO, Y.-H., CHU, Y.-Q., et al., 2012, "The Large Sky Area Multi-Object Fiber Spectroscopic Telescope (LAMOST)", *Research in Astronomy and Astrophysics*, v. 12, n. 9 (set.), pp. 1197–1242. doi: 10.1088/1674-4527/12/9/003.

DELEUIL, M., BARGE, P., DEFAY, C., et al., 2000, "COROT: A Space Mission for the Search for Extrasolar Planets (Contributed Talk)". In: Garzón, G., Eiroa, C., de Winter, D., et al. (Eds.), *Disks, Planetesimals, and Planets*, v. 219, *Astronomical Society of the Pacific Conference Series*, p. 656, jan.

DELEUIL, M., AIGRAIN, S., MOUTOU, C., et al., 2018, "Planets, candidates, and binaries from the CoRoT/Exoplanet programme. The CoRoT transit catalogue", Astron. Astrophys., 619:A97. doi: 10.1051/0004-6361/201731068.

DIAS, W. S., MONTEIRO, H., MOITINHO, A., et al., 2021, "Updated parameters of 1743 open clusters based on Gaia DR2", Mon. Not, Roy. Astron. Soc., v. 504, n. 1 (jun.), pp. 356–371. doi: 10.1093/mnras/stab770.

DUMUSQUE, X., LOVIS, C., SÉGRANSAN, D., et al., 2011, "The HARPS search for southern extra-solar planets. XXX. Planetary systems around stars with solar-like magnetic cycles and short-term activity variation", Astron. Astrophys., 535: A55. doi: 10.1051/0004-6361/201117148.

DUNCAN, D. K., VAUGHAN, A. H., WILSON, O. C., et al., 1991, "CA II H and K Measurements Made at Mount Wilson Observatory, 1966–1983", Astrophys. J. Suppl., v. 76 (maio), pp. 383. doi: 10.1086/191572.

EGELAND, R., SOON, W., BALIUNAS, S., et al., 2017, "The Mount Wilson Observatory S-index of the Sun", Astrophys. J., 835(1):25. doi: 10.3847/1538-4357/835/1/25.

EVERETT, M. E., HOWELL, S. B., SILVA, D. R., et al., 2013, "SPECTROSCOPY OF FAINT KEPLER MISSION EXOPLANET CANDIDATE HOST STARS", *The Astrophysical Journal*, v. 771, n. 2 (jun), pp. 107. doi: 10.1088/0004-637X/771/2/107. Disponível em: <https://dx.doi.org/10.1088/0004-637X/771/2/107>.

FISCHER, D. A., VALENTI, J., 2005, "The Planet-Metallicity Correlation", Astrophys. J., v. 622 (abr.), pp. 1102–1117. doi: 10.1086/428383.

FULTON, B. J., PETIGURA, E. A., HOWARD, A. W., et al., 2017, "The California-Kepler Survey. III. A Gap in the Radius Distribution of Small Planets", Astron. J., 154:109. doi: 10.3847/1538-3881/aa80eb.

FULTON, B. J., PETIGURA, E. A., 2018, "The California-Kepler Survey. VII. Precise Planet Radii Leveraging Gaia DR2 Reveal the Stellar Mass Dependence of the Planet Radius Gap", Astron. J., 156(6):264. doi: 10.3847/1538-3881/aae828.

GAIA COLLABORATION, PRUSTI, T., DE BRUIJNE, J. H. J., et al., 2016, "The Gaia mission", Astron. Astrophys., 595:A1. doi: 10.1051/0004-6361/201629272.

GAIA COLLABORATION, VALLENARI, A., BROWN, A. G. A., et al., 2023, "Gaia Data Release 3. Summary of the content and survey properties", Astron. Astrophys., 674:A1. doi: 10.1051/0004-6361/202243940.

GARCÍA PÉREZ, A. E., ALLENDE PRIETO, C., HOLTZMAN, J. A., et al., 2016, "ASPCAP: The APOGEE Stellar Parameter and Chemical Abundances Pipeline", Astron. J., 151:144. doi: 10.3847/0004-6256/151/6/144.

GHEZZI, L., CUNHA, K., SCHULER, S. C., et al., 2010, "Metallicities of Planet-hosting Stars: A Sample of Giants and Subgiants", Astrophys. J., v. 725, n. 1 (dez.), pp. 721–733. doi: 10.1088/0004-637X/725/1/721.

GHEZZI, L., MONTET, B. T., JOHNSON, J. A., 2018, "Retired A Stars Revisited: An Updated Giant Planet Occurrence Rate as a Function of Stellar Metallicity and Mass", Astrophys. J., 860(2):109. doi: 10.3847/1538-4357/aac37c.

GHEZZI, L., MARTINEZ, C. F., WILSON, R. F., et al., 2021, "A Spectroscopic Analysis of the California-Kepler Survey Sample. II. Correlations of Stellar Metallicities with Planetary Architectures", Astrophys. J., 920(1):19. doi: 10.3847/1538-4357/ac14c3.

GINZBURG, S., SCHLICHTING, H. E., SARI, R., 2016, "Super-Earth Atmospheres: Self-consistent Gas Accretion and Retention", Astrophys. J., 825:29. doi: 10.3847/0004-637X/825/1/29.

GINZBURG, S., SCHLICHTING, H. E., SARI, R., 2018, "Core-powered mass-loss and the radius distribution of small exoplanets", Mon. Not, Roy. Astron. Soc., v. 476 (maio), pp. 759–765. doi: 10.1093/mnras/sty290.

GOMES DA SILVA, J., SANTOS, N. C., ADIBEKYAN, V., et al., 2021, "Stellar chromospheric activity of 1674 FGK stars from the AMBRE-HARPS sample. I. A catalogue of homogeneous chromospheric activity", Astron. Astrophys., 646: A77. doi: 10.1051/0004-6361/202039765.

GONZALEZ, G., 1997, "The stellar metallicity-giant planet connection", Mon. Not, Roy. Astron. Soc., v. 285 (fev.), pp. 403–412. doi: 10.1093/mnras/285.2.403.

GONZÁLEZ HERNÁNDEZ, J. I., BONIFACIO, P., 2009, "A new implementation of the infrared flux method using the 2MASS catalogue", Astron. Astrophys., v. 497, n. 2 (abr.), pp. 497–509. doi: 10.1051/0004-6361/200810904.

GRAY, D. F., 2005, *The Observation and Analysis of Stellar Photospheres*.

GRAY, R. O., CORBALLY, C. J., GARRISON, R. F., et al., 2006, "Contributions to the Nearby Stars (NStars) Project: Spectroscopy of Stars Earlier than M0 within 40 pc-The Southern Sample", Astron. J., v. 132, n. 1 (jul.), pp. 161–170. doi: 10.1086/504637.

GREVESSE, N., ASPLUND, M., SAUVAL, A. J., 2007, "The Solar Chemical Composition", Space Sci. Rev., v. 130 (jun.), pp. 105–114. doi: 10.1007/s11214-007-9173-7.

GUPTA, A., SCHLICHTING, H. E., 2019, "Sculpting the valley in the radius distribution of small exoplanets as a by-product of planet formation: the core-powered mass-loss mechanism", Mon. Not, Roy. Astron. Soc., v. 487, n. 1 (jul.), pp. 24–33. doi: 10.1093/mnras/stz1230.

GUSTAFSSON, B., EDVARDSSON, B., ERIKSSON, K., et al., 2008, "A grid of MARCS model atmospheres for late-type stars. I. Methods and general properties", Astron. Astrophys., v. 486, n. 3 (ago.), pp. 951–970. doi: 10.1051/0004-6361:200809724.

HALL, J. C., LOCKWOOD, G. W., SKIFF, B. A., 2007, "The Activity and Variability of the Sun and Sun-like Stars. I. Synoptic Ca II H and K Observations", Astron. J., v. 133, n. 3 (mar.), pp. 862–881. doi: 10.1086/510356.

HAN, H., WANG, S., BAI, Y., et al., 2023, "Stellar Chromospheric Activities Revealed from the LAMOST-K2 Time-domain Survey", Astrophys. J. Suppl., 264(1):12. doi: 10.3847/1538-4365/ac9eac.

HAYWOOD, R. D., COLLIER CAMERON, A., QUELOZ, D., et al., 2014, "Planets and stellar activity: hide and seek in the CoRoT-7 system", Mon. Not, Roy. Astron. Soc., v. 443, n. 3 (set.), pp. 2517–2531. doi: 10.1093/mnras/stu1320.

HEKKER, S., JOHNSON, J. A., 2019, "Origin of $\alpha$-rich young stars: clues from C, N, and O", Mon. Not, Roy. Astron. Soc., v. 487, n. 3 (ago.), pp. 4343–4354. doi: 10.1093/mnras/stz1554.

HENRY, T. J., SODERBLOM, D. R., DONAHUE, R. A., et al., 1996, "A Survey of Ca II H and K Chromospheric Emission in Southern Solar-Type Stars", Astron. J., v. 111 (jan.), pp. 439. doi: 10.1086/117796.

HINKEL, N. R., TIMMES, F. X., YOUNG, P. A., et al., 2014, "Stellar Abundances in the Solar Neighborhood: The Hypatia Catalog", Astron. J., 148(3):54. doi: 10.1088/0004-6256/148/3/54.

HOWELL, S. B., SOBECK, C., HAAS, M., et al., 2014, "The K2 Mission: Characterization and Early Results", Publ. Astron. Soc. Pacific, v. 126, n. 938 (abr.), pp. 398. doi: 10.1086/676406.

HUBER, D., BRYSON, S. T., HAAS, M. R., et al., 2016, "The K2 Ecliptic Plane Input Catalog (EPIC) and Stellar Classifications of 138,600 Targets in Campaigns 1-8", Astrophys. J. Suppl., 224(1):2. doi: 10.3847/0067-0049/224/1/2.

IBEN, ICKO, J., 1967, "Stellar Evolution.VI. Evolution from the Main Sequence to the Red-Giant Branch for Stars of Mass 1 M_{sun}, 1.25 M_{sun}, and 1.5 M_{sun}", Astrophys. J., v. 147 (fev.), pp. 624. doi: 10.1086/149040.

IDA, S., LIN, D. N. C., 2004, "Toward a Deterministic Model of Planetary Formation. I. A Desert in the Mass and Semimajor Axis Distributions of Extrasolar Planets", Astrophys. J., v. 604 (mar.), pp. 388–413. doi: 10.1086/381724.

ISAACSON, H., FISCHER, D., 2010, "Chromospheric Activity and Jitter Measurements for 2630 Stars on the California Planet Search", Astrophys. J., v. 725, n. 1 (dez.), pp. 875–885. doi: 10.1088/0004-637X/725/1/875.

IZZARD, R. G., PREECE, H., JOFRE, P., et al., 2018, "Binary stars in the Galactic thick disc", Mon. Not, Roy. Astron. Soc., v. 473, n. 3 (jan.), pp. 2984–2999. doi: 10.1093/mnras/stx2355.

JACOBSON, H. R., PILACHOWSKI, C. A., FRIEL, E. D., 2011, "A Chemical Abundance Study of 10 Open Clusters Based on WIYN-Hydra Spectroscopy", Astron. J., 142:59. doi: 10.1088/0004-6256/142/2/59.

JOFRÉ, P., JORISSEN, A., AGUILERA-GÓMEZ, C., et al., 2023, "Cannibals in the thick disk. II. Radial-velocity monitoring of the young $\alpha$-rich stars", Astron. Astrophys., 671:A21. doi: 10.1051/0004-6361/202244524.

JOHNSON, J. A., PETIGURA, E. A., FULTON, B. J., et al., 2017, "The California-Kepler Survey. II. Precise Physical Properties of 2025 Kepler Planets and Their Host Stars", Astron. J., 154(3):108. doi: 10.3847/1538-3881/aa80e7.

JÖNSSON, H., HOLTZMAN, J. A., ALLENDE PRIETO, C., et al., 2020, "APOGEE Data and Spectral Analysis from SDSS Data Release 16: Seven Years of Observations Including First Results from APOGEE-South", Astron. J., 160(3):120. doi: 10.3847/1538-3881/aba592.

KARAKAS, A. I., LATTANZIO, J. C., 2014, "The Dawes Review 2: Nucleosynthesis and Stellar Yields of Low- and Intermediate-Mass Single Stars", Publ. Astron. Soc. Australia, 31:e030. doi: 10.1017/pasa.2014.21.

KOCH, D. G., BORUCKI, W. J., BASRI, G., et al., 2010, "Kepler Mission Design, Realized Photometric Performance, and Early Science", Astrophys. J. Lett., v. 713 (abr.), pp. L79–L86. doi: 10.1088/2041-8205/713/2/L79.

KRUSE, E., AGOL, E., LUGER, R., et al., 2019, "Detection of Hundreds of New Planet Candidates and Eclipsing Binaries in K2 Campaigns 0-8", Astrophys. J. Suppl., 244(1):11. doi: 10.3847/1538-4365/ab346b.

LAGARDE, N., DECRESSIN, T., CHARBONNEL, C., et al., 2012, "Thermohaline instability and rotation-induced mixing. III. Grid of stellar models and asymptotic asteroseismic quantities from the pre-main sequence up to the AGB for low- and intermediate-mass stars of various metallicities", Astron. Astrophys., 543:A108. doi: 10.1051/0004-6361/201118331.

LEIGHTON, R. B., 1959, "Observations of Solar Magnetic Fields in Plage Regions." Astrophys. J., v. 130 (set.), pp. 366. doi: 10.1086/146727.

LINSKY, J. L., 2017, "Stellar Model Chromospheres and Spectroscopic Diagnostics", Ann. Rev. Astron. Astrohys., v. 55, n. 1 (ago.), pp. 159–211. doi: 10.1146/annurev-astro-091916-055327.

LISSAUER, J. J., STEWART, G. R., 1993, "Growth of Planets from Planetesimals". In: Levy, E. H., Lunine, J. I. (Eds.), *Protostars and Planets III*, p. 1061, jan.

LIVINGSTON, J. H., CROSSFIELD, I. J. M., PETIGURA, E. A., et al., 2018, "Sixty Validated Planets from K2 Campaigns 5-8", Astron. J., 156(6):277. doi: 10.3847/1538-3881/aae778.

LOPEZ, E. D., FORTNEY, J. J., 2013, "The Role of Core Mass in Controlling Evaporation: The Kepler Radius Distribution and the Kepler-36 Density Dichotomy", Astrophys. J., 776:2. doi: 10.1088/0004-637X/776/1/2.

MAGRINI, L., RANDICH, S., ROMANO, D., et al., 2014, "The Gaia-ESO Survey: Abundance ratios in the inner-disk open clusters Trumpler 20, NGC 4815, NGC 6705", Astron. Astrophys., 563:A44. doi: 10.1051/0004-6361/201322977.

MAJEWSKI, S. R., SCHIAVON, R. P., FRINCHABOY, P. M., et al., 2017, "The Apache Point Observatory Galactic Evolution Experiment (APOGEE)", Astron. J., 154: 94. doi: 10.3847/1538-3881/aa784d.

MALDONADO, J., VILLAVER, E., EIROA, C., 2018, "Chemical fingerprints of hot Jupiter planet formation", Astron. Astrophys., 612:A93. doi: 10.1051/0004-6361/201732001.

MARCY, G. W., BUTLER, R. P., WILLIAMS, E., et al., 1997, "The Planet around 51 Pegasi", Astrophys. J., v. 481, n. 2 (maio), pp. 926–935. doi: 10.1086/304088.

MARTINEZ, C. F., CUNHA, K., GHEZZI, L., et al., 2019, "A Spectroscopic Analysis of the California-Kepler Survey Sample. I. Stellar Parameters, Planetary Radii, and a Slope in the Radius Gap", Astrophys. J., 875:29. doi: 10.3847/1538-4357/ab0d93.

MAYO, A. W., VANDERBURG, A., LATHAM, D. W., et al., 2018, "275 Candidates and 149 Validated Planets Orbiting Bright Stars in K2 Campaigns 0-10", Astron. J., 155(3):136. doi: 10.3847/1538-3881/aaadff.

MAYOR, M., PEPE, F., QUELOZ, D., et al., 2003, "Setting New Standards with HARPS", *The Messenger*, v. 114 (dez.), pp. 20–24.

MAYOR, M., LOVIS, C., PEPE, F., et al., 2011, "The road to Earth twins", *Astronomische Nachrichten*, v. 332, n. 5 (jun.), pp. 429. doi: 10.1002/asna.201111558.

MAYOR, M., QUELOZ, D., 1995, "A Jupiter-mass companion to a solar-type star", Nature, v. 378, n. 6555 (nov.), pp. 355–359. doi: 10.1038/378355a0.

MELÉNDEZ, J., RAMÍREZ, I., KARAKAS, A. A. I., et al., 2014, "18 Sco: A Solar Twin Rich in Refractory and Neutron-capture Elements. Implications for Chemical Tagging", Astrophys. J., 791(1):14. doi: 10.1088/0004-637X/791/1/14.

METCALFE, T. S., VAN SADERS, J., 2017, "Magnetic Evolution and the Disappearance of Sun-Like Activity Cycles", Sol. Phys., 292(9):126. doi: 10.1007/s11207-017-1157-5.

MIDDELKOOP, F., 1982, "Magnetic structure in cool stars. IV - Rotation and CA II H and K emission of main-sequence stars", Astron. Astrophys., v. 107, n. 1 (mar.), pp. 31–35.

MORDASINI, C., KLAHR, H., ALIBERT, Y., et al., 2014, "Grain opacity and the bulk composition of extrasolar planets. I. Results from scaling the ISM opacity", Astron. Astrophys., 566:A141. doi: 10.1051/0004-6361/201321479.

MORTIER, A., SANTOS, N. C., SOUSA, S. G., et al., 2013, "New and updated stellar parameters for 90 transit hosts. The effect of the surface gravity", Astron. Astrophys., 558:A106. doi: 10.1051/0004-6361/201322240.

MULDERS, G. D., PASCUCCI, I., APAI, D., et al., 2016, "A Super-solar Metallicity for Stars with Hot Rocky Exoplanets", Astron. J., 152(6):187. doi: 10.3847/0004-6256/152/6/187.

NARANG, M., MANOJ, P., FURLAN, E., et al., 2018, "Properties and Occurrence Rates for Kepler Exoplanet Candidates as a Function of Host Star Metallicity from the DR25 Catalog", Astron. J., 156(5):221. doi: 10.3847/1538-3881/aae391.

NOYES, R. W., HARTMANN, L. W., BALIUNAS, S. L., et al., 1984, "Rotation, convection, and magnetic activity in lower main-sequence stars." Astrophys. J., v. 279 (abr.), pp. 763–777. doi: 10.1086/161945.

OWEN, J. E., WU, Y., 2013, "Kepler Planets: A Tale of Evaporation", Astrophys. J., 775:105. doi: 10.1088/0004-637X/775/2/105.

PALACIOS, A., CHARBONNEL, C., TALON, S., et al., 2006, "Rotational mixing in low-mass stars. II. Self-consistent models of Pop II RGB stars", Astron. Astrophys., v. 453, n. 1 (jul.), pp. 261–278. doi: 10.1051/0004-6361:20053065.

PETIGURA, E. A., HOWARD, A. W., MARCY, G. W., et al., 2017, "The California-Kepler Survey. I. High-resolution Spectroscopy of 1305 Stars Hosting Kepler Transiting Planets", Astron. J., 154(3):107. doi: 10.3847/1538-3881/aa80de.

PETIGURA, E. A., CROSSFIELD, I. J. M., ISAACSON, H., et al., 2018a, "Planet Candidates from K2 Campaigns 5-8 and Follow-up Optical Spectroscopy", Astron. J., 155(1):21. doi: 10.3847/1538-3881/aa9b83.

PETIGURA, E. A., MARCY, G. W., WINN, J. N., et al., 2018b, "The California-Kepler Survey. IV. Metal-rich Stars Host a Greater Diversity of Planets", Astron. J., 155(2):89. doi: 10.3847/1538-3881/aaa54c.

PINSONNEAULT, M. H., ELSWORTH, Y. P., TAYAR, J., et al., 2018, "The Second APOKASC Catalog: The Empirical Approach", Astrophys. J. Suppl., 239:32. doi: 10.3847/1538-4365/aaebfd.

PLEZ, B., 2012. "Turbospectrum: Code for spectral synthesis". Astrophysics Source Code Library, record ascl:1205.004, maio.

POLLACK, J. B., HUBICKYJ, O., BODENHEIMER, P., et al., 1996, "Formation of the Giant Planets by Concurrent Accretion of Solids and Gas", Icarus, v. 124, n. 1 (nov.), pp. 62–85. doi: 10.1006/icar.1996.0190.

POPE, B. J. S., PARVIAINEN, H., AIGRAIN, S., 2016, "Transiting exoplanet candidates from K2 Campaigns 5 and 6", Mon. Not, Roy. Astron. Soc., v. 461, n. 4 (out.), pp. 3399–3409. doi: 10.1093/mnras/stw1373.

PRŠA, A., HARMANEC, P., TORRES, G., et al., 2016, "Nominal Values for Selected Solar and Planetary Quantities: IAU 2015 Resolution B3", Astron. J., 152(2): 41. doi: 10.3847/0004-6256/152/2/41.

QUELOZ, D., HENRY, G. W., SIVAN, J. P., et al., 2001, "No planet for HD 166435", Astron. Astrophys., v. 379 (nov.), pp. 279–287. doi: 10.1051/0004-6361:20011308.

RAMÍREZ, I., MELÉNDEZ, J., BEAN, J., et al., 2014, "The Solar Twin Planet Search. I. Fundamental parameters of the stellar sample", Astron. Astrophys., 572:A48. doi: 10.1051/0004-6361/201424244.

RANDICH, S., GILMORE, G., MAGRINI, L., et al., 2022, "The Gaia-ESO Public Spectroscopic Survey: Implementation, data products, open cluster survey, science, and legacy", Astron. Astrophys., 666:A121. doi: 10.1051/0004-6361/202243141.

RICKER, G. R., WINN, J. N., VANDERSPEK, R., et al., 2015, "Transiting Exoplanet Survey Satellite (TESS)", *Journal of Astronomical Telescopes, Instruments, and Systems*, 1:014003. doi: 10.1117/1.JATIS.1.1.014003.

RIZZUTO, A. C., MANN, A. W., VANDERBURG, A., et al., 2017, "Zodiacal Exoplanets in Time (ZEIT). V. A Uniform Search for Transiting Planets in Young Clusters Observed by K2", Astron. J., 154(6):224. doi: 10.3847/1538-3881/aa9070.

RUTTEN, R. G. M., 1984, "Magnetic structure in cool stars. VII. Absolute surface flux in CA IIH and K line cores." Astron. Astrophys., v. 130 (jan.), pp. 353–360.

SANTOS, N. C., ISRAELIAN, G., MAYOR, M., 2001, "The metal-rich nature of stars with planets", Astron. Astrophys., v. 373 (jul.), pp. 1019–1031. doi: 10.1051/0004-6361:20010648.

SANTOS, N. C., ISRAELIAN, G., MAYOR, M., 2004, "Spectroscopic [Fe/H] for 98 extra-solar planet-host stars. Exploring the probability of planet formation", Astron. Astrophys., v. 415 (mar.), pp. 1153–1166. doi: 10.1051/0004-6361:20034469.

SEAGER, S., MALLÉN-ORNELAS, G., 2003, "A Unique Solution of Planet and Star Parameters from an Extrasolar Planet Transit Light Curve", Astrophys. J., v. 585 (mar.), pp. 1038–1055. doi: 10.1086/346105.

SHARMA, S., STELLO, D., BLAND-HAWTHORN, J., et al., 2019, "The K2-HERMES Survey: age and metallicity of the thick disc", Mon. Not, Roy. Astron. Soc., v. 490, n. 4 (dez.), pp. 5335–5352. doi: 10.1093/mnras/stz2861.

SILVA AGUIRRE, V., BOJSEN-HANSEN, M., SLUMSTRUP, D., et al., 2018, "Confirming chemical clocks: asteroseismic age dissection of the Milky Way disc(s)", Mon. Not, Roy. Astron. Soc., v. 475, n. 4 (abr.), pp. 5487–5500. doi: 10.1093/mnras/sty150.

SKUMANICH, A., 1972, "Time Scales for Ca II Emission Decay, Rotational Braking, and Lithium Depletion", Astrophys. J., v. 171 (fev.), pp. 565. doi: 10.1086/151310.

SMILJANIC, R., ROMANO, D., BRAGAGLIA, A., et al., 2016, "The Gaia-ESO Survey: Sodium and aluminium abundances in giants and dwarfs. Implications for stellar and Galactic chemical evolution", Astron. Astrophys., 589:A115. doi: 10.1051/0004-6361/201528014.

SNEDEN, C., 1973, "The nitrogen abundance of the very metal-poor star HD 122563." Astrophys. J., v. 184 (set.), pp. 839–849. doi: 10.1086/152374.

SOUBIRAN, C., LE CAMPION, J.-F., BROUILLET, N., et al., 2016, "The PASTEL catalogue: 2016 version", Astron. Astrophys., 591:A118. doi: 10.1051/0004-6361/201628497.

SOUSA, S. G., SANTOS, N. C., MAYOR, M., et al., 2008, "Spectroscopic parameters for 451 stars in the HARPS GTO planet search program. Stellar [Fe/H] and the frequency of exo-Neptunes", Astron. Astrophys., v. 487, n. 1 (ago.), pp. 373–381. doi: 10.1051/0004-6361:200809698.

SOUSA, S. G., SANTOS, N. C., ISRAELIAN, G., et al., 2011, "Spectroscopic stellar parameters for 582 FGK stars in the HARPS volume-limited sample. Revising the metallicity-planet correlation", Astron. Astrophys., 533:A141. doi: 10.1051/0004-6361/201117699.

SOUSA, S. G., SANTOS, N. C., ADIBEKYAN, V., et al., 2015, "ARES v2: new features and improved performance", Astron. Astrophys., 577:A67. doi: 10.1051/0004-6361/201425463.

SUSA, H., HASEGAWA, K., TOMINAGA, N., 2014, "The Mass Spectrum of the First Stars", Astrophys. J., 792(1):32. doi: 10.1088/0004-637X/792/1/32.

TAUTVAIŠIENĖ, G., DRAZDAUSKAS, A., MIKOLAITIS, S., et al., 2015, "VizieR Online Data Catalog: Gaia-ESO Survey: Tr 20, NGC4815, NGC6705 (Tautvaisiene+, 2015)", *VizieR Online Data Catalog*, v. 357 (nov.).

THOMPSON, S. E., COUGHLIN, J. L., HOFFMAN, K., et al., 2018, "Planetary Candidates Observed by Kepler. VIII. A Fully Automated Catalog with Measured Completeness and Reliability Based on Data Release 25", Astrophys. J. Suppl., 235:38. doi: 10.3847/1538-4365/aab4f9.

TRAN, H. D., BERRIMAN, G. B., GELINO, C. R., et al., 2015, "The Science Content and Usage of the the Keck Observatory Archive". In: *American Astronomical Society Meeting Abstracts #225*, v. 225, *American Astronomical Society Meeting Abstracts*, p. 336.61, jan.

TRURAN, J. W., J., HEGER, A., 2003, "Origin of the Elements", *Treatise on Geochemistry*, v. 1 (dez.), pp. 711. doi: 10.1016/B0-08-043751-6/01059-8.

VALENTI, J. A., FISCHER, D. A., 2005, "Spectroscopic Properties of Cool Stars (SPOCS). I. 1040 F, G, and K Dwarfs from Keck, Lick, and AAT Planet Search Programs", Astrophys. J. Suppl., v. 159, n. 1 (jul.), pp. 141–166. doi: 10.1086/430500.

VAN EYLEN, V., AGENTOFT, C., LUNDKVIST, M. S., et al., 2018, "An asteroseismic view of the radius valley: stripped cores, not born rocky", Mon. Not, Roy. Astron. Soc., v. 479 (out.), pp. 4786–4795. doi: 10.1093/mnras/sty1783.

VANDERBURG, A., LATHAM, D. W., BUCHHAVE, L. A., et al., 2016, "Planetary Candidates from the First Year of the K2 Mission", Astrophys. J. Suppl., 222 (1):14. doi: 10.3847/0067-0049/222/1/14.

VAUGHAN, A. H., PRESTON, G. W., 1980, "A survey of chromospheric CA II H and K emission in field stars of the solar neighborhood." Publ. Astron. Soc. Pacific, v. 92 (ago.), pp. 385–391. doi: 10.1086/130683.

VAUGHAN, A. H., PRESTON, G. W., WILSON, O. C., 1978, "Flux measurements of Ca II and K emission." Publ. Astron. Soc. Pacific, v. 90 (jun.), pp. 267–274. doi: 10.1086/130324.

WANG, J., FISCHER, D. A., 2015, "Revealing a Universal Planet-Metallicity Correlation for Planets of Different Sizes Around Solar-type Stars", Astron. J., 149(1): 14. doi: 10.1088/0004-6256/149/1/14.

WEISS, L. M., ISAACSON, H. T., MARCY, G. W., et al., 2018, "The California-Kepler Survey. VI. Kepler Multis and Singles Have Similar Planet and Stellar Properties Indicating a Common Origin", Astron. J., 156(6):254. doi: 10.3847/1538-3881/aae70a.

WILSON, O. C., 1963, "A Probable Correlation Between Chromospheric Activity and Age in Main-Sequence Stars." Astrophys. J., v. 138 (out.), pp. 832. doi: 10.1086/147689.

WILSON, O. C., 1978, "Chromospheric variations in main-sequence stars." Astrophys. J., v. 226 (dez.), pp. 379–396. doi: 10.1086/156618.

WILSON, O. C., SKUMANICH, A., 1964, "Dependence of Chromospheric Activity upon Age in Main-Sequence Stars: Additional Evidence." Astrophys. J., v. 140 (nov.), pp. 1401. doi: 10.1086/148046.

WILSON, R. F., TESKE, J., MAJEWSKI, S. R., et al., 2018, "Elemental Abundances of Kepler Objects of Interest in APOGEE. I. Two Distinct Orbital Period Regimes Inferred from Host Star Iron Abundances", Astron. J., 155:68. doi: 10.3847/1538-3881/aa9f27.

WITTENMYER, R. A., SHARMA, S., STELLO, D., et al., 2018, "The K2-HERMES Survey. I. Planet-candidate Properties from K2 Campaigns 1-3", Astron. J., 155 (2):84. doi: 10.3847/1538-3881/aaa3e4.

YANA GALARZA, J., MELÉNDEZ, J., LORENZO-OLIVEIRA, D., et al., 2019, "The effect of stellar activity on the spectroscopic stellar parameters of the young solar twin HIP 36515", Mon. Not, Roy. Astron. Soc., v. 490, n. 1 (nov.), pp. L86–L90. doi: 10.1093/mnrasl/slz153.

ZHU, W., 2019, "Influence of Stellar Metallicity on Occurrence Rates of Planets and Planetary Systems", Astrophys. J., 873(1):8. doi: 10.3847/1538-4357/ab0205.

ZHU, W., WANG, J., HUANG, C., 2016, "Dependence of Small Planet Frequency on Stellar Metallicity Hidden by Their Prevalence", Astrophys. J., 832(2):196. doi: 10.3847/0004-637X/832/2/196.

# Apêndice A

# A Formação de Linhas Espectrais

De maneira geral, os espectros estelares apresentam linhas de absorção ou de emissão associadas à transição de níveis de energia dos átomos presentes na atmosfera estelar. Essas linhas fornecem informações importantes não somente sobre o tipo espectral da estrela, assim como sobre sua velocidade radial, temperatura efetiva, gravidade superficial, composição química estelar e sobre os processos físicos que ocorrem na atmosfera estelar. Considerando que uma grande parte do entendimento e conhecimento sobre as estrelas provém da análise dos espectros estelares, neste capítulo descreveremos como a radiação eletromagnética emitida pelas estrelas se origina e como o processo de interação da radiação com a matéria na atmosfera estelar dá origem às linhas de absorção nos espectros estelares.

## A.1 Interação entre radiação e matéria

Uma estrela do tipo solar pode ser dividida em uma parte interna e uma parte externa chamada de atmosfera. A parte interna contém quase toda a massa da estrela e, por sua vez, pode ser subdividida em uma região central (núcleo da estrela, onde a energia é gerada por meio de reações termo-nucleares), uma zona radiativa (onde a energia é transportada pelo processo de difusão radiativa) e uma zona de convecção (onde a energia é transferida por convecção). Por outro lado, conforme representado na Figura A.1, a atmosfera da estrela é subdividida em quatro camadas, cada uma com características distintas. A camada mais interna é a fotosfera, seguida pela cromosfera, uma camada de transição e, finalmente, a coroa. É importante destacar que os limites dessas regiões não são bem definidos e podem variar em tamanho, dependendo do tipo de estrela. Por exemplo, para uma estrela com tamanho do Sol ($R_\odot = 695,700$ km, PRŠA *et al.*, 2016), a fotosfera tem uma espessura de $\sim$ 300 km, a espessura da cromosfera é $\sim$ 2000 km, a região de transição tem uma espessura de 100 km e a coroa estendendo-se até valores $> 10^5$ km (ASCHWANDEN, 2007).

No contexto da formação das linhas espectrais, a camada da fotosfera é a mais im-

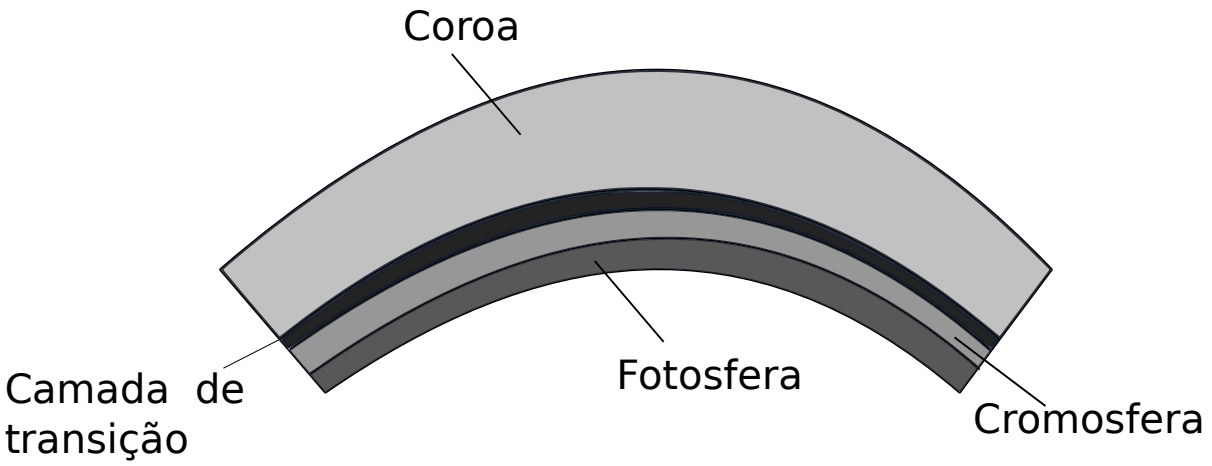


**Figura A.1** – Camadas que compõem a atmosfera estelar.

portante, dado que a maior contribuição de energia no espectro observado e a formação das linhas vêm dessa região. Após uma longa viagem (que pode variar de alguns milhares a alguns milhões de anos, no caso do Sol), a radiação produzida no núcleo das estrelas atravessa a zona radiativa e a zona convectiva, interagindo, por fim, com a matéria presente na fotosfera. A partir desse ponto, ela escapa para o meio interestelar, originando o espectro estelar que é analisado para inferir as propriedades físicas e químicas das estrelas. Portanto, é crucial compreender o processo de interação da radiação com a matéria.

Esse processo pode ser abordado do ponto de vista macroscópico, e nesta abordagem, o transporte de radiação na presença de matéria (sem considerar processos de dispersão) é dado pela Equação A.1, conhecida como equação de transferência radiativa. Onde $I_\nu$ é a intensidade de radiação, $\tau_\nu$ a profundidade ótica estelar, e $S_\nu$ é a função fonte. Por sua vez, $S_\nu$ é definida como a razão entre o coeficiente de emissão ($j_\nu$) e o coeficiente de absorção ($k_\nu$).

$$\frac{dI_\nu}{d\tau_\nu} = -I_\nu + S_\nu \tag{A.1}$$

Em geral, a equação não possui uma solução analítica, sendo necessário recorrer a métodos numéricos. No entanto, se considerarmos o equilíbrio termodinâmico (ET), a análise da equação pode ser simplificada consideravelmente. A seguir, são descritas algumas características do sistema em ET.

No caso do ET, o número de partículas com velocidades no intervalo $v + dv$ é dado pela distribuição de Maxwell-Boltzmann,

$$dn_v = 4\pi n \left(\frac{m}{2\pi k_B T}\right)^{3/2} v^2 e^{-\frac{mv^2}{2k_B T}} dv, \tag{A.2}$$

onde $n$ é o número total de partículas por unidade de volume, $m$ é a massa das partículas, $k_B$ é a constante de Boltzmann, e $T$ representa a temperatura do sistema.

Em ET, a proporção do número de átomos no estado excitado ($n_e$), com energia $E$ acima do estado fundamental, em relação ao número de átomos no estado fundamental ($n_0$), é dada pela lei de distribuição de Boltzmann.

$$\frac{n_e}{n_0} = \exp\left(-\frac{E}{k_B T}\right) \tag{A.3}$$

No sistema, além de possuir átomos nos estados excitado e fundamental, é possível ter átomos no estado de ionização. Neste caso, no estado de ET, a fração de átomos que serão ionizados, representada por $x$, em uma determinada temperatura $T$ e pressão $P$, é dada pela equação de Saha,

$$\frac{x^2}{1-x} = \frac{(2\pi m_e)^{3/2}}{h^3}\frac{(k_B T)^{5/2}}{P}\exp\left(-\frac{\chi}{k_B T}\right) \tag{A.4}$$

onde $\chi$ representa o potencial de ionização (quantidade de energia necessária para remover um elétron do átomo) e $m_e$ é a massa do elétron.

No ET, a função fonte é dada pela lei de Planck e depende unicamente da temperatura,

$$S_\nu \equiv \frac{\eta_\nu}{\kappa_\nu} = B_\nu(T) = \frac{1}{2h\nu^3}\cdot\frac{1}{e^{\frac{h\nu}{kT}}-1} \tag{A.5}$$

## A.2 Equilíbrio Termodinâmico Local

Obviamente, o ET é um caso ideal e não se aplicaria às estrelas, onde a temperatura varia com o raio e a densidade não é constante. No entanto, existe a aproximação de equilíbrio termodinâmico local (ETL), onde algumas das camadas estelares podem ser consideradas como estando em ET, e as equações descritas acima seriam válidas. Um parâmetro importante para considerar uma região em ETL é o percurso ou o livre caminho médio que é definido como a medida da distância média percorrida por uma partícula entre colisões sucessivas com outras partículas em um meio. Se o livre caminho médio for menor em comparação com o comprimento sobre o qual a temperatura varia significativamente, a região pode ser considerada como estando em ETL. Para a região da fotosfera, onde os processos de colisão são frequentes, o ETL é considerado uma boa aproximação.

## A.3 Modelos de Atmosfera

Como mencionado anteriormente, o conhecimento cientifico sobre as estrelas provém da análise da radiação que elas emitem. No entanto, para interpretar e extrair informações dos espectros estelares, é necessário definir um modelo que possa descrever a atmosfera estelar e resolver as equações de transferência radiativa a partir do modelo considerado. Os modelos de atmosfera são modelos numéricos que descrevem o estado físico do plasma

nas camadas exteriores de uma estrela e são usados para calcular quantidades observáveis, como o espectro emergente ou as cores estelares (BONIFACIO *et al.*, 2011).

Modelos em uma dimensão (1D) que assumem a validade do ETL oferecem uma simplificação do problema, e são amplamente utilizados na determinação de parâmetros estelares e abundâncias químicas na literatura. Esses modelos supõem que a atmosfera é estratificada e é composto por varias camadas sucessivas, dentro das quais são válidas a equação de equilíbrio hidrostático (onde a pressão é equilibrada pela gravidade), e a aproximação de ETL, descrevendo a estrutura e as propriedades físicas das camadas exteriores das estrelas por meio dos seguintes parâmetros: profundidade óptica ($\tau$), temperatura (T), pressão gasosa ($P_g$) e densidade eletrônica ($N_e$). Em particular, a profundidade ótica refere-se à medida da opacidade que os fótons enfrentam ao atravessar uma determinada camada da atmosfera estelar, sendo que na superfície da estrela $\tau = 0$ e a profundidade ótica aumenta em direção ao centro da estrela.

Dentre os modelos de atmosfera mais utilizados na literatura, destacam-se os modelos de Kurucz (CASTELLI e KURUCZ, 2004) e MARCS (GUSTAFSSON *et al.*, 2008). Os modelos de Kurucz descrevem a atmosfera estelar usando uma geometria plano-paralela, enquanto os modelos MARCS descrevem a atmosfera estelar usando tanto geometria plano-paralela (para estrelas anãs) quanto esférica (para estrelas gigantes vermelhas).

Embora modelos 1D em ETL sejam amplamente utilizados e sejam uma boa aproximação para descrever as atmosferas estelares, modelos de atmosfera em três dimensões (3D) e em não-ETL seriam em princípio mais adequados e mais precisos. Modelos 3D resultam da solução das equações hidrodinâmicas de conservação de massa, momento e energia, acopladas à equação de transferência radiativa (ASPLUND, 2000). Ao contrário dos modelos 1D, os modelos 3D não invocam quaisquer parâmetros livres (como velocidades de micro e macro-turbulência) que são ajustados no caso 1D para que haja um bom acordo com vínculos observacionais.

Cálculos em 3D e não ETL para o Sol, por exemplo, evidenciam que as abundâncias dos elementos C, N e O em particular são mais baixas quando comparadas às abundâncias obtidas usando modelos 1D (ASPLUND *et al.*, 2005; GREVESSE *et al.*, 2007). Por exemplo, as abundâncias solares de C, N, e O calculadas por GREVESSE *et al.* (2007) utilizando modelos 3D são: A(C) = 8,39, A(N) = 7,85 e A(O) = 8,64. Estas abundâncias são significativamente menores do que as abundâncias solares que haviam sido amplamente utilizadas anteriormente na literatura (provenientes da compilação de ANDERS e GREVESSE (1989)), correspondendo a uma diminuição nas abundâncias de -0,17 dex para o carbono, -0,20 dex para o nitrigênio, e -0,29 dex para o oxigênio. As determinações mais recentes das abundâncias solares usando modelos 3D de ASPLUND *et al.* (2021), também encontram valores mais baixos que em 1D, porém a diferença é um pouco menor: -0,06 dex para o carbono, -0,09 dex para o nitrogênio e -0,14 dex para o oxigênio.

## A.4 Formação de linhas espectrais

As linhas espectrais referem-se a características distintas na distribuição contínua do espectro de radiação emitida por uma estrela. No processo de interação da radiação com a matéria, a radiação pode ser redistribuída em comprimentos de onda de forma contínua (criando o chamado espectro continuo, resultado da modificação da forma da radiação continua que foi gerada no centro da estrela), ou pode absorver energia de comprimentos de onda específicos, originando as linhas espectrais. Ou seja, ao atravessar a radiação pela fotosfera, alguns dos fótons podem ser absorbidos e esse fenômeno é explicado pelo coeficiente de absorção (um valor para cada comprimento de onda). Adicionalmente, há a possibilidade de surgirem fótons adicionais que não estavam presentes inicialmente, sendo tal fenômeno explicado pelo coeficiente de emissão. No caso contínuo, processos como a fotoionização (ligado-livre) e espalhamento (livre-livre) dos átomos ocorrem durante a interação com a radiação. Por outro lado, no caso discreto, temos o processo de excitação atômica (ligado-ligado). Vale ressaltar que, no contexto contínuo, o hidrogênio desempenha um papel fundamental, sendo predominante na composição química das estrelas.

A seguir, focaremos ao caso discreto, que está relacionado à formação das linhas espectrais. A ideia central aqui é que, se a diferença de energia entre dois estados eletrônicos em um átomo coincidir com a energia de um fóton, há uma probabilidade quântica de que esse fóton seja absorvido pelo elétron. Isso resulta na excitação do elétron para um nível de energia superior ao inicial, com a diferença de energia entre os níveis sendo precisamente igual à energia do fóton absorvido. Como consequência desse processo, vários fótons com energias específicas são absorvidos pelo material presente na atmosfera, originando as linhas espectrais que se manifestam como quedas no fluxo no espectro contínuo. É importante notar que os átomos excitados dessa maneira também podem desexcitar-se, geralmente em frações de segundo, emitindo um fóton com energia equivalente à diferença entre os níveis. Contudo, esse fóton não necessariamente seguirá na mesma direção que antes.

Dessa forma, ao considerarmos os modelos de atmosfera e ao aplicarmos a teoria da formação das linhas espectrais, podemos calcular as abundâncias dos elementos a partir das linhas espectrais que se manifestam no espectro. Essa análise, baseada nos comprimentos de onda específicos das linhas espectrais, proporciona informação sobre a abundancia química e os estados de excitação e ionização do material na fotosfera.

### A.4.1 Perfil de linhas espectrais

O perfil de uma linha espectral representa a variação da densidade de fluxo (intensidade) com o comprimento de onda. A forma de uma linha espectral é chamada de perfil da linha, esta inclui uma parte central ou núcleo da linha e uma parte mais afastada do centro que são as asas. Cada uma dessas partes do perfil da linha são formadas em diferentes regiões

da atmosfera estelar. Por exemplo, o contínuo é formado nas regiões mais internas a aproximadamente profundidade ótica $\tau = 2/3$ (CARROLL e OSTLIE, 2017), as asas são formadas nas regiões menos altas e o centro da linha é formada nas regiões mais altas, onde a temperatura é mais baixa. Portanto, a forma da linha reflete as propriedades da atmosfera da estrela: temperatura, pressão, gravidade superficial, densidade e velocidade das partículas.

O perfil de uma linha espectral não é infinitamente fino, mas, ao contrário, apresenta um alargamento que é explicado de forma física e matemática por meio dos diferentes processos de alargamento das linhas. Além disso o perfil observado de uma dada linha também é alargado pelo perfil instrumental.

#### A.4.1.1 Alargamentos das linhas Espectrais

Os principais mecanismos responsáveis pelo alargamento de uma linha espectral são o alargamento natural, o alargamento Doppler, o alargamento colisional e o alargamento por velocidade de rotação, os quais serão descritos a seguir.

**Alargamento Natural:** A energia de um elétron em um nível atômico específico é determinada, de acordo com o princípio da incerteza, sendo proporcional ao inverso do tempo de vida naquele nível. Consequentemente, um conjunto de átomos originará linhas de absorção ou emissão com uma variação mínima nas frequências dos fótons ($\Delta\nu$), conhecida como largura natural. Essa largura natural é da ordem de:

$$\Delta\nu = \frac{\Delta E}{h} \propto \frac{1}{\Delta t} \tag{A.6}$$

onde $E$ representa a energia, $h$ é a constante de Planck e $t$ é o tempo de vida do elétron no nível correspondente.

**Alargamento Doppler térmico:** Este processo está intrinsecamente vinculado à temperatura e à composição química do gás na atmosfera da estrela. Os átomos na fase gasosa exibem velocidades aleatórias resultantes do seu movimento térmico. Essas velocidades seguem uma distribuição Gaussiana (ou Maxwelliana), influenciando o alargamento da linha espectral devido ao deslocamento Doppler na radiação emitida ou absorvida como resultado dos movimentos dos átomos ao longo da linha de visada.

A energia removida de um feixe com intensidade unitária no espaço de comprimento de onda é descrita pela seguinte relação:

$$\alpha d\lambda \propto \frac{\lambda_0^2}{c} \frac{1}{\Delta\lambda_D} exp\left[ -\left( \frac{\lambda - \lambda_0}{\Delta\lambda_D} \right)^2 \right] d\lambda, \tag{A.7}$$

onde $\alpha$ é definida como o coeficiente de absorção térmica, $\lambda_0$ é o comprimento de onda

central da linha espectral e $c$ é a velocidade da luz. $\Delta\lambda_D$ representa a diferença no deslocamento da linha observada em relação a $\lambda_0$, que é o comprimento de onda da linha sem qualquer deslocamento (determinado em laboratório), e é dada por:

$$\frac{\Delta\lambda_D}{\lambda_0} = \frac{v_r}{c} = \frac{\lambda_0}{c}\left(\frac{2kT}{m}\right)^{1/2} \tag{A.8}$$

onde $v_r$ é a velocidade radial em termos da velocidade mais provável, $k$ é a constante de Boltzmann, $T$ representa a temperatura da fotosfera estelar, e $m$ é a massa do átomo.

**Alargamento Colisional ou de Pressão:** Os níveis de energia de um átomo sofrem perturbações, ou seja, deslocamentos, devido à influência de partículas vizinhas, especialmente aquelas partículas carregadas, como íons e elétrons. Em um gás, essas perturbações ocorrem de maneira aleatória, resultando no alargamento das linhas espectrais. A largura dessas linhas espectrais é diretamente proporcional à densidade de partículas (e, por conseguinte, à pressão) no gás, sendo este processo crucial para o alargamento de linhas intensas, como $H_\alpha$, $H_\beta$, entre outras.

A variação de energia de um nível perturbado, decorrente de uma colisão, é descrita pela expressão $\Delta E \propto R^{-n}$, onde $R$ denota a distância entre as partículas perturbadora e absorvedora, e $n$ representa a ordem dessa separação. Quando $n = 2$, surge o efeito Stark linear, originado pela interação entre a transição de um átomo e prótons/elétrons, afetando principalmente as linhas de hidrogênio. Para $n = 4$, observamos o efeito Stark quadrático, resultante da interação entre a partícula emissora e o perturbador (íons/elétrons), sendo significativo em estrelas quentes e na maioria das linhas espectrais. No caso de $n = 6$, ocorre o efeito de Van der Waals ou damping Van der Waals, mais prevalente em estrelas frias, onde o perturbador, nesse caso, é o hidrogênio neutro atuando sobre o átomo em transição. As expressões que descrevem os efeitos Stark quadráticos e van der Waals estão apresentadas nas Equações (A.9) e (A.10), respectivamente.

$$\log\gamma_4 = 19 + \frac{2}{3}\log C_4 + \log P_e - \frac{5}{6}\log T \tag{A.9}$$

onde, $C_4$ é uma constante de iteração medida em laboratorio para varias linhas, $P_e$ é a pressão eletrônica e T a temperatura.

$$\log\gamma_6 = \log Cte + 0.4\log C_6 + \log P_g - 0.7\log T \tag{A.10}$$

onde $C_6$ constante de iteração, $P_g$ pressão de gás e T a temperatura.

**Alargamento por velocidade de rotação:** O movimento rotacional de uma estrela provoca um deslocamento Doppler em cada uma das linhas presentes em seu espectro. A largura dessas linhas é influenciada pela taxa de rotação e pelo ângulo de inclinação

do eixo de rotação em relação à linha de visão. Essa taxa é quantificada pelo parâmetro $v$ sen $i$. Em termos gerais, estrelas mais quentes (das classes O e B) tendem a girar rapidamente, enquanto estrelas semelhantes ao Sol têm rotações mais lentas. Portanto, se a estrela apresenta maior rotação a linha vai ter maior alargamento.

Outros efeitos em escala microscópica, como o Efeito Zeeman, que implica o desdobramento de linhas na presença de um campo magnético, também desempenham um papel no alargamento das linhas. Quando um campo magnético está presente, ele exerce uma força sobre os elétrons em movimento nos átomos, alterando as propriedades das linhas espectrais. O efeito Zeeman é notável principalmente em linhas espectrais produzidas por átomos ou íons que possuem momento magnético intrínseco, como átomos com elétrons desemparelhados.

Além dos alargamentos mencionados acima, outra fonte que contribuí ao alargamento da linha é o próprio alargamento instrumental.

## A.5 Métodos para Determinar a Composição Química Estelar

A composição química da atmosfera de uma estrela, assim como os parâmetros estelares temperatura efetiva, gravidade superficial, e metalicidade, podem ser determinados em última análise pela razão das profundidades e profundidades relativas das linhas espectrais, as quais dependem da temperatura e da pressão na região de formação das linhas. A determinação da abundância química de um elemento é realizada através da avaliação da intensidade de suas linhas espectrais. Em outras palavras, em termos gerais, quanto maior for a intensidade de uma linha, maior será a abundância do elemento químico na estrela. Nesta seção discutiremos a inferência de abundâncias químicas a partir de medidas de linhas espectrais. A determinação de parâmetros estelares espectroscópicos também pode se basear em medidas de linhas espectrais (em particular de linhas de Fe I e Fe II, conforme a metodologia adotada nesta tese e discutida no Capitulo **2**).

Antes de prosseguirmos vale notar que as abundâncias dos elementos mais pesados do que o He (também chamados de metais) são usualmente definidas com relação ao H e estas são expressas como o logaritmo decimal da quantidade de partículas por unidade de volume à do H:

$$A(X) = \log_{10}\left(\frac{N_X}{N_H}\right) + 12 \tag{A.11}$$

fazendo a transformação logarítmica obtemos diretamente a relação de $N_X/N_H$,

$$\left(\frac{N_X}{N_H}\right) = 10^{A(X)+12} \tag{A.12}$$

onde, A(X) representa a abundância do elemento de interesse. No entanto, de maneira convencional, as abundâncias de elementos químicos serão apresentadas normalizadas em relação à abundância solar:

$$\left[\frac{X}{Fe}\right] = \log\left(\frac{X}{Fe}\right)_{\star} - \log\left(\frac{X}{Fe}\right)_{\odot} \tag{A.13}$$

onde $[Fe/H]$ representa a abundância do ferro relativa à abundância do hidrogênio (metalicidade), $[X/Fe]$ é a abundância do elemento "X" relativa ao ferro e $A(X)_{\odot}$ é abundância solar.

Existem duas formas básicas de determinar quantitativamente as abundâncias químicas dos elementos nas fotosferas estelares: por meio de medidas de larguras equivalentes e utilizando síntese espectral. Entretanto, os preceitos teóricos, como transferência radiativa, são os mesmos. A seguir discutiremos estes dois métodos.

## A.5.1 Medidas de Larguras Equivalentes

No caso de linhas espectrais isoladas, podemos medir a intensidade em uma linha de absorção para determinar a abundância do elemento químico que formou essa linha. Isso é obtido ao medir a área entre o perfil da linha e o contínuo, os quais estão relacionados ao número de absorvedores na linha de visada e à força de oscilador da transição, que é uma medida da probabilidade com que uma transição atômica emite ou absorve radiação. A quantidade associada a essa área é a largura equivalente, denotada como $W_\lambda$, que corresponde à largura que a linha teria se fosse um retângulo, conforme ilustrado na Figura A.2.

A definição da largura equivalente é dada por:

$$W_\lambda = \int \frac{F_{\lambda_c} - F_\lambda}{F_c} d\lambda \tag{A.14}$$

Onde $F_c$ e $F_\lambda$ são as medidas do fluxo do continuo e do perfil da linha respetivamente, $W_\lambda$ é a largura equivalente da linha para o comprimento de onda $\lambda$.

### A.5.1.1 Curva de Crescimento

A função que representa a mudança na largura equivalente em relação à abundância é chamada de curva de crescimento ou seja, ao considerar a curva de crescimento, podemos observar como a largura equivalente das linhas de absorção aumenta proporcionalmente ao número de átomos que contribuem para a formação das linhas. A largura equivalente, por sua vez, é influenciada pelo número de átomos absorvedores, abrangendo três fases distintas:

- Quando a densidade desses átomos é pequena, as larguras equivalentes crescem linearmente com sua densidade (N). Esta fase ocorre quando a linha é fraca e dominada

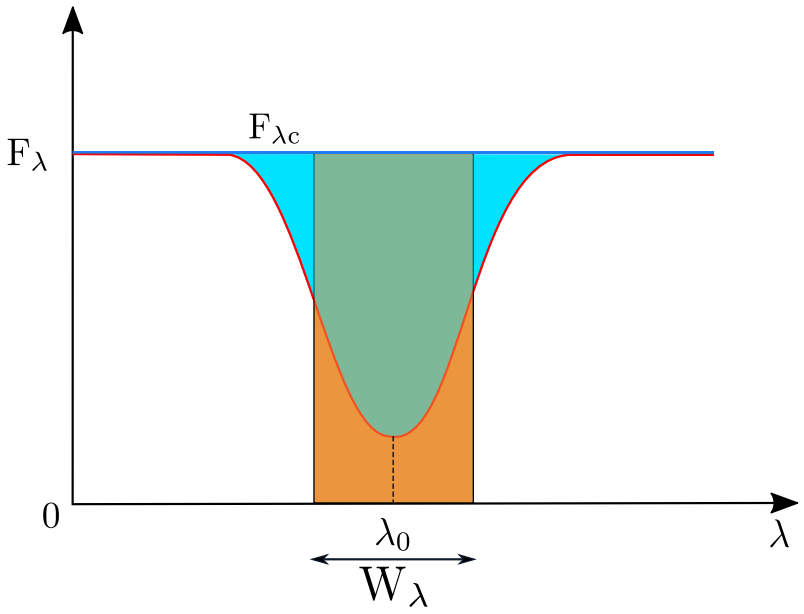


**Figura A.2** – Largura equivalente ($W_\lambda$) do perfil de uma linha isolada. O diagrama representa a intensidade ($F_\lambda$) como função do comprimento de onda ($\lambda$). $W_\lambda$ refere-se à área contida no retângulo laranja, a qual é equivalente à área sob o perfil da linha (azúl claro), considerando o nível do contínuo ($F_{\lambda_c}$). A profundidade máxima da linha indica o ponto de maior absorção, representado por $F_{\lambda_0}$.

pelo alargamento Doppler; nesta fase, a profundidade da linha (largura equivalente) cresce proporcionalmente ao aumento na abundância química.

- Quando a densidade aumenta, as larguras equivalentes tendem a saturar e, portanto, não podem ser usadas como uma indicação da abundância dos átomos. Essa fase ocorre à medida que a profundidade da linha se aproxima de seu valor máximo, resultando na saturação da linha, tornando a largura equivalente uma medida menos precisa da abundância

- Finalmente para linhas fortes as larguras equivalentes são novamente proporcionais à abundância ($\sqrt{N}$). Nesta fase as assas da linha de absorção tornam-se comparáveis à opacidade do contínuo ($k_\nu$) e a linha desenvolve asas de amortecimento.

As três fases da curva de crescimento são mostradas no lado esquerdo da Figura A.3, e no lado direito da figura mostramos o comportamento de um perfil de linha correspondente a estas três fases. O perfil da linha é influenciado pelos parâmetros atmosféricos da estrela, tais como a temperatura efetiva e gravidade superficial. Assim, a relação entre a abundância química de um elemento e a largura equivalente (ou largura equivalente reduzida, $W/\lambda$) é descrita pela seguinte equação:

$$\log\left(\frac{W_\lambda}{\lambda}\right) = B + A(X) + \log(gf) + \log(\lambda) - \theta_{exc}\chi - \log(k_{cont}) \qquad \text{(A.15)}$$

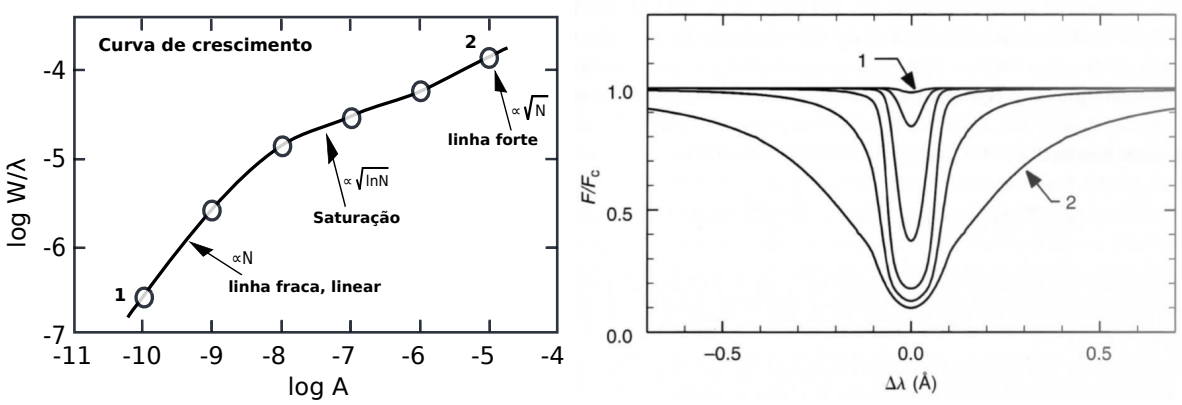


**Figura A.3** – Curva de crescimento mostrando suas três fases: linear, saturada e forte (esquerda). Comportamento de um perfil de linha com a mudança na abundância química (direita). Perfil marcado com número 1 representa uma abundância menor que perfil marcado com número 2. Figura extraída e adaptada de GRAY (2005).

onde $B$ é uma constante para uma determinada estrela e um determinado íon, A(X) é a abundancia, definida na Equação A.11, $gf$ é o produto do peso estatístico (g) pela força de oscilador (f), $\lambda$ é o comprimento de onda, $\chi$ é o potencial de excitação, $\theta = 5040/\mathrm{T_{ef}}$ que indica a dependência com a temperatura efetiva da estrela e e $k_{cont}$ é a opacidade do contínuo. Esta equação mostra como a largura equivalente de uma linha muda com a abundância química, com as propriedades da transição radiativa e com a temperatura da estrela.

Fica evidente que, através da análise do comportamento da curva de crescimento, é possível determinar abundâncias de elementos com base na larguras equivalentes medidas na primeira parte da curva (fase linear), onde não há problemas de saturação, possibilitando uma determinação confiável das abundâncias. Essa metodologia é utilizada em particular para se examinar as larguras equivalentes das linhas metálicas, e constituem, atualmente, a abordagem mais comum e precisa para a determinação dos parâmetros estelares por meio de espectros estelares.

### A.5.2 Síntese Espectral

Este método consiste em comparar um espectro sintético ou teórico com um espectro observado, onde a abundância de um dado elemento pode ser obtida através do melhor ajuste entre estes dois espectros. O método de síntese espectral é crucial caso os espectros observados a serem modelados tenham muitas linhas espectrais misturadas ("blends"), onde o método de larguras equivalente já não pode ser utilizado dado que este necessita medir larguras equivalentes de linhas completamente isoladas ou relativamente isoladas.

Os espectros sintéticos são gerados utilizando um código de transferência radiativa e necessitam (assim como no caso de análise via medidas de larguras equivalentes) de modelos de atmosferas. Conforme discutido anteriormente, o cálculo de espectros sin-

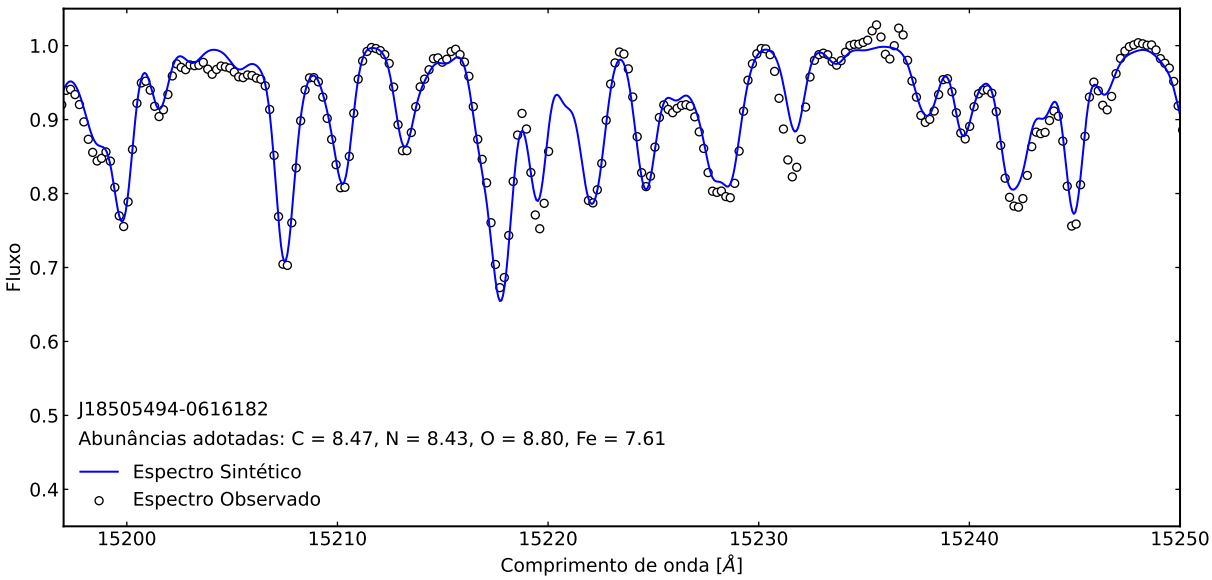


**Figura A.4** – Comparação entre o espectro observado (círculos abertos) e o espectro sintético (linha azul) de uma estrela gigante vermelha pertencente ao aglomerado aberto NGC 6705.

téticos para modelar linhas fotosféricas, deve levar em consideração os mecanismos de alargamento das linhas devido, por exemplo, ao efeito Doppler e ao amortecimento Van der Waals, e Stark. Além disso, é necessário considerar o alargamento instrumental, rotacional e da macroturbulência.

Da literatura, destacamos dois códigos de transferência radiativa. Um deles é o código MOOG, desenvolvido por SNEDEN (1973), amplamente utilizado na determinação da composição química estelar, que assume a validade do ETL e adota camadas plano-paralelas. Outro código relevante também muito utilizado na literatura é o código Turbospectrum (ALVAREZ e PLEZ, 1998; PLEZ, 2012) que produz espectros sintéticos em equilíbrio termodinâmico local. Uma das vantagens deste código é que ele pode ser usado tanto em geometrias plano-paralelas quanto esféricas. Geometrias esféricas são importantes para estrelas que têm atmosferas extensas como as gigantes vermelhas.

Nesta tese utilizamos o método de medida de larguras equivalentes das linhas isoladas de Fe I e Fe II para determinar os parâmetros estelares de estrelas que hospedam planetas que são apresentados nos Capítulos 2 e 3, usando o código de transferência radiativa MOOG. Enquanto que para determinar as abundâncias químicas das estrelas pertencentes ao aglomerado aberto NGC 6705, apresentado no Capítulo 4, fazemos uso do método de síntese espectral e usamos o código de transferência radiativa Turbospectrum.

Na Figura A.4 apresentamos como exemplo uma pequena janela espectral entre $\sim$ 1.52 e 1.525 micron comparando o espectro observado obtido pelo levantamento SDSS APOGEE (bolinhas) e o espectro sintético (linha azul) calculado para a estrela J18505494-0616182 pertencente ao aglomerado aberto NGC 6705. O espectro sintético apresentado na figura foi calculado com o código Turbospectrum, utilizando um modelo de atmosferas

esférico MARCS com $T_{eff}$ = 4704 K; $\log g = 2,279$ dex e [m/H]=0,15 dex. A região espectral apresentada contém linhas de Mg I $\lambda$15.231,8, Fe I $\lambda$15.207,5, Mn I $\lambda$15.217,0 (cujas abundâncias foram analisadas no Capítulo 4).

# Apêndice B

# Tabelas Eletrônicas

Neste apêndice, reproduzimos as tabelas 1, 3 e 6 do Artigo I e as tabelas 1, 2, 3 e 4 do Artigo II, as quais serão publicadas apenas no formato eletrônico. O formato é o mesmo das mostrado nos artigos.

**Tabela B.1** – Main sample data (Table 1 of Paper I)

| ID | Host Name | UT Date | RA | DEC | V (mag) | Exposure (s) | S/N |
|---|---|---|---|---|---|---|---|
| EPIC201166680 | K2-243 | 2019 May 12 | 12:04:29 | -04:53:57 | 10.97 | 1 x 1800 | 170 |
| EPIC201211526 | K2-244 | 2019 May 12 | 12:13:53 | -03:49:55 | 11.78 | 3 x 1800 | 150 |
| EPIC201295312 | K2-44 | 2016 Mar 17 | 11:36:03 | -02:31:15 | 12.27 | 2 x 1800 | 100 |
| EPIC201384232 | K2-6 | 2016 Jan 23 | 11:52:46 | -01:11:55 | 12.66 | 2 x 1800 | 150 |
| EPIC201390048 | K2-162 | 2018 May 28 | 12:24:09 | -01:06:41 | 12.28 | 2 x 1800 | 115 |
| EPIC201393098 | K2-7 | 2016 Feb 22 | 11:08:23 | -01:03:57 | 13.45 | 3 x 1200 | 150 |
| EPIC201403446 | K2-46 | 2017 Dec 06 | 11:37:04 | -00:54:26 | 12.14 | 2 x 1800 | 160 |
| EPIC201445392 | K2-8 | 2016 Mar 17 | 11:19:10 | -00:17:04 | 14.80 | 3 x 1800 | 120 |
| EPIC201460826 | K2-164 | 2016 Mar 18 | 11:27:44 | -00:03:46 | 11.35 | 2 x 600 | 170 |
| EPIC201505350 | K2-19 | 2016 Feb 22 | 11:39:50 | 00:36:13 | 13.02 | 3 x 1200 | 120 |
| EPIC201528215 | EPIC201528215 | 2017 Feb 10 | 11:31:13 | 00:57:31 | 13.98 | 3 x 1800 | 200 |
| EPIC201546283 | K2-27 | 2016 Mar 16 | 11:26:04 | 01:13:51 | 12.69 | 2 x 1500 | 140 |
| EPIC201569483 | EPIC201569483 | 2017 Feb 10 | 11:08:41 | 01:34:39 | 12.33 | 2 x 1800 | 250 |
| EPIC201577035 | K2-10 | 2016 Jan 23 | 11:28:29 | 01:41:26 | 12.43 | 2 x 1800 | 150 |
| EPIC201596316 | K2-11 | 2017 Jan 06 | 11:16:10 | 01:59:13 | 13.41 | 2 x 1800 | 100 |
| EPIC201613023 | K2-12 | 2016 Jan 22 | 11:32:46 | 02:14:42 | 12.38 | 2 x 1800 | 150 |
| EPIC201629650 | K2-13 | 2016 Jan 21 | 11:20:37 | 02:30:10 | 12.88 | 2 x 1800 | 70 |
| EPIC201713348 | K2-36 | 2017 Feb 08 | 11:17:48 | 03:51:59 | 11.73 | 2 x 1800 | 150 |
| EPIC201736247 | K2-15 | 2016 Mar 16 | 11:52:26.59 | 04:15:17.10 | 14.76 | 2 x 1800 | 50 |
| EPIC202071289 | EPIC202071289 | 2016 Jan 22 | 06:20:44 | 24:54:15 | 11.55 | 2 x 1800 | 250 |
| EPIC202086968 | EPIC202086968 | 2016 Feb 22 | 06:28:01 | 16:23:20 | 12.38 | 2 x 1800 | 150 |
| EPIC202089657 | EPIC202089657 | 2016 Jan 25 | 06:05:49 | 23:29:04 | 11.71 | 2 x 1200 | 250 |
| EPIC202091388 | EPIC202091388 | 2016 Mar 17 | 06:05:27 | 21:15:22 | 13.49 | 2 x 1500 | 100 |
| EPIC202126847 | EPIC202126847 | 2016 Jan 25 | 06:48:48 | 17:09:43 | 12.37 | 2 x 1500 | 200 |
| EPIC206011496 | K2-265 | 2018 Oct 17 | 22:48:08 | -14:29:41 | 11.19 | 3 x 1800 | 90 |
| EPIC206026904 | K2-58 | 2017 Nov 04 | 22:15:17 | -14:02:59 | 12.42 | 3 x 1800 | 110 |
| EPIC206101302 | K2-63 | 2017 Nov 05 | 22:13:42 | -12:03:59 | 12.98 | 3 x 1800 | 160 |
| EPIC206153219 | K2-66 | 2018 Oct 18 | 22:06:06 | -10:42:42 | 11.71 | 3 x 1800 | 185 |
| EPIC206159027 | K2-68 | 2017 Nov 05 | 22:16:05 | -10:34:02 | 12.99 | 3 x 1800 | 120 |
| EPIC206181769 | K2-70 | 2017 Dec 06 | 22:33:54.19 | -10:05:05.80 | 13.07 |  | 80 |
| EPIC210363145 | K2-77 | 2017 Feb 08 | 03:40:55 | 12:34:21 | 12.22 | 2 x 1800 | 180 |
| EPIC210400751 | K2-78 | 2017 Jan 06 | 03:48:54 | 13:29:01 | 12.18 | 2 x 1800 | 200 |
| EPIC210402237 | K2-79 | 2016 Jan 24 | 03:41:01 | 13:31:01 | 12.15 | 2 x 900 | 190 |
| EPIC210403955 | K2-80 | 2016 Sep 16 | 03:56:09 | 13:33:33 | 12.69 | 2 x 1800 | 140 |

**Table B.1 continued from previous page**

| ID | Host Name | UT Date | RA | DEC | V (mag) | Exposure (s) | S/N |
|---|---|---|---|---|---|---|---|
| EPIC210423938 | EPIC210423938 | 2016 Jan 24 | 04:01:29 | 14:00:01 | 12.98 | 2 x 1500 | 150 |
| EPIC210512842 | K2-173 | 2016 Jan 21 | 04:01:30 | 15:37:30 | 12.52 | 3 x 1200 | 100 |
| EPIC210558622 | K2-174 | 2016 Jan 21 | 04:03:10 | 16:20:51 | 12.46 | 2 x 1800 | 250 |
| EPIC210577548 | K2-84 | 2016 Jan 25 | 03:43:14 | 16:38:04 | 13.39 | 2 x 1800 | 100 |
| EPIC210643811 | K2-175 | 2016 Jan 21 | 03:30:01 | 17:35:03 | 10.84 | 2 x 900 | 250 |
| EPIC210667381 | K2-176 | 2016 Jan 24 | 03:53:05 | 17:54:25 | 12.91 | 2 x 1200 | 250 |
| EPIC210707130 | K2-85 | 2017 Jan 06 | 03:57:51 | 18:27:55 | 12.42 | 2 x 1800 | 70 |
| EPIC210718708 | K2-86 | 2016 Jan 25 | 03:26:13 | 18:38:08 | 13.04 | 2 x 1500 | 150 |
| EPIC210754505 | EPIC210754505 | 2017 Feb 10 | 04:18:35 | 19:10:45 | 13.57 | 2 x 1800 | 200 |
| EPIC210775710 | EPIC210775710 | 2015 Dec 26 | 03:37:05.80 | 19:29:59 | 11.76 | 4 x 1200 | 80 |
| EPIC210857328 | K2-177 | 2019 Mar 16 | 03:40:55 | 20:44:10 | 12.68 | 2 x 1800 | 130 |
| EPIC210957318 | K2-30 | 2017 Jan 07 | 03:29:22 | 22:17:58 | 13.55 | 3 x 1800 | 150 |
| EPIC210961508 | EPIC210961508 | 2017 Feb 08 | 03:59:41 | 22:21:58 | 13.15 | 2 x 1800 | 250 |
| EPIC211089792 | K2-29 | 2016 Sep 16 | 04:10:41 | 24:24:07 | 12.53 | 2 x 1800 | 90 |
| EPIC211152484 | K2-92 | 2017 Jan 06 | 04:00:17 | 25:28:48 | 12.48 | 3 x 1800 | 100 |
| EPIC211351816 | K2-97 | 2017 Dec 29 | 08:31:03 | 10:50:51 | 12.49 | 3 x 1800 | 150 |
| EPIC211355342 | K2-181 | 2018 Apr 02 | 08:30:13 | 10:54:37 | 12.67 | 2 x 1800 | 100 |
| EPIC211359660 | K2-182 | 2018 Apr 02 | 08:40:43 | 10:58:59 | 11.83 | 2 x 1800 | 160 |
| EPIC211391664 | K2-98 | 2017 Dec 29 | 08:25:57 | 11:30:40 | 12.22 | 2 x 1800 | 235 |
| EPIC211442297 | K2-115 | 2017 Dec 30 | 08:26:13 | 12:16:55 | 13.44 | 3 x 1800 | 155 |
| EPIC211525389 | K2-105 | 2017 Dec 29 | 08:21:41 | 13:29:51 | 11.75 | 2 x 1800 | 150 |
| EPIC211562654 | K2-183 | 2018 Apr 02 | 08:20:02 | 14:01:10 | 12.87 | 2 x 1800 | 130 |
| EPIC211594205 | K2-184 | 2018 Apr 01 | 08:36:34 | 14:27:43 | 10.35 | 2 x 1800 | 150 |
| EPIC211611158 | K2-185 | 2018 Apr 01 | 08:41:02 | 14:41:25 | 12.24 | 2 x 1800 | 230 |
| EPIC211736671 | K2-108 | 2017 Dec 30 | 08:13:32 | 16:25:11 | 12.34 | 3 x 1200 | 145 |
| EPIC211818569 | K2-121 | 2017 Dec 30 | 08:27:45 | 17:34:46 | 13.23 | 2 x 1800 | 100 |
| EPIC211906650 | K2-186 | 2018 Apr 01 | 09:01:20 | 18:49:32 | 12.41 | 2 x 1800 | 170 |
| EPIC211913977 | K2-101 | 2017 Nov 05 | 08:41:23 | 18:56:02 | 12.89 | 6 x 1800 | 100 |
| EPIC211970147 | K2-102 | 2018 May 27 | 08:40:13.45 | 19:46:43.71 | 13.08 | 2 x 1800 | 65 |
| EPIC211990866 | K2-100 | 2017 Dec 29 | 08:38:24 | 20:06:22 | 10.65 | 3 x 1800 | 250 |
| EPIC212110888 | K2-34 | 2017 Jan 06 | 08:30:19 | 22:14:09 | 11.45 | 2 x 1800 | 250 |
| EPIC212164470 | K2-188 | 2018 Apr 02 | 08:39:15 | 23:21:27 | 12.66 | 2 x 1800 | 120 |
| EPIC212686205 | K2-128 | 2019 May 13 | 13:37:45 | -08:35:49 | 12.58 | 2 x 2400 | 100 |
| EPIC212691422 | K2-196 | 2019 Mar 18 | 13:21:50 | -08:28:18 | 12.24 | 3 x 1800 | 100 |
| EPIC212768333 | K2-198 | 2019 Mar 17 | 13:15:23 | -06:27:54 | 10.97 | 2 x 1800 | 150 |
| EPIC212779596 | K2-199 | 2019 Mar 17 | 13:55:36 | -06:08:10 | 12.36 | 3 x 1800 | 110 |
| EPIC212782836 | K2-279 | 2019 Mar 16 | 13:39:07 | -06:02:29 | 11.49 | 3 x 1800 | 110 |
| EPIC220241529 | K2-209 | 2018 Oct 17 | 00:58:46 | 01:23:02 | 11.06 | 2 x 1800 | 180 |
| EPIC220250254 | K2-210 | 2018 Oct 17 | 01:10:34 | 01:34:42 | 11.54 | 2 x 1800 | 175 |
| EPIC220397060 | EPIC220397060 | 2017 Dec 30 | 00:34:47 | 04:39:28 | 13.05 | 1 x 1800 | 128 |
| EPIC220592745 | K2-219 | 2018 Oct 17 | 00:51:23 | 08:52:04 | 12.09 | 3 x 1800 | 95 |
| EPIC220621788 | K2-220 | 2017 Dec 30 | 00:51:05 | 09:31:01 | 11.87 | 2 x 1800 | 155 |
| EPIC220674823 | K2-106 | 2017 Dec 29 | 00:52:19 | 10:47:41 | 12.10 | 1 x 1800 | 130 |
| EPIC228721452 | K2-223 | 2018 Apr 03 | 12:21:13 | -10:16:55 | 11.44 | 2 x 1200 | 120 |
| EPIC228754001 | K2-132 | 2019 May 20 | 12:08:40 | -08:44:50 | 12.07 | 2 x 2400 | 160 |
| EPIC228760097 | K2-227 | 2018 Apr 03 | 12:43:48 | -08:28:42 | 12.02 | 2 x 1800 | 210 |
| EPIC228801451 | K2-229 | 2018 May 27 | 12:27:30 | -06:43:19 | 10.99 | 2 x 1800 | 140 |
| KOI-41 | Kepler-100 | 2016 Mar 15 | 19:25:33 | 41:59:25 | 11.06 | 2 x 1800 | 120 |
| KOI-1989 | Kepler-1040 | 2018 May 27 | 18:52:27 | 48:07:53 | 13.61 | 2 x 1800 | 95 |
| KOI-116 | Kepler-106 | 2016 Sep 17 | 20:03:27 | 44:20:15 | 12.92 | 2 x 1800 | 170 |
| KOI-2079 | Kepler-1087 | 2016 Sep 16 | 19:39:55 | 46:00:20 | 12.97 | 2 x 1800 | 160 |
| KOI-2087 | Kepler-1088 | 2016 Sep 18 | 18:46:15 | 42:27:02 | 11.47 | 2 x 1800 | 160 |
| KOI-2484 | Kepler-1253 | 2016 Sep 17 | 18:55:32 | 47:38:14 | 12.59 | 2 x 1800 | 200 |
| KOI-274 | Kepler-128 | 2018 Sep 17 | 18:49:58 | 43:58:49 | 11.69 | 3 x 1800 | 185 |
| KOI-282 | Kepler-130 | 2016 Mar 17 | 19:13:48 | 40:14:43 | 11.57 | 2 x 1500 | 100 |
| KOI-284 | Kepler-132 | 2016 Sep 17 | 18:52:57 | 41:20:35 | 11.92 | 2 x 1800 | 130 |

**Table B.1 continued from previous page**

| ID | Host Name | UT Date | RA | DEC | V (mag) | Exposure (s) | S/N |
|---|---|---|---|---|---|---|---|
| KOI-2754 | Kepler-1339 | 2016 Sep 17 | 18:54:59 | 48:22:24 | 12.34 | 2 x 1800 | 160 |
| KOI-316 | Kepler-139 | 2018 Sep 17 | 18:49:34 | 43:53:22 | 12.78 | 3 x 1800 | 170 |
| KOI-3245 | Kepler-1445 | 2016 Sep 18 | 18:41:00 | 43:54:54 | 12.41 | 2 x 1800 | 80 |
| KOI-3892 | Kepler-1525 | 2016 Sep 18 | 19:22:14 | 49:56:35 | 12.80 | 2 x 1800 | 160 |
| KOI-4032 | Kepler-1542 | 2016 Sep 16 | 19:02:55 | 42:39:16 | 12.73 | 2 x 1800 | 140 |
| KOI-5447 | Kepler-1629 | 2016 Sep 17 | 18:40:50 | 43:46:28 | 12.79 | 2 x 1800 | 190 |
| KOI-87 | Kepler-22 | 2016 Mar 14 | 19:16:52 | 47:53:04 | 11.75 | 2 x 1800 | 100 |
| KOI-719 | Kepler-220 | 2018 May 27 | 19:26:01 | 46:53:45 | 13.05 | 3 x 1800 | 120 |
| KOI-986 | Kepler-260 | 2019 May 13 | 19:27:42 | 38:00:50 | 14.25 | 2 x 1800 | 70 |
| KOI-2173 | Kepler-367 | 2018 May 28 | 19:49:10 | 49:58:54 | 13.19 | 2 x 1800 | 100 |
| KOI-2672 | Kepler-396 | 2019 May 20 | 19:44:32 | 48:58:39 | 12.26 | 2400 + 1800 | 155 |
| KOI-321 | Kepler-406 | 2016 Sep 16 | 19:27:24 | 44:58:06 | 12.60 | 2 x 1800 | 180 |
| KOI-1925 | Kepler-409 | 2019 May 20 | 19:34:43 | 46:51:10 | 9.64 | 2 x 1200 | 215 |
| KOI-3158 | Kepler-444 | 2019 May 20 | 19:19:01 | 41:38:05 | 8.87 | 2 x 1200 | 255 |
| KOI-365 | Kepler-538 | 2018 May 28 | 19:49:57 | 49:37:24 | 11.27 | 1 x 1800 | 140 |
| KOI-374 | Kepler-540 | 2018 Sep 17 | 19:22:30 | 44:52:26 | 12.29 | 3 x 1800 | 145 |
| KOI-701 | Kepler-62 | 2018 Apr 02 | 18:52:51 | 45:21:00 | 13.97 | 2 x 1800 | 125 |
| KOI-1119 | KOI-1119 | 2015 Sep 11 | 19:37:57 | 38:11:09 | 11.19 | 2 x 1200 | 200 |
| KOI-1614 | KOI-1614 | 2015 Sep 11 | 18:45:05 | 47:46:13 | 10.66 | 3 x 1200 | 120 |
| KOI-293 | KOI-293 | 2019 May 20 | 19:45:26 | 48:51:49 | 11.85 | 2400 + 1800 | 170 |
| KOI-319 | KOI-319 | 2018 Sep 17 | 19:20:28 | 44:52:23 | 12.68 | 3 x 1800 | 180 |
| KOI-3889 | KOI-3889 | 2018 Sep 16 | 19:30:29 | 48:04:53 | 13.74 | 2 x 1800 | 130 |
| KOI-5782 | KOI-5782 | 2018 May 27 | 19:25:27 | 47:19:43 | 11.27 | 3 x 1800 | 160 |
| KOI-6 | KOI-6 | 2019 May 12 | 19:38:24 | 38:22:00 | 12.34 | 3 x 1800 | 190 |
| HIP 81512 | HIP81512 | 2016 Mar 18 | 16:38:59 | 45:35:22 | 9.30 | 3 x 300 | 250 |

**Tabela B.2** – Stellar Parameters, Radii and Masse (Table 3 of Paper I)

| ID | $T_{\rm eff}$ (K) | $\delta T_{\rm eff}$ (K) | $\log g$ (dex) | $\delta \log g$ (dex) | A(Fe) (dex) | $\delta$A(Fe) (dex) | $\xi$ (km s$^{-1}$) | $\delta\xi$ (km s$^{-1}$) | $R_{star}$ ($R_\odot$) | $\delta R_{star}$ ($R_\odot$) | $M_{star}$ ($M_\odot$) | $\delta M_{star}$ ($M_\odot$) |
|---|---|---|---|---|---|---|---|---|---|---|---|---|
| EPIC201166680 | 6051 | 289 | 4.01 | 0.49 | 7.39 | 0.11 | 1.45 | 0.37 | 1.45 | 0.16 | 1.09 | 0.06 |
| EPIC201211526 | 5717 | 176 | 4.13 | 0.39 | 7.21 | 0.08 | 1.07 | 0.17 | 0.92 | 0.03 | 0.89 | 0.04 |
| EPIC201295312 | 6130 | 122 | 4.50 | 0.26 | 7.75 | 0.08 | 1.68 | 0.19 | 1.30 | 0.07 | 1.23 | 0.04 |
| EPIC201384232 | 5673 | 138 | 4.31 | 0.38 | 7.43 | 0.09 | 0.63 | 0.24 | 0.94 | 0.04 | 0.93 | 0.04 |
| EPIC201390048 | 4795 | 228 | 4.55 | 0.34 | 7.26 | 0.08 | 1.09 | 0.35 | 0.66 | 0.02 | 0.71 | 0.02 |
| EPIC201393098 | 5707 | 224 | 4.01 | 0.47 | 7.25 | 0.14 | 1.09 | 0.26 | 1.55 | 0.17 | 0.98 | 0.04 |
| EPIC201403446 | 5899 | 247 | 3.69 | 0.58 | 7.05 | 0.12 | 1.45 | 0.36 | 1.54 | 0.16 | 0.97 | 0.05 |
| EPIC201445392 | 5125 | 235 | 4.51 | 0.41 | 7.32 | 0.14 | 1.73 | 0.49 | 0.69 | 0.04 | 0.74 | 0.04 |
| EPIC201460826 | 5987 | 205 | 3.91 | 0.55 | 7.25 | 0.09 | 1.29 | 0.16 | 1.77 | 0.15 | 1.12 | 0.04 |
| EPIC201505350 | 5440 | 93 | 4.40 | 0.26 | 7.60 | 0.08 | 1.18 | 0.24 | 0.86 | 0.03 | 0.89 | 0.03 |
| EPIC201528215 | 5433 | 172 | 4.53 | 0.35 | 7.07 | 0.09 | 1.29 | 0.24 | 0.69 | 0.03 | 0.74 | 0.03 |
| EPIC201546283 | 5368 | 130 | 4.54 | 0.19 | 7.74 | 0.06 | 0.84 | 0.24 | 0.88 | 0.04 | 0.91 | 0.04 |
| EPIC201569483 | 5268 | 274 | 4.52 | 0.39 | 7.80 | 0.11 | 1.14 | 0.35 | 0.94 | 0.03 | 0.92 | 0.04 |
| EPIC201577035 | 5712 | 135 | 4.70 | 0.27 | 7.52 | 0.10 | 1.06 | 0.24 | 0.91 | 0.03 | 0.94 | 0.04 |
| EPIC201596316 | 5288 | 156 | 4.40 | 0.38 | 7.51 | 0.10 | 1.28 | 0.35 | 0.82 | 0.03 | 0.85 | 0.03 |
| EPIC201613023 | 5740 | 132 | 4.24 | 0.33 | 7.58 | 0.09 | 0.98 | 0.17 | 1.03 | 0.06 | 0.99 | 0.05 |
| EPIC201629650 | 5595 | 93 | 4.15 | 0.18 | 7.43 | 0.06 | 1.03 | 0.13 | 0.93 | 0.03 | 0.90 | 0.04 |
| EPIC201713348 | 4980 | 158 | 4.45** | 0.36 | 7.57 | 0.09 | 0.96 | 0.24 | 0.72 | 0.02 | 0.77 | 0.02 |
| EPIC201736247 | 5195 | 158 | 4.60** | 0.36 | 7.15 | 0.13 | 0.96 | 0.24 | 0.71 | 0.03 | 0.75 | 0.03 |
| EPIC202071289 | 5900 | 189 | 4.40 | 0.59 | 7.40 | 0.13 | 1.56 | 0.24 | 1.46a | 0.77 | 1.08a | 0.20 |
| EPIC202086968 | 5894 | 158 | 4.00 | 0.37 | 7.63 | 0.09 | 1.52 | 0.15 | 1.53 | 0.10 | 1.14 | 0.05 |
| EPIC202089657 | 6130 | 200 | 4.24 | 0.43 | 7.32 | 0.11 | 1.20 | 0.23 | 1.42 | 0.14 | 1.11 | 0.06 |
| EPIC202091388 | 5605 | 185 | 4.55 | 0.26 | 7.65 | 0.10 | 0.81 | 0.32 | 0.94 | 0.04 | 0.94 | 0.04 |
| EPIC202126847 | 5941 | 112 | 4.43 | 0.33 | 7.47 | 0.09 | 1.35 | 0.15 | 1.03 | 0.04 | 1.02 | 0.04 |

**Table B.2 continued from previous page**

| ID | $T_{\rm eff}$ (K) | $\delta T_{\rm eff}$ (K) | $\log g$ (dex) | $\delta \log g$ (dex) | A(Fe) (dex) | $\delta$A(Fe) (dex) | $\xi$ ($\rm km\,s^{-1}$) | $\delta\xi$ ($\rm km\,s^{-1}$) | $R_{star}$ ($R_\odot$) | $\delta R_{star}$ ($R_\odot$) | $M_{star}$ ($M_\odot$) | $\delta M_{star}$ ($M_\odot$) |
|---|---|---|---|---|---|---|---|---|---|---|---|---|
| EPIC206011496 | 5484 | 144 | 4.44 | 0.50 | 7.58 | 0.15 | 1.22 | 0.33 | 0.89 | 0.03 | 0.90 | 0.04 |
| EPIC206026904 | 5151 | 172 | 4.61 | 0.28 | 7.71 | 0.05 | 1.49 | 0.31 | 0.80 | 0.02 | 0.84 | 0.03 |
| EPIC206101302 | 5815 | 192 | 4.11 | 0.34 | 7.46 | 0.10 | 0.93 | 0.25 | 1.19 | 0.10 | 1.00 | 0.05 |
| EPIC206153219 | 5987 | 211 | 4.17 | 0.49 | 7.35 | 0.05 | 1.79 | 0.26 | 1.97 | 0.18 | 1.22 | 0.04 |
| EPIC206159027 | 4802 | 158 | 4.55** | 0.36 | 7.31 | 0.12 | 0.96 | 0.24 | 0.66 | 0.02 | 0.71 | 0.02 |
| EPIC206181769 | 5294 | 137 | 4.46 | 0.47 | 7.62 | 0.12 | 1.30 | 0.34 | 0.77 | 0.02 | 0.82 | 0.03 |
| EPIC210363145 | 4803 | 158 | 4.50** | 0.36 | 7.72 | 0.08 | 1.05 | 0.24 | 0.75 | 0.02 | 0.80 | 0.02 |
| EPIC210400751 | 5230 | 126 | 4.50 | 0.28 | 7.20 | 0.08 | 0.50 | 0.49 | 0.71 | 0.02 | 0.75 | 0.03 |
| EPIC210402237 | 5849 | 140 | 4.21 | 0.30 | 7.57 | 0.09 | 0.91 | 0.19 | 0.95 | 0.03 | 0.97 | 0.04 |
| EPIC210403955 | 5273 | 159 | 4.51 | 0.27 | 7.49 | 0.08 | 1.11 | 0.22 | 0.76 | 0.02 | 0.80 | 0.03 |
| EPIC210423938 | 4705 | 158 | 4.55** | 0.36 | 7.31 | 0.14 | 1.20 | 0.24 | 0.63 | 0.01 | 0.69 | 0.02 |
| EPIC210512842 | 6025 | 158 | 4.65** | 0.36 | 7.17 | 0.10 | 1.31 | 0.24 | 1.14a | 0.29 | 0.99a | 0.08 |
| EPIC210558622 | 4296 | 158 | 4.60** | 0.36 | 7.50 | 0.07 | 0.70 | 0.24 | 0.62 | 0.01 | 0.67 | 0.02 |
| EPIC210577548 | 5309 | 123 | 4.25 | 0.29 | 7.65 | 0.08 | 1.31 | 0.19 | 0.79 | 0.03 | 0.84 | 0.03 |
| EPIC210643811 | 5923 | 113 | 3.91 | 0.34 | 7.61 | 0.08 | 1.13 | 0.11 | 1.43 | 0.06 | 1.13 | 0.05 |
| EPIC210667381 | 5375 | 136 | 4.33 | 0.37 | 7.62 | 0.10 | 1.13 | 0.25 | 0.81 | 0.02 | 0.85 | 0.03 |
| EPIC210707130 | 4973 | 191 | 4.57 | 0.33 | 7.31 | 0.07 | 1.67 | 0.26 | 1.04 | 0.04 | 0.88 | 0.03 |
| EPIC210718708 | 5125 | 158 | 4.35** | 0.36 | 7.02 | 0.08 | 0.87 | 0.24 | 0.72 | 0.03 | 0.75 | 0.03 |
| EPIC210754505 | 5977 | 219 | 4.09 | 0.43 | 7.34 | 0.12 | 1.43 | 0.25 | 1.58a | 0.79 | 1.11a | 0.21 |
| EPIC210775710 | 5950 | 158 | 4.21* | 0.36 | 7.76 | 0.09 | 0.92 | 0.24 | 1.05 | 0.05 | 1.03 | 0.04 |
| EPIC210857328 | 5912 | 259 | 4.02 | 0.43 | 7.76 | 0.11 | 1.12 | 0.26 | 1.85a | 0.94 | 1.26a | 0.26 |
| EPIC210957318 | 5579 | 127 | 4.47 | 0.43 | 7.63 | 0.09 | 0.81 | 0.21 | 0.81 | 0.02 | 0.87 | 0.03 |
| EPIC210961508 | 5130 | 158 | 3.64* | 0.36 | 7.61 | 0.15 | 1.22 | 0.24 | 2.72a | 1.33 | 1.24a | 0.32 |
| EPIC211089792 | 5360 | 165 | 4.54 | 0.28 | 7.61 | 0.09 | 1.30 | 0.28 | 0.76 | 0.02 | 0.81 | 0.03 |
| EPIC211152484 | 6208 | 247 | 4.06 | 0.44 | 7.24 | 0.11 | 1.38 | 0.25 | 1.24 | 0.10 | 1.05 | 0.06 |
| EPIC211351816 | 4892 | 176 | 3.04 | 0.33 | 7.84 | 0.08 | 1.00 | 0.19 | 4.10 | 0.36 | 1.22 | 0.17 |
| EPIC211355342 | 5528 | 195 | 4.36 | 0.47 | 7.68 | 0.12 | 0.88 | 0.45 | 1.07 | 0.07 | 0.97 | 0.05 |
| EPIC211359660 | 5169 | 233 | 4.53 | 0.39 | 7.56 | 0.13 | 1.23 | 0.35 | 0.82 | 0.03 | 0.84 | 0.03 |
| EPIC211391664 | 6013 | 163 | 3.93 | 0.43 | 7.38 | 0.11 | 1.03 | 0.17 | 1.59 | 0.11 | 1.13 | 0.05 |
| EPIC211442297 | 5567 | 109 | 4.33 | 0.28 | 7.35 | 0.10 | 0.95 | 0.23 | 0.88 | 0.04 | 0.88 | 0.04 |
| EPIC211525389 | 5446 | 116 | 4.52 | 0.18 | 7.82 | 0.06 | 0.90 | 0.18 | 0.97 | 0.03 | 0.97 | 0.04 |
| EPIC211562654 | 5523 | 106 | 4.21 | 0.23 | 7.63 | 0.06 | 1.01 | 0.18 | 0.93 | 0.04 | 0.93 | 0.04 |
| EPIC211594205 | 5289 | 132 | 4.45 | 0.40 | 7.37 | 0.11 | 1.25 | 0.28 | 0.78 | 0.02 | 0.81 | 0.03 |
| EPIC211611158 | 5847 | 241 | 4.51 | 0.39 | 7.46 | 0.10 | 1.05 | 0.24 | 0.96 | 0.04 | 0.94 | 0.04 |
| EPIC211736671 | 5451 | 132 | 4.17 | 0.28 | 7.74 | 0.08 | 0.71 | 0.32 | 1.70 | 0.13 | 1.08 | 0.04 |
| EPIC211818569 | 4651 | 158 | 4.67* | 0.36 | 7.41 | 0.13 | 1.02 | 0.24 | 0.65 | 0.01 | 0.70 | 0.02 |
| EPIC211906650 | 5893 | 145 | 4.61 | 0.28 | 7.48 | 0.08 | 1.67 | 0.19 | 1.03 | 0.05 | 1.01 | 0.05 |
| EPIC211913977 | 5045 | 307 | 4.53 | 0.42 | 7.60 | 0.10 | 1.55 | 0.44 | 0.73 | 0.02 | 0.77 | 0.03 |
| EPIC211970147 | 5084 | 158 | 4.55** | 0.36 | 7.65 | 0.19 | 0.98 | 0.24 | 0.71 | 0.02 | 0.76 | 0.02 |
| EPIC211990866 | 6167 | 103 | 4.39 | 0.28 | 7.72 | 0.08 | 1.75 | 0.15 | 1.12 | 0.03 | 1.15 | 0.03 |
| EPIC212110888 | 6067 | 140 | 4.27 | 0.31 | 7.56 | 0.07 | 1.31 | 0.14 | 1.47 | 0.08 | 1.18 | 0.05 |
| EPIC212164470 | 5967 | 177 | 4.61 | 0.34 | 7.46 | 0.08 | 1.15 | 0.17 | 1.12 | 0.07 | 1.04 | 0.05 |
| EPIC212686205 | 4900 | 158 | 4.65** | 0.36 | 7.27 | 0.10 | 1.68 | 0.24 | 0.61 | 0.01 | 0.67 | 0.02 |
| EPIC212691422 | 6067 | 264 | 3.77 | 0.55 | 7.46 | 0.14 | 1.41 | 0.31 | 1.71 | 0.19 | 1.18 | 0.06 |
| EPIC212768333 | 5175 | 137 | 4.41 | 0.39 | 7.58 | 0.09 | 1.09 | 0.35 | 0.85 | 0.02 | 0.86 | 0.03 |
| EPIC212779596 | 4822 | 158 | 4.70** | 0.36 | 7.39 | 0.18 | 0.66 | 0.24 | 0.63 | 0.02 | 0.69 | 0.02 |
| EPIC212782836 | 5565 | 209 | 4.29 | 0.45 | 7.26 | 0.14 | 0.57 | 0.50 | 0.93 | 0.04 | 0.89 | 0.04 |
| EPIC220241529 | 4904 | 218 | 4.58 | 0.31 | 7.51 | 0.08 | 1.14 | 0.45 | 0.70 | 0.02 | 0.75 | 0.02 |
| EPIC220250254 | 5359 | 78 | 4.45 | 0.26 | 7.62 | 0.07 | 0.89 | 0.16 | 0.96 | 0.03 | 0.91 | 0.04 |
| EPIC220397060 | 5257 | 152 | 3.85 | 0.47 | 7.45 | 0.11 | 0.83 | 0.30 | 2.27 | 0.20 | 1.15 | 0.06 |
| EPIC220592745 | 5677 | 169 | 4.09 | 0.33 | 7.29 | 0.08 | 1.83 | 0.20 | 1.18 | 0.07 | 0.93 | 0.04 |
| EPIC220621788 | 5546 | 130 | 4.28 | 0.31 | 7.54 | 0.10 | 0.82 | 0.28 | 1.00 | 0.05 | 0.93 | 0.04 |
| EPIC220674823 | 5503 | 63 | 4.41 | 0.20 | 7.65 | 0.06 | 0.81 | 0.14 | 0.97 | 0.03 | 0.95 | 0.04 |
| EPIC228721452 | 5845 | 125 | 4.47 | 0.39 | 7.70 | 0.06 | 1.07 | 0.11 | 1.01 | 0.04 | 1.03 | 0.04 |
| EPIC228754001 | 4881 | 221 | 3.71 | 0.54 | 7.59 | 0.11 | 0.75 | 0.29 | 3.43 | 0.28 | 1.15 | 0.15 |
| EPIC228760097 | 5667 | 225 | 4.59 | 0.38 | 7.40 | 0.10 | 0.85 | 0.28 | 0.83 | 0.03 | 0.86 | 0.03 |

**Table B.2 continued from previous page**

| ID | $T_{\rm eff}$ (K) | $\delta T_{\rm eff}$ (K) | $\log g$ (dex) | $\delta \log g$ (dex) | A(Fe) (dex) | $\delta$A(Fe) (dex) | $\xi$ (km s$^{-1}$) | $\delta\xi$ (km s$^{-1}$) | $R_{star}$ ($R_\odot$) | $\delta R_{star}$ ($R_\odot$) | $M_{star}$ ($M_\odot$) | $\delta M_{star}$ ($M_\odot$) |
|---|---|---|---|---|---|---|---|---|---|---|---|---|
| EPIC228801451 | 5285 | 259 | 4.53 | 0.38 | 7.47 | 0.10 | 1.29 | 0.32 | 0.80 | 0.02 | 0.83 | 0.03 |
| Kepler-100 | 5904 | 205 | 4.10 | 0.43 | 7.57 | 0.10 | 1.52 | 0.24 | 1.68 | 0.14 | 1.17 | 0.05 |
| Kepler-1040 | 5709 | 162 | 4.41 | 0.52 | 7.56 | 0.13 | 1.11 | 0.27 | 0.94 | 0.05 | 0.94 | 0.04 |
| Kepler-106 | 5883 | 102 | 4.27 | 0.24 | 7.35 | 0.07 | 1.25 | 0.12 | 1.03 | 0.05 | 0.98 | 0.04 |
| Kepler-1087 | 5380 | 93 | 4.32 | 0.25 | 7.78 | 0.07 | 1.28 | 0.15 | 1.01 | 0.04 | 0.95 | 0.04 |
| Kepler-1088 | 5969 | 56 | 4.21 | 0.13 | 7.53 | 0.05 | 1.01 | 0.10 | 1.24 | 0.03 | 1.08 | 0.04 |
| Kepler-1253 | 5695 | 151 | 4.07 | 0.31 | 7.01 | 0.07 | 1.09 | 0.17 | 1.52 | 0.15 | 0.92 | 0.04 |
| Kepler-128 | 6131 | 150 | 3.95 | 0.42 | 7.41 | 0.08 | 1.53 | 0.13 | 1.48 | 0.08 | 1.15 | 0.05 |
| Kepler-130 | 5979 | 152 | 4.31 | 0.40 | 7.34 | 0.10 | 1.09 | 0.19 | 1.31 | 0.08 | 1.05 | 0.05 |
| Kepler-132 | 5914 | 136 | 4.28 | 0.33 | 7.27 | 0.10 | 1.14 | 0.19 | 1.38 | 0.08 | 1.02 | 0.05 |
| Kepler-1339 | 5913 | 81 | 4.33 | 0.22 | 7.38 | 0.07 | 1.21 | 0.15 | 0.96 | 0.02 | 0.99 | 0.04 |
| Kepler-139 | 5613 | 181 | 4.37 | 0.51 | 7.73 | 0.13 | 1.19 | 0.31 | 1.09 | 0.07 | 1.00 | 0.05 |
| Kepler-1445 | 5947 | 112 | 4.37 | 0.32 | 7.30 | 0.08 | 1.57 | 0.18 | 1.44 | 0.07 | 1.06 | 0.04 |
| Kepler-1525 | 5685 | 146 | 4.17 | 0.31 | 7.77 | 0.07 | 1.19 | 0.25 | 1.07 | 0.06 | 1.02 | 0.05 |
| Kepler-1542 | 5636 | 161 | 4.12 | 0.31 | 7.54 | 0.09 | 1.18 | 0.21 | 1.09 | 0.07 | 0.96 | 0.05 |
| Kepler-1629 | 5556 | 138 | 4.10 | 0.25 | 7.40 | 0.07 | 1.22 | 0.19 | 0.96 | 0.04 | 0.90 | 0.04 |
| Kepler-22 | 5638 | 131 | 4.52 | 0.23 | 7.31 | 0.10 | 0.88 | 0.26 | 0.89 | 0.03 | 0.89 | 0.04 |
| Kepler-220 | 4500 | 158 | 4.35** | 0.36 | 7.43 | 0.22 | 0.78 | 0.24 | 0.67 | 0.02 | 0.72 | 0.02 |
| Kepler-260 | 5408 | 297 | 4.52 | 0.44 | 7.61 | 0.14 | 1.50 | 0.44 | 0.94 | 0.04 | 0.92 | 0.04 |
| Kepler-367 | 4883 | 158 | 4.75** | 0.36 | 7.54 | 0.15 | 0.96 | 0.24 | 0.70 | 0.03 | 0.75 | 0.03 |
| Kepler-396 | 5657 | 154 | 4.61 | 0.27 | 7.60 | 0.09 | 1.31 | 0.22 | 0.88 | 0.03 | 0.91 | 0.03 |
| Kepler-406 | 5723 | 129 | 4.35 | 0.38 | 7.79 | 0.09 | 1.03 | 0.20 | 1.07 | 0.05 | 1.04 | 0.04 |
| Kepler-409 | 5396 | 172 | 4.52 | 0.25 | 7.65 | 0.10 | 0.88 | 0.34 | 0.91 | 0.03 | 0.91 | 0.04 |
| Kepler-444 | 5181 | 149 | 4.53 | 0.28 | 7.00 | 0.08 | 0.71 | 0.31 | 0.72 | 0.02 | 0.75 | 0.03 |
| Kepler-538 | 5548 | 200 | 4.60 | 0.37 | 7.40 | 0.08 | 1.18 | 0.22 | 0.90 | 0.03 | 0.89 | 0.04 |
| Kepler-540 | 5865 | 235 | 4.29 | 0.59 | 7.29 | 0.13 | 1.45 | 0.30 | 1.21 | 0.10 | 0.98 | 0.06 |
| Kepler-62 | 5084 | 117 | 4.48 | 0.36 | 7.10 | 0.11 | 0.94 | 0.34 | 0.66 | 0.02 | 0.71 | 0.02 |
| KOI-1119 | 5295 | 125 | 4.45 | 0.38 | 7.34 | 0.09 | 0.87 | 0.32 | 0.80 | 0.02 | 0.82 | 0.03 |
| KOI-1614 | 5803 | 111 | 3.73 | 0.25 | 7.27 | 0.06 | 1.33 | 0.13 | 1.87 | 0.14 | 1.10 | 0.04 |
| KOI-293 | 6365 | 163 | 4.07 | 0.26 | 7.61 | 0.07 | 1.35 | 0.17 | 2.24 | 0.13 | 1.48 | 0.06 |
| KOI-319 | 6007 | 214 | 4.27 | 0.48 | 7.64 | 0.10 | 1.41 | 0.23 | 1.61 | 0.14 | 1.21 | 0.06 |
| KOI-3889 | 5811 | 222 | 4.23 | 0.48 | 7.69 | 0.12 | 1.25 | 0.25 | 1.19 | 0.10 | 1.05 | 0.06 |
| KOI-5782 | 4935 | 104 | 3.47 | 0.51 | 7.45 | 0.09 | 1.13 | 0.15 | 3.85 | 0.19 | 1.18 | 0.14 |
| KOI-6 | 6297 | 104 | 4.29 | 0.24 | 7.58 | 0.06 | 1.21 | 0.10 | 1.24 | 0.04 | 1.20 | 0.03 |
| HIP 81512 | 5752 | 113 | 4.34 | 0.33 | 7.48 | 0.06 | 1.06 | 0.10 | 1.05 | 0.05 | 0.98 | 0.04 |

**Tabela B.3** – Planetary Radii (Table 6 of Paper I)

| Star ID | Planet Name | $\Delta F$ (ppm) | $R_{pl}$ ($R_\oplus$) | $\delta R_{pl}$ ($R_\oplus$) |
|---|---|---|---|---|
| EPIC 201166680 | K2-243 b | 160.0 | 2.00 | 0.12 |
| EPIC 201166680 | K2-243 c | 190.0 | 2.18 | 0.12 |
| EPIC 201211526 | K2-244 b | 300.0 | 1.74 | 0.12 |
| EPIC 201295312 | K2-44 b | 334.2 | 2.60 | 0.14 |
| EPIC 201384232 | K2-6 b | 724.0 | 2.75 | 0.12 |
| EPIC 201390048 | K2-162 b | 266.9 | 1.17 | 0.12 |
| EPIC 201393098 | K2-7 b | 681.0 | 4.43 | 0.48 |
| EPIC 201403446 | K2-46 b | 333.0 | 3.08 | 0.33 |
| EPIC 201445392 | K2-8 b | 1470.0 | 2.88 | 0.17 |

**Table B.3 continued from previous page**

| Star ID | Planet Name | $\Delta F$ (ppm) | $R_{pl}$ ($R_\oplus$) | $\delta R_{pl}$ ($R_\oplus$) |
|---|---|---|---|---|
| EPIC 201445392 | K2-8 c | 993.0 | 2.37 | 0.14 |
| EPIC 201460826 | K2-164 b | 211.0 | 2.81 | 0.25 |
| EPIC 201505350 | K2-19 b | 6673.0 | 7.64 | 0.26 |
| EPIC 201505350 | K2-19 c | 2325.0 | 4.51 | 0.16 |
| EPIC 201505350 | K2-19 d | 190.0 | 1.29 | 0.12 |
| EPIC 201546283 | K2-27 b | 2804.0 | 5.08 | 0.23 |
| EPIC 201577035 | K2-10 b | 1691.0 | 4.09 | 0.14 |
| EPIC 201596316 | K2-11 b | 916.0 | 2.72 | 0.11 |
| EPIC 201613023 | K2-12 b | 481.0 | 2.46 | 0.14 |
| EPIC 201629650 | K2-13 b | 565.0 | 2.40 | 0.12 |
| EPIC 201713348 | K2-36 b | 345.0 | 1.46 | 0.04 |
| EPIC 201713348 | K2-36 c | 1210.0 | 2.73 | 0.12 |
| EPIC 201736247 | K2-15 b | 1329.0 | 2.81 | 0.13 |
| EPIC 206011496 | K2-265 b | 319.4 | 1.74 | 0.06 |
| EPIC 206026904 | K2-58 b | 1030.0 | 2.80 | 0.09 |
| EPIC 206026904 | K2-58 c | 375.0 | 1.69 | 0.06 |
| EPIC 206026904 | K2-58 d | 425.0 | 1.80 | 0.06 |
| EPIC 206101302 | K2-63 b | 481.0 | 2.86 | 0.24 |
| EPIC 206101302 | K2-63 c | 790.0 | 3.66 | 0.30 |
| EPIC 206153219 | K2-66 b | 288.0 | 3.64 | 0.12 |
| EPIC 206159027 | K2-68 b | 668.0 | 1.85 | 0.06 |
| EPIC 206181769 | K2-70 b | 1076.0 | 2.77 | 0.09 |
| EPIC 210363145 | K2-77 b | 1007.0 | 2.60 | 0.08 |
| EPIC 210402237 | K2-79 b | 1050.0 | 3.35 | 0.11 |
| EPIC 210403955 | K2-80 b | 562.0 | 1.96 | 0.08 |
| EPIC 210403955 | K2-80 c | 301.0 | 1.43 | 0.06 |
| EPIC 210403955 | K2-80 d | 864.0 | 2.43 | 0.08 |
| EPIC 210512842 | K2-173 b | 200.0 | 1.76 | 0.45 |
| EPIC 210558622 | K2-174 b | 1500.0 | 2.61 | 0.05 |
| EPIC 210577548 | K2-84 b | 814.0 | 2.47 | 0.09 |
| EPIC 210577548 | K2-84 c | 704.0 | 2.30 | 0.10 |
| EPIC 210667381 | K2-176 b | 260.0 | 1.42 | 0.06 |
| EPIC 210707130 | K2-85 b | 400.0 | 2.26 | 0.10 |
| EPIC 210718708 | K2-86 b | 865.0 | 2.32 | 0.10 |
| EPIC 210957318 | K2-30 b | 17119.0 | 11.53 | 0.34 |
| EPIC 211089792 | K2-29 b | 19011.0 | 11.44 | 0.35 |
| EPIC 211351816 | K2-97 b | 680.0 | 11.67 | 1.05 |
| EPIC 211355342 | K2-181 b | 828.0 | 3.35 | 0.22 |

**Table B.3 continued from previous page**

| Star ID | Planet Name | $\Delta F$ (ppm) | $R_{pl}$ ($R_\oplus$) | $\delta R_{pl}$ ($R_\oplus$) |
|---|---|---|---|---|
| EPIC 211359660 | K2-182 b | 1178.0 | 3.06 | 0.09 |
| EPIC 211391664 | K2-98 b | 1043.0 | 5.60 | 0.39 |
| EPIC 211442297 | K2-115 b | 17257.0 | 12.55 | 0.55 |
| EPIC 211525389 | K2-105 b | 1338.0 | 3.86 | 0.14 |
| EPIC 211562654 | K2-183 b | 215.2 | 1.48 | 0.07 |
| EPIC 211562654 | K2-183 c | 901.0 | 3.03 | 0.12 |
| EPIC 211562654 | K2-183 d | 947.0 | 3.11 | 0.13 |
| EPIC 211594205 | K2-184 b | 265.0 | 1.38 | 0.04 |
| EPIC 211611158 | K2-185 b | 162.0 | 1.33 | 0.09 |
| EPIC 211611158 | K2-185 c | 757.0 | 2.87 | 0.14 |
| EPIC 211736671 | K2-108 b | 973.0 | 5.78 | 0.45 |
| EPIC 211818569 | K2-121 b | 13112.0 | 8.09 | 0.18 |
| EPIC 211906650 | K2-186 b | 980.0 | 3.50 | 0.18 |
| EPIC 211913977 | K2-101 b | 749.0 | 2.17 | 0.08 |
| EPIC 211970147 | K2-102 b | 200.0 | 1.09 | 0.12 |
| EPIC 211990866 | K2-100 b | 723.6 | 3.30 | 0.08 |
| EPIC 212110888 | K2-34 b | 7493.0 | 13.90 | 0.75 |
| EPIC 212164470 | K2-188 c | 520.0 | 2.78 | 0.18 |
| EPIC 212164470 | K2-188 b | 108.2 | 1.27 | 0.31 |
| EPIC 212686205 | K2-128 b | 332.0 | 1.22 | 0.04 |
| EPIC 212768333 | K2-198 b | 2737.0 | 4.87 | 0.14 |
| EPIC 212768333 | K2-198 d | 1082.0 | 3.06 | 0.09 |
| EPIC 212768333 | K2-198 c | 180.0 | 1.25 | 0.12 |
| EPIC 212779596 | K2-199 b | 726.0 | 1.87 | 0.05 |
| EPIC 212779596 | K2-199 c | 1739.0 | 2.89 | 0.07 |
| EPIC 212782836 | K2-279 b | 207.0 | 1.46 | 0.07 |
| EPIC 220592745 | K2-219 b | 117.3 | 1.39 | 0.09 |
| EPIC 220592745 | K2-219 c | 140.0 | 1.52 | 0.10 |
| EPIC 220592745 | K2-219 d | 419.0 | 2.64 | 0.15 |
| EPIC 220621788 | K2-220 b | 537.0 | 2.53 | 0.13 |
| EPIC 220674823 | EPIC 220674823 b | 284.7 | 1.78 | 0.06 |
| EPIC 220674823 | EPIC 220674823 c | 903.0 | 3.17 | 0.10 |
| EPIC 228721452 | K2-223 b | 100.0 | 1.10 | 0.12 |
| EPIC 228721452 | K2-223 c | 200.0 | 1.55 | 0.12 |
| EPIC 228801451 | K2-229 b | 162.5 | 1.11 | 0.12 |
| EPIC 228801451 | K2-229 c | 532.5 | 2.01 | 0.12 |
| KOI-41 | Kepler-100 b | 68.7 | 1.52 | 0.13 |
| KOI-41 | Kepler-100 d | 99.7 | 1.83 | 0.15 |

**Table B.3 continued from previous page**

| Star ID | Planet Name | $\Delta F$ (ppm) | $R_{pl}$ ($R_\oplus$) | $\delta R_{pl}$ ($R_\oplus$) |
|---|---|---|---|---|
| KOI-41 | Kepler-100 c | 220.5 | 2.73 | 0.22 |
| KOI-1989 | Kepler-1040 b | 584.8 | 2.48 | 0.14 |
| KOI-116 | Kepler-106 c | 511.7 | 2.55 | 0.12 |
| KOI-116 | Kepler-106 e | 615.2 | 2.80 | 0.13 |
| KOI-116 | Kepler-106 d | 104.0 | 1.15 | 0.06 |
| KOI-116 | Kepler-106 b | 55.8 | 0.84 | 0.05 |
| KOI-2079 | Kepler-1087 b | 49.3 | 0.77 | 0.04 |
| KOI-2087 | Kepler-1088 b | 157.3 | 1.69 | 0.06 |
| KOI-2484 | Kepler-1253 b | 143.9 | 1.99 | 0.21 |
| KOI-274 | Kepler-128 b | 77.8 | 1.42 | 0.08 |
| KOI-274 | Kepler-128 c | 62.9 | 1.28 | 0.08 |
| KOI-282 | Kepler-130 b | 77.4 | 1.26 | 0.08 |
| KOI-282 | Kepler-130 d | 136.5 | 1.67 | 0.13 |
| KOI-282 | Kepler-130 c | 639.2 | 3.61 | 0.21 |
| KOI-284 | Kepler-132 d | 177.7 | 2.01 | 0.12 |
| KOI-284 | Kepler-132 c | 121.0 | 1.66 | 0.10 |
| KOI-284 | Kepler-132 b | 101.9 | 1.52 | 0.09 |
| KOI-284 | Kepler-132 e | 145.3 | 1.81 | 0.12 |
| KOI-2754 | Kepler-1339 b | 58.2 | 0.80 | 0.03 |
| KOI-316 | Kepler-139 b | 547.1 | 2.79 | 0.18 |
| KOI-316 | Kepler-139 c | 551.4 | 2.80 | 0.18 |
| KOI-3245 | Kepler-1445 b | 60.9 | 1.23 | 0.08 |
| KOI-3892 | Kepler-1525 b | 83.6 | 1.06 | 0.06 |
| KOI-4032 | Kepler-1542 b | 60.9 | 0.93 | 0.06 |
| KOI-4032 | Kepler-1542 c | 44.3 | 0.79 | 0.06 |
| KOI-4032 | Kepler-1542 d | 69.8 | 0.99 | 0.07 |
| KOI-4032 | Kepler-1542 e | 65.1 | 0.96 | 0.07 |
| KOI-5447 | Kepler-1629 b | 58.6 | 0.80 | 0.05 |
| KOI-87 | Kepler-22 b | 529.1 | 2.24 | 0.08 |
| KOI-719 | Kepler-220 c | 577.6 | 1.75 | 0.04 |
| KOI-719 | Kepler-220 d | 194.3 | 1.01 | 0.03 |
| KOI-719 | Kepler-220 e | 361.8 | 1.38 | 0.04 |
| KOI-719 | Kepler-220 b | 160.3 | 0.92 | 0.03 |
| KOI-986 | Kepler-260 b | 517.6 | 2.32 | 0.10 |
| KOI-986 | Kepler-260 c | 445.9 | 2.16 | 0.11 |
| KOI-2173 | Kepler-367 b | 286.4 | 1.29 | 0.07 |
| KOI-2173 | Kepler-367 c | 224.9 | 1.14 | 0.07 |
| KOI-2672 | Kepler-396 c | 2518.7 | 4.80 | 0.14 |

**Table B.3 continued from previous page**

| Star ID | Planet Name | $\Delta F$ (ppm) | $R_{pl}$ ($R_\oplus$) | $\delta R_{pl}$ ($R_\oplus$) |
|---|---|---|---|---|
| KOI-2672 | Kepler-396 b | 1120.1 | 3.20 | 0.11 |
| KOI-321 | Kepler-406 b | 185.4 | 1.58 | 0.07 |
| KOI-321 | Kepler-406 c | 62.0 | 0.92 | 0.05 |
| KOI-1925 | Kepler-409 b | 123.3 | 1.10 | 0.04 |
| KOI-3158 | Kepler-444 c | 76.5 | 0.69 | 0.02 |
| KOI-3158 | Kepler-444 d | 83.2 | 0.72 | 0.02 |
| KOI-3158 | Kepler-444 e | 77.8 | 0.69 | 0.02 |
| KOI-3158 | Kepler-444 f | 121.4 | 0.87 | 0.03 |
| KOI-3158 | Kepler-444 b | 50.2 | 0.56 | 0.02 |
| KOI-365 | Kepler-538 b | 628.8 | 2.47 | 0.09 |
| KOI-374 | Kepler-540 b | 659.1 | 3.39 | 0.29 |
| KOI-701 | Kepler-62 d | 943.2 | 2.21 | 0.06 |
| KOI-701 | Kepler-62 b | 425.9 | 1.49 | 0.04 |
| KOI-701 | Kepler-62 e | 711.1 | 1.92 | 0.06 |
| KOI-701 | Kepler-62 c | 78.4 | 0.64 | 0.03 |
| KOI-701 | Kepler-62 f | 471.9 | 1.56 | 0.06 |

**Tabela B.4** – Sample K2 Stars (Table 1 of Paper II)

| ID | Host Name | R.A. (deg) | Decl. (deg) | B (mag) | V (mag) | Camp |
|---|---|---|---|---|---|---|
| EPIC211319617 | K2-180 | 126.463933 | 10.246968 | 13.334 | 12.601 | C5 |
| EPIC211331236 | K2-117 | 133.855682 | 10.469131 | 16.137 | 14.655 | C5 |
| EPIC211342524 | | 128.098694 | 10.677239 | 13.052 | 12.422 | C5 |
| EPIC211351816 | K2-97 | 127.762836 | 10.847586 | 13.770 | 12.611 | C5 |
| EPIC211355342 | K2-181 | 127.554034 | 10.910294 | 13.494 | 12.749 | C5 |
| EPIC211359660 | K2-182 | 130.180327 | 10.982941 | 12.868 | 11.997 | C5 |
| EPIC211391664 | K2-98 | 126.488289 | 11.511145 | 12.646 | 12.166 | C5 |
| EPIC211399359 | | 128.067142 | 11.630727 | 15.643 | 14.636 | C5 |
| EPIC211401787 | | 126.896955 | 11.667474 | 10.173 | 9.607 | C5 |
| EPIC211413752 | K2-268 | 133.709545 | 11.848265 | 14.775 | 13.853 | C5 |
| EPIC211418729 | K2-114 | 127.882962 | 11.922265 | 15.626 | 14.556 | C5 |
| EPIC211439059 | | 131.973530 | 12.231904 | 14.049 | 13.292 | C5 |
| EPIC211442297 | K2-115 | 126.553444 | 12.281936 | 14.008 | 13.362 | C5 |
| EPIC211490999 | | 130.798847 | 13.009593 | 14.318 | 13.604 | C5 |
| EPIC211491383 | K2-269 | 130.155165 | 13.014676 | 12.366 | 11.784 | C5 |
| EPIC211525389 | K2-105 | 125.420277 | 13.497530 | 12.683 | 11.752 | C5 |
| EPIC211529065 | K2-270 | 131.266597 | 13.549833 | 14.824 | 13.782 | C5 |
| EPIC211562654 | K2-183 | 125.007160 | 14.019461 | 13.632 | 12.846 | C5 |
| EPIC211578235 | | 135.061436 | 14.237560 | 15.328 | 14.560 | C5 |
| EPIC211594205 | K2-184 | 129.140107 | 14.461936 | 11.227 | 10.345 | C5 |
| EPIC211645912 | | 124.997087 | 15.177895 | 13.196 | 12.619 | C5 |
| EPIC211713099 | K2-271 | 125.223881 | 16.090947 | 14.475 | 13.827 | C5 |
| EPIC211736671 | K2-108 | 123.381875 | 16.419609 | 13.094 | 12.339 | C5 |
| EPIC211743874 | | 129.389699 | 16.522103 | 13.101 | 12.573 | C5 |
| EPIC211770696 | | 127.761182 | 16.900568 | 12.955 | 12.414 | C5 |

**Table B.4 continued from previous page**

| ID | Host Name | R.A. (deg) | Decl. (deg) | B (mag) | V (mag) | Camp |
|---|---|---|---|---|---|---|
| EPIC211770795 | K2-119 | 132.009734 | 16.901853 | 15.974 | 14.883 | C5 |
| EPIC211816003 | K2-272 | 132.621120 | 17.542445 | 14.577 | 13.841 | C5 |
| EPIC211818569 | K2-121 | 126.936720 | 17.579397 | 14.391 | 13.319 | C5 |
| EPIC211825866 | | 124.332765 | 17.683943 | 14.797 | 13.986 | C5 |
| EPIC211886472 | | 137.132531 | 18.528543 | 11.722 | 11.275 | C5 |
| EPIC211916756 | K2-95 | 129.362743 | 18.976685 | 18.304 | 17.236 | C5 |
| EPIC211919004 | K2-273 | 129.777047 | 19.010023 | 14.282 | 13.371 | C5 |
| EPIC211929937 | | 129.178454 | 19.173812 | 15.223 | 14.434 | C5 |
| EPIC211941472 | | 130.448577 | 19.347497 | 12.633 | 11.949 | C5 |
| EPIC211945201 | K2-236 | 136.573975 | 19.402252 | 10.937 | 10.154 | C5 |
| EPIC211978909 | | 130.905798 | 19.915660 | 14.243 | 13.394 | C5 |
| EPIC211990866 | K2-100 | 129.601250 | 20.106063 | 11.233 | 10.651 | C5 |
| EPIC212006318 | | 130.501328 | 20.359306 | 13.734 | 13.043 | C5 |
| EPIC212006344 | K2-122 | 126.476311 | 20.359569 | 14.550 | 13.150 | C5 |
| EPIC212008766 | K2-274 | 129.282438 | 20.399373 | 13.961 | 13.086 | C5 |
| EPIC212012119 | K2-275 | 132.169895 | 20.455076 | 13.018 | 12.063 | C5 |
| EPIC212069861 | K2-123 | 134.444189 | 21.453533 | 16.292 | 14.781 | C5 |
| EPIC212110888 | K2-34 | 127.578770 | 22.235908 | 12.018 | 11.447 | C5 |
| EPIC212130773 | K2-276 | 125.952752 | 22.634023 | 15.584 | 14.627 | C5 |
| EPIC212138198 | | 126.023559 | 22.783290 | 14.114 | 13.205 | C5 |
| EPIC212157262 | K2-187 | 132.523609 | 23.192601 | 13.871 | 13.081 | C5 |
| EPIC212164470 | K2-188 | 129.813631 | 23.357481 | 13.219 | 12.657 | C5 |
| EPIC212300977 | | 203.758102 | -17.503550 | 12.689 | 11.753 | C6 |
| EPIC212357477 | K2-277 | 202.016632 | -15.937820 | 11.080 | 10.364 | C6 |
| EPIC212393193 | | 210.546997 | -15.069540 | 12.667 | 11.922 | C6 |
| EPIC212394689 | K2-189 | 203.621292 | -15.036359 | 13.015 | 12.399 | C6 |
| EPIC212435047 | | 202.130722 | -14.126292 | 13.163 | 12.500 | C6 |
| EPIC212460519 | K2-126 | 203.546539 | -13.576928 | 14.154 | 12.918 | C6 |
| EPIC212521166 | K2-110 | 207.349533 | -12.284491 | 12.834 | 11.915 | C6 |
| EPIC212585579 | | 204.815765 | -10.906977 | 13.411 | 12.813 | C6 |
| EPIC212586030 | | 205.858154 | -10.896922 | 13.116 | 12.019 | C6 |
| EPIC212587672 | K2-307 | 205.444702 | -10.862432 | 12.691 | 12.487 | C6 |
| EPIC212651120 | | 204.837585 | -9.420724 | 11.011 | 10.525 | C6 |
| EPIC212689874 | K2-195 | 199.831512 | -8.509480 | 13.132 | 12.497 | C6 |
| EPIC212697709 | K2-41 | 201.655197 | -8.317560 | 12.959 | 12.914 | C6 |
| EPIC212703473 | | 201.236542 | -8.171739 | 11.489 | 10.973 | C6 |
| EPIC212735333 | K2-197 | 202.393661 | -7.374002 | 12.884 | 12.157 | C6 |
| EPIC212768333 | K2-198 | 198.843811 | -6.464886 | 11.798 | 10.971 | C6 |
| EPIC212779596 | K2-199 | 208.901703 | -6.136143 | 13.323 | 12.289 | C6 |
| EPIC212782836 | K2-279 | 204.779724 | -6.041594 | 12.327 | 11.491 | C6 |
| EPIC212803289 | K2-99 | 208.773743 | -5.442466 | 11.750 | 11.149 | C6 |
| EPIC213546283 | | 289.376862 | -29.049206 | 12.624 | 12.207 | C7 |
| EPIC213743957 | | 289.687836 | -28.410261 | 12.559 | 11.665 | C7 |
| EPIC213920015 | | 293.078705 | -27.884281 | 10.895 | 10.174 | C7 |
| EPIC214889247 | | 294.212097 | -25.408228 | 10.808 | 10.118 | C7 |
| EPIC215346008 | | 282.451660 | -24.412184 | 14.115 | 12.330 | C7 |
| EPIC215938010 | | 291.401642 | -23.260845 | 12.839 | 12.234 | C7 |
| EPIC215969174 | K2-145 | 291.478699 | -23.202793 | 15.060 | 14.386 | C7 |
| EPIC216334329 | | 288.076660 | -22.534388 | 13.934 | 13.150 | C7 |
| EPIC216468514 | K2-107 | 284.985382 | -22.293402 | 13.639 | 12.917 | C7 |
| EPIC216494238 | K2-280 | 291.595337 | -22.247662 | 13.269 | 12.536 | C7 |
| EPIC216892056 | | 291.673187 | -21.539055 | 14.948 | 13.499 | C7 |
| EPIC217192839 | | 288.026917 | -21.007643 | 14.063 | 13.010 | C7 |
| EPIC217393088 | | 289.439117 | -20.654375 | 16.398 | 15.575 | C7 |
| EPIC217671466 | K2-142 | 290.810120 | -20.166346 | 14.080 | 13.276 | C7 |
| EPIC218131080 | K2-144 | 289.202393 | -19.355907 | 13.284 | 12.767 | C7 |

**Table B.4 continued from previous page**

| ID | Host Name | R.A. (deg) | Decl. (deg) | B (mag) | V (mag) | Camp |
|---|---|---|---|---|---|---|
| EPIC218155470 | | 285.436249 | -19.312134 | 9.807 | 9.653 | C7 |
| EPIC218621322 | | 285.468811 | -18.467922 | 13.332 | 12.532 | C7 |
| EPIC218711655 | | 285.477173 | -18.298365 | 12.137 | 11.493 | C7 |
| EPIC218916923 | K2-139 | 289.066528 | -17.910688 | 12.433 | 11.653 | C7 |
| EPIC219256848 | | 285.678833 | -17.177280 | 14.541 | 13.509 | C7 |
| EPIC219388192 | | 289.391815 | -16.871611 | 13.284 | 12.535 | C7 |
| EPIC219420915 | | 287.510864 | -16.793495 | 13.811 | 13.057 | C7 |
| EPIC220187552 | | 19.975456 | -0.483490 | 15.085 | 13.575 | C8 |
| EPIC220209578 | | 19.462019 | 0.341995 | 15.430 | 14.659 | C8 |
| EPIC220294712 | | 18.161898 | 2.521875 | 12.947 | 12.341 | C8 |
| EPIC220321605 | K2-212 | 18.423407 | 3.096936 | 14.401 | 13.100 | C8 |
| EPIC220376054 | K2-214 | 14.876077 | 4.227798 | 12.146 | 11.805 | C8 |
| EPIC220383386 | K2-96 | 8.739684 | 4.381468 | 9.767 | 8.941 | C8 |
| EPIC220397060 | | 8.697182 | 4.657757 | 13.930 | 13.033 | C8 |
| EPIC220436208 | | 12.236118 | 5.416503 | 14.737 | 14.035 | C8 |
| EPIC220481411 | K2-216 | 11.480249 | 6.346971 | 13.563 | 12.476 | C8 |
| EPIC220487418 | K2-217 | 11.298392 | 6.481562 | 12.813 | 12.187 | C8 |
| EPIC220493203 | | 16.424431 | 6.609616 | 11.070 | 10.260 | C8 |
| EPIC220501947 | K2-295 | 19.609900 | 6.816871 | 15.072 | 13.946 | C8 |
| EPIC220503133 | | 14.581059 | 6.844311 | 7.797 | 6.725 | C8 |
| EPIC220504338 | K2-113 | 19.449286 | 6.868895 | 14.445 | 13.684 | C8 |
| EPIC220542353 | | 14.744520 | 7.719333 | 9.104 | 8.677 | C8 |
| EPIC220554210 | K2-282 | 13.432017 | 7.995316 | 14.859 | 14.042 | C8 |
| EPIC220565349 | | 18.702745 | 8.251449 | 15.291 | 14.431 | C8 |
| EPIC220621788 | K2-220 | 12.769862 | 9.516806 | 12.656 | 11.873 | C8 |
| EPIC220643470 | | 12.397556 | 10.020078 | 12.696 | 11.076 | C8 |
| EPIC220650439 | K2-221 | 16.654982 | 10.189687 | 13.343 | 12.703 | C8 |
| EPIC220674823 | K2-106 | 13.079780 | 10.794699 | 12.577 | 12.101 | C8 |
| EPIC220709978 | K2-222 | 16.462280 | 11.753423 | 10.038 | 9.543 | C8 |
| EPIC201295312 | K2-44 | 174.011630 | -2.520880 | 12.782 | 12.189 | C1 |
| EPIC201367065 | K2-3 | 172.334970 | -1.454800 | 13.524 | 12.167 | C1 |
| EPIC201384232 | K2-6 | 178.192250 | -1.198473 | 13.302 | 12.660 | C1 |
| EPIC201403446 | K2-46 | 174.266340 | -0.907270 | 12.485 | 12.029 | C1 |
| EPIC201445392 | | 169.793670 | -0.284371 | 15.726 | 14.609 | C1 |
| EPIC201505350 | K2-19 | 174.960330 | 0.603576 | 13.798 | 13.002 | C1 |
| EPIC201546283 | K2-27 | 171.515170 | 1.230739 | 13.506 | 12.644 | C1 |
| EPIC201549860 | K2-35 | 170.103080 | 1.285951 | 15.556 | 14.366 | C1 |
| EPIC201577035 | K2-10 | 172.121960 | 1.690632 | 13.138 | 12.429 | C1 |
| EPIC201613023 | K2-12 | 173.192050 | 2.244885 | 12.990 | 12.258 | C1 |
| EPIC201677835 | K2-48 | 176.123520 | 3.272426 | 15.288 | 14.277 | C1 |
| EPIC201713348 | K2-36 | 169.449100 | 3.866391 | 12.569 | 11.726 | C1 |
| EPIC201754305 | K2-16 | 175.097250 | 4.557338 | 15.647 | 14.648 | C1 |
| EPIC201828749 | | 175.654340 | 5.894297 | 12.476 | 11.789 | C1 |
| EPIC201912552 | K2-18 | 172.560490 | 7.588404 | 15.005 | 13.496 | C1 |
| EPIC201920032 | | 174.106900 | 7.753100 | 13.779 | 13.068 | C1 |
| EPIC202071401 | | 100.377920 | 20.922860 | 13.947 | 12.719 | C0 |
| EPIC202083828 | K2-26 | 94.206560 | 24.596332 | 15.968 | 14.528 | C0 |
| EPIC202900527 | K2-51 | 246.811160 | -27.957038 | 14.256 | 13.183 | C2 |
| EPIC203771098 | K2-24 | 242.573740 | -24.990350 | 12.222 | 11.275 | C2 |
| EPIC203826436 | K2-37 | 243.451020 | -24.787063 | 13.463 | 12.568 | C2 |
| EPIC204221263 | K2-38 | 240.033580 | -23.189258 | 12.344 | 11.344 | C2,C15 |
| EPIC204890128 | K2-53 | 244.141810 | -20.400517 | 13.473 | 12.634 | C2 |
| EPIC205071984 | K2-32 | 252.426080 | -19.542820 | 13.278 | 12.307 | C2 |
| EPIC205924614 | K2-55 | 333.751940 | -17.250705 | 14.746 | 13.546 | C3 |
| EPIC205944181 | | 333.924920 | -16.563531 | 13.420 | 12.595 | C3 |
| EPIC205947161 | | 340.959690 | -16.462448 | 11.873 | 11.274 | C3 |

**Table B.4 continued from previous page**

| ID | Host Name | R.A. (deg) | Decl. (deg) | B (mag) | V (mag) | Camp |
|---|---|---|---|---|---|---|
| EPIC206011496 | K2-265 | 342.031520 | -14.494678 | 11.972 | 11.187 | C3 |
| EPIC206011691 | K2-21 | 340.303690 | -14.488986 | 14.126 | 12.846 | C3 |
| EPIC206026136 | K2-57 | 342.691720 | -14.069892 | 15.679 | 14.501 | C3 |
| EPIC206026904 | K2-58 | 333.821820 | -14.049809 | 13.317 | 12.378 | C3 |
| EPIC206027655 | K2-59 | 338.942350 | -14.027747 | 15.129 | 14.226 | C3 |
| EPIC206028176 | | 330.300310 | -14.014560 | 12.769 | 12.281 | C3 |
| EPIC206038483 | K2-60 | 338.606190 | -13.731711 | 13.562 | 12.789 | C3 |
| EPIC206044803 | K2-61 | 339.674750 | -13.560013 | 13.689 | 12.991 | C3 |

**Tabela B.5** – Iron Line List (Table 2 of Paper II)

| $\lambda$ (Å) | Species | $\chi$ (eV) | $\log gf$ | *Sensitive* |
|---|---|---|---|---|
| 4088.560 | 26.0 | 3.640 | -1.720 | Y |
| 4091.560 | 26.0 | 2.830 | -2.310 | Y |
| 4365.896 | 26.0 | 2.990 | -2.250 | N |
| 4389.245 | 26.0 | 0.052 | -4.583 | Y |
| 4445.471 | 26.0 | 0.087 | -5.441 | N |
| 4485.970 | 26.0 | 3.640 | -2.530 | Y |
| 4523.400 | 26.0 | 3.650 | -1.960 | N |
| 4556.925 | 26.0 | 3.250 | -2.660 | N |
| 4593.555 | 26.0 | 3.940 | -2.030 | N |
| 4602.001* | 26.0 | 1.608 | -3.154 | Y |
| 4779.439 | 26.0 | 3.415 | -2.020 | Y |
| 4994.129* | 26.0 | 0.915 | -3.080 | Y |
| 5044.211* | 26.0 | 2.851 | -2.058 | Y |
| 5054.642 | 26.0 | 3.640 | -1.921 | N |
| 5127.359* | 26.0 | 0.915 | -3.307 | Y |
| 5127.679 | 26.0 | 0.052 | -6.125 | N |
| 5198.711* | 26.0 | 2.223 | -2.135 | Y |
| 5225.525 | 26.0 | 0.110 | -4.789 | Y |
| 5228.383 | 26.0 | 4.220 | -1.090 | N |
| 5242.491 | 26.0 | 3.634 | -0.967 | Y |
| 5247.050 | 26.0 | 0.087 | -4.946 | Y |
| 5250.208 | 26.0 | 0.121 | -4.938 | Y |
| 5250.650* | 26.0 | 2.197 | -4.938 | Y |
| 5295.312 | 26.0 | 4.415 | -1.490 | N |
| 5322.041 | 26.0 | 2.279 | -2.800 | N |
| 5373.709 | 26.0 | 4.473 | -0.770 | Y |
| 5379.574 | 26.0 | 3.694 | -1.514 | Y |
| 5386.334 | 26.0 | 4.154 | -1.740 | N |
| 5406.779 | 26.0 | 4.370 | -1.120 | N |
| 5432.955 | 26.0 | 4.440 | -0.740 | N |
| 5434.520* | 26.0 | 1.010 | -2.110 | Y |
| 5466.396* | 26.0 | 4.371 | -0.565 | Y |
| 5466.987 | 26.0 | 3.573 | -2.230 | N |
| 5522.446 | 26.0 | 4.209 | -1.310 | Y |
| 5546.506 | 26.0 | 4.371 | -1.180 | Y |
| 5560.211 | 26.0 | 4.434 | -1.160 | N |
| 5576.090* | 26.0 | 3.430 | -0.940 | Y |
| 5577.020 | 26.0 | 5.033 | -1.455 | N |
| 5618.633 | 26.0 | 4.209 | -1.276 | N |
| 5636.696 | 26.0 | 3.640 | -2.560 | N |
| 5638.262 | 26.0 | 4.220 | -0.810 | Y |

**Table B.5 continued from previous page**

| $\lambda$ (Å) | Species | $\chi$ (eV) | $\log gf$ | *Sensitive* |
|---|---|---|---|---|
| 5649.987 | 26.0 | 5.100 | -0.800 | N |
| 5651.469 | 26.0 | 4.473 | -1.750 | N |
| 5661.348 | 26.0 | 4.284 | -1.756 | N |
| 5679.023 | 26.0 | 4.652 | -0.750 | Y |
| 5696.089 | 26.0 | 4.548 | -1.720 | N |
| 5701.544* | 26.0 | 2.559 | -2.216 | Y |
| 5705.464 | 26.0 | 4.301 | -1.355 | N |
| 5778.453 | 26.0 | 2.588 | -3.430 | N |
| 5784.658 | 26.0 | 3.396 | -2.532 | N |
| 5793.914 | 26.0 | 4.220 | -1.700 | Y |
| 5809.218 | 26.0 | 3.883 | -1.609 | N |
| 5852.219 | 26.0 | 4.548 | -1.170 | N |
| 5855.076 | 26.0 | 4.608 | -1.478 | N |
| 5905.672 | 26.0 | 4.652 | -0.690 | N |
| 5916.247 | 26.0 | 2.453 | -2.936 | Y |
| 5927.789 | 26.0 | 4.652 | -1.040 | Y |
| 5934.655* | 26.0 | 3.928 | -1.070 | N |
| 5956.694 | 26.0 | 0.859 | -4.605 | Y |
| 5987.065 | 26.0 | 4.795 | -0.212 | N |
| 6003.012* | 26.0 | 3.881 | -1.060 | Y |
| 6005.541 | 26.0 | 2.588 | -3.430 | N |
| 6024.058* | 26.0 | 4.548 | -0.020 | Y |
| 6027.050 | 26.0 | 4.076 | -1.090 | Y |
| 6056.005 | 26.0 | 4.733 | -0.450 | N |
| 6065.482* | 26.0 | 2.609 | -1.530 | Y |
| 6079.009 | 26.0 | 4.652 | -1.100 | Y |
| 6082.711 | 26.0 | 2.223 | -3.573 | Y |
| 6093.644 | 26.0 | 4.607 | -1.300 | N |
| 6096.665 | 26.0 | 3.984 | -1.810 | N |
| 6136.994 | 26.0 | 2.198 | -2.950 | Y |
| 6151.618 | 26.0 | 2.176 | -3.299 | N |
| 6157.728 | 26.0 | 4.076 | -1.220 | N |
| 6165.360 | 26.0 | 4.143 | -1.460 | N |
| 6173.335 | 26.0 | 2.223 | -2.880 | Y |
| 6187.990 | 26.0 | 3.943 | -1.670 | N |
| 6200.313 | 26.0 | 2.609 | -2.437 | Y |
| 6213.430* | 26.0 | 2.223 | -2.520 | Y |
| 6219.281* | 26.0 | 2.198 | -2.433 | Y |
| 6226.736 | 26.0 | 3.883 | -2.100 | N |
| 6229.232 | 26.0 | 2.840 | -2.810 | N |
| 6240.646 | 26.0 | 2.223 | -3.233 | Y |
| 6252.555* | 26.0 | 2.404 | -1.687 | Y |
| 6265.134* | 26.0 | 2.176 | -2.550 | Y |
| 6270.225 | 26.0 | 2.858 | -2.540 | Y |
| 6271.279 | 26.0 | 3.332 | -2.703 | Y |
| 6380.743 | 26.0 | 4.186 | -1.376 | N |
| 6392.539 | 26.0 | 2.279 | -4.030 | N |
| 6393.610* | 26.0 | 2.420 | -1.650 | Y |
| 6400.000* | 26.0 | 3.600 | -0.290 | Y |
| 6593.871 | 26.0 | 2.433 | -2.422 | Y |
| 6597.561 | 26.0 | 4.795 | -0.980 | N |
| 6625.022 | 26.0 | 1.011 | -5.336 | N |
| 6677.987* | 26.0 | 2.692 | -1.418 | Y |
| 6703.567 | 26.0 | 2.759 | -3.023 | N |
| 6705.102 | 26.0 | 4.607 | -0.980 | N |
| 6710.319 | 26.0 | 1.485 | -4.880 | N |

**Table B.5 continued from previous page**

| $\lambda$ (Å) | Species | $\chi$ (eV) | $\log gf$ | *Sensitive* |
|---|---|---|---|---|
| 6713.745 | 26.0 | 4.795 | -1.400 | N |
| 6725.357 | 26.0 | 4.103 | -2.190 | N |
| 6726.667 | 26.0 | 4.607 | -1.030 | N |
| 6733.151 | 26.0 | 4.638 | -1.470 | N |
| 6739.522 | 26.0 | 1.557 | -4.790 | N |
| 6750.152 | 26.0 | 2.424 | -2.621 | N |
| 6752.707 | 26.0 | 4.638 | -1.204 | N |
| 6793.259* | 26.0 | 4.076 | -2.326 | N |
| 6806.845 | 26.0 | 2.727 | -3.110 | N |
| 6810.263 | 26.0 | 4.607 | -0.986 | N |
| 6837.006 | 26.0 | 4.593 | -1.687 | N |
| 6839.830 | 26.0 | 2.559 | -3.350 | N |
| 6843.656 | 26.0 | 4.548 | -0.860 | N |
| 6858.150 | 26.0 | 4.607 | -0.930 | N |
| 4508.288 | 26.1 | 2.855 | -2.250 | Y |
| 4520.224 | 26.1 | 2.806 | -2.600 | Y |
| 4576.340 | 26.1 | 2.844 | -2.950 | N |
| 4993.358 | 26.1 | 2.807 | -3.620 | N |
| 5197.577* | 26.1 | 3.231 | -2.220 | N |
| 5234.625 | 26.1 | 3.222 | -2.180 | N |
| 5264.812 | 26.1 | 3.230 | -3.130 | N |
| 5325.553 | 26.1 | 3.222 | -3.160 | N |
| 5414.073 | 26.1 | 3.222 | -3.580 | N |
| 5425.257 | 26.1 | 3.200 | -3.220 | N |
| 6084.111 | 26.1 | 3.200 | -3.790 | N |
| 6149.258 | 26.1 | 3.889 | -2.690 | N |
| 6247.557 | 26.1 | 3.892 | -2.300 | N |
| 6369.462 | 26.1 | 2.891 | -4.110 | N |
| 6416.919 | 26.1 | 3.892 | -2.640 | N |

**Tabela B.6** – Stellar Parameters (Table 3 of Paper II)

| ID | $\langle S_{HK} \rangle$ | $\sigma$ | $\langle \log R'_{HK} \rangle$ | $\sigma$ | # Sp | $T_{eff}$ (K) | log g (dex) | A(Fe) (dex) | $\xi$ (km.s$^{-1}$) | $R_{star}$ ($R_\odot$) | $M_{star}$ ($M_\odot$) |
|---|---|---|---|---|---|---|---|---|---|---|---|
| EPIC211319617 | 0.166 | 0.019 | -5.024 | 0.123 | 15 | 5281 ± 54 | 4.77 ± 0.15 | 6.82 ± 0.03 | 0.89 ± 0.29 | 0.68 ± 0.01 | 0.73 ± 0.02 |
| EPIC211331236 | 2.488 | | -4.648 | | 1 | | | | | | |
| EPIC211342524 | 0.259 | | -4.571 | | 1 | 6007 ± 163 | 4.17 ± 0.28 | 7.08 ± 0.11 | 2.53 ± 1.64 | 1.61 ± 0.11 | 1.06 ± 0.05 |
| EPIC211351816 | 0.110 | 0.023 | -5.374 | 0.108 | 7 | 4706 ± 74 | 3.26 ± 0.22 | 7.62 ± 0.07 | 1.44 ± 0.14 | 3.64 ± 0.14 | 1.05 ± 0.08 |
| EPIC211355342 | 0.149 | 0.017 | -5.139 | 0.138 | 9 | 5514 ± 23 | 4.46 ± 0.06 | 7.62 ± 0.03 | 1.02 ± 0.14 | 0.99 ± 0.02 | 0.97 ± 0.02 |
| EPIC211359660 | 0.340 | 0.084 | -4.643 | 0.135 | 6 | | | | | | |
| EPIC211391664 | 0.138 | 0.015 | -4.936 | 0.117 | 8 | | | | | | |
| EPIC211399359 | 0.790 | | -4.378 | | 1 | 5298 ± 65 | 4.88 ± 0.15 | 7.40 ± 0.04 | 2.06 ± 0.31 | | |
| EPIC211401787 | 0.152 | | -4.962 | | 1 | | | | | | |
| EPIC211413752 | 0.334 | | -4.677 | | 1 | 5004 ± 42 | 4.78 ± 0.10 | 7.45 ± 0.02 | 0.74 ± 0.15 | 0.72 ± 0.01 | 0.80 ± 0.02 |
| EPIC211418729 | 0.251 | 0.049 | -4.986 | 0.092 | 2 | 4933 ± 100 | 4.55 ± 0.16 | 7.66 ± 0.06 | 1.43 ± 0.26 | 0.78 ± 0.02 | 0.82 ± 0.02 |
| EPIC211439059 | 0.181 | | -4.953 | | 1 | | | | | | |
| EPIC211442297 | 0.208 | 0.026 | -4.762 | 0.106 | 5 | 5502 ± 42 | 4.40 ± 0.13 | 7.18 ± 0.04 | 1.34 ± 0.31 | 0.86 ± 0.02 | 0.85 ± 0.03 |
| EPIC211490999 | 0.159 | | -5.034 | | 1 | 5452 ± 21 | 4.46 ± 0.08 | 7.44 ± 0.03 | 0.78 ± 0.15 | 0.87 ± 0.01 | 0.91 ± 0.02 |
| EPIC211491383 | 0.143 | | -5.004 | | 1 | | | | | | |
| EPIC211525389 | 0.225 | 0.035 | -4.911 | 0.116 | 23 | | | | | | |
| EPIC211529065 | 0.879 | | -4.378 | | 1 | 4619 ± 67 | 4.29 ± 0.16 | 7.73 ± 0.05 | 0.81 ± 0.26 | 0.75 ± 0.01 | 0.78 ± 0.02 |
| EPIC211562654 | 0.123 | | -5.338 | | 1 | 5390 ± 24 | 4.42 ± 0.08 | 7.50 ± 0.03 | 0.92 ± 0.14 | 0.91 ± 0.03 | 0.89 ± 0.02 |
| EPIC211578235 | 0.374 | | -4.474 | | 1 | 5791 ± 59 | 4.77 ± 0.14 | 7.44 ± 0.04 | 1.29 ± 0.22 | 0.88 ± 0.01 | 0.97 ± 0.02 |
| EPIC211594205 | 0.300 | | -4.692 | | 1 | | | | | | |
| EPIC211645912 | 0.353 | | -4.338 | | 1 | 5791 ± 42 | 4.49 ± 0.09 | 7.30 ± 0.03 | 1.67 ± 0.19 | 0.92 ± 0.01 | 0.98 ± 0.02 |
| EPIC211713099 | 0.194 | | -4.811 | | 1 | 5487 ± 44 | 4.71 ± 0.11 | 7.06 ± 0.03 | 0.43 ± 0.45 | 0.90 ± 0.02 | 0.82 ± 0.02 |
| EPIC211736671 | 0.119 | 0.013 | -5.469 | 0.228 | 20 | 5457 ± 26 | 4.01 ± 0.06 | 7.77 ± 0.02 | 1.09 ± 0.07 | 1.63 ± 0.03 | 1.08 ± 0.01 |
| EPIC211743874 | 0.162 | | -4.854 | | 1 | 5943 ± 98 | 4.09 ± 0.15 | 7.35 ± 0.06 | 1.79 ± 0.36 | 1.36 ± 0.05 | 1.06 ± 0.04 |
| EPIC211770696 | 0.151 | | -4.934 | | 1 | | | | | | |
| EPIC211770795 | 0.574 | | -4.647 | | 1 | 4677 ± 101 | 4.63 ± 0.17 | 7.41 ± 0.05 | 0.59 ± 0.47 | 0.64 ± 0.01 | 0.70 ± 0.02 |
| EPIC211816003 | 0.167 | | -5.012 | | 1 | 5325 ± 47 | 4.51 ± 0.09 | 7.10 ± 0.03 | 0.85 ± 0.22 | 0.78 ± 0.02 | 0.79 ± 0.02 |
| EPIC211818569 | 1.114 | 0.162 | -4.307 | 0.071 | 5 | 4719 ± 30 | 4.35 ± 0.13 | 7.20 ± 0.03 | 1.43 ± 0.16 | | |

**Table B.6 continued from previous page**

| ID | $\langle S_{HK} \rangle$ | $\sigma$ | $\langle \log R'_{HK} \rangle$ | $\sigma$ | # Sp | $T_{eff}$ (K) | log g (dex) | A(Fe) (dex) | $\xi$ (km.s$^{-1}$) | $R_{star}$ ($R_\odot$) | $M_{star}$ ($M_\odot$) |
|---|---|---|---|---|---|---|---|---|---|---|---|
| EPIC211825866 | 0.340 | | -4.566 | | 1 | 5240 ± 42 | 4.50 ± 0.10 | 7.22 ± 0.02 | 0.34 ± 0.24 | 0.72 ± 0.01 | 0.80 ± 0.02 |
| EPIC211886472 | 0.151 | | -4.802 | | 1 | 6547 ± 178 | 4.51 ± 0.18 | 7.33 ± 0.10 | 3.25 ± 1.59 | 1.40 ± 0.09 | 1.29 ± 0.04 |
| EPIC211916756 | 2.864 | | -3.898 | | 1 | | | | | | |
| EPIC211919004 | 0.178 | | -5.026 | | 1 | 5014 ± 35 | 4.34 ± 0.09 | 7.50 ± 0.03 | 0.92 ± 0.16 | 0.81 ± 0.01 | 0.80 ± 0.02 |
| EPIC211929937 | 0.207 | | -4.867 | | 1 | 5423 ± 58 | 4.35 ± 0.17 | 7.51 ± 0.04 | 1.45 ± 0.20 | | |
| EPIC211941472 | 0.144 | | -5.137 | | 1 | | | | | | |
| EPIC211945201 | 0.135 | 0.032 | -5.303 | 0.331 | 33 | | | | | | |
| EPIC211978909 | 0.106 | | -5.436 | | 1 | | | | | | |
| EPIC211990866 | 0.332 | 0.036 | -4.386 | 0.071 | 26 | | | | | | |
| EPIC212006318 | 0.118 | | -5.436 | | 1 | 5828 ± 67 | 4.14 ± 0.11 | 7.41 ± 0.05 | 1.54 ± 0.20 | 1.45 ± 0.05 | 1.05 ± 0.02 |
| EPIC212006344 | 1.799 | | -4.645 | | 1 | | | | | | |
| EPIC212008766 | 0.294 | | -4.707 | | 1 | 4988 ± 27 | 4.34 ± 0.07 | 7.22 ± 0.02 | 0.54 ± 0.13 | 0.72 ± 0.01 | 0.74 ± 0.02 |
| EPIC212012119 | 0.839 | | -4.277 | | 1 | 4726 ± 42 | 4.26 ± 0.10 | 7.42 ± 0.03 | 0.64 ± 0.14 | 0.70 ± 0.01 | 0.73 ± 0.02 |
| EPIC212069861 | 2.371 | | -4.740 | | 1 | | | | | | |
| EPIC212110888 | 0.116 | | -5.329 | | 1 | | | | | | |
| EPIC212130773 | 0.134 | | -5.169 | | 1 | 5057 ± 48 | 4.21 ± 0.10 | 7.43 ± 0.03 | 1.01 ± 0.13 | 0.74 ± 0.01 | 0.78 ± 0.02 |
| EPIC212138198 | 0.323 | | -4.682 | | 1 | 4988 ± 34 | 4.36 ± 0.10 | 7.53 ± 0.03 | 0.90 ± 0.14 | 0.78 ± 0.02 | 0.80 ± 0.02 |
| EPIC212157262 | 0.293 | | -4.638 | | 1 | 5403 ± 15 | 4.43 ± 0.05 | 7.62 ± 0.02 | 0.91 ± 0.09 | 0.86 ± 0.01 | 0.95 ± 0.01 |
| EPIC212164470 | 0.144 | | -5.024 | | 1 | 6013 ± 46 | 4.65 ± 0.08 | 7.40 ± 0.03 | 1.49 ± 0.20 | 1.03 ± 0.02 | 1.09 ± 0.02 |
| EPIC212300977 | 0.153 | | -5.115 | | 1 | 5947 ± 31 | 4.37 ± 0.07 | 7.43 ± 0.02 | 1.25 ± 0.13 | 1.08 ± 0.06 | 1.06 ± 0.02 |
| EPIC212357477 | 0.200 | 0.024 | -4.829 | 0.110 | 24 | 5727 ± 27 | 4.51 ± 0.06 | 7.54 ± 0.02 | 1.15 ± 0.14 | | |
| EPIC212393193 | 0.257 | | -4.647 | | 1 | 5993 ± 112 | 4.49 ± 0.22 | 7.10 ± 0.07 | 3.17 ± 1.01 | 1.12 ± 0.10 | 0.98 ± 0.04 |
| EPIC212394689 | 0.160 | 0.036 | -4.878 | 0.143 | 8 | 5391 ± 20 | 4.35 ± 0.06 | 7.34 ± 0.02 | 0.83 ± 0.09 | 0.92 ± 0.03 | 0.85 ± 0.02 |
| EPIC212435047 | 0.163 | | -4.971 | | 1 | 5753 ± 33 | 4.25 ± 0.07 | 7.42 ± 0.03 | 1.15 ± 0.11 | 1.03 ± 0.02 | 0.97 ± 0.02 |
| EPIC212460519 | 1.080 | | -4.526 | | 1 | 4665 ± 87 | 4.51 ± 0.20 | 6.99 ± 0.07 | 1.67 ± 0.51 | | |
| EPIC212521166 | 0.187 | 0.019 | -4.978 | 0.072 | 8 | 4899 ± 29 | 4.27 ± 0.08 | 7.15 ± 0.02 | 0.51 ± 0.16 | 0.66 ± 0.01 | 0.70 ± 0.02 |
| EPIC212585579 | 0.169 | 0.013 | -4.872 | 0.075 | 4 | 5937 ± 57 | 4.59 ± 0.09 | 7.43 ± 0.04 | 1.25 ± 0.25 | 1.00 ± 0.02 | 1.06 ± 0.02 |
| EPIC212586030 | 0.129 | | -5.224 | | 1 | 4615 ± 55 | 3.25 ± 0.14 | 7.63 ± 0.05 | 1.31 ± 0.10 | 3.29 ± 0.12 | 1.00 ± 0.03 |
| EPIC212587672 | 0.146 | | -5.018 | | 1 | 5926 ± 41 | 4.48 ± 0.11 | 7.19 ± 0.03 | 1.48 ± 0.25 | 0.97 ± 0.05 | 0.99 ± 0.02 |
| EPIC212651120 | 0.297 | | -4.339 | | 1 | | | | | | |
| EPIC212689874 | 0.145 | 0.018 | -5.097 | 0.149 | 3 | 5633 ± 34 | 4.27 ± 0.08 | 7.29 ± 0.03 | 0.97 ± 0.17 | 0.95 ± 0.02 | 0.91 ± 0.02 |
| EPIC212697709 | 0.158 | | -5.057 | | 1 | 5704 ± 15 | 4.48 ± 0.04 | 7.70 ± 0.02 | 1.00 ± 0.10 | 1.00 ± 0.03 | 1.07 ± 0.02 |
| EPIC212703473 | 0.190 | | -4.689 | | 1 | 5913 ± 52 | 4.63 ± 0.09 | 7.61 ± 0.04 | 1.47 ± 0.17 | 1.05 ± 0.05 | 1.10 ± 0.02 |
| EPIC212735333 | 0.215 | | -4.793 | | 1 | 5526 ± 23 | 4.36 ± 0.06 | 7.46 ± 0.02 | 1.00 ± 0.10 | 1.04 ± 0.07 | 0.91 ± 0.02 |
| EPIC212768333 | 0.657 | | -4.230 | | 1 | 5114 ± 22 | 4.50 ± 0.05 | 7.32 ± 0.02 | 1.30 ± 0.12 | 0.78 ± 0.02 | 0.79 ± 0.02 |
| EPIC212779596 | 0.375 | 0.218 | -4.905 | 0.445 | 18 | 4664 ± 33 | 4.38 ± 0.12 | 7.23 ± 0.02 | 0.72 ± 0.17 | 0.63 ± 0.01 | 0.68 ± 0.02 |
| EPIC212782836 | 0.159 | | -5.075 | | 1 | 5480 ± 30 | 4.74 ± 0.08 | 6.94 ± 0.02 | 0.92 ± 0.23 | 0.74 ± 0.02 | 0.81 ± 0.02 |
| EPIC212803289 | 0.128 | 0.002 | -5.221 | 0.022 | 2 | | | | | | |
| EPIC213546283 | 0.166 | 0.019 | -4.621 | 0.080 | 11 | 5792 ± 31 | 4.50 ± 0.06 | 7.33 ± 0.02 | 1.02 ± 0.12 | 0.96 ± 0.04 | 0.98 ± 0.02 |
| EPIC213743957 | 1.444 | | -3.883 | | 1 | | | | | | |
| EPIC213920015 | 0.252 | | -4.622 | | 1 | 5609 ± 33 | 4.55 ± 0.06 | 7.28 ± 0.03 | 0.67 ± 0.20 | 0.88 ± 0.03 | 0.92 ± 0.02 |
| EPIC214889247 | 0.316 | | -4.443 | | 1 | 5758 ± 29 | 4.20 ± 0.06 | 7.57 ± 0.02 | 0.92 ± 0.11 | 1.33 ± 0.10 | 1.06 ± 0.03 |
| EPIC215346008 | 0.089 | | -5.781 | | 1 | 4317 ± 69 | 1.75 ± 0.24 | 7.09 ± 0.08 | 2.03 ± 0.12 | 11.95 ± 0.50 | 1.17 ± 0.28 |
| EPIC215938010 | 0.145 | | -5.009 | | 1 | 6151 ± 70 | 4.31 ± 0.11 | 7.50 ± 0.05 | 1.83 ± 0.29 | 1.26 ± 0.15 | 1.17 ± 0.05 |
| EPIC215969174 | 0.231 | | -4.665 | | 1 | 5848 ± 103 | 4.68 ± 0.18 | 7.48 ± 0.07 | 2.42 ± 0.55 | 1.04 ± 0.10 | 1.03 ± 0.04 |
| EPIC216334329 | 0.138 | | -5.187 | | 1 | 5854 ± 47 | 4.20 ± 0.09 | 7.52 ± 0.03 | 1.54 ± 0.15 | 1.34 ± 0.15 | 1.08 ± 0.04 |
| EPIC216468514 | 0.127 | | -5.156 | | 1 | 5983 ± 43 | 4.25 ± 0.09 | 7.46 ± 0.03 | 1.95 ± 0.16 | 1.31 ± 0.14 | 1.11 ± 0.04 |
| EPIC216494238 | 0.128 | 0.037 | -5.787 | 0.998 | 10 | 5674 ± 30 | 4.22 ± 0.07 | 7.69 ± 0.03 | 1.26 ± 0.09 | 1.31 ± 0.10 | 1.08 ± 0.03 |
| EPIC216892056 | 1.055 | | -4.878 | | 1 | | | | | | |
| EPIC217192839 | 0.529 | | -4.503 | | 1 | 4700 ± 40 | 4.34 ± 0.12 | 7.06 ± 0.03 | 0.38 ± 0.34 | 0.61 ± 0.01 | 0.66 ± 0.02 |
| EPIC217393088 | 0.075 | | | | 1 | 5692 ± 108 | 4.40 ± 0.29 | 7.47 ± 0.08 | 3.02 ± 0.71 | 1.18 ± 0.30 | 1.00 ± 0.08 |
| EPIC217671466 | 0.124 | | -5.347 | | 1 | 5734 ± 31 | 4.32 ± 0.08 | 7.94 ± 0.03 | 1.24 ± 0.10 | 1.20 ± 0.11 | 1.14 ± 0.03 |
| EPIC218131080 | 0.153 | | -4.791 | | 1 | 6572 ± 140 | 4.60 ± 0.21 | 7.36 ± 0.07 | 2.60 ± 0.61 | 1.30 ± 0.14 | 1.26 ± 0.06 |
| EPIC218155470 | 0.804 | | -3.769 | | 1 | | | | | | |
| EPIC218621322 | 0.138 | | -5.094 | | 1 | 5805 ± 30 | 4.47 ± 0.06 | 7.17 ± 0.03 | 1.17 ± 0.21 | 0.95 ± 0.05 | 0.94 ± 0.02 |
| EPIC218711655 | 0.115 | | -5.056 | | 1 | 6362 ± 197 | 4.04 ± 0.26 | 7.33 ± 0.10 | 3.18 ± 1.05 | 1.74 ± 0.54 | 1.27 ± 0.16 |
| EPIC218916923 | 0.442 | 0.017 | -4.331 | 0.021 | 2 | 5341 ± 35 | 4.51 ± 0.06 | 7.62 ± 0.03 | 1.25 ± 0.15 | 0.90 ± 0.04 | 0.92 ± 0.02 |
| EPIC219256848 | 0.060 | | | | 1 | | | | | | |
| EPIC219388192 | 0.462 | | -4.288 | | 1 | 5643 ± 42 | 4.15 ± 0.09 | 7.46 ± 0.03 | 1.25 ± 0.12 | 1.37 ± 0.17 | 0.99 ± 0.04 |
| EPIC219420915 | 0.162 | | -4.995 | | 1 | 5655 ± 47 | 4.25 ± 0.10 | 7.63 ± 0.04 | 1.43 ± 0.17 | 1.23 ± 0.15 | 1.03 ± 0.04 |
| EPIC220187552 | 2.595 | | -4.687 | | 1 | | | | | | |
| EPIC220209578 | 0.197 | | -4.886 | | 1 | 5503 ± 98 | 4.23 ± 0.20 | 6.88 ± 0.07 | 2.75 ± 0.92 | 1.13 ± 0.46 | 0.83 ± 0.08 |
| EPIC220294712 | 0.139 | | -5.100 | | 1 | 6078 ± 72 | 4.56 ± 0.12 | 7.19 ± 0.05 | 2.82 ± 0.72 | 1.03 ± 0.07 | 1.04 ± 0.03 |
| EPIC220376054 | 0.141 | 0.032 | -4.771 | 0.215 | 22 | 5795 ± 37 | 4.17 ± 0.07 | 7.51 ± 0.03 | 0.89 ± 0.10 | 1.38 ± 0.12 | 1.06 ± 0.03 |
| EPIC220383386 | 0.154 | 0.021 | -5.117 | 0.155 | 211 | 5203 ± 17 | 4.41 ± 0.05 | 7.46 ± 0.02 | 0.61 ± 0.11 | 0.87 ± 0.02 | 0.83 ± 0.01 |
| EPIC220397060 | 0.162 | | -5.047 | | 1 | 5146 ± 45 | 3.68 ± 0.12 | 7.09 ± 0.04 | 0.96 ± 0.19 | 2.46 ± 0.40 | 1.06 ± 0.11 |
| EPIC220436208 | 0.081 | | | | 1 | 5596 ± 68 | 4.50 ± 0.15 | 7.69 ± 0.06 | 1.44 ± 0.23 | 1.05 ± 0.11 | 1.02 ± 0.04 |
| EPIC220481411 | 0.728 | 0.065 | -4.507 | 0.041 | 19 | 4674 ± 84 | 4.36 ± 0.22 | 7.30 ± 0.06 | 0.76 ± 0.38 | 0.64 ± 0.03 | 0.70 ± 0.02 |
| EPIC220487418 | 0.154 | | -4.992 | | 1 | 6142 ± 40 | 4.72 ± 0.07 | 7.50 ± 0.03 | 1.78 ± 0.18 | | |
| EPIC220493203 | 0.115 | | -5.402 | | 1 | 5059 ± 42 | 2.93 ± 0.18 | 6.86 ± 0.04 | 1.91 ± 0.18 | 6.41 ± 1.86 | 1.42 ± 0.35 |
| EPIC220501947 | 0.347 | | -4.889 | | 1 | 4451 ± 60 | 4.31 ± 0.17 | 7.64 ± 0.04 | 0.17 ± 0.79 | 0.64 ± 0.02 | 0.69 ± 0.02 |
| EPIC220503133 | 0.118 | | -5.254 | | 1 | 4799 ± 45 | 2.69 ± 0.13 | 7.42 ± 0.04 | 1.53 ± 0.09 | 9.32 ± 1.80 | 1.96 ± 0.44 |
| EPIC220504338 | 0.100 | | -5.762 | | 1 | 5627 ± 20 | 4.43 ± 0.07 | 7.76 ± 0.02 | 0.99 ± 0.08 | 1.05 ± 0.07 | 1.05 ± 0.02 |
| EPIC220542353 | 0.198 | | -4.525 | | 1 | | | | | | |
| EPIC220554210 | 0.109 | | -5.508 | | 1 | 5444 ± 38 | 4.66 ± 0.08 | 7.60 ± 0.03 | 1.16 ± 0.17 | 0.89 ± 0.03 | 0.95 ± 0.02 |
| EPIC220565349 | 0.176 | | -4.993 | | 1 | 5328 ± 51 | 4.42 ± 0.18 | 7.23 ± 0.05 | 1.20 ± 0.29 | 0.84 ± 0.11 | 0.82 ± 0.03 |
| EPIC220621788 | 0.135 | 0.024 | -5.203 | 0.155 | 20 | 5474 ± 29 | 4.16 ± 0.06 | 7.40 ± 0.02 | 1.06 ± 0.10 | 1.34 ± 0.12 | 0.92 ± 0.03 |

**Table B.6 continued from previous page**

| ID | $\langle S_{HK} \rangle$ | $\sigma$ | $\langle \log R'_{HK} \rangle$ | $\sigma$ | # Sp | $T_{eff}$ (K) | log g (dex) | A(Fe) (dex) | $\xi$ (km.s$^{-1}$) | $R_{star}$ ($R_\odot$) | $M_{star}$ ($M_\odot$) |
|---|---|---|---|---|---|---|---|---|---|---|---|
| EPIC220643470 | 0.161 | | -5.844 | | 1 | $4476 \pm 41$ | $2.02 \pm 0.13$ | $6.68 \pm 0.04$ | $1.60 \pm 0.11$ | $12.15 \pm 0.24$ | $1.00 \pm 0.17$ |
| EPIC220650439 | 0.177 | | -4.875 | | 1 | $5607 \pm 21$ | $4.39 \pm 0.06$ | $7.51 \pm 0.02$ | $1.01 \pm 0.09$ | $1.02 \pm 0.06$ | $0.96 \pm 0.02$ |
| EPIC220674823 | 0.130 | 0.023 | -5.008 | 0.315 | 30 | $5439 \pm 25$ | $4.29 \pm 0.07$ | $7.52 \pm 0.02$ | $0.99 \pm 0.12$ | $1.10 \pm 0.09$ | $0.90 \pm 0.02$ |
| EPIC220709978 | 0.134 | 0.027 | -4.988 | 0.246 | 45 | $5982 \pm 26$ | $4.48 \pm 0.07$ | $7.13 \pm 0.02$ | $1.54 \pm 0.23$ | $0.98 \pm 0.05$ | $0.99 \pm 0.02$ |
| EPIC201295312 | 0.136 | | -5.129 | | 1 | | | | | | |
| EPIC201367065 | 1.245 | | -4.729 | | 1 | | | | | | |
| EPIC201384232 | 0.195 | | -4.820 | | 1 | | | | | | |
| EPIC201403446 | 0.156 | | -4.804 | | 1 | | | | | | |
| EPIC201445392 | 0.230 | | -5.066 | | 1 | | | | | | |
| EPIC201505350 | 0.304 | 0.032 | -4.632 | 0.060 | 2 | | | | | | |
| EPIC201546283 | 0.143 | 0.029 | -5.183 | 0.182 | 3 | | | | | | |
| EPIC201549860 | 0.706 | | -4.685 | | 1 | | | | | | |
| EPIC201577035 | 0.137 | | -5.211 | | 1 | | | | | | |
| EPIC201613023 | 0.139 | | -5.196 | | 1 | | | | | | |
| EPIC201677835 | 0.584 | | -4.473 | | 1 | | | | | | |
| EPIC201713348 | 0.628 | 0.007 | -4.269 | 0.005 | 2 | | | | | | |
| EPIC201754305 | 0.298 | | -4.828 | | 1 | | | | | | |
| EPIC201828749 | 0.211 | 0.010 | -4.783 | 0.038 | 2 | | | | | | |
| EPIC201912552 | 1.523 | | -4.844 | | 1 | | | | | | |
| EPIC201920032 | 0.134 | | -5.239 | | 1 | | | | | | |
| EPIC202071401 | 0.329 | 0.004 | -4.888 | 0.006 | 2 | | | | | | |
| EPIC202083828 | 1.279 | 0.056 | -3.846 | 0.020 | 2 | | | | | | |
| EPIC202900527 | 0.572 | | -4.045 | | 1 | | | | | | |
| EPIC203771098 | 0.136 | 0.004 | -5.207 | 0.029 | 2 | | | | | | |
| EPIC203826436 | 0.226 | 0.001 | -4.700 | 0.004 | 2 | | | | | | |
| EPIC204221263 | 0.147 | 0.001 | -5.141 | 0.003 | 2 | | | | | | |
| EPIC204890128 | 0.271 | | -4.277 | | 1 | | | | | | |
| EPIC205071984 | 0.193 | 0.003 | -4.831 | 0.015 | 2 | | | | | | |
| EPIC205924614 | 1.014 | | -4.559 | | 1 | | | | | | |
| EPIC205944181 | 0.176 | | -4.997 | | 1 | | | | | | |
| EPIC205947161 | 0.229 | | -4.635 | | 1 | | | | | | |
| EPIC206011496 | 0.227 | 0.007 | -4.792 | 0.022 | 2 | | | | | | |
| EPIC206011691 | 0.950 | 0.037 | -4.706 | 0.017 | 2 | | | | | | |
| EPIC206026136 | 1.029 | | -4.494 | | 1 | | | | | | |
| EPIC206026904 | 0.477 | | -4.516 | | 1 | | | | | | |
| EPIC206027655 | 0.225 | | -4.870 | | 1 | | | | | | |
| EPIC206028176 | 0.133 | | -4.985 | | 1 | | | | | | |
| EPIC206038483 | 0.137 | | -5.210 | | 1 | | | | | | |
| EPIC206044803 | 0.150 | | -5.090 | | 1 | | | | | | |

**Tabela B.7** – Planetary Radii (Table 4 of Paper II)

| Star ID | Planet Name | $\Delta F$ (ppm) | $R_{pl}$ ($R_\oplus$) | $\delta R_{pl}$ ($R_\oplus$) |
|---|---|---|---|---|
| EPIC211319617 | K2-180 b | 1189.0 | 2.64 | 0.05 |
| EPIC211351816 | K2-97 b | 680.0 | 10.97 | 0.49 |
| EPIC211355342 | K2-181 b | 828.0 | 3.26 | 0.08 |
| EPIC211413752 | K2-268 b | 398.0 | 1.60 | 0.08 |
| EPIC211413752 | K2-268 c | 1239.0 | 2.83 | 0.07 |
| EPIC211413752 | K2-268 d | 531.0 | 1.85 | 0.06 |
| EPIC211413752 | K2-268 e | 436.0 | 1.68 | 0.06 |
| EPIC211413752 | K2-268 f | 1025.0 | 2.57 | 0.09 |
| EPIC211418729 | K2-114 b | 16232.0 | 11.49 | 0.21 |
| EPIC211442297 | K2-115 b | 17257.0 | 12.84 | 0.25 |
| EPIC211490999 | K2-372 b | 1093.0 | 3.34 | 0.06 |
| EPIC211529065 | K2-270 b | 286.0 | 1.41 | 0.04 |
| EPIC211529065 | K2-270 c | 1682.0 | 3.41 | 0.06 |
| EPIC211562654 | K2-183 b | 215.2 | 1.51 | 0.06 |

**Table B.7 continued from previous page**

| Star ID | Planet Name | $\Delta F$ (ppm) | $R_{pl}$ ($R_\oplus$) | $\delta R_{pl}$ ($R_\oplus$) |
|---|---|---|---|---|
| EPIC211562654 | K2-183 c | 901.0 | 3.09 | 0.10 |
| EPIC211562654 | K2-183 d | 947.0 | 3.17 | 0.11 |
| EPIC211713099 | K2-271 b | 5513.0 | 7.54 | 0.12 |
| EPIC211736671 | K2-108 b | 973.0 | 5.77 | 0.10 |
| EPIC211743874 | K2-335 b | 314.0 | 2.43 | 0.08 |
| EPIC211770795 | K2-119 b | 1233.0 | 2.48 | 0.06 |
| EPIC211816003 | K2-272 b | 1225.0 | 3.05 | 0.07 |
| EPIC211919004 | K2-273 b | 1434.0 | 3.42 | 0.05 |
| EPIC212006318 | K2-375 b | 298.0 | 2.86 | 0.12 |
| EPIC212008766 | K2-274 b | 974.0 | 2.48 | 0.04 |
| EPIC212012119 | K2-275 b | 968.0 | 2.42 | 0.03 |
| EPIC212012119 | K2-275 c | 1095.0 | 2.57 | 0.04 |
| EPIC212130773 | K2-276 b | 1816.0 | 3.54 | 0.07 |
| EPIC212157262 | K2-187 b | 237.0 | 1.46 | 0.04 |
| EPIC212157262 | K2-187 c | 390.0 | 1.88 | 0.05 |
| EPIC212157262 | K2-187 d | 1224.0 | 3.33 | 0.06 |
| EPIC212157262 | K2-187 e | 748.0 | 2.60 | 0.05 |
| EPIC212164470 | K2-188 c | 520.0 | 2.64 | 0.08 |
| EPIC212300977 | WASP-55 b | 18355.0 | 16.48 | 0.96 |
| EPIC212357477 | K2-277 b | 450.0 | 2.16 | 0.04 |
| EPIC212394689 | K2-189 b | 300.0 | 1.77 | 0.07 |
| EPIC212394689 | K2-189 c | 784.0 | 2.86 | 0.10 |
| EPIC212521166 | K2-110 b | 1361.0 | 2.74 | 0.04 |
| EPIC212587672 | EPIC 212587672 b | 187.0 | 1.46 | 0.10 |
| EPIC212587672 | EPIC 212587672 c | 506.0 | 2.40 | 0.15 |
| EPIC212689874 | K2-195 b | 1118.0 | 3.64 | 0.07 |
| EPIC212689874 | K2-195 c | 747.0 | 2.98 | 0.07 |
| EPIC212697709 | WASP-157 b | 7628.0 | 9.55 | 0.27 |
| EPIC212768333 | K2-198 b | 2737.0 | 4.47 | 0.12 |
| EPIC212768333 | K2-198 d | 1082.0 | 2.81 | 0.08 |
| EPIC212779596 | K2-199 b | 726.0 | 1.82 | 0.04 |
| EPIC212779596 | K2-199 c | 1739.0 | 2.81 | 0.07 |
| EPIC212782836 | K2-279 b | 207.0 | 1.17 | 0.05 |
| EPIC215969174 | HATS-36 b | 13791.0 | 13.32 | 1.33 |
| EPIC216468514 | K2-107 b | 6658.0 | 11.71 | 1.21 |
| EPIC216494238 | K2-280 b | 3463.0 | 8.45 | 0.66 |
| EPIC217192839 | K2-381 b | 209.0 | 0.97 | 0.07 |
| EPIC217192839 | K2-381 c | 947.0 | 2.07 | 0.04 |

**Table B.7 continued from previous page**

| Star ID | Planet Name | $\Delta F$ (ppm) | $R_{pl}$ ($R_\oplus$) | $\delta R_{pl}$ ($R_\oplus$) |
|---|---|---|---|---|
| EPIC217192839 | K2-381 d | 522.0 | 1.53 | 0.04 |
| EPIC217671466 | HATS-9 b | 8470.0 | 12.07 | 1.14 |
| EPIC218131080 | HATS-12 b | 4291.0 | 9.34 | 1.04 |
| EPIC218916923 | K2-139 b | 11093.0 | 10.41 | 0.52 |
| EPIC220321605 | K2-212 b | 1603.0 | 2.58 | 0.13 |
| EPIC220376054 | K2-214 b | 400.0 | 3.02 | 0.28 |
| EPIC220481411 | K2-216 b | 620.0 | 1.84 | 0.73 |
| EPIC220501947 | K2-295 b | 21878.0 | 31.74 | 1.70 |
| EPIC220504338 | K2-113 b | 8378.0 | 10.52 | 0.70 |
| EPIC220522262 | K2-281 b | 12388.0 | 10.05 | 0.95 |
| EPIC220554210 | EPIC 220554210 c | 262.0 | 1.58 | 0.08 |
| EPIC220554210 | K2-282 b | 935.0 | 2.98 | 0.12 |
| EPIC220621788 | K2-220 b | 537.0 | 3.38 | 0.30 |
| EPIC220629489 | K2-283 b | 1967.0 | 3.97 | 0.53 |
| EPIC220650439 | K2-221 b | 312.0 | 1.98 | 0.13 |
| EPIC220674823 | EPIC 220674823 b | 284.7 | 2.03 | 0.17 |
| EPIC220674823 | EPIC 220674823 c | 903.0 | 3.62 | 0.30 |
| EPIC212735333 | K2-197 b | 550.0 | 2.65 | 0.18 |
| EPIC212768333 | K2-198 c | 180.0 | 1.15 | 0.08 |
| EPIC220383386 | HD 3167 b | 294.0 | 1.63 | 0.08 |
| EPIC220383386 | HD 3167 c | 946.0 | 2.92 | 0.08 |